DARK MATTER AND SUPERSYMMETRY IN THE LHC ERA

by

NIRMAL RAJ

A DISSERTATION

Presented to the Department of Physics
and the Graduate School of the University of Oregon
in partial fulfillment of the requirements
for the degree of
Doctor of Philosophy

June 2015

DISSERTATION APPROVAL PAGE

Student: Nirmal Raj

Title: Dark Matter and Supersymmetry in the LHC Era

This dissertation has been accepted and approved in partial fulfillment of the requirements for the Doctor of Philosophy degree in the Department of Physics by:

Dr. Spencer Chang	Chairperson
Dr. Graham Kribs	Advisor
Dr. Stephanie Majewski	Core Member
Dr. James Isenberg	Institutional Representative

and

Scott L. Pratt	Dean of the Graduate School

Original approval signatures are on file with the University of Oregon Graduate School.

Degree awarded June 2015

DISSERTATION ABSTRACT

Nirmal Raj

Doctor of Philosophy

Department of Physics

June 2015

Title: Dark Matter and Supersymmetry in the LHC Era

We report investigations of physical possibilities beyond the Standard Model, performed in the years between Runs I and II of the Large Hadron Collider (LHC).

First, we explore the feasibility of using a hadron collider to unmask hidden sectors by means of a novel signal, the "monocline". Dilepton production provides the cleanest channel to anticipate a monocline. A compelling sector to seek is dark matter with scalar messengers coupling it to standard fermions. We present current bounds from dilepton spectrum measurements at the LHC and make predictions for sensitivities at Run II of the LHC as well as at a future 100 TeV collider.

Second, we corner the space of parameters of supersymmetric frameworks with an appreciable Yukawa coupling between the Higgs fields and a gauge singlet, the so-called Fat Higgs and λ-SUSY models, in the context of the discovery of the 125 GeV Higgs particle. These models are motivated by their alleviation of the electroweak fine-tuning that supersymmetry breaking entails, via raising the tree-

level quartic coupling Higgs boson. Heavy Higgs scalars that couple strongly to the standard Higgs boson induce large radiative corrections to the Higgs quartic coupling, which is crucial to phenomenology; in particular, a very large ratio of the Higgs VEVs ($\tan\beta$), that was previously presumed unfavorable in these models, becomes viable and can be probed by future experiments. In such regions, the most stringent limits come from dark matter constraints on the lightest neutralino.

Finally, we place limits on colored scalar production at the LHC in supersymmetric models where gauginos acquire both Dirac and Majorana masses, that we call "mixed gauginos". While it was known that purely Dirac gluinos were less constrained by LHC searches than their purely Majorana counterparts, we find that the constraints further weaken or strengthen depending on which of the "mixed" colored fermions acquires a Majorana mass. Also explored are the effects on squark production of turning on Majorana masses for electroweak gauginos.

This dissertation consists of previously published and unpublished co-authored material.

CURRICULUM VITAE

NAME OF AUTHOR: Nirmal Raj

GRADUATE AND UNDERGRADUATE SCHOOLS ATTENDED:

University of Oregon, Eugene, Oregon
Indian Institute of Technology Madras, Chennai, India

DEGREES AWARDED:

Doctor of Philosophy in Physics, 2015, University of Oregon
Bachelor of Technology in Engineering Physics, 2009, Indian Institute of Technology Madras

AREAS OF SPECIAL INTEREST:

Particle Physics, Cosmology, Astrophysics

PROFESSIONAL EXPERIENCE:

Graduate Research Assistant,
University of Oregon, 06/2012 - 06/2015
Graduate Teaching Fellow,
University of Oregon, 09/2009 - 06/2015

GRANTS, AWARDS AND HONORS:

PITT PACC Travel Award, PHENO 2014 , University of Pittsburgh

Most Exciting Presentation Prize, SLAC Summer Institute 2014, SLAC, Menlo Park

PUBLICATIONS:

A. Menon, N. Raj, "A 125 GeV Fat Higgs: Opening the window to large $\tan\beta$", In press.

W. Altmanshoffer, P. Fox, R. Harnik, G. Kribs, N. Raj, "Dark matter signals in dilepton production at hadron colliders", Accepted at Phys. Rev. D, arXiv: 1411.6743 [hep-ph].

G. Kribs, N. Raj, "Mixed gauginos sending mixed messages to the LHC", Phys. Rev. D **89**, 055011 (2014), arXiv: 1307.7197 [hep-ph].

S. Chang, C. Newby, N. Raj, C. Wanotoyoroj, "Revisiting theories with enhanced higgs couplings to weak gauge bosons", Phys. Rev. D **86**, 095015 (2012), arXiv: 1207.0493 [hep-ph].

ACKNOWLEDGEMENTS

I am indebted to the following people for the richness of my PhD experience, and for contributing to the pleasure with which I shall reminisce about it.

For her unflagging support and courage that I fed off of, my mother, Santhi;

for ever stoking in me a curiosity about the world, and for his friendship, my father, Krishna Raj;

for her fierce confidence in me throughout my grad student days, and a love that is bottomless, my fiancée, Shyamala Venkataramani;

for pointing the way to Oregon and his constant inquiries into my well-being and academic condition, Rajesh Narayanan;

for suggesting particle physics, thus opening the portal to its untrammeled delight, John Toner;

for readily extending his guidance in the infancy of my research, and his kind patronage through the years, Nilendra Deshpande;

for lending me all the benefit of experience, for encouragement and a door that was opened instantly every time I knocked, Arjun Menon;

for a collaboration of indelible lessons and for helping me grow better as a physicist by interaction and inspiration, Spencer Chang;

for a wondrous course in phenomenology that uncorked a comprehension of what this pursuit was all about, Jim Brau;

for redefining normalcy and intuition in a month's time, and, in a fellow student's phrasing, for making the universe its souvenir, TASI 2013;

for entertaining and instructive discussions, Dave Soper, Rudy Hwa, Zhenyu Han, Dietrich Belitz, Jim Isenberg and my fellow Oregon physics students; particularly, Mark Kuzyk, George de Coster, Imran Mirza and Dileep Reddy, and my particle colleagues Chris Newby, Max Wanotayaroj, Peter Radloff, Liza Brost, Gabriel Barello and Ian Snyder;

for encouragement and for impressing in me why one practises phenomenology, Stephanie Majewski;

for a collaboration educative, elevating and fun, Paddy Fox, Roni Harnik and, with special gratitude, Wolfgang Altmannshofer;

for his exemplary ways and countless illuminating conversations, Sripoorna Bharadwaj.

And Graham Kribs, for practically all of the above and the contagion of a lifetime.

To Jonathan and Esther Driscoll, heroes.

TABLE OF CONTENTS

LIST OF FIGURES

Figure Page

Figure Page

Figure Page

LIST OF TABLES

Table Page

CHAPTER I

INTRODUCTION

The discovery of the long-awaited Higgs boson at the Large Hadron Collider (LHC) in 2012 is a spectacular triumph of science. It sealed the Standard Model (SM) of particle physics as a robust framework for accurately describing all microscopic phenomena observed to date.

Yet the Standard Model cannot be the final theory of Nature. Tellingly, it does not explain the mechanism behind electroweak symmetry breaking (EWSB), the very phenomenon that motivated the SM's original formulation [1]. The SM only succeeds in providing a renormalizable theory for EWSB at low energies (long distances). As we shall see soon, this is one of the numerous instances of the SM being a descriptive theory of effects at long distances as opposed to a predictive theory of causes at short distances – in short, the SM is an *effective* theory.

Furthermore, it fails to accommodate some simple empirical observations:

- *Dark matter.* It is by now well-established that four-fifths of the universe's matter content is uncharged, uncolored and non-baryonic. The SM does not provide a candidate for dark matter consistent with its known properties.

- *Matter-antimatter asymmetry.* There is an enormous imbalance in the number of baryons and antibaryons in the observable universe. If this asymmetry was

triggered primordially by a process of baryogenesis, the SM accounts for it very inadequately.

- *Flavor puzzle.* Matter comes in three generations with peculiar patterns of masses and mixings. Neutrinos are severely light. The origin of CP-violation is unknown. It is not observed in the strong sector, though theoretically allowed. The SM does not inform the reasons behind these.

These shortcomings alone warrant the need for new physics beyond the Standard Model (BSM). The energy scales at which we tend to look for BSM physics is suggested by yet another problem with the SM, a psychological one:

- *Hierarchy problem.* Chiral symmetries and gauge invariances forbid fermions and vectors respectively from acquiring masses in the unbroken electroweak phase. No such forbidding symmetry exists for the scalar Higgs field. Consequently, it is unprotected against quantum corrections from new scales of physics. Denoting such a cutoff scale by $\Lambda_{\rm NP}$ and assuming the Higgs couples to some fermion with strength $\lambda \sim \mathcal{O}(1)$, the correction to the bare Higss mass, by simple dimensional analysis, is

$$\mu^2_{\rm obs} = \mu^2_{\rm bare} + \frac{\lambda^2}{16\pi^2}\Lambda^2_{\rm NP} \quad . \tag{I.1}$$

  Hence we say that the Higgs mass is quadratically sensitive to high cutoff scales. In the SM, the largest corrections come from the top quark, with $\lambda \simeq 1$. The observation of the physical Higgs boson at 125 GeV fixes $\mu^2_{\rm obs} =$

$-(89\ \text{GeV})^2$. If the EWSB scale is separated by many orders from $\Lambda_{\rm NP}$, $\mu^2_{\rm bare}$ must be extraordinarily fine-tuned against it to give the right size of $\mu^2_{\rm obs}$ (for instance, if $\Lambda_{\rm NP}$ is the Planck scale, this fine-tuning is one part in 10^34). It then offends the principle of *naturalness* [2] — the vast hierarchy between the electroweak and the high cutoff scales appears to be maintained by unnatural means [3, 4, 5, 6].

Short of accepting this fine-tuning as a fundamental construct of reality and/or invoking the anthropic principle, one could potentially explain it by two arguments. One, it might be that there are no new scales of physics. This is to say that couplings in the ultraviolet may be scale-invariant and gravity at the Planck scale may be described by something other than quantum fields. Two, some sort of symmetry protects the Higgs mass in the ultraviolet. This automatically necessitates an extension of the SM to accommodate new *partner* fields. $\mu^2_{\rm bare}$ is now quadratically sensitive to the scale at which these parners lie. To keep the fine-tuning to acceptable values, say 1-10%, their masses must be of the order of a TeV.

The TeV scale, also called the weak scale (since it separates the unbroken and broken regimes of electroweak symmetry), is capable of addressing several issues of particle physics simultaneously. Fortunately, it is within the reach of present-day and near-future colliders. And thereby hang the hopes of a major discovery inside our lifetimes.

This dissertation considers BSM models that deal with dark matter, mentioned above, and with supersymmetry, a remedy for many of the Standard Model's ills. The rest of the introduction provides a brief survey of these two themes and will motivate their searches at the weak scale.

Dark Matter

There is growing evidence that roughly 80% of the matter content of the universe, accounting for a quarter of its energy budget, is non-luminous and non-absorptive, viz., dark. Therefore, its constituent particles are most likely electrically neutral. Since all the testimony to its existence (as we shall outline shortly) is gravitational in nature, we understand it has mass. And since no decay of dark matter has been observed, it must be stable on cosmological timescales.

It is unlikely that dark matter is built of baryons. We infer so from three disparate observations: *(1)* measurements of the cosmic microwave bacground (CMB) indicate that dark matter has little non-gravitational interaction with visible matter and radiation [7], *(2)* the negative results of searches for gravitational microlensing from dark compact objects hint that they can make up only a small fraction of the dark matter in our galaxy [8, 9, 10], *(3)* the large-scale structure of the universe implies that its matter density is 30% of the critical density [11]; however, Big Bang nucleosynthesis predicts that baryons make up only 5% of the same [12].

The large-scale structure is an indicant of the velocity dispersion of dark particles. Simulations with $\mathcal{O}(10^9)$ of them suggest that, to be consistent with the observed structures, these particles must be non-relativistic [13]. For this reason, and because most theoretical candidates are naturally non-relativistic in the early universe, *cold dark matter* is the best studied and searched-for model of dark matter.

Despite this accumulation of knowledge of dark matter's character, its microstructure is a mystery. Physicists have constructed a myriad of models satisfying its conditions, with candidates ranging from Weakly Interacting Massive Particles (WIMPs), axions, sterile neutrinos to primordial black holes, to name a few. There have also been alternative theories to explain early anomalies, most notably modifications of gravity such as Modified Newtonian Dynamics (MOND). These models have suffered considerable disadvantage since experimental cosmology entered its era of precision in the 1990s. This section, and Chapters II and III, will focus on a particulate explanation – WIMPs.

The rest of this section is organized as follows. We first enumerate the evidences for dark matter, followed by a discussion of thermal relics, in particular WIMPs. We then conclude with a presentation of the experimental status of WIMP searches.

Evidence

All the evidence amassed in favor of the existence of dark matter has been

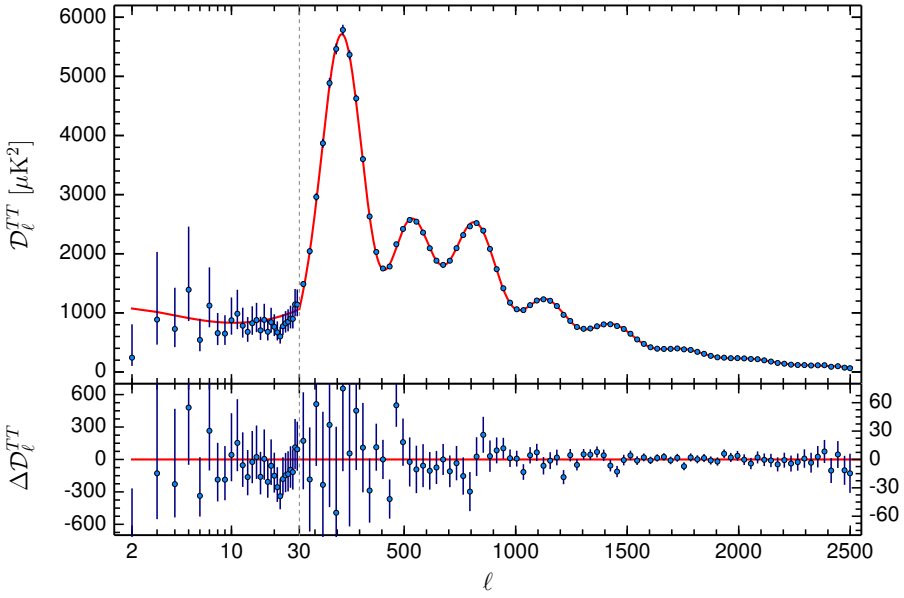

Figure 1.1.: Angular power spectrum of the CMB anisotropies measured by Planck (Fig. 1 from Ref. [7]). The heights and locations of the peaks provide information about cosmological parameters. The best theoretical fit is provided by a model with cold dark matter and the cosmological constant, known as ΛCDM.

through its gravitational interaction with ordinary matter. We collect some salient ones here, not necessarily in historical order.

- In increasing order of precision, the COBE, WMAP and Planck satellites measured the angular power spectrum of thermal anisotropies in the CMB to extract information about the early universe. Fig. 1.1. shows the latest results by Planck. The relative amplitudes of the peaks and their locations

are used to fit the parameters of specific models of cosmology. The best fit overwhelmingly favors cold dark matter.

- Gravitational lensing effects by galaxy clusters enable the observation of objects that would otherwise be hidden in the background. From multiple images near the cluster core (strong lensing) and shape distortions at the outer edges (weak lensing), several cluster masses have been measured. These measurements demonstrate that clusters contain far more invisible mass than the mass of the visible galaxies and gas .

- In the high-velocity merger of the Bullet Cluster 1E0657-56, it is observed that X-ray-emitting hot gas lags behind the subcluster galaxies. This is inferred from weak-lensing maps, which reveal that most of the mass has passed through the collision and now lies ahead of the gas (which is being slowed down by electromagnetic forces). This empirical observation is often touted as the best current evidence of dark matter and rules out many popular models of MOND. As of March 2015, a total of 72 colliding galaxy clusters have been observed with the above features. See [14].

- The existence of dark matter was historically inferred from anomalous speeds of luminous objects in the sky such as globular clusters, galaxies, gas clouds and stars. Galactic rotation curves are a celebrated example of this category. The rotational velocity v of an object orbiting the centre of a galaxy at a

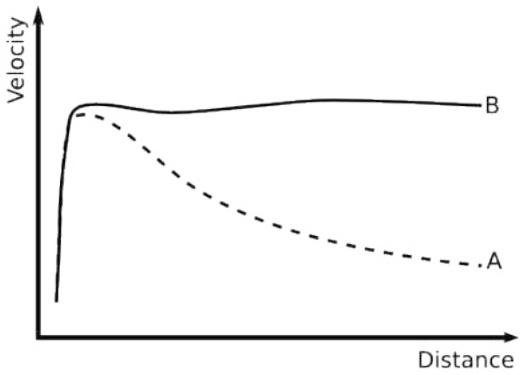

Figure 1.2.: A typical galaxy rotation curve. The dashed curve is what one would expect from Keplerian dynamics, as explained in the text. The solid curve is what is usually observed, suggesting that most of the galaxy's mass in invisible and contained in a halo. This figure is taken from https : //goo.gl/HBqv3l.

radius r, with a galactic mass $M(r)$ inside the orbit, is $v(r) \sim \sqrt{M(r)/r}$. This should lead to the "Keplerian decline" tracked by the dashed curve in Fig. 1.2., which shows the rotation speed of stars in a typical galaxy as a function of orbital radius. Instead, measurements find that in most galaxies $v(r)$ scales as a constant at large r, as shown by the solid line, a "flat rotation curve". This suggests the existence of missing mass, packed in a *dark halo* of mass density $\rho(r) \sim 1/r^2$.

Thermal Relics

We provide now a brief overview of some thermodynamical aspects of the formation of relics from the Big Bang and the process of dark matter freezeout in special relation to WIMPs.

From a thermal point of view, primordial particle species may be classed in two manners: (i) relativistic or *hot* and non-relativistic or *cold*, (ii) particles in equilibrium and particles out of equilibrium. A species of mass m at a temperature T is hot if $T \gg m$ and cold if $T \ll m$. A species A is said to be in thermal equilibrium if the rate of its forward reactions, say its annihilation into various species Z in the thermal bath, $AA \to ZZ$, matches the rate of the backward reactions $ZZ \to AA$. If for some reason the population of A dilutes, the forward process grows rarer, and sustaining equilibrium may be unachievable. These particles then decouple from the ambient plasma.

The rate of interaction of A is given by $\Gamma_A \sim n_A \cdot \sigma \cdot v$, where n_A is its number density, σ its cross-section of interaction and v its typical velocity. The number density falls with the expansion of the universe ($n_A \sim 1/a^3$, where a is the scale factor) and may eventually drop below the requirement for equilibrium; for instance, the visible matter of today is no longer in equilibrium with the background plasma, now made of CMB photons. Occasionally, though, a species may quit equilibrium suddenly, a phenomenon called *freezeout*. This process we will inspect closer in the non-relativistic regime, since it bears directly upon cold dark matter.

The evolution of the number density n_χ of dark matter χ in the early universe is governed by the Boltzmann equation

$$\frac{dn_\chi}{dt} = -3Hn_\chi - \langle \sigma_{\rm ann} v_{\rm rel} \rangle (n_\chi^2 - n_{\rm eq}^2), \tag{I.2}$$

where H is the Hubble parameter, $n_{\rm eq}$ is the equilibrium number density, $\sigma_{\rm ann}$ is the

annihilation cross section of, and $v_{\rm rel}$ the relative velocity between, two χ's. The angular brackets imply thermal averaging. From quantum statistics, one finds that $n_{\rm eq} \sim T^3$ when χ is relativistic ($T \gg m_\chi$). When non-relativistic ($T < m_\chi$), $n_{\rm eq} \sim (m_\chi T)^{3/2} \exp(-m_\chi/T)$, reflecting that χ's abundance is exponentially suppressed with respect to other species, a consequence of the difficulty of producing χ pairs from the thermal bath.

The evolution in I.2 can be understood in three regimes. (i) At $T \gg m_\chi$, n_χ follows $n_{\rm eq}$ closely: χ is in equilibrium with the visible sector through $\chi\chi \to ff$, where f denotes any Standard Model field. (ii) Once the temperature drops below m_χ, the population density plummets exponentially but χ manages to stay in equilibrium. (iii) The rate of expansion of the universe eventually exceeds the interaction rate of χ, at which point it goes out of equilibrium, its abundance freezing out to a fixed value. These three regimes are depicted in Fig. 1.3., which plots the co-moving number density of χ against $X \equiv m_\chi/T$, a measure of time. The solid curve traces the equilibrium number density. The dashed lines depict the number density of the thermal relic that is frozen out, with increasing cross sections resulting in smaller abundances.

The exact point of freezeout can be obtained from the full solution to the Boltzmann equation, which requires numerical integration. However, we can gain a qualitative, albeit accurate, understanding by the following approximation. First, recognizing that in the radiation-dominated era the energy density of the universe

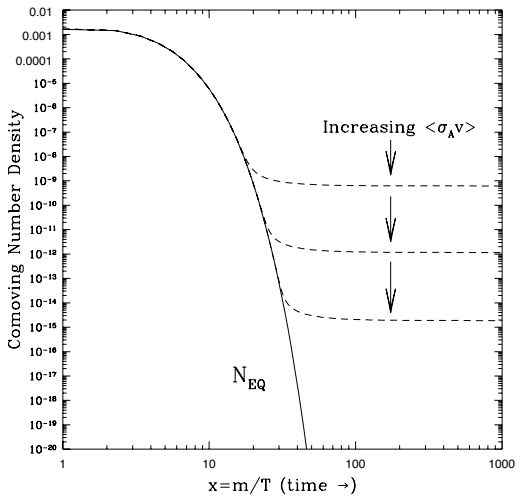

Figure 1.3.: An illustration of dark matter freezeout (Fig. 5 in Ref. [17]). The solid curve depicts the equilibrium number density. The dashed curves depict the number density of the thermal relic, with increasing cross sections resulting in smaller abundances.

scaled as $\rho \sim T^4$, we obtain the Hubble constant from the Friedmann equation as

$$H \sim \frac{\sqrt{\rho}}{M_{\rm Pl}} \sim \frac{T^2}{M_{\rm Pl}}, \tag{I.3}$$

where $M_{\rm Pl}$ is the Planck scale. We then solve for $X_f \equiv m_\chi/T_f$ at freezeout by equating the interaction rate of χ with the expansion rate of the universe:

$$\begin{aligned}
\Gamma_{\rm ann} &\sim H \\
\Rightarrow \quad n_\chi \langle \sigma_{\rm ann} v_{\rm rel} \rangle &\sim \frac{T_f^2}{M_{\rm Pl}} \\
\Rightarrow \quad \left(\frac{m_\chi^2}{X_f}\right)^{3/2} e^{-x_f} \langle \sigma_{\rm ann} v_{\rm rel} \rangle &\sim \frac{m_\chi^2}{X_f^2 M_{\rm Pl}} \\
\Rightarrow \quad X_f &\sim \log\left(m_\chi \langle \sigma_{\rm ann} v_{\rm rel} \rangle M_{\rm Pl} \sqrt{X_f}\right)
\end{aligned} \tag{I.4}$$

X_f is seen only to be logarithmically sensitive to the properties of χ. Plugging in typical values for m_χ ($\sim$ 100 GeV) and $\langle\sigma_{\rm ann}v_{\rm rel}\rangle$ ($\sim 10^{-26}{\rm cm}^3/{\rm s}$), one simply obtains $X_f \simeq 25$, which clearly shows that dark matter emerges already cold/ non-relativistic at the point of decoupling from the plasma.

The current mass abundance of the thermal relic χ, usually given as a fraction of the critical density $\rho_\chi/\rho_{\rm crit}$, is given by

$$\Omega_{\rm DM}h^2 \simeq {\rm const.}\frac{T_{\rm today}^3}{M_{\rm Pl}^3} \simeq 0.1\frac{3\cdot 10^{-26}{\rm cm}^3/{\rm s}}{\langle\sigma_{\rm ann}v_{\rm rel}\rangle} \tag{I.5}$$

where $T_{\rm today}$ is the current CMB temperature. Roughly, $\sigma_{\rm ann} \sim g_\chi^4/m_\chi^2$ by dimensional analysis, where g_χ is the interaction strength of dark matter. If DM is a freezeout particle, we must have $\langle\sigma_{\rm ann}v_{\rm rel}\rangle \sim 3\cdot 10^{-26}$ cm^3/s to obtain the observed relic abundance, $\Omega_{\rm DM}h^2 \simeq 0.1$.

Theoretical efforts to understand weak interactions (like supersymmetry or Little Higgs models) typically introduce new states at the weak scale, with interactions of electroweak strength. These states are referred to as Weakly Interacting Massive Particles (WIMPs). Strikingly, if we admit dark matter to be part of the WIMP program, with $m_\chi \in [10, 1000]$ GeV and $g_\chi \in [0.1, 1]$, we obtain $\langle\sigma_{\rm ann}v_{\rm rel}\rangle \sim 3\cdot 10^{-26}$ cm^3/s. This is the same figure obtained from Eq. I.5, with the quantities $T_{\rm today}$ and $M_{\rm Pl}$! Therefore, WIMPs gratify both particle physics and cosmology, and direct both to the same meeting point of dynamics (couplings) and kinematics (masses) for discovery prospects, a coincidence known in the literature

as the "WIMP miracle". The lightest neutralino of a supersymmetric model is the quintessential WIMP.

WIMP Searches

Searches for WIMPs proceed on three broad fronts – direct, indirect and collider searches [1]. These can be roughly depicted by the diagram in Fig. 1.4.. The principle of direct searches is to let WIMPs scatter off SM particles, generally nucleons, and study the resultant recoil. These experiments will be used to constrain the models discussed in Chapters II and III, and will be the focus of this section. Indirect searches avail the present-day annihilation of WIMP pairs to measure the energy spectra of such end-products as gamma rays, neutrinos, anti-electrons and anti-protons. Collaborations in this line include Fermi LAT (γ), SuperKamiokande and IceCube (ν), and PAMELA and AMS02 (e^+, p^+). Collider searches work in the opposite direction. Dark matter is created from SM particles and its properties sought with signatures involving large missing energy in events. The current best limits are provided by the two LHC collaborations, ATLAS [15] and CMS [16]. In general, the above three strategies probe the parameter space of WIMP models in complementary regions.

The typical velocity v of WIMPs inhabiting the Milky Way orbiting the galactic center is $0.75 \times 10^{-3}c$ near the Solar System. If they scatter off atomic nuclei, the nuclear recoil energy $m_\chi^\odot v^2/2$ (where $m_\chi^\odot$ is the WIMP-nucleus reduced mass)

[1] These are sometimes referred to as "shake it, break it, make it".

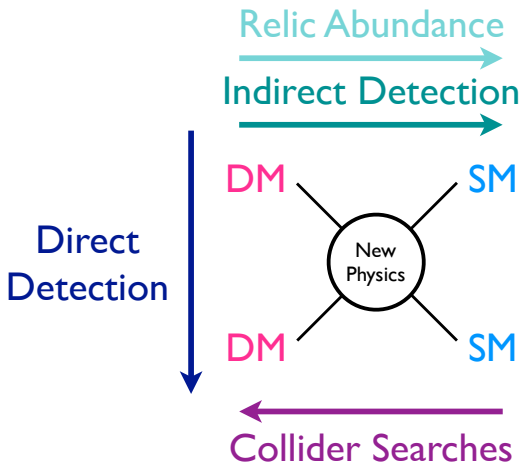

Figure 1.4.: A rough depiction of WIMP searches. The three strategies usually complement each other in WIMP parameter space. This picture is taken from a talk by Pearl Sandick at PHENO 2014.

would be of order $[10^{-6}, 10^{-4}]$ GeV for WIMP masses $\in [10, 10^4]$ GeV. Direct searches are geared to detect WIMPS in this range of recoil energies. Detectors are conventionally made of pure semiconductor or a heavy noble gas. To minimize backgrounds from cosmic rays and natural radioactivity on the Earth's surface, the experiment is carried out in a subterranean laboratory.

The rate of WIMP-nucleon interaction is

$$\begin{aligned} \Gamma_{\chi N} &= \text{cross section } \cdot \text{ local WIMP flux} \\ &= \sigma_{\chi N} \cdot \ n_\chi v \\ &= \left(\frac{\sigma_{\chi N}}{m_\chi}\right) \rho_\chi v \end{aligned} \tag{I.6}$$

The mass density ρ_χ is 0.39 GeV cm^{-3} and v is predicted by taking a Maxwellian

distribution of WIMP velocities. The limits are then presented as contours in a $\sigma_{\chi N} - m_\chi$ plane, assuming elastic scattering and that WIMPs interact with protons and neutrons roughly equally. Since the WIMPs are non-relativistic, spin must be factored in; spin-dependent and spin-independent WIMP currents lead to very different nuclear responses and hence distinguished.

At low WIMP masses, small recoil energies cut down the number of events that pass detector thresholds. At high WIMP masses, we see from Eq. I.6 that $\Gamma_{\chi N} \propto m_\chi^{-1}$ (from which one expects $\sigma_{\chi N}$ to scale as m_χ in the exclusion contours). Both these factors weaken the sensitivity of a search. The maximum sensitivity is achieved for $m_\chi \simeq$ mass of the nucleus. These features are reflected in Fig. 1.5. that shows the 90% C.L. exclusion limits provided by LUX [18], who set the current best bounds on spin-independent direct searches at the end of 85.3 live-days. Similar features are seen in the results of earlier collaborations.

We close with a final remark on direct detection experiments. The techniques above cannot be continued arbitrarily, as they may eventually encounter an irreducible neutrino-induced background (the "neutrino floor"). It has been computed that these experiments, thanks to this background, become insensitive to WIMPs scattering below a cross-section of $[10^{-45}, 10^{-49}]$ cm^3/s for $m_\chi \in [10, 100]$ GeV[19].

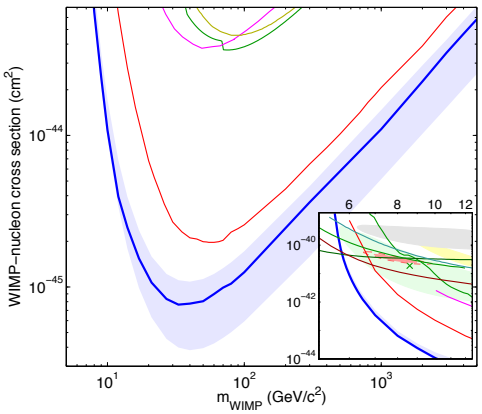

Figure 1.5.: The latest bounds on WIMP detection provided by LUX (Fig. 5 from Ref. [18]), indicated by the blue curve. Also shown are earlier limits set by other collaborations. The shape of the curves is explained in the text.

Supersymmetry

Coleman and Mandula [20] in 1967 reported and proved a series of no-go theorems that forbade fields from having their spacetime coordinates and internal quantum numbers transformed simultaneously. That is, a symmetry group S_G of the S-matrix can only be a direct product of the Poincaré group and an internal symmetry group. This statement presumed that particle statistics was preserved in the transformation under S_G. Six years later, Wess and Zumino [21] identified a Lagrangian that respected what they named *supergauge invariance*, a symmetry that provided a link between the fermions and bosons of the theory. The next year,

Haag, Lopuszański and Sohnius [22] generalized the Coleman-Mandula theorem to include supergauge invariance, which had by then been renamed *supersymmetry*.

Supersymmetry (SUSY) was initially pursued by theorists for its aesthetic value. In time, it was discovered to carry powerful phenomenological merits as well. Chief among them are –

- Its symmetry serves as a custodian of the electroweak scale against corrections from large UV cutoffs, greatly mitigating the fine-tuning discussed earlier [23, 24, 25, 26, 27].

- Sometimes advertised as an indirect evidence of weak scale supersymmetry, it provides the right number of new degrees of freedom (superpartners) to redirect the running of the three gauge couplings and successfully enable their unification at a high scale [28, 26, 29, 30, 31].

- A class of models that conserves R-parity can provide a viable candidate for cold dark matter that may be discovered at the weak scale [32, 33].

While it settles some hefty issues, SUSY may be accompanied by problems of its own. The simplest supersymmetric extensions of the Standard Model reintroduce a residual fine-tuning between the electroweak and superpartner scales; they predict a Higgs boson mass that is too low at tree level; they generically predict rapid decays of protons and large flavor-changing neutral currents, both of which are not

observed. For a more detailed discussion of the problems of supersymmetry, see [140].

In the rest of this section, we present the essentials of building a supersymmetric model, making use of the language of superfields. This is followed by a discussion of soft SUSY-breaking. Next, we apply these two topics to a minimal supersymmetric extension of the SM. We then conclude with the current status of searches for superpartners.

Lagrangians

For a pedagogical review of SUSY model-building, I recommend *A Supersymmetry Primer* by S. Martin [140] – who also enlarged on it in his TASI 2011 lectures [35] – and the textbooks *Weak Scale Supersymmetry* by X. Tata and H. Baer, and *Theory and Phenomenology of Sparticles* by M. Drees, R. M. Godbole and P. Roy.

A supersymmetric transformation continuously transmutes the fermions and bosons of a theory, and a supersymmetric theory is one in which the transformation leaves the action invariant. Implicit in this statement is the assumption that the fermionic and bosonic degrees of freedom (DOFs) are equinumerous — an assumption worth testing.

Imagine a simple theory with a complex scalar $\phi(x)$ and a Weyl fermion $\psi_a(x)$, both massless. The index a $(= 1, 2)$ is a left-handed spinor index; in the following, a dotted index would denote a right-handed spinor index. When off-shell, $\phi(x)$ has two DOFs, a count that does not change when the scalar goes off-shell, with

the DOFs now associated with the polarization states. On the other hand, as it is complex and contains two components, $\psi_a(x)$ has four DOFs off-shell. On-shell, its canonical conjugate momentum $\pi(x) \sim \psi^\dagger_{\dot{a}}(x)$, eliminating two DOFs. In summary, the number of fermionic and bosonic DOFs are equal on-shell but not off-shell. Fortunately, we may mend this mismatch by introducing a scalar field, F, such that it has the customary two DOFs off-shell, but has no dynamical evolution so that it vanishes on-shell: $F = 0$. Such a non-propagating field – an *auxiliary field* – is an essential ingredient of all supersymmetric theories and is paramount to our (limited) understanding of supersymmetry breaking mechanisms, an instance of which occurs in the introductory passages of Chapter IV.

The Lagrangian for our simple theory, known as the Wess-Zumino model [21] can now be written as

$$\mathcal{L} = -\partial^\mu \phi^* \partial_\mu \phi + i\psi^\dagger \overline{\sigma}^\mu \partial_\mu \psi + F^* F. \tag{I.7}$$

One then imposes the following set of supersymmetric transformations mapping bosonic fields to fermionic, and vice-versa:

$$\begin{aligned} \delta\phi = \epsilon\psi, \qquad & \delta\phi^* = \psi^\dagger \epsilon^\dagger; \\ \delta\psi_\alpha = -i(\sigma^\mu \epsilon^\dagger)_\alpha \partial_\mu \phi + \epsilon_\alpha F, \qquad & \delta\psi^\dagger_{\dot{\alpha}} = i(\epsilon\sigma^\mu)_{\dot{\alpha}} \partial_\mu \phi^* + \epsilon^\dagger_{\dot{\alpha}} F^*; \\ \delta F = -i\epsilon^\dagger \overline{\sigma}^\mu \partial_\mu \psi, \qquad & \delta F^* = i\partial_\mu \psi^\dagger \sigma^\mu \epsilon. \end{aligned} \tag{I.8}$$

Here, ϵ_α, the infinitesimal parametrizer of the continuous transfomations above, is a Weyl spinor – the hallmark of supersymmetry. It can be seen that applying Eq. I.8

to Eq. I.7 fetches us an infinitesimal shift in the Lagrangian given by

$$\delta\mathcal{L} = -\partial_\mu \left(\epsilon\sigma^\nu\overline{\sigma}^\mu\psi\, \partial_\nu\phi^* + \epsilon\psi\, \partial^\mu\phi^* + \epsilon^\dagger\psi^\dagger\, \partial^\mu\phi \right), \tag{I.9}$$

which, being a total derivative, gives a vanishing surface integral in the action $S = \int d^4x\ \mathcal{L}$. Therefore, the shift in the action $\delta S = 0$; in words, the supersymmetric transformations have left the action invariant under them. A set of fields $\{\phi, \psi, F\}$ whose SUSY transformations leave the action thus invariant is known as a *chiral supermultiplet*. Similarly, a *vector supermultiplet* is one that contains a vector boson, its fermionic superpartner and a corresponding auxiliary field for matching their off-shell DOFs.

The Lie algebra of a supersymmetry contains anticommutators in addition to the usual commutators. The supersymmetric algebra is

$$\begin{aligned} \{Q_\alpha, Q_\beta\} = 0, \qquad & \{Q^\dagger_{\dot\alpha}, Q^\dagger_{\dot\beta}\} = 0, \\ \{Q_\alpha, Q^\dagger_{\dot\alpha}\} \;&=\; -2\sigma^\mu_{\alpha\dot\alpha} P_\mu, \\ [Q_\alpha, P_\mu] = 0, \qquad & \left[Q^\dagger_{\dot\alpha}, P_\mu\right] = 0 \end{aligned} \tag{I.10}$$

where Q_α and $Q^\dagger_{\dot\alpha}$ are (spinorial) generators of supersymmetry transformations. From the last line of the algebra it can be seen that

$$[Q_\alpha, P^2] = [Q^\dagger_{\dot\alpha}, P^2] = 0 \tag{I.11}$$

It then follows that the component particles of a supermultiplet must have the same mass.

Our discussion has hitherto been confined to a free theory. Interactions quickly complicate the picture. It can be rigorously shown that for an ensemble of chiral supermultiplets (distinguished by the label i), the only masses and interactions that preserve supersymmetry are

$$\begin{aligned}
\mathcal{L} &= -\frac{1}{2}M^{ij}\psi_i\psi_j - \frac{1}{2}M^*_{ij}\psi^{\dagger i}\psi^{\dagger j} - \frac{1}{2}\lambda^{ijk}\phi_i\psi_j\psi_k - \frac{1}{2}\lambda^*_{ijk}\phi^{*i}\psi^{\dagger j}\psi^{\dagger k} - V(\phi,\phi^*); \\
V(\phi,\phi^*) &= M^*_{ik}M^{kj}\phi^{*i}\phi_j + \frac{1}{2}M^{in}\lambda^*_{jkn}\phi_i\phi^{*j}\phi^{*k} \\
&\quad + \frac{1}{2}M^*_{in}\lambda^{jkn}\phi^{*i}\phi_j\phi_k + \frac{1}{4}\lambda^{ijn}\lambda^*_{kln}\phi_i\phi_j\phi^{*k}\phi^{*l},
\end{aligned} \tag{I.12}$$

where one has eliminated the auxiliary fields F_i for dynamical fields. Notice that the fermion-fermion-scalar coupling strengths reappear in the scalar trilinear and quartic couplings in the scalar potential $V(\phi,\phi^*)$. It is always true that, in a supersymmetric theory, the scalar potential is determined entirely by the interactions outside it. This is a feature unique to supersymmetry – it arranges relations between fermions and bosons not only in their masses, but also in their interactions.

Given a set of fields and internal symmetries (both global and local) of a theory, it can become cumbersome to employ Eq. I.12 to determine all its supersymmetric interactions. The situation only complicates when it is necessary to identify interactions allowed by gauge invariances. It would be exceedingly convenient to have a formalism by which the components of a supermultiplet can be grouped together into a single object such that SUSY transformations are implicitly taken

care of. In other words, one should like to characterize a supermultiplet in a *manifestly* supersymmetric fashion.

A *superfield* is just such an entity. A *chiral superfield*, for example, is one in which the components of a chiral supermultiplet are embedded:

$$\begin{aligned} \Phi &= \phi + \sqrt{2}\theta\psi + \theta\theta F \ , \\ \Phi^* &= \phi^* + \sqrt{2}\theta^\dagger\psi^\dagger + \theta^\dagger\theta^\dagger F, \end{aligned} \tag{I.13}$$

where $\theta_\alpha, \theta^\dagger_{\dot{\alpha}}$ are constant Weyl spinors of mass dimension -1/2, constituting the fermionic coordinates of a manifold called *superspace*. The bosonic coordinates of superspace are the usual spacetime coordinates x^μ. A translation in superspace amounts to a supersymmetry transformation, and hence this formalism gives the concept of supersymmetry a simple geometric interpretation, reminiscent of Wilson lines and Wilson loops vis-a-vis gauge transformations.

A *vector superfield* is defined simply as a superfield that is real. In the Wess-Zumino gauge, a general vector superfield can be written as

$$V(x,\theta,\theta^\dagger) = \theta^\dagger\overline{\sigma}^\mu\theta A_\mu(x) + \theta^\dagger\theta^\dagger\theta\lambda(x) + \theta\theta\theta^\dagger\lambda^\dagger(x) + \frac{1}{2}\theta\theta\theta^\dagger\theta^\dagger D(x), \tag{I.14}$$

where $A_\mu(x)$ is a vector field, $\lambda(x)$ is its superpartner fermion and D is an auxiliary field required to match the number of off-shell DOFs of $A_\mu(x)$ and $\lambda(x)$.

If the theory is gauged, could one embed quantities invariant under the gauge transformations in a *field strength superfield*? Consider the components of V in Eq. I.14 in a simple Abelian theory. The gauge-invariants one can construct from

them are the usual field strength $F^{\mu\nu}$, the quantity $(\sigma^\mu \partial_\mu \lambda^\dagger)_\alpha$, and the fermion λ_α and the scalar D by themselves. One can collect them in a field strength superfield as

$$\begin{aligned} \mathcal{W}_\alpha &= \lambda_\alpha + \theta_\alpha D + \frac{i}{2}(\sigma^\mu \overline{\sigma}^\nu \theta)_\alpha F_{\mu\nu} + i\theta\theta(\sigma^\mu \partial_\mu \lambda^\dagger)_\alpha, \\ \mathcal{W}^\dagger_{\dot{\alpha}} &= \lambda^\dagger_{\dot{\alpha}} + \theta^\dagger_{\dot{\alpha}} D - \frac{i}{2}(\overline{\sigma}^\mu \sigma^\nu \theta^\dagger)_{\dot{\alpha}} F_{\mu\nu} + i\theta^\dagger\theta^\dagger(\overline{\sigma}^\mu \partial_\mu \lambda)_{\dot{\alpha}} \end{aligned} \tag{I.15}$$

Observe that $\mathcal{W}_\alpha$ is a chiral superfield. The mass dimensions of Φ, V and $\mathcal{W}_\alpha$ can be read off as 1, 0 and 3/2 respectively.

One now has all the ingredients for setting down a general supersymmetric Lagrangian. Given a set of fundamental superfields, one first constructs all possible composites with them. For instance, owing to the anticommuting nature of θ_α and $\theta^\dagger_{\dot{\alpha}}$, any holomorphic function of a chiral superfield is in itself a chiral superfield. Also, a vector superfield can be built from a chiral superfield Φ and its conjugate Φ^*, e.g., $\Phi^*\Phi$.

Next, one notes that the F terms of chiral superfields and D terms of vector superfields transform as a total derivative under SUSY transformations, leaving the action invariant under them. These terms are therefore the only candidates for inclusion in a SUSY Lagrangian.

Putting the above remarks together, one may now write the most general Lagrangian in a supersymmetric gauged (Abelian) theory as

$$\mathcal{L}_{\text{SUSY}} = \left([W(\Phi_i)]_F + \frac{1}{4}([\mathcal{W}^\alpha \mathcal{W}_\alpha]_F + \text{c.c.} \right) + \left[\Phi_i^* e^{2gq_i V} \Phi_i\right]_D , \tag{I.16}$$

where V is the Lagrangian density on superspace, given by

$$A = \int d^4x \int d^2\theta d^2\theta^\dagger \; V, \tag{I.17}$$

$W(\Phi_i)$ is the most general holomorphic polynomial obtainable from the chiral superfields Φ_i:

$$W(\Phi_i) = L_i\Phi_i + \frac{1}{2}M_{ij}\Phi_i\Phi_j + \frac{1}{6}\Phi_i\Phi_j\Phi_k. \tag{I.18}$$

The subscripts in Eq. I.16 denote the corresponding F and D terms, which may be extracted by the following superspace integrals:

$$\begin{aligned} [S_\chi]_F &= \int d^2\theta \; S_\chi, \\ [S_V]_D &= \int d^2\theta \; d^2\theta^\dagger \; S_V \quad . \end{aligned} \tag{I.19}$$

Ignoring the brackets in Eq. I.16, the first term is known as the *superpotential*, and the last term the *Kähler potential*. These are not field theoretic potentials in the usual sense – their mass dimensions are 3 and 2 respectively, as opposed to 4 – but are useful artefacts from which supersymmetric mass and interaction terms can be derived. The superpotential generates the masses and interactions presented in Eq. I.12. The Kähler potential produces the following terms:

$$\begin{aligned} S \supset \int d^4x \left[\Phi^{*i} e^{2gq_iV}\Phi_i\right]_D &= \int d^4x \; (F^{*i}F_i - \nabla_\mu\phi^{*i}\nabla^\mu\phi_i + i\psi^{\dagger i}\overline{\sigma}^\mu\nabla_\mu\psi_i \\ &\quad -\sqrt{2}gq_i(\phi^{*i}\psi_i\lambda + \lambda^\dagger\psi^{\dagger i}\phi_i) + gq_i\phi^{*i}\phi_i D), \end{aligned} \tag{I.20}$$

where ∇_μ is the usual gauge-covariant derivative.

The second term in Eq. I.16 (ignoring brackets) is called the *gauge kinetic function*. The terms obtained from it are

$$S \supset \int d^4x \left[\mathcal{W}^\alpha \mathcal{W}_\alpha\right]_F = \int d^4x \left(\frac{1}{2}D^2 + i\lambda^\dagger \overline{\sigma}^\mu \partial_\mu \lambda - \frac{1}{4}F^{\mu\nu}F_{\mu\nu}\right) \tag{I.21}$$

Breaking

If Nature is supersymmetric, experiments must have observed superpartners degenerate with the known Standard Model particles. Since this is untrue, SUSY must be a broken symmetry. The mechanism of the symmetry-breaking in the ultraviolet is unknown; nevertheless, one could parametrize it in the infrared by documenting a set of explicit symmetry breaking terms. In so doing, one usually refrains from including terms with dimensionless couplings. Such terms upset the SUSY-dictated relationship between the coupling strengths of the interactions of a given scalar, a relationship crucial for the delicate cancellation of the quadratic divergence of the scalar's mass. Hence these terms would run counter to our wish of having supersymmetry kill an unnatural hierarchy between the electroweak and high cutoff scales. The terms that remain – those with couplings of positive dimension – are, on the other hand, still capable of keeping the scalar masses from exploding and hence constitute *soft supersymmetry breaking*. The authors of [36] rigorously determined the various terms that are allowed in this kind of SUSY-

breaking, and these are given by

$$\mathcal{L}_{\text{soft}} = -\frac{1}{2}M_a\lambda^a\lambda^a - \frac{1}{2}[b_{ij}\ \phi_i\phi_j + m^2_{ij}\ \phi^*_i\phi_j] - \frac{1}{6}A_{ijk}\ \phi_i\phi_j\phi_k - \xi_i\ \phi_i + \text{c.c.} \tag{I.22}$$

The first term gives masses to the fermions of the vector supermultiplets (*gauginos*) for each gauge group, the second and third scalar squared masses, the fourth scalar trilinear couplings, and the last tadpole couplings. $\mathcal{L}_{\text{soft}}$ confers masses to all the scalars and gauginos of a theory even if its gauge bosons and the fermions of the chiral supermultiplets are massless. In supersymmetric extensions of the Standard Model, in the band of energy scales where electroweak symmetry is unbroken but supersymmetry is not, all SM fermions and vectors are massless while their superpartners are not.

The MSSM

The best-studied model of supersymmetry applied to the real world is a simple SUSY extension of the $SU(3)_c \times SU(2)_W \times U(1)_Y$ gauge symmetries with flavor structure, known as the Minimal Supersymmetric Standard Model (MSSM). Its most general superpotential is given by

$$\begin{aligned} W_{\text{MSSM}} &= \mathbf{Y_u}^{ij} H_u Q_i \overline{u}_j - \mathbf{Y_d}^{ij} H_d Q_i \overline{d}_j - \mathbf{Y_e}^{ij} H_d L_i \overline{e}_j + \mu H_u H_d + W_{\text{BLV}}; \\ W_{\text{BLV}} &= \lambda_1^{ijk} \overline{u}_i \overline{d}_j \overline{d}_k + \lambda_2^{ijk} L_i L_j \overline{e}_k + \lambda_3^{ijk} L_i Q_j \overline{d}_k + \mu_*^i L_i H_u, \end{aligned} \tag{I.23}$$

where $i, j, k = \{1, 2, 3\}$ are family indices. W_{MSSM} begets the Yukawa couplings of

the theory and a supersymmetric mass for the Higgs superfields, along with some interactions violating B and L that are collected in $W_{\rm BLV}$.

Unconstrained couplings in $W_{\rm BLV}$ can in general lead to dangerous proton decay processes. One could fix this simply by making the $W_{\rm BLV}$ term vanish. But forcing the B and L violating couplings to go to zero may seem ad hoc: after all, in the Standard Model the conservation of baryon and lepton numbers was an accidental fallout of the gauge structure. One may wish to retain B and L conservation in supersymmetric models with similar elegance. To that end, the authors of [37] imposed a new discrete symmetry called *matter parity*, a multiplicative quantum number assigned to each superfield, defined by

$$\mathbf{M_p} = (-1)^{3B+L} \tag{I.24}$$

Then, all the quark and lepton superfields have $\mathbf{M_p} = -1$ and the Higgs (and gauge) superfields have $\mathbf{M_p} = +1$. If $\mathbf{M_p}$ is conserved, $W_{\rm BLV}$ automatically vanishes while the rest of $W_{\rm MSSM}$ survives. We can apply matter parity to each individual particle of spin s, and define *R-parity* as

$$\mathbf{R_p} \equiv (-1)^{2s}\mathbf{M_p} \tag{I.25}$$

Supersymmetry always commutes with internal symmetries. Therefore, in unbroken SUSY, the only dissimilarity in the quantum numbers of a supermultiplet's components is in the spin. However, if the fermionic co-ordinates $\theta_\alpha, \theta^\dagger_{\dot\alpha}$ themselves transform under some continuous symmetry, the particles embedded in a superfield

are forced to carry different charges under it. The invariance accommodating this is called an *R symmetry*. From this name comes the misnomer "R-parity". The "*R* " is fictitious here since $\mathbf{R_p}$ merely distinguishes between the spins of a supermultiplet. But since it is multiplied by $\mathbf{M_p}$, it has a momentous consequence: it renders $\mathbf{R_p} = -1$ for scalar quarks (*squarks*), scalar leptons (*sleptons*), higgs fermions (*higgsinos*) and gauginos, and $\mathbf{R_p} = +1$ for quarks, leptons, Higgs and gauge bosons. Put differently, $\mathbf{R_p}$ separates Standard Model particles from their superpartners!

A very weighy repercussion of that statement is that, if a SUSY model of the world has *R*-parity built into it, the decay products of a superparticle must always contain an odd number of superparticles. As a consequence, should these particles be produced in an energetic environment (a collider or a young universe), they would undergo a cascade of decays until only the lightest supersymmetric partner (LSP) is left – which will remain stable! If the LSP is electrically neutral, as is the case for the lightest neutralino, it can very well be a dark matter candidate. Moreover, the stability of the LSP will enable it to escape a detector unnoticed[2], carrying with it missing energy. Consequently, a large missing transverse energy (MET) is an important component of the signature of many collider searches for SUSY.

[2]One assumes, reasonably, that the interaction cross-section of dark matter with the detector material of a collider is negligible.

Status

Complete evidence for supersymmetry in Nature would constitute the discovery of all the superpartners in whatever model SUSY is realized in, the establishment of coupling constant relationships decreed by supersymmetry and the revelation of the exact mechanism of supersymmetry breaking. Of these, the latter is a highly unlikely prospect since most models put the scale of SUSY-breaking several decades of energy above the electroweak scale. Nevertheless, a glimpse of the spectrum and interaction behaviour of superpartners at lower scales would go a long way in advancing our understanding of how supersymmetry is realized in Nature.

The presence of superpartners can be inferred either directly by producing them at colliders or indirectly by studying their effects on low energy processes, e.g., through loops. If the principle of naturalness is to serve as a guide, the soft masses, collectively denoted by m_{SUSY}, must be $\mathcal{O}(\text{TeV})$ in order to mitigate fine-tuning between the electroweak scale v and m_{SUSY}. Encouraged by the fact that the TeV scale is within the current reach of technology, collider experiments over the past three decades have undertaken the task of discovery through direct sparticle production.

At the time of writing, no conclusive evidence for the existence of supersymmetric particles has emerged yet. The LHC collaborations ATLAS and CMS have set several limits on sparticle production, chiefly in the Constrained MSSM with R-parity. Many of these bounds are presented in the language of "simplified models",

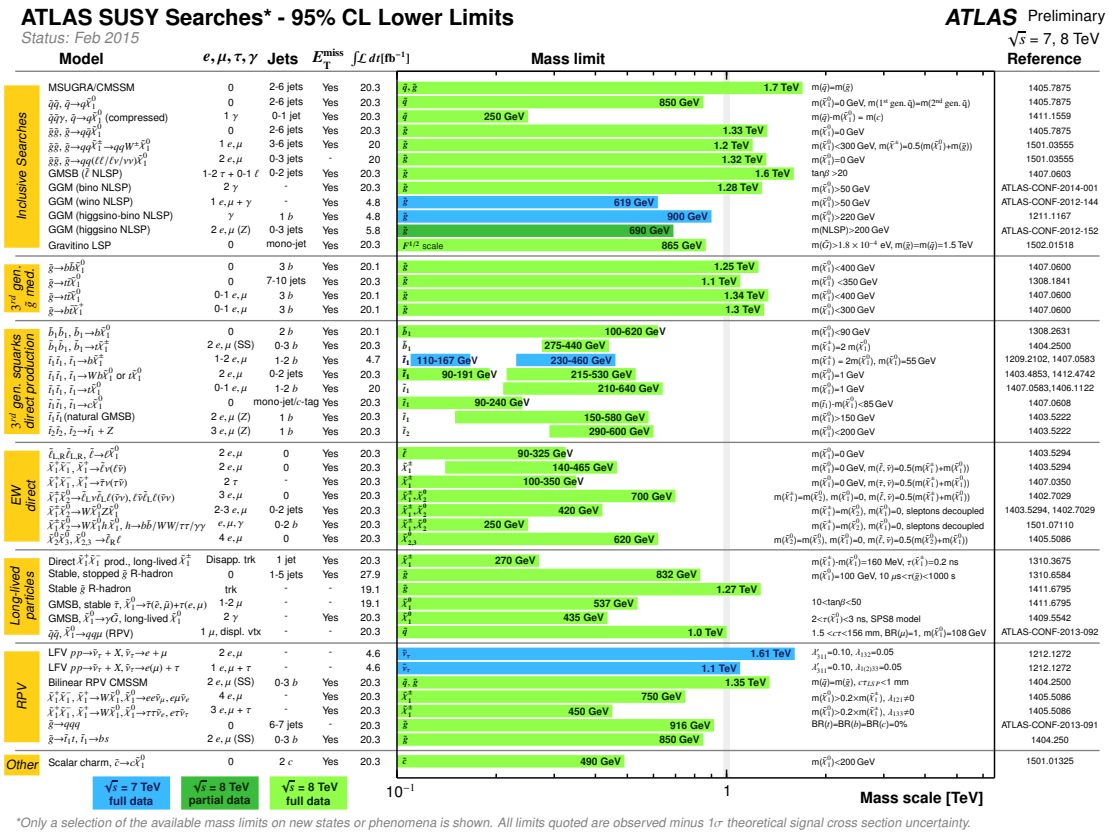

*Only a selection of the available mass limits on new states or phenomena is shown. All limits quoted are observed minus 1σ theoretical signal cross section uncertainty.

Figure 1.6.: Status of searches for supersymmetric particles by the ATLAS collaboration (figure taken from https://goo.gl/7Hvka). A similar plot is published by CMS that can found in their public results website.

in which only particles specific to a certain search are taken into account and the rest of the SUSY spectrum is decoupled. The most recent results of searches conducted by ATLAS are summarized in Fig. 1.6.. A similar summary of CMS searches can be found at [38].

Outline

The theme of this dissertation is colliders probing the TeV scale in search of BSM models in relation to dark matter and supersymmetry. Roughly speeaking, Chapter II concerns the first without reference to the second, Chapter III combines the two topics and Chapter IV separates them again to deal with the second. Specifically, Chapter II explores a simple dark matter model that can be discovered or constrained at hadron colliders, such as at the Run II of the LHC or a future 100 TeV proton-proton collider; Chapter III investigates, in light of the Higgs discovery at 125 GeV, the phenomenology of a supersymmetric model with large Yukawa couplings between the Higgses and a gauge singlet, with emphasis on neutralino dark matter searches; Chapter IV discusses the LHC signals of the production of colored superpartner fermions in a non-minimal model where the breaking of supersymmetry bequeaths gauge superpartners with both Dirac and Majorana masses.

Chapter II contains previously published material co-authored with W. Altmannshofer, P. J. Fox, R. Harnik and G. D. Kribs; Chapter III contains unpublished material co-authored with A. Menon; Chapter IV contains previously published material co-authored with G. D. Kribs.

CHAPTER II

DARK MATTER IN DILEPTONS

This work has appeared as a pre-print at http://arxiv.org/abs/1411.6743. Wolfgang Altmannshofer, Patrick Fox, Roni Harnik and Graham Kribs initiated the project; Nirmal Raj performed the calculations and produced the plots and tables in this chapter.

Now that the Higgs has been discovered, one of the highest priorities for the LHC in the next run is to find (or place strong bounds on) particle dark matter. The standard approach is to look for dark matter pair production as missing transverse momentum (MET) in association with some initial state radiation. Processes of that type could arise from effective operators [39, 40, 41, 42, 43, 44, 45, 46, 47] or UV-complete simplified models involving various types of mediators [42, 44, 46, 48, 49, 50, 51, 52, 53, 54, 55, 56, 57, 58, 59]. One of the principal results from these works is that there is complementarity between the bounds from direct detection and the bounds from the various types of LHC searches for evidence of dark matter and its mediators.

The simplest models contain only a few parameters: the dark matter mass, the mediator mass(es), and the coupling(s) of the dark matter to one (or more) Standard Model (SM) field(s). Consider the case where the dark matter is a fermion,

the mediator is a scalar (but with the $SU(3) \times SU(2) \times U(1)$ quantum numbers of a Standard Model quark), and there is a renormalizable interaction between a light quark, the dark fermion, and the scalar mediator. While there are several constraints, the dominant ones are [50]:

(i) direct detection for small mass splittings between the dark fermion and scalar mediator;

(ii) jets + MET constraints from LHC for large mass splittings caused by scalar mediator production and decay to dark fermions and jets.

These constraints tend to push the dark fermion and scalar mediator masses to larger values with moderate mass splittings. However, the dark matter annihilation cross section, that sets the thermal relic abundance, scales with positive powers of the coupling multiplying *negative* powers of the dark fermion mass (or scalar mediator mass – it doesn't matter since their mass scales are highly correlated). The downward march of the experimental bounds must therefore be accompanied by an upward march of the coupling constant(s), which in some cases, can now be $\gtrsim 1$ [50].

Couplings $\gtrsim 1$ provide a potential new avenue for exploration and discovery at collider experiments. Namely, they open up the possibility of experimentally measurable radiative corrections of dark fermions and mediators to Standard Model processes. There are several types of radiative corrections that we could consider.

(Earlier work that has considered radiative corrections of dark matter include [60, 61, 62]) In this chapter, we focus on the radiative corrections to dilepton production at hadron colliders. For the model, we assume there is a dark fermion (that can acquire Dirac and Majorana masses) as well as scalar messengers: scalar quarks that couple to light quarks and the dark fermion with coupling strength $\lambda_{\tilde{q}}$, and scalar leptons that couple to leptons and the dark fermion with coupling strength $\lambda_{\tilde{\ell}}$.

Dilepton production is well known to be a harbinger for new physics (NP). New gauge bosons (Z's), extra dimensions, and effective operators are well known examples that have already been bounded by ATLAS [63, 64] and CMS [65, 66] using the shape and normalization of dilepton production as a function of the dilepton invariant mass, $\sqrt{\hat{s}} = m_{\ell\ell}$. Our primary interest is the new dark sector "box" contributions to $q\bar{q} \to \ell^+\ell^-$, that are proportional to $\lambda_{\tilde{q}}^2\lambda_{\tilde{\ell}}^2/(16\pi^2)$ in the amplitude, interfering with the usual Drell-Yan contribution from the Standard Model. New kinematical features in the dilepton invariant mass spectrum arise at invariant masses of twice the dark matter mass, $\sqrt{\hat{s}} \simeq 2m_\chi$, from both the real part of the new physics box amplitude as well as an imaginary part for $\sqrt{\hat{s}} > 2m_\chi$. Unlike a Z' search, however, the box contribution does *not* look anything like a resonance. In fact, there can be both constructive and destructive interference effects that depend on the model and the strength of the couplings. At large, but still perturbative couplings (roughly $\lambda_{\tilde{q}}, \lambda_{\tilde{\ell}} \gtrsim 1.4$), we find that the $|\text{box amplitude}|^2$

contribution dominates. This leads to a unique monocline[1] feature in the dilepton invariant mass. Standard "bump-hunter" approaches are not appropriate, and could miss an otherwise observable feature in the spectrum. Like a Z' or extra dimension search, nontrivial contributions to the forward backward asymmetry $A_{\rm FB}$ are also present. Unlike a Z' or extra dimension search, there is further nontrivial angular dependence that can potentially be uncovered using strategies implemented in searches for the new physics contributions to the dijet angular distribution [68].[2]

All of these features arise from the box function contribution to the amplitude that, we stress, cannot be captured by effective four-fermion operators. Instead, it is crucial to "scan" over finite $\sqrt{\hat{s}} = m_{\ell\ell}$ to uncover the dominant features of the box contribution that appear for $\sqrt{\hat{s}} \gtrsim 2m_\chi$. Given that we expect the mediator masses larger than but of the order of the dark matter mass (to obtain the correct relic abundance with non-perturbative couplings), there is no regime where the dark matter or the mediator can be "integrated out" while leaving a finite signal. Indeed, one of our most important results is that the *mass scale* of the dark fermions appears as a kinematical feature in the radiatively corrected dilepton invariant mass distribution. This is a completely distinct approach to measuring a putative dark matter particle mass at a collider.

We say "putative" since we still have no collider probe of the stability of the

[1] In geology, a step-like feature in rock strata consisting of rapid rise and a gentle falloff. A common example is the Waterpocket fold in Capitol Reef National Park, Utah, USA [67].

[2] We thank G. Perez for pointing this out to us.

dark matter. Indeed, we should emphasize that the signal we propose to look for, namely kinematical features in the dilepton invariant mass spectrum and angular distributions consistent with radiative corrections from a new "dark" sector, could arise from other new physics sectors that have nothing to do with dark matter. In this work we focus on one concrete dark matter model.

We have organized the chapter as follows. First, we present the model in Sec. II.1. Next, we discuss the dark sector box contributions to the dilepton invariant mass distribution in Sec. II.2, with angular distributions discussed in Sec. II.2.4. In Sec. II.3 we consider constraints on the model from collider searches, dark matter direct detection experiments, and the dark matter relic abundance. Then, we compare the sensitivity of the dilepton signal with these other constraints on the parameter space in Secs. II.4 and II.5. Specifically, we find that the 20 fb^{-1} 8 TeV dataset from LHC experiments could constrain a modest region of parameter space that, in some cases, is not yet excluded by other constraints. Once the LHC goes up to 14 TeV with larger luminosity, a much more substantial region of the parameter space can be probed. In addition to our projected sensitivities at 14 TeV, we also briefly consider the impact of a 100 TeV collider, finding that it has excellent sensitivity.

The Model: Mixed (Pseudo-Dirac) Fermionic Dark Matter

The model we propose consists of two SM singlet fermions $\chi_{1,2}$, as well as colored

Field	Spin	$SU(3)_c \otimes SU(2)_W \otimes U(1)_Y$	Z_2
χ_1, χ_2	$\mathbf{1/2}$	$(\mathbf{1}, \mathbf{1}, \mathbf{0})$	$\mathbf{-1}$
$\tilde{u}$	$\mathbf{0}$	$(\mathbf{3}, \mathbf{1}, \frac{\mathbf{2}}{\mathbf{3}})$	$\mathbf{-1}$
$\tilde{d}$	$\mathbf{0}$	$(\mathbf{3}, \mathbf{1}, -\frac{\mathbf{1}}{\mathbf{3}})$	$\mathbf{-1}$
$\tilde{\ell} = \tilde{e}, \tilde{\mu}$	$\mathbf{0}$	$(\mathbf{1}, \mathbf{1}, \mathbf{-1})$	$\mathbf{-1}$

Table 2.1.: The field content of our model and the corresponding quantum numbers. To ensure the stability of the dark matter candidate, the Lagrangian is assumed to be invariant under a Z_2 parity.

and uncolored scalars $\tilde{u}$, $\tilde{d}$ and $\tilde{\ell}$ for mediating the interactions between the singlet fermions and the SM fermions. The field content along with their quantum numbers is summarized in Table 2.1.. We impose a Z_2 parity under which the dark matter fermions as well as the mediators are odd, while all SM fields are even. In this way, the lighter SM singlet fermion is stable and therefore a dark matter candidate. We describe the singlet fermions with two two-component (Weyl) spinors χ_A and χ_B. We allow for both Dirac and Majorana masses, a scenario that we refer to as "mixed" dark matter (recently discussed by two of us in a supersymmetric context in [69]). In the case where the Majorana mass is small compared to the Dirac mass, such a scenario is also referred to as pseudo-Dirac dark matter [182, 196]. The

Lagrangian is given in two-component language by

$$\begin{aligned}\mathcal{L} \;=\; & i\chi_A^\dagger \bar{\sigma}^\mu \partial_\mu \chi_A + i\chi_B^\dagger \bar{\sigma}^\mu \partial_\mu \chi_B + \mathcal{L}_{\text{DM mass}} \\ & - \sum_{q=u,d} |D_\mu \tilde{q}|^2 - M_{\tilde{q}}^2 \tilde{q}\tilde{q}^* - (\sqrt{2}\ \lambda_{\tilde{q}} \tilde{q}^* \chi_B^\dagger q_R^\dagger + \text{h.c.}) \\ & - \sum_{\ell=e,\mu} |D_\mu \tilde{\ell}|^2 - M_{\tilde{\ell}}^2 \tilde{\ell}\tilde{\ell}^* - (\sqrt{2}\ \lambda_{\tilde{\ell}} \tilde{\ell}^* \chi_B^\dagger \ell_R^\dagger + \text{h.c.})\,,\end{aligned} \tag{II.1}$$

where $q_R^\dagger$ and $\ell_R^\dagger$ are the right-handed components of the SM quarks and leptons respectively that are $SU(2)_W$ singlets, $\tilde{u}$, $\tilde{d}$ and $\tilde{\ell}$ are the colored and uncolored scalar mediators and $M_{\tilde{u}}$, $M_{\tilde{d}}$ and $M_{\tilde{\ell}}$ are their masses. In the Lagrangian we omitted quartic couplings involving the scalar mediators since they have negligible impact on the phenomenology we discuss below.

We make four assumptions about the model:

1. We assume χ_B interacts with the SM fermions through the mediators, while χ_A does not. This type of interaction is loosely inspired by "mixed" gaugino supersymmetric models [69] where the gaugino interacts with the quarks and squarks, while the fermionic Dirac partner does not. Having said this, we do not assume the interactions or masses are otherwise supersymmetrizable. This can be parameterized in the context of dimensionless supersymmetry breaking [72]. Taking the alternate route of allowing couplings for χ_A would tend to reshuffle the effective strength of the couplings, and this does not change the qualitative results. The only exception to this is the possibility of additional CP-violating phases in the couplings. However, we do not consider

any of the couplings within the model to violate CP in this work, so this does not add anything to our discussion.

2. We assume the hidden sector couples only to one or both of u_R and d_R. It is crucial that we have couplings to the light fermions, though the handedness and isospin is not particularly important. We could also generalize to couplings with all flavors of quarks and leptons, i.e. the mediator couplings $\lambda_{\tilde{u}_i}$, $\lambda_{\tilde{d}_i}$ and $\lambda_{\tilde{\ell}_i}$ could be non-zero for all SM flavors i. This is strongly constrained by flavor changing neutral current processes. For the purposes of this dissertation we assume that the mediator couplings are aligned with the SM Yukawa couplings such that the colored mediators couple only to the first generation of right-handed quarks.[3] We choose right-handed quarks to allow us to separate the effects of a up-type mediator from a down-type mediator. Moreover, due to $SU(2)_W$ invariance, an exact alignment would not be possible for couplings to the left-handed SM quark doublets.

3. We assume the hidden sector couples only to right-handed electrons and muons, e_R and μ_R, through their respective mediators $\tilde{e}$ and $\tilde{\mu}$ with no flavor-violating couplings. This could be trivially extended to include τ_R, but

[3] An alternative approach to control flavor changing neutral currents would be to introduce 3 generations of mediators. This would allow to implement a minimal flavor violation structure, such that the mediator couplings are diagonal in flavor space and each generation of mediators couples to only one generation of SM fermions. Yet another possibility which we do not explore would be to assume that dark matter carries flavor [73, 74, 75, 76, 77].

since di-tau production is considerably more difficult to measure accurately compared with di-electron or di-muon production, we only consider the latter.

4. Finally, we assume there are no CP violating phases in the mass and coupling parameters.

The mass Lagrangian for the dark matter sector, $\mathcal{L}_{\rm DM\,mass}$, is given in two-component notation by

$$\mathcal{L}_{\rm DM\,mass} = \begin{pmatrix} \chi_A & \chi_B \end{pmatrix} \begin{pmatrix} \Delta M & M_d \\ M_d & \Delta M' \end{pmatrix} \begin{pmatrix} \chi_A \\ \chi_B \end{pmatrix} + \text{h.c.} \,, \tag{II.2}$$

where M_d is a Dirac mass and ΔM and $\Delta M'$ are Majorana masses. Although our fourth assumption above makes all mass terms real, we first, for completeness, present general results for the mass eigenstates. From the mixing of χ_A and χ_B, the mass matrix above gets diagonalized by some unitary matrix U, and we obtain eigenmasses given by

$$\begin{aligned} \bar{M}_1^2 &= \frac{1}{2}\Big[|\Delta M|^2 + |\Delta M'|^2 + 2|M_d|^2 \\ &\qquad -\sqrt{4|\Delta M M_d^* + \Delta M'^* M_d|^2 + (|\Delta M|^2 - |\Delta M'|^2)^2)}\Big] \\ \bar{M}_2^2 &= \frac{1}{2}\Big[|\Delta M|^2 + |\Delta M'|^2 + 2|M_d|^2 \\ &\qquad +\sqrt{4|\Delta M M_d^* + \Delta M'^* M_d|^2 + (|\Delta M|^2 - |\Delta M'|^2)^2)}\Big] \end{aligned}$$

Given our assumption that the physical phase in the mass Lagrangian vanishes,

the mass eigenstates are

$$\begin{pmatrix} \chi_1 \\ \chi_2 \end{pmatrix} = \begin{pmatrix} \cos\theta & \sin\theta \\ -\sin\theta & \cos\theta \end{pmatrix} \begin{pmatrix} \chi_A \\ \chi_B \end{pmatrix} , \tag{II.3}$$

with mixing angle given by

$$\cos\theta \;=\; \frac{1}{\sqrt{2}} \left(1 + \frac{\Delta M' - \Delta M}{\sqrt{(\Delta M' - \Delta M)^2 + 4M_d^2}} \right)^{1/2} . \tag{II.4}$$

Given that only one dark fermion χ_B couples to the SM, we can further simplify these expressions. Specifically, we can take $\Delta M' = 0$, which implies the heavier eigenstate $\chi_2 \simeq \chi_A$ is the one that decouples from the SM. This gives the correct Majorana limit, i.e., the lightest dark fermion is the one that maximally couples to the SM. This was explored previously in the context of "mixed gauginos" in supersymmetry [69]. The mass eigenvalues simplify to

$$\begin{aligned} \bar{M}_1^2 &= M_d^2 + \frac{\Delta M^2}{2} - \Delta M \sqrt{M_d^2 + \frac{\Delta M^2}{4}} \\ \bar{M}_2^2 &= M_d^2 + \frac{\Delta M^2}{2} + \Delta M \sqrt{M_d^2 + \frac{\Delta M^2}{4}} . \end{aligned} \tag{II.5}$$

Note that in this limit $|\bar{M}_2| - |\bar{M}_1| = \Delta M$, and with our choice of mixing matrix in Eq. (IV.8) without any additional phases, $\bar{M}_1 < 0$ and $\bar{M}_2 > 0$. In order to avoid the frequent use of minus signs in the following, we define $M_1 \equiv -\bar{M}_1,\ M_2 \equiv \bar{M}_2$ such that $M_1, M_2 > 0$. By holding the lighter eigenmass M_1 constant, we can interpolate between the Dirac and Majorana limits by using ΔM as a control parameter. In particular, $\Delta M = 0$ gives us the pure Dirac limit with $\cos\theta = 1/\sqrt{2}$, and $\Delta M \to \infty$ corresponds to the pure Majorana limit with $\cos\theta = 0$. We will see shortly that this

method of interpolation is most useful for studying the phenomenology of pseudo-Dirac dark matter.

Simplified Models

In addition to the four assumptions about the structure of the model, we will further simplify the parameter space in order to capture the main results of the chapter. We do this using "simplified models", which take the model from the previous section, and consider several distinct simplifying assumptions about the parameters. This is analogous to what is regularly done by the LHC collaborations to examine the impact of their experimental searches on, for example, low energy supersymmetry.

We consider three simplified models which are summarized in Table 2.2.. The difference among these models are:

- Model U has χ coupling exclusively to right-handed up quarks,
- Model D has χ coupling exclusively to right-handed down quarks, and
- Model UD has χ coupling to both right-handed quarks of the first generation.

In all three models, the colored and uncolored scalar mediators are taken degenerate with mass M_ϕ, and all fermion-scalar-dark matter couplings are assumed equal, denoted by λ. The mass of the lighter dark fermion state is denoted by M_χ in all three simplified models. The mass of the heavier dark fermion state is given by $M_\chi + \Delta M$.

Model	Couplings	Mediator masses
U	$\lambda \equiv \lambda_{\tilde{\ell}} = \lambda_{\tilde{u}}$, $\lambda_{\tilde{d}} = 0$	$M_\phi \equiv M_{\tilde{\ell}} = M_{\tilde{u}}$
D	$\lambda \equiv \lambda_{\tilde{\ell}} = \lambda_{\tilde{d}}$, $\lambda_{\tilde{u}} = 0$	$M_\phi \equiv M_{\tilde{\ell}} = M_{\tilde{d}}$
UD	$\lambda \equiv \lambda_{\tilde{\ell}} = \lambda_{\tilde{u}} = \lambda_{\tilde{d}}$	$M_\phi \equiv M_{\tilde{\ell}} = M_{\tilde{u}} = M_{\tilde{d}}$

Table 2.2.: The simplified models considered in the chapter.

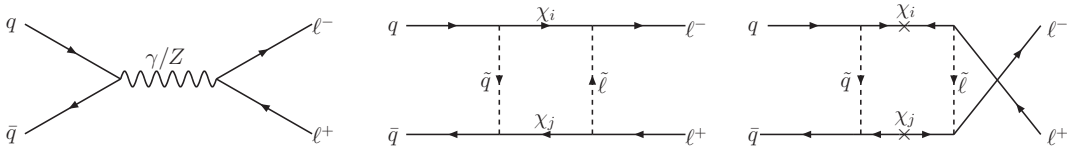

Figure 2.1.: Feynman diagrams of the most important processes that contribute to dilepton production in our model. The tree-level s-channel photon-mediated and Z-mediated diagrams in the SM (left) interfere with the standard box diagrams (center) and the crossed box diagrams (right). The indices on the dark fermions are $i = 1, 2$ and $j = 1, 2$, thus making four combinations each of standard and crossed box diagram.

Dilepton Signatures

Overview

At the LHC, dilepton production, $pp \to \ell^+\ell^-$, is dominated by the Drell-Yan process, $q\bar{q} \to \ell^+\ell^-$, with subdominant contributions from the production of tops,

dibosons, dijets and W+jet. Since our interest is in new physics contributions that interfere with Drell-Yan, we neglect these subdominant processes when computing Standard Model rates. This is a good approximation for at least LHC energies. We also do not incorporate QCD or electroweak NLO corrections, since consistency would require also incorporating these corrections to the new physics contribution, and this is beyond the scope of this dissertation. Hence, Standard Model dilepton production is approximated solely by the tree-level $s-$channel photon– and Z–mediated contributions shown in the left diagram of Fig. 2.1.. (At least some of the NLO corrections would be common to both Drell-Yan and our new physics contribution, dropping out of the ratio.) We also evaluate the couplings at a fixed scale in perturbation theory. RG improvement is straightforward to incorporate, but does not significantly affect our results other than redefining the new physics couplings $\lambda_{\tilde{q}}, \lambda_{\tilde{\ell}}$ relative to the modest RG evolution of the electroweak couplings.

At the one-loop level of our model, the dark fermions and mediators give corrections to dilepton production $pp \to \ell^+\ell^-$ through self-energy corrections, vertex corrections and box diagrams. The box diagram is enhanced relative to the self energies and the vertex corrections by a factor λ^2/g^2, where g is an electro-weak coupling. As we will see below, in the interesting regions of parameter space that can be probed at current and future hadron colliders, the coupling λ is considerably larger than the electroweak couplings g, g'. Self-energy and vertex correction amplitudes can be safely neglected. The gauge boson self-energy diagrams would

contribute to the running of the electroweak coupling at scales above the masses of the dark states. Ref. [78] discusses methods to probe hidden sectors at high energy scales by measuring deviations of the electroweak running from the SM at lower energies. Our approach, by taking only the box diagrams into account, probes the new physics sector directly at the mass scales of the particles involved. This is done by means of examining threshold effects, i.e., new terms in the amplitude that appear when states running in the loop go on-shell. We briefly review some salient aspects of these effects here. For a comprehensive review of dispersion relations in Feynman amplitudes, see [79].

Consider a general one-particle irreducible one-loop diagram of a $2 \to 2$ scattering process. Let the masses of the propagator states that connect the initial and final states be M_n. The amplitude develops an imaginary part for $\sqrt{s} > \sum_n |M_n|$, where s is the Mandelstam variable. This imaginary part is given by the optical theorem, which states that

$$2\,\mathrm{Im}\mathcal{M}(\mathbf{in} \to \mathbf{out}) = \sum_n \int d\Pi_n \mathcal{M}^*(\mathbf{out} \to n)\mathcal{M}(\mathbf{in} \to n)\,, \tag{II.6}$$

where **in** and **out** are the initial and final states respectively, n denotes the intermediate on-shell states and $\int d\Pi_n$ is the integral over the phase space of n.

When applied to the box diagram shown in the center of Fig. 2.1., the imaginary

part appears in the amplitude for $\sqrt{s} > M_{\chi_i} + M_{\chi_j}$ and Eq. (II.6) becomes

$$2\,\mathrm{Im}\mathcal{M}(q\bar{q} \to \ell^+\ell^-) = \sum_{\chi} \int d\Pi_{\chi\chi} \mathcal{M}^*(\ell^+\ell^- \to \chi\chi)\mathcal{M}(q\bar{q} \to \chi\chi)\,. \tag{II.7}$$

In addition to the turn-on of $\mathrm{Im}\mathcal{M}$,[4] the real part of the amplitude, $\mathrm{Re}\mathcal{M}$, undergoes a continuous but sharp rise as well, a consequence of the dispersion relations that follow from the unitarity of the S-matrix [79].

Since the couplings of our model are only to right-handed SM fermions, the new physics amplitude interferes only with that part of the SM amplitude involving right-handed external fermions. That is, if we denote the Standard Model amplitude by,

$$\mathcal{M}_{\mathrm{SM}} = \mathcal{M}_{\mathrm{SM}}^{\mathrm{LL}} + \mathcal{M}_{\mathrm{SM}}^{\mathrm{LR}} + \mathcal{M}_{\mathrm{SM}}^{\mathrm{RL}} + \mathcal{M}_{\mathrm{SM}}^{\mathrm{RR}}\,, \tag{II.8}$$

where the first (second) letter of each superscript denotes the chirality of the initial state quark (final state lepton), then only $\mathcal{M}_{\mathrm{SM}}^{\mathrm{RR}}$ interferes with the new physics contributions given our assumptions about how the new fermions couple in the model. Including the corresponding "left-handed" mediators would allow interference with all of the terms above.

Dilepton Rates: Dirac Case

We now discuss the role of interferences and threshold effects in generating the

[4]Note that even if we allowed the masses $\Delta M, \Delta M', M_d$ and couplings $\lambda_{\tilde{q}}$, $\lambda_{\tilde{\ell}}$ in Eq. (II.2) to be complex, no extra phase would appear in $\mathcal{M}_{\mathrm{box}}$, as only absolute values of these quantities enter: $\mathcal{M}_{\mathrm{box}} \propto |\lambda_{\tilde{q}}|^2 |\lambda_{\tilde{\ell}}|^2$.

various signatures of our model. We first consider the simple case of a dark matter candidate that is a Dirac fermion.

The only box diagram that contributes in this case is shown in the center of Fig. 2.1.. We can then write the total amplitude at the parton level as

$$\mathcal{M}_{\rm total} = \mathcal{M}_{\rm SM} + \mathcal{M}_{\rm box}\,, \tag{II.9}$$

where the Standard Model amplitude $\mathcal{M}_{\rm SM}$ corresponds to the sum of the s-channel photon- and Z-mediated tree-level amplitudes with all polarizations shown in the left diagram of Fig. 2.1.,

$$\mathcal{M}_{\rm SM} = \mathcal{M}_{\rm photon} + \mathcal{M}_{\rm Z}\,. \tag{II.10}$$

Neglecting the masses of the quarks and leptons, we can write the double differential parton level $q\bar{q} \to \ell^+\ell^-$ cross section as

$$\begin{aligned} d\sigma_{\rm total} &\equiv \frac{d^2\sigma_{\rm total}}{d\cos\theta dm_{\ell\ell}} \\ &= d\sigma_{\rm SM} + d\sigma_{\rm int} + d\sigma_{\rm box}^{\rm Re} + d\sigma_{\rm box}^{\rm Im}\,. \end{aligned} \tag{II.11}$$

Here, θ is the angle between the outgoing dilepton axis and incoming diquark axis in the center-of momentum frame. The terms in Eq. (II.11) are given by

$$d\sigma_{\rm SM} = \frac{1}{32\pi s}|\mathcal{M}_{\rm SM}|^2\,, \tag{II.12}$$

$$d\sigma_{\rm int} = \frac{1}{32\pi s}2{\rm Re}(\mathcal{M}_{\rm SM}^{\rm RR}\mathcal{M}_{\rm box}^*), \tag{II.13}$$

$$d\sigma_{\rm box}^{\rm Re} = \frac{1}{32\pi s}|{\rm Re}\mathcal{M}_{\rm box}|^2\,, \tag{II.14}$$

$$d\sigma_{\rm box}^{\rm Im} = \frac{1}{32\pi s}|{\rm Im}\mathcal{M}_{\rm box}|^2\,, \tag{II.15}$$

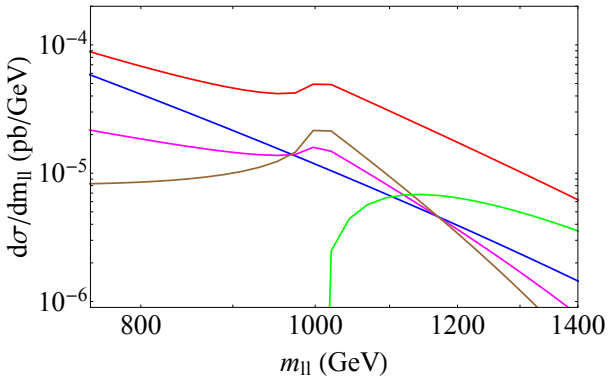

Figure 2.2.: The differential $pp \to \ell^+\ell^-$ cross sections as a function of the dilepton invariant mass in Model U with $\Delta M = 0$ (pure Dirac limit), $\lambda = 1.8$ and $M_\chi = M_\phi = 500$ GeV. Here, blue: $d\sigma_{\rm SM}$, brown: $d\sigma^{\rm Re}_{\rm box}$, green: $d\sigma^{\rm Im}_{\rm box}$, magenta: $d\sigma_{\rm int}$, red: $d\sigma_{\rm total}$, where these quantities are defined in Eqs. (II.11) and (II.12) - (II.15).

where $\mathcal{M}^{\rm RR}_{\rm SM}$ is defined in Eq. (II.8). Our analytic results for the box contributions to the parton level cross section are collected in Appendix A.

As we vary the dilepton invariant mass $m_{\ell\ell}$, we expect, for $m_{\ell\ell} \ll 2M_\chi$, $d\sigma_{\rm total}$ to mimic the behavior of a non-resonant process generated by a higher-dimensional contact operator. The effects of such contact operators in dilepton production are being searched for by CMS [66] and ATLAS [63]. As we approach the kinematic threshold, $m_{\ell\ell} = 2M_\chi$, the contact operator description breaks down and a "monocline" feature arises from the contributions to:

(i) $d\sigma_{\rm int}$, due to threshold effects in ${\rm Re}\mathcal{M}_{\rm box}$,

(ii) $d\sigma^{\rm Re}_{\rm box}$, which for sizeable couplings λ can dominate over $d\sigma_{\rm int}$ due to its containing eight powers of the coupling against four, and

(iii) $d\sigma^{\rm Im}_{\rm box}$, which turns on at $m_{\ell\ell} \geq 2M_\chi$.

We illustrate this behavior with an example in Fig. 2.2., which shows the differential $pp \to \ell^+\ell^-$ cross section integrated over $\cos\theta$ for Model U at the LHC with 8 TeV center of mass energy. To obtain the proton level $pp \to \ell^+\ell^-$ cross section, throughout this work, we convolute the parton level results from Appendix A with MSTW2008NNLO parton distribution functions [80]. In the plot we set the mass splitting of the dark fermions to $\Delta M = 0$, corresponding to the pure Dirac limit. The mediator couplings are set to $\lambda = 1.8$ and we chose the masses of the dark fermions and the mediators as $M_\chi = M_\phi = 500$ GeV. The various curves correspond to $\sigma_{\rm SM}$ (blue); $\sigma^{\rm Re}_{\rm box}$ (brown); $\sigma^{\rm Im}_{\rm box}$ (green); $\sigma_{\rm int}$ (magenta); $\sigma_{\rm total}$ (red); where these quantities are defined in Eqs. (II.11) and (II.12) - (II.15).

Note that the example point shown in Fig. 2.2. falls in a region of parameter space where the new physics signal is dominated by $d\sigma_{\rm box} \propto |\mathcal{M}_{\rm box}|^2$. At lower couplings, the dominant contribution to the signal becomes the interference term $d\sigma_{\rm int}$ as defined in Eqs. (II.13). Numerically, we find that these two regimes are separated by $\lambda \simeq 1.4$ in the presence of a pure Dirac fermion. This comes into consideration when we deal with constraints on our model from dilepton spectrum measurements and in projecting results for future colliders.

The blue, magenta and brown curves in Fig. 2.2. (corresponding to $d\sigma_{\rm SM}$, $d\sigma_{\rm int}$,

and $d\sigma^{\rm Re}_{\rm box}$ respectively) appear to intersect at $m_{\ell\ell} \sim 950$ GeV and $m_{\ell\ell} \sim 1150$ GeV. This intersection is a coincidence for the parameters presented and not a physical effect of our model. It arises from the difference in which initial states contribute to $\mathcal{M}_{\rm SM}$ and $\mathcal{M}_{\rm box}$. Since both up and down quarks contribute to $\mathcal{M}_{\rm SM}$, both these PDFs are convolved with the partonic level rates to obtain $d\sigma_{\rm SM}$. In Model U, only the up quark contributes to $\mathcal{M}_{\rm box}$, hence its PDF alone is convolved with the partonic rates to obtain $d\sigma_{\rm int}$ and $d\sigma^{\rm Re}_{\rm box}$. Therefore, the apparent intersection seen here would be absent if we had presented partonic level rates, or used Model D or Model UD for illustration in Fig. 2.2.. Furthermore, with model U if the coupling is increased (decreased) the point where magenta and brown curves intersect moves up (down), and will not lie on the SM curve. Similarly, if M_ϕ is altered the triple intersection would go away.

Dilepton Rates: Mixed (Pseudo-Dirac) Case

Since a mixed dark matter candidate can be written as two Majorana eigenstates, we first begin with a brief discussion of the Majorana limit, that will be useful in understanding the pseudo-Dirac case. In addition to the standard box diagram, Majorana fermions have a "crossed box" diagram (with clashing fermion flow arrows) contributing at one-loop order, as shown by the right diagram in Fig. 2.1.. The total amplitude becomes the sum

$$\mathcal{M}_{\rm total} = \mathcal{M}_{\rm SM} + \mathcal{M}_{\rm box} + \mathcal{M}_{\rm xbox} \ , \tag{II.16}$$

where $\mathcal{M}_{\rm xbox}$ is the amplitude for the crossed box diagram. Importantly, $\mathcal{M}_{\rm xbox}$

comes with a minus sign relative to $\mathcal{M}_{\rm box}$ due to the different ordering of the external spinors. Thus, the direct and crossed box diagrams interfere destructively, and we expect the new physics effects in the cross section to be much less pronounced in the Majorana case than in the Dirac case. In particular, we find that over large parts of the parameter space the "monocline" feature noticed in the Dirac scenario is washed out by the destructive interference. Even for sizeable couplings $\lambda \gtrsim 1.4$, the largest contribution to the deviation from the Standard Model cross section comes typically from the interference term between the tree and box amplitudes, which carries only four powers of the coupling λ.

We now turn to the most general case of mixed (pseudo-Dirac) dark matter. Four contributions arise from direct box diagrams and four additional contributions from the crossed box diagrams, corresponding to the four combinations of χ_1 and χ_2 in the loop, as shown in Fig. 2.1.. The total amplitude is now given by

$$\mathcal{M}_{\rm total} = \mathcal{M}_{\rm SM} + \sum_{i=1,2}\sum_{j=1,2} (\mathcal{M}^{ij}_{\rm box} + \mathcal{M}^{ij}_{\rm xbox}) \ , \tag{II.17}$$

where $\mathcal{M}^{ij}_{\rm (x)box}$ is the (crossed) box amplitude with χ_i in the upper fermion propagator and χ_j in the lower fermion propagator. It is illustrative to inspect the

analytical form of the direct and crossed box amplitudes:

$$\begin{aligned}\mathcal{M}^{ij}_{\text{box}} &\propto [\bar{u}(p_4)\gamma_\mu P_R u(p_1)][\bar{v}(p_2)\gamma_\nu P_R v(p_3)] \\ &\quad \times \int \frac{d^4q}{(2\pi)^4} \frac{q^\mu (q+p_1+p_2)^\nu}{D_{ij}} \ , \end{aligned} \tag{II.18a}$$

$$\begin{aligned}\mathcal{M}^{ij}_{\text{xbox}} &\propto [\bar{u}(p_3)P_R u(p_1)][\bar{v}(p_2)P_L v(p_4)] \\ &\quad \times \int \frac{d^4q}{(2\pi)^4} \frac{\bar{M}_i \bar{M}_j}{D_{ij}} \ , \end{aligned} \tag{II.18b}$$

where p_1, p_2, p_3, and p_4 are the momenta of the incoming quark, incoming anti-quark, outgoing positron, and outgoing electron, respectively, and D_{ij} is the product of the denominators of the propagators in the loop; finally, $\bar{M}_1 = -M_1$ and $\bar{M}_2 = M_2$ (see Eq. (IV.10)). The chirality projection operators in the Feynman amplitude pick out the $\not{p}$ terms in the propagators of the standard box, and the mass terms in those of the crossed box, which is also indicated by the mass insertions in the right diagram of Fig. 2.1..

In the summation in Eq. (II.17), the combinations with the same dark fermion in the upper and lower propagator $\mathcal{M}^{11}_{\text{box}}+\mathcal{M}^{11}_{\text{xbox}}$ and $\mathcal{M}^{22}_{\text{box}}+\mathcal{M}^{22}_{\text{xbox}}$, are suppressed due to destructive interference as discussed above. This leaves us with $(\mathcal{M}^{12}_{\text{box}} + \mathcal{M}^{12}_{\text{xbox}}) + (\mathcal{M}^{21}_{\text{box}} + \mathcal{M}^{21}_{\text{xbox}})$.

From Eq. (II.18b), we see that the crossed box diagrams with two different dark fermions in the upper and lower propagator come with a relative minus sign with respect to the crossed box diagrams that contain only one dark fermion species (the numerators are $\bar{M}_1\bar{M}_2 = -M_\chi(M_\chi + \Delta M)$, and $\bar{M}_1^2 = M_\chi^2$ or $\bar{M}_2^2 = (M_\chi + \Delta M)^2$,

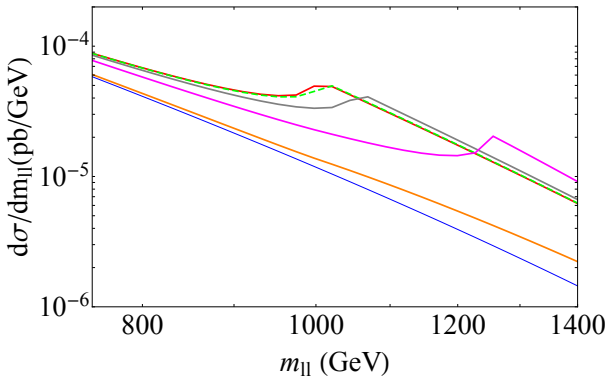

Figure 2.3.: The differential $pp \to \ell^+\ell^-$ cross section as a function of the dilepton invariant mass for a mixed dark matter particle χ, in Model U. Here, $\lambda = 1.8$ and $M_\chi = M_\phi = 500$ GeV. The color code is – blue: $\sigma_{\rm SM}$, red: $\Delta M = 0$ (pure Dirac), green dashed: $\Delta M = 5$ GeV, grey: $\Delta M = 50$ GeV, magenta: $\Delta M = 200$ GeV, orange: $\Delta M \to \infty$ (pure Majorana).

respectively). Therefore, $\mathcal{M}^{12}_{\rm box} = \mathcal{M}^{21}_{\rm box}$ interferes *constructively* with $\mathcal{M}^{12}_{\rm xbox} = \mathcal{M}^{21}_{\rm xbox}$. Consequently, in the mixed dark matter case we expect that the monocline feature in the cross section appears at a dilepton invariant mass of $m_{\ell\ell} \simeq M_1 + M_2 = 2M_\chi + \Delta M$.

The pure Dirac and Majorana limits discussed above can now be more readily understood. When $\Delta M = 0$ (Dirac limit), the monocline feature appears at $m_{\ell\ell} \simeq 2M_\chi$, as seen in Fig. 2.2.. When $\Delta M \to \infty$ (Majorana limit), the monocline feature is at $m_{\ell\ell} \to \infty$ and is not observed. As an illustration, we provide in Fig. 2.3. the dilepton invariant mass distribution in Model U with $\lambda = 1.8$ and

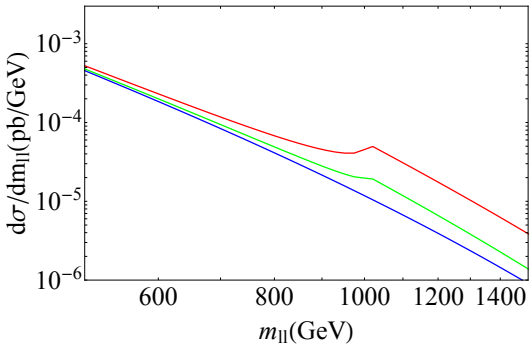

Figure 2.4.: The differential $pp \to \ell^+\ell^-$ cross section as a function of the dilepton invariant mass in Model U. Shown here are the effects of variation in λ keeping $M_\chi = 500$ GeV fixed, with $M_\phi = M_\chi$ and $\Delta M = 0$. Here, red: $\lambda = 1.8$, green: $\lambda = 1.4$, blue: SM.

$M_\chi = M_\phi = 500$ GeV for intermediate values of the dark fermion mass splitting ΔM = 5, 50 and 200 GeV, given by green dashed, grey and magenta curves respectively. The monocline is featured at $m_{\ell\ell} \simeq 1005, 1050$ and 1200 GeV, respectively. For comparison, Fig. 2.3. also shows the pure Dirac (red) and pure Majorana limits (orange). We observe that a splitting of $\Delta M = 5$ GeV, a value that corresponds to the pseudo-Dirac case, results in nearly identical behavior to that of pure Dirac dark matter. To summarize, introducing two Weyl fields in the dark matter sector with the two eigenstates split by a small mass – a scenario called pseudo-Dirac dark matter – can give a dilepton invariant mass distribution that has almost exactly the same features as a pure Dirac dark matter particle in dilepton production.

We end this section by discussing aspects of the dependence of the monocline

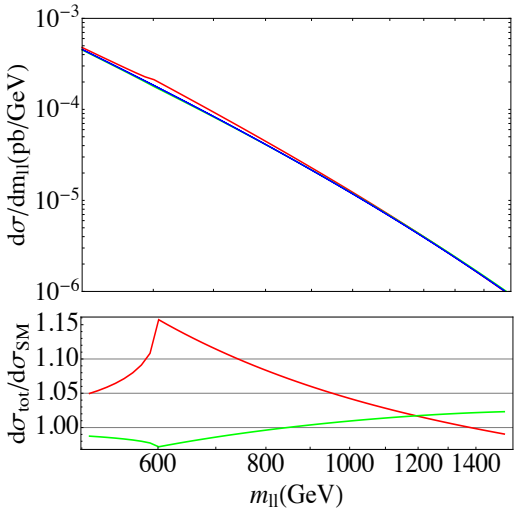

Figure 2.5.: Upper plot: The differential $pp \to \ell^+\ell^-$ cross section as a function of the dilepton invariant mass. Lower plot: the ratio $d\sigma_{\rm tot}/d\sigma_{\rm SM}$ as a function of $m_{\ell\ell}$. We set $\lambda = 1$ and $M_\chi = 300$ GeV, with $M_\phi = M_\chi$ and $\Delta M = 0$. Here red: Model U, green: Model D, blue: SM.

feature on the mediator coupling λ and the dark matter mass. The change in the size of the monocline feature for several values of the coupling λ is shown in Fig. 2.4., where we fix $M_\chi = 500$ GeV and $\Delta M = 0$. The red curve corresponds to $\lambda = 1.8$ and the green curve to $\lambda = 1.4$, with the blue curve depicting the Standard Model LO value. As one would expect, the deviations from SM become less significant as the coupling is decreased.

In Fig. 2.5., we show the behavior of dilepton spectrum in the regime where the new physics signal is dominated by the interference term $d\sigma_{\rm int}$. For illustration, we have taken $\lambda = 1$ and $M_\chi = 300$ GeV. The upper and lower plots indicate

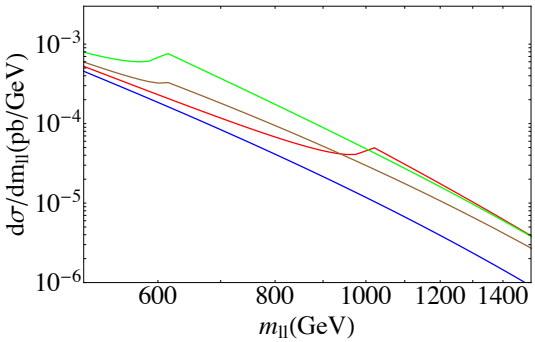

Figure 2.6.: The differential $pp \to \ell^+\ell^-$ cross section as a function of the dilepton invariant mass in Model U. Shown here are the effects of variation in M_χ and M_ϕ holding $\lambda = 1.8$ fixed and $\Delta M = 0$. Here, red: $M_\chi = M_\phi = 500$ GeV, green: $M_\chi = M_\phi = 300$ GeV, brown: $M_\chi = 300$ GeV, $M_\phi = 500$ GeV, blue: SM.

the distribution $d\sigma/dm_{\ell\ell}$ and the ratio $d\sigma_{\rm tot}/d\sigma_{\rm SM}$ respectively. The red and green curves in both plots represent Model U and D respectively, with the blue curve in the upper plot denoting the SM at LO. As expected, due to the smaller couplings the new physics effect on the dilepton rate is much smaller. Also seen are the interesting effects of destructive interference with the SM amplitude. In Model U, we see a reduction of the dilepton rate with respect to the SM ($d\sigma_{\rm tot}/d\sigma_{\rm SM} < 1$) for invariant masses considerably above the kinematic threshold $m_{\ell\ell} \gtrsim 1300$ GeV. In Model D on the other hand, destructive interference is present below and near the threshold, while for large invariant masses $m_{\ell\ell} \gtrsim 850$ GeV, the interference becomes again constructive. Note that in both models the new physics amplitudes

have the same sign, while the sign of the SM amplitude differs due to the differing electric charge of the initial state quarks.

The variation of the signature as a function of the masses is seen in Fig. 2.6., where the coupling is fixed at $\lambda = 1.8$ and $\Delta M = 0$. The green and red curves take $M_\chi = M_\phi$ for two values, 300 and 500 GeV respectively. Notice that even though the location of the monocline is different for different M_χ's, the size of the deviation from the Standard Model is approximately independent of M_χ. This is because when the new physics contribution is dominated by $|\mathcal{M}_{\rm box}|^2$ and $|\mathcal{M}_{\rm xbox}|^2$, as is the case for $\lambda \gtrsim 1.4$, for a fixed ratio of mediator to dark matter mass, M_ϕ/M_χ, the ratio $d\sigma_{\rm total}/d\sigma_{\rm LO}$ is determined mainly by the coupling. We also show the effect of splitting M_ϕ from M_χ in the brown curve. Notice that the sharp monocline rise is less pronounced near $m_{\ell\ell} = 2M_\chi$ (compared with the green curve), and the size of the effect for $\sqrt{\hat{s}} > 2M_\phi$ slowly asymptotes to the green and red curves.

Angular Distribution

The loop corrections in the model also leave their imprint in the angular distribution of the rates $d^2\sigma/dm_{\ell\ell}dc_\theta$, where $c_\theta \equiv \cos\theta$ with the angle θ already introduced in Eq. (II.11). In general, the angular distribution $d^2\sigma/dm_{\ell\ell}dc_\theta$ can be written as

$$\frac{d^2\sigma}{dm_{\ell\ell}dc_\theta} = \sum_{n=0}^{\infty} a_n c_\theta^n \ , \qquad a_n \in \mathcal{R} \ . \tag{II.19}$$

In general, the a_n coefficients are functions of m_{ll}. For an s-channel–mediated process (including the SM Drell-Yan process at tree level), $a_0 = a_2$ and $a_{n\geq 3} = 0$.

Hence we can write [81]

$$\frac{d^2\sigma_{s-\text{chan.}}}{dm_{\ell\ell}dc_\theta} \propto \frac{3}{8}(1+c_\theta^2) + A_{\text{FB}}(m_{\ell\ell})\ c_\theta\ , \tag{II.20}$$

where $A_{\text{FB}}(m_{\ell\ell})$ is the forward-backward asymmetry. Therefore, the measurement of the forward-backward asymmetry $A_{\text{FB}}(m_{\ell\ell})$ characterizes the shape of the differential distribution for an s-channel–mediated process. For a general distribution as given in Eq. (II.19), more observables must be measured to determine the coefficients a_n.

The forward-backward asymmetry can be formally obtained as:

$$\begin{aligned} A_{\text{FB}}(m_{\ell\ell}) &\equiv \frac{\int_0^1 dc_\theta(d^2\sigma/dm_{\ell\ell}dc_\theta) - \int_{-1}^0 dc_\theta(d^2\sigma/dm_{\ell\ell}dc_\theta)}{\int_{-1}^1 dc_\theta(d^2\sigma/dm_{\ell\ell}dc_\theta)} \\ &= \frac{(d\sigma/dm_{\ell\ell})_F - (d\sigma/dm_{\ell\ell})_B}{(d\sigma/dm_{\ell\ell})_{\text{tot}}}\,. \end{aligned} \tag{II.21}$$

The $A_{\text{FB}}(m_{\ell\ell})$ computed at *partonic* level in Model U is illustrated in the plot on the left-hand side of Fig. 2.7.. The red curve corresponds to $\lambda = 1.8$ and the green curve to $\lambda = 1.4$, with $M_\chi = M_\phi = 500$ GeV with $\Delta M = 0$ for both curves. The blue line denotes the Standard Model prediction at LO. We notice a significant increase of A_{FB} at the threshold, which is the result of three different effects at $m_{\ell\ell} \simeq 2M_\chi$:

(a) an increase in $[(d\sigma/dm_{\ell\ell})_F^{\text{box}} - (d\sigma/dm_{\ell\ell})_B^{\text{box}}]/\ (d\sigma/dm_{\ell\ell})_{\text{tot}}$ due to a huge increase in $\sigma_{\text{box}}^{\text{Fwd}}$,

(b) a slight increase in $[(d\sigma/dm_{\ell\ell})_F^{\text{int}} - (d\sigma/dm_{\ell\ell})_B^{\text{int}}]/\ (d\sigma/dm_{\ell\ell})_{\text{tot}}$, and

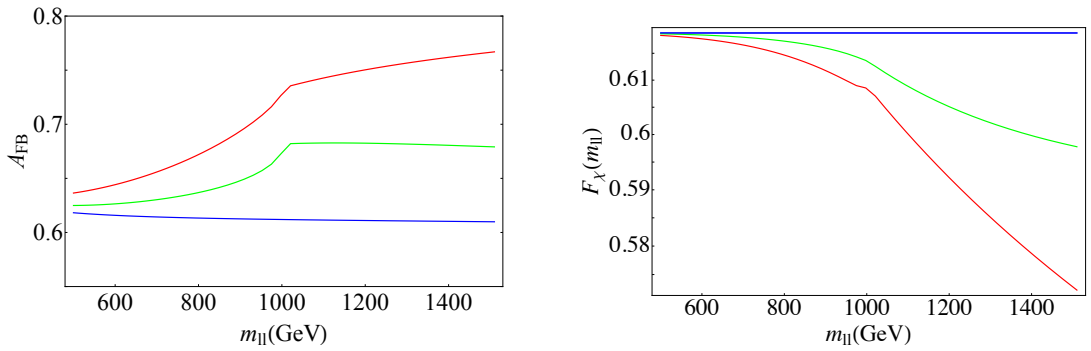

Figure 2.7.: LEFT: The forward-backward asymmetry as defined in Eq. (II.21) as a function of the dilepton invariant mass; RIGHT: $F_\chi(m_{\ell\ell})$ as defined in Eq. (II.22) as a function of the dilepton invariant mass. In both plots, Model U is used and masses are set to $M_\chi = M_\phi = 500$ GeV and $\Delta M = 0$. Here, blue: Standard Model at LO ($\lambda = 0$), green: $\lambda = 1.4$, red: $\lambda = 1.8$. All curves are commuted at the the partonic level.

(c) a decrease in $[(d\sigma/dm_{\ell\ell})_F^{\rm LO} - (d\sigma/dm_{\ell\ell})_B^{\rm LO}]/\,(d\sigma/dm_{\ell\ell})_{\rm tot}$, due to the increase in $(d\sigma/dm_{\ell\ell})_{\rm tot}$.

A search for new physics in dilepton production using $A_{\rm FB}$ has been carried out by the ATLAS collaboration in [63] using 20 fb^{-1} of 8 TeV data. Due to the inherent uncertainties in the direction of the initial (anti)quark and the transverse momenta of the partons in a proton-proton collider, events are reconstructed by first boosting along a longitudinal direction and identifying the dilepton center-of-momentum frame. The quark, due to its predominantly valence nature, is then assumed to have originated in the direction of the boost. The details of constructing

the angle of scattering θ^* in this so-called Collins-Soper (CS) frame [82] are provided in [63]. The inevitable misidentification of quarks (antiquarks) that comes with this procedure leads to "mistagging" a fraction of forward (backward) events as backward (forward), thus diluting the asymmetry. Higher order QCD corrections to the differential Standard Model cross section further symmetrize the forward-backward events. As a result, the $m_{\ell\ell}$-dependent Standard Model values for $A_{\rm FB}$ shown in [63] are smaller than the ones in Fig. 2.7. by a factor of 1.5 – 3. A full fledged angular analysis that uses the CS frame and takes into account higher order corrections is beyond the scope of this work.

A complementary way to probe the angular distribution are observables that quantify the preference of dilepton events in a predefined central region of the detector over events in the outer region. Measuring such observables does not require knowledge of the direction of the initial parton, making them potentially advantageous at a proton-proton collider. An example of this is the ATLAS measurement of the observable $F_\chi(m_{jj})$ in dijet distributions at $\sqrt{s} = 7$ TeV [68]. It is defined as $F_\chi \equiv N_{\rm central}/N_{\rm total}$, where $N_{\rm total}$ is the total number of events, and $N_{\rm central}$ is the number of dijet events in a central region defined by $\chi \equiv \exp(2|y|) < \chi_{\rm max}$, where y is the rapidity of each jet in the dijet CM frame. In the ATLAS analysis, the observable F_χ is used to distinguish between isotropic new physics processes and QCD backgrounds, that prefer the forward direction. As a simple

illustration of their applicability to our model, we compute the quantity,

$$F_\chi(m_{\ell\ell}) \equiv \frac{\int_{-a}^{a}(d\sigma/dc_\theta)dc_\theta}{\int_{-1}^{1}(d\sigma/dc_\theta)dc_\theta} \ , \tag{II.22}$$

where the central region is defined by $-a \leq c_\theta \leq a$. Choosing $a = 1/2$ (which corresponds to $\chi = 3$), we plot $F_\chi(m_{\ell\ell})$ at the partonic level in Model U with $M_\chi = M_\phi = 500$ GeV and $\Delta M = 0$ on the right-hand side of Fig. 2.7.. The red curve corresponds to $\lambda = 1.8$, the green curve to $\lambda = 1.4$, and the blue curve depicts the Standard Model at LO.

The SM curve appears flat which can be understood as follows. One sees from Eq. (II.20) that for a given $m_{\ell\ell}$, the angular distribution can be written as $d\sigma/dc_\theta(m_{\ell\ell}, c_\theta) = f(m_{\ell\ell})[\frac{3}{8}(1 + c_\theta^2) + A_{\rm FB}(m_{\ell\ell})c_\theta]$. From the left-hand plot in Fig. 2.7., we see that in the SM $A_{\rm FB}$ is largely insensitive to $m_{\ell\ell}$ for the range considered because all SM states can be taken as massless for this range and there is no mass scale in the problem. Thus $d\sigma/dc_\theta(m_{\ell\ell}, c_\theta)$ can be approximately written as $f(m_{\ell\ell})[\frac{3}{8}(1+c_\theta^2)+A_{\rm FB}c_\theta]$. Therefore, to a good approximation, $f(m_{\ell\ell})$ drops out of $F_\chi(m_{\ell\ell})$. In general no such approximate factorization can be made for the new physics effects in our model. We find that the new physics box amplitude tends to slightly favor the outer regions over the central region. The values for $F_\chi(m_{\ell\ell})$ in our model are therefore always smaller than the Standard Model's unless interference effects lead to a deficit in rates with respect to the SM. The preference for the outer regions gets more pronounced for $m_{\ell\ell} \gtrsim 2M_\chi$, where also the imaginary part in the amplitude turns on. This behavior is reflected in the red curve by a kink at ~ 1000

GeV on the right-hand-side plot in Fig. 2.7., to the right of which the distribution falls steeper.

Dilepton Spectrum Constraints

We can compare the predicted dilepton spectra of our model to measurements by the LHC collaborations [64, 65] by conducting a shape analysis. The dominant Standard Model background in these searches is the Drell-Yan process, which at tree-level is $s-$channel photon– and Z–mediated as shown in Fig. 2.1.. Subdominant backgrounds come from the production of tops, dibosons, dijets and W+jet. Both ATLAS and CMS find their observed dilepton spectra are consistent with the Standard Model.

ATLAS has dilepton events with invariant masses as high as ~ 1600 GeV (1800 GeV) for m_{ee} ($m_{\mu\mu}$), whereas CMS has events up to ~ 1750 GeV (1850 GeV). The ATLAS and CMS measurements can be translated into constraints of our model. In our analysis we only consider $m_{\ell\ell}$ bins that are far from the Z-resonance given the dark fermion masses we consider. In order to generate signal spectra, we first analytically compute the $pp \to \ell^+\ell^-$ cross section ratios $d\sigma_{\text{total}}/d\sigma_{\text{SM}}$ bin by bin using the MSTW2008NNLO parton distribution functions, where $d\sigma_{\text{total}}$ and $d\sigma_{\text{SM}}$ are as defined in Eq. (II.11). We choose the squared factorization scale and Q^2 to be m_{ll}^2. We then scale the experimentally provided Drell-Yan NNLO backgrounds by these ratios. We do not consider the subdominant backgrounds.

Bounds on the model parameter space can be set by comparing the dilepton

spectra of our model with the Standard Model predictions, by computing $\Delta\chi^2 = \chi^2_{\rm NP} - \chi^2_{\rm SM}$, where

$$\chi^2_{\rm NP} = \sum_{i=1}^{N_{\rm bins}} \frac{(N^i_{\rm obs} - N^i_{\rm NP})^2}{N^i_{\rm NP} + \sigma^2_{\rm SM}} \ , \tag{II.23}$$

$$\chi^2_{\rm SM} = \sum_{i=1}^{N_{\rm bins}} \frac{(N^i_{\rm obs} - N^i_{\rm SM})^2}{N^i_{\rm SM} + \sigma^2_{\rm SM}} \ , \tag{II.24}$$

with $N^i_{\rm NP}$ the number of events expected by our model, $N^i_{\rm SM}$ the number of events predicted by the SM, $N^i_{\rm obs}$ the number of events observed and $\sigma_{\rm SM}$ is the background systematic uncertainty. By setting $\Delta\chi^2 = 5.99$, we obtain a 95% C.L. exclusion limit in the $\lambda - M_\chi$ plane with respect to the Standard Model. In the following, we compare the model with the ATLAS results [64]. ATLAS and CMS have comparable sensitivities and their results are in good agreement with each other. Therefore, using the CMS results [65] would lead to very similar exclusion limits. We do not attempt a statistical combination of the ATLAS and CMS results.

As one would expect, in general the shape of the dilepton spectrum is sensitive to λ. For instance, depending on the Model (U, D or UD) used for setting constraints, it is possible to obtain also a slight *deficit* in model events with respect to the background, due to interference effects for dilepton invariant masses below the kinematic threshold (see also [83] for a recent study of destructive interference effects at colliders.). This typically occurs at $\lambda \lesssim 1$. We will find, however, that our $\Delta\chi^2$ analysis at $\sqrt{s} = 8$ TeV is only sensitive to $\lambda \gtrsim 1.4$, where the signal is dominated by $d\sigma_{\rm box} \propto |\mathcal{M}_{\rm box}|^2$. Thus, the nature of the model spectrum is as

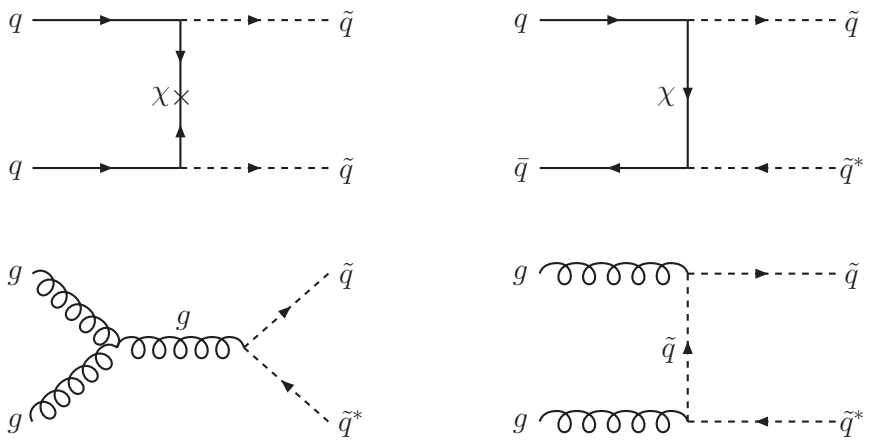

Figure 2.8.: Example Feynman diagrams with the highest contribution to the pair production of the colored mediator, resulting in jets+MET signals.

discussed in Subsection II.2.3. It then follows that the largest contributions to $\Delta\chi^2$ comes from the contribution near $m_{\ell\ell} \simeq M_1 + M_2$, where the monocline feature leads to the largest signal over background.

We will discuss the results of the χ^2 analysis in Sec. II.4 along with additional constraints on our parameter space from dedicated dark matter searches at the LHC, from direct detection experiments and from the dark matter relic abundance.

Related Constraints

The primary focus of our dissertation is on the new signals of radiative corrections of dark matter on the dilepton kinematical and angular distributions. There are, of course, several correlated implications, from LHC predictions, the thermal relic density, to the predictions for the scattering rates in direct detection

experiments. In this section we consider the *constraints* that these correlated implications place on the parameter space of the simplified models that we consider. We consider the bounds set by jets + MET searches at the LHC [84, 85], the bounds from nucleon-dark matter scattering in direct detection experiments [86, 18, 87], and the dark matter thermal relic abundance (now best determined by Planck [88]). Additional constraints can arise from the anomalous magnetic moment of the muon [89] as well as from LEP results on four-lepton contact interactions [90]. In this section we step through each of these, detailing the various mechanisms behind each probe and how they place constraints on the model. A summary of all constraints and a comparison to the dilepton signal will be presented in Sec. II.4.

LHC constraints

While searches for dark matter signals in the form of missing transverse energy (MET)+initial state radiation, the so-called mono-X signatures, are ongoing, the strongest constraints on our model come from recasted supersymmetry searches for jets+MET signatures from ATLAS and CMS [84, 85]. Indeed, pair production of the colored mediators, followed by the decay of the mediators into dark matter and a light quark contribute to the jets+MET signal. Some important diagrams are shown in Fig. 2.8.. For recasting, we use the CMS T2qq simplified model in [84], where the gluino is assumed decoupled and squark pair production is followed by prompt decay to a pair of LSPs with a branching ratio of 100%. Contours of the exclusion cross-

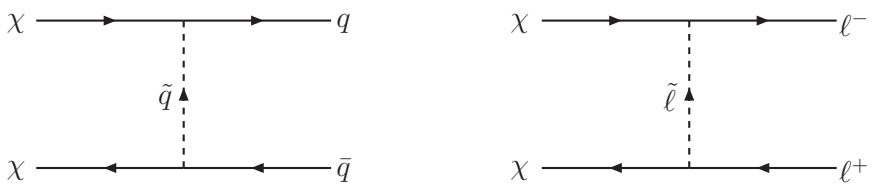

Figure 2.9.: Example dark matter annihilation diagrams that set the thermal relic abundance.

sections in the plane of LSP mass and squark mass are provided, which we compare with our signal cross-sections generated at leading order using MadGraph5 [217] with CTEQ6L1 parton distribution functions [92]. We will present the results of the numerical analysis in Sec. II.4, where we also compare the bounds with those obtained from the dilepton spectra.

Note that the supersymmetry search assumes the squarks are pair-produced predominantly via an s-channel gluon whereas the dominant production channel in our model is t-channel exchange of χ_1 and χ_2. While in principle this leads to different detector acceptances for the two processes, in practice we find that these two acceptances are similar within a few percent, validating our use of the CMS bounds for constraining our model.

Relic Abundance

If χ is a thermal relic of freeze-out, the diagrams in Fig. 2.9. contribute to its annihilation into SM fermions in the early universe. We can then calculate the relic abundance as a function of the masses and couplings in our model by solving the

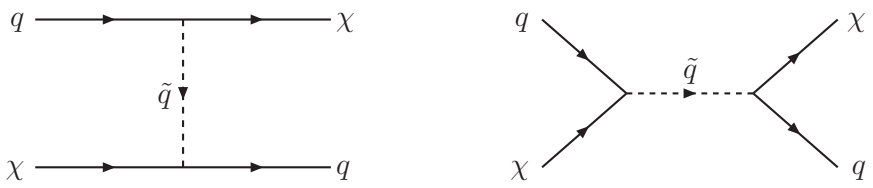

Figure 2.10.: Feynman diagrams contributing to direct detection signatures.

Boltzmann equation under the freeze-out condition. For the case of a pseudo-Dirac dark matter candidate (i.e. for small mass splitting between the two dark fermion states χ_1 and χ_2), coannihilations between the two eigenstates ($\chi_1\chi_2 \to f\bar{f}$ and $\chi_2\chi_2 \to f\bar{f}$) play an important role in setting the abundance. We incorporate these effects through an effective cross-section [152]

$$\sigma_{\text{eff}}(x) = \frac{\sigma_{11} + 2\sigma_{12}(1+\delta)^{3/2}e^{-x\delta} + \sigma_{22}(1+\delta)^3 e^{-2x\delta}}{(1+(1+\delta)^{3/2}e^{-x\delta})^2} \,, \tag{II.25}$$

where $x \equiv T/M_\chi$ is the ratio of temperature and dark matter mass and $\delta \equiv \Delta M/M_\chi$ is the fractional mass splitting between the dark matter states. For a splitting less than or comparable to the freeze-out temperature ($\Delta M/M_\chi \lesssim 1/x_F$), efficient $s-$wave annihilation of the σ_{12} term in Eq. (II.25) leads to small relic abundances that do not overproduce dark matter for large ranges of parameters in our model. For ($\Delta M/M_\chi \gg 1/x_F$), exponential suppression of the coannihilation terms in Eq. (II.25) implies $\sigma_{\text{eff}} \approx \sigma_{11}$, whose $s-$wave component is chirality-suppressed by a factor of $(m_f/M_\chi)^2$. The dominant component in that case is p-wave suppressed, leading to larger relic abundances. While there is potentially a sub-dominant contribution from coannihilation between the scalar mediators and dark matter for

$M_\phi/M_\chi \lesssim 1.1$. We neglect these effects in setting our bounds, since, as discussed below, we will find that constraints from direct detection are typically stronger than constraints from the dilepton spectrum in these regions of parameter space.

The relic abundance is given by

$$\Omega_\chi h^2 \approx \frac{1.07 \times 10^9 \text{ GeV}^{-1}}{M_{\rm Pl}} \frac{x_F}{\sqrt{g_*}} \frac{1}{I_a + 3I_b/x_F} \ , \tag{II.26}$$

where the freezeout temperature x_F can be determined through

$$e^{x_F} = \frac{5}{4}\sqrt{\frac{45}{8}} \frac{M_1 M_{\rm Pl}(I_a + 6I_b/x_F)}{\pi^3 \sqrt{g_*}\sqrt{x_F}} \ . \tag{II.27}$$

The terms I_a and I_b quantify the integration over thermal history of the annihilating species before freeze-out, and are given by

$$I_a = x_F \int_{x_F}^\infty \frac{dx}{x^2}\ a_{\rm eff} \ , \quad I_b = 2x_F^2 \int_{x_F}^\infty \frac{dx}{x^3}\ b_{\rm eff} \ , \tag{II.28}$$

where $\langle \sigma_{\rm eff} v_{\rm rel} \rangle = a_{\rm eff} + b_{\rm eff} v_{\rm rel}^2$. Expressions for $a_{\rm eff}$ and $b_{\rm eff}$ in our model are given in Appendix B.

The constraints on the model parameter space from the relic abundance will be shown in Sec. II.4.

Direct Detection

Dark matter is also constrained by underground experiments studying the recoil spectra of local galactic dark matter scattering off nuclei of heavy elements. Fig. 2.10. shows the dominant diagrams in our model contributing to the scattering cross-section.

The current best bounds for spin-independent scattering are set by results of the 85.3 day-run of the Large Underground Xenon (LUX) experiment [18] and those for spin-dependent scattering by the XENON100 experiment [87]. The energy transfer in these scattering experiments is $\mathcal{O}(10\text{ keV})$, hence for a sufficiently large splitting in the eigenmasses of pseudo-Dirac dark matter, only the lighter eigenstate takes part in the scattering. Such a scenario emulates a Majorana dark matter candidate scattering off the nucleus. In the Majorana case, the leading contribution to spin-independent scattering comes from a quark twist-2 operator, which is suppressed by $1/M_\phi^8$. Therefore one only obtains modest bounds from spin-independent scattering. Constraints from spin-dependent scattering are typically comparable.

On the other hand, in the pure Dirac limit ($\Delta M = 0$) and in the pseudo-Dirac case with a sufficiently small splitting in the dark fermion masses, the spin-independent scattering cross-section is dominated by the vector-vector interaction operator (which is absent for a Majorana fermion). These cases are subject to very stringent limits by spin-independent direct detection. Constraints from spin-dependent scattering of Dirac dark matter (where one finds a cross-section that is four times smaller than in the Majorana case) are however not relevant.

Following [50], the direct detection cross sections spin-independent scattering σ_{SI} and spin-dependent scattering σ_{SD} predicted by our model can be calculated using the formulae given in Appendix C.

LEP Constraints

LEP analyses of four lepton contact interactions that contribute to $e^+e^- \to \ell^+\ell^-$ can also be used to place constraints on the parameter space of our model. Box diagrams with dark fermions and lepton mediators will generate four fermion interactions of the type $(\bar{e}\gamma_\mu P_R e)^2$. However, in agreement with [61] we find that the LEP results collected in [90] give only mild constraints on our scenario. In particular, couplings $\lambda \lesssim 2$ are only constrained for very light dark matter masses of $M_\chi \lesssim 250$ GeV.

Anomalous Magnetic Moment of the Muon

One additional constraint in the case the dark fermions of our model interact with muons comes in principle from the anomalous magnetic moment of the muon, $(g-2)_\mu$. Indeed, loops with dark fermions and scalar mediators can contribute to $(g-2)_\mu$. The sign of the contribution to $(g-2)_\mu$ is fixed, and turns out to *increase* the longstanding discrepancy of the observed value with respect to the theory prediction [89, 94]. Requiring that the model prediction for $(g-2)_\mu$ does not deviate by more than 5σ from the measured value, we find constraints only in extreme corners of parameter space with $\lambda_\mu \gtrsim 2$ and $M_\chi \sim M_\phi \lesssim 200$ GeV.

Summary of all Constraints

We can now combine all the constraints discussed in the sections above. Figs. 2.11., 2.12. and 2.13. depict the regions of parameter space in the plane of

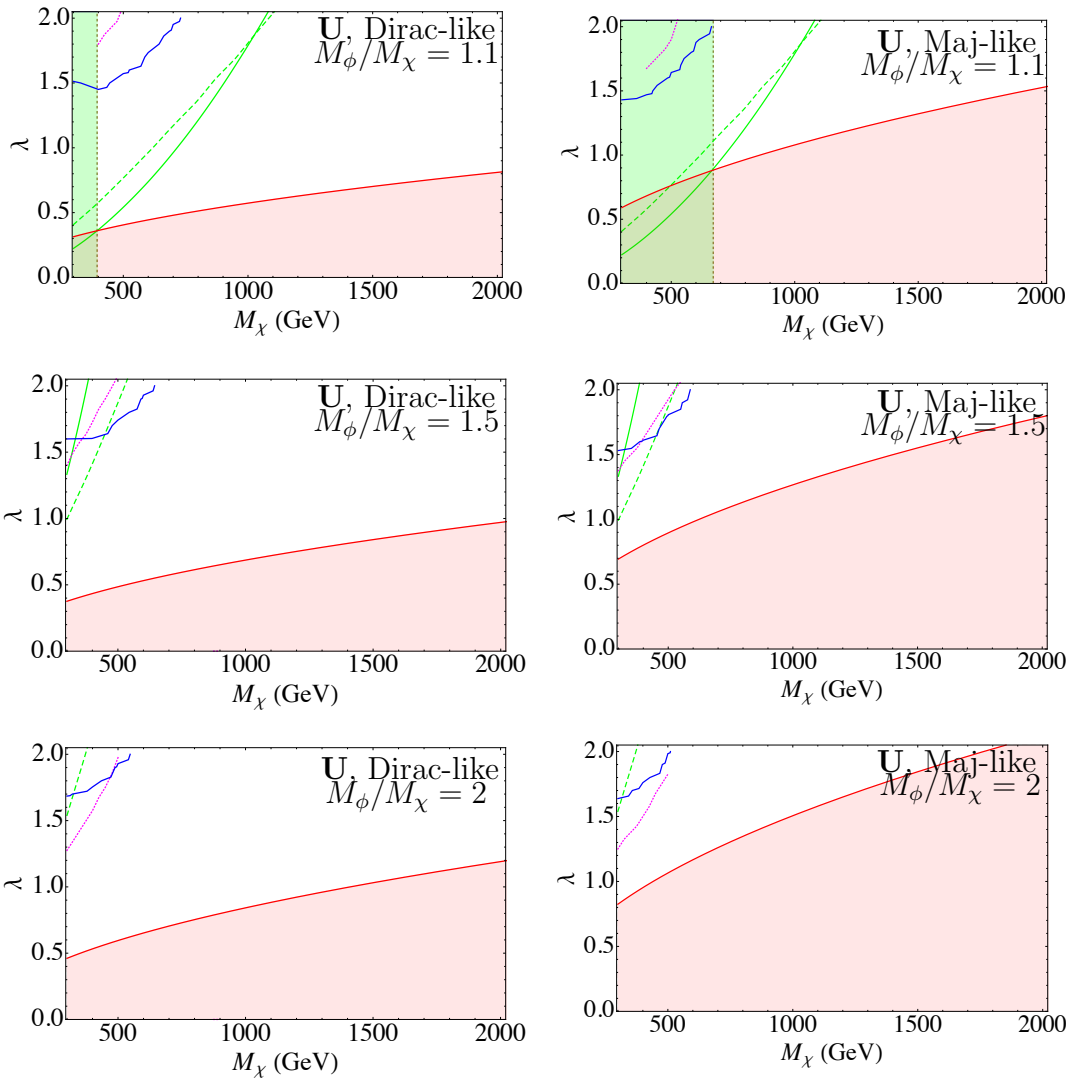

Figure 2.11.: Constraints in the plane of dark matter mass M_χ vs. coupling λ in Model U. LEFT: $\Delta M/M_\chi = 0.1$ (Dirac-like at freeze-out), RIGHT: $\Delta M/M_\chi = 0.5$ (Majorana-like at freezeout). The first, second and third rows correspond, respectively, to $M_\phi/M_\chi = 1.1$, 1.5 and 2. The color scheme is explained in the text.

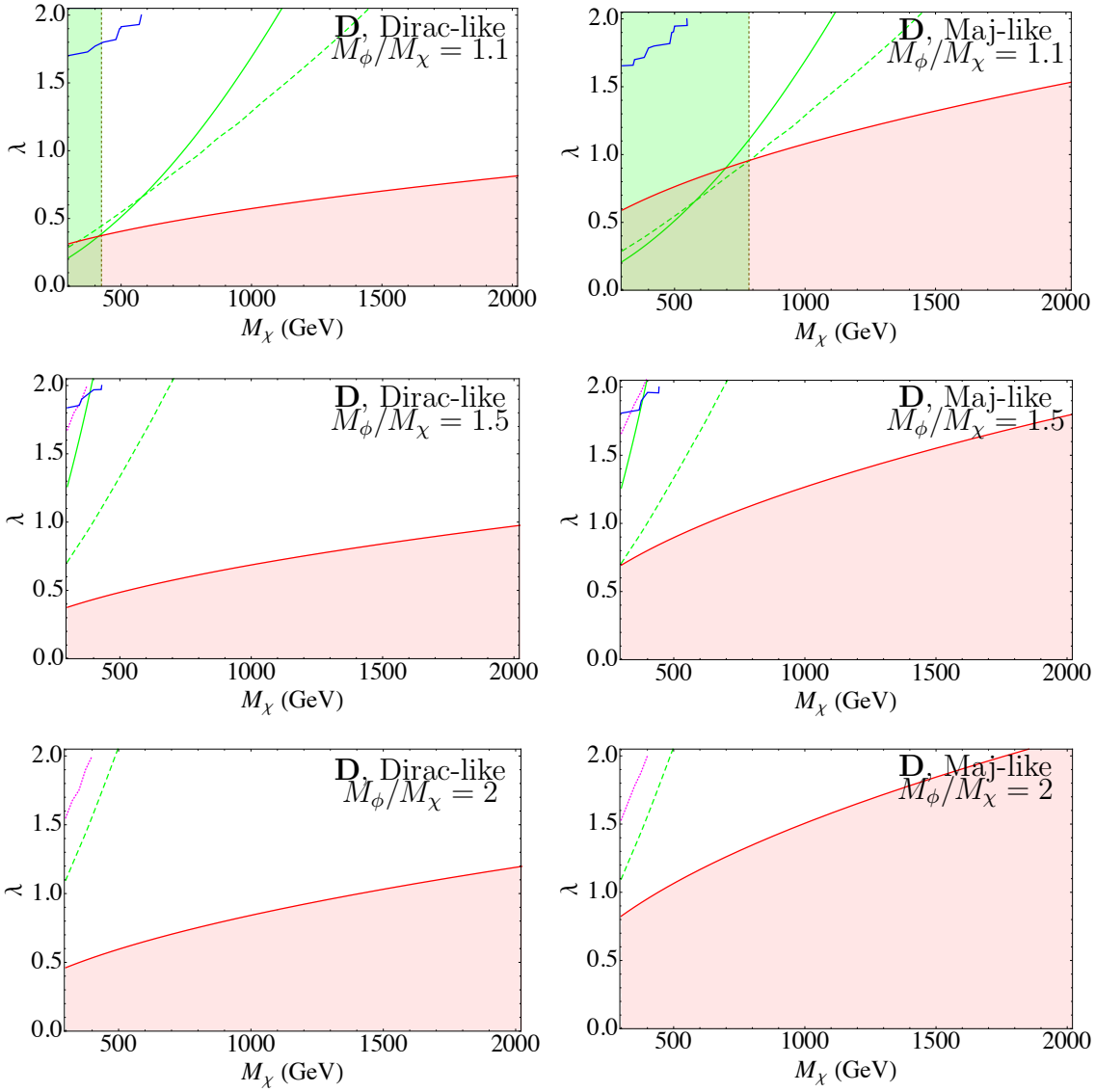

Figure 2.12.: Constraints in the plane of dark matter mass M_χ vs. coupling λ in Model D. Plots and color coding as in Fig. 2.11..

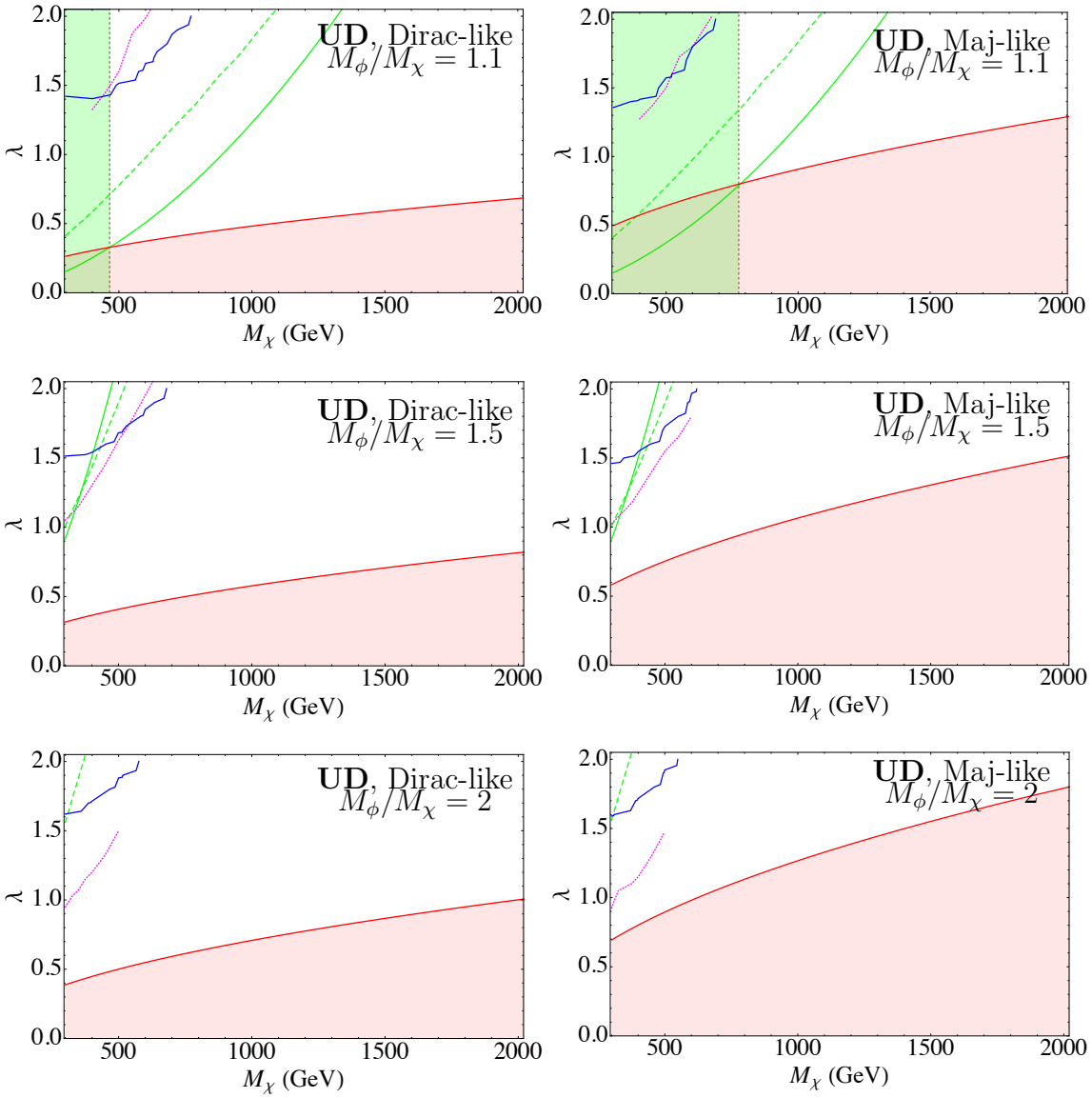

Figure 2.13.: Constraints in the plane of dark matter mass M_χ vs. coupling λ in Model UD. Plots and color coding as in Fig. 2.11..

mediator coupling λ and dark matter mass M_χ that are allowed by all experimental bounds for Models U, D and UD respectively. In all three figures, the plots on the left-hand side correspond to a mass splitting between the dark matter states of $\Delta M/M_\chi = 0.1$ (to represent a χ that is Dirac-like at freeze-out). The plots on the right-hand side correspond to $\Delta M/M_\chi = 0.5$ (Majorana-like at freeze-out). The rows correspond to ratios of mediator mass to dark matter mass of $M_\phi/M_\chi = 1.1, 1.5$ and 2 respectively. The blue curves show the 95% C.L. exclusion limit for a comparison between our model and the dilepton spectrum measured by the ATLAS collaboration at 8 TeV [64]. The dotted magenta curves depict the jets+MET bounds, recast from the CMS search for supersymmetry [84]. In the shaded red region the model overcloses the universe at freeze-out, with $\Omega_\chi h^2 \gtrsim 0.12$. Along the red curves the local dark matter density predicted by our model saturates the experimental value, i.e., $\Omega_{\rm model} h^2 = 0.12$.

The solid and dashed green curves are, respectively, bounds from the 90% C.L. exclusion limits set by LUX [18] for spin-independent cross-sections and XENON100 [87] for spin-dependent cross-sections assuming the canonical local dark matter density of $\rho_\chi \simeq 0.3$ GeV/cm^3. For a purely thermal origin of the dark fermions, this bound only applies at the crossing of the green curves with the red curve. Above the red curve, the green lines correspond to the constraint on the parameter space assuming there is some other origin of the dark fermion abundance that makes up the correct cosmological density (and thus local density)

that we observe today. The shaded green region, by contrast, is ruled out even if the abundance of the dark fermions *is* the predicted (subdominant) thermal abundance associated with those parameters. In this case, even if there were another (inert) component of dark matter to make up the difference in relic density, the small thermal abundance of the dark fermions ($\propto 1/\lambda^4$) is compensated by an enhanced direct detection scattering cross section ($\propto \lambda^4$).

In the following we remark on the various features of the constraints in Figs. 2.11., 2.12. and 2.13..

We first note that the dilepton spectrum constraints are generically tighter for Models U and UD than for Model D. This follows from the PDFs of the initial state up quarks in comparison to initial state down quarks, leading to higher production rates when the former are present in the new physics process. Note that the constraints from the dilepton spectrum lie in the region where the new physics signal is dominated by $|\mathcal{M}_{\rm box}|^2$, hence the largest contributions to the significance arise from the region around $m_{\ell\ell} \simeq M_1 + M_2$. For the set of parameters spanned by the blue curve, this does not give rise to a significant difference between the $\Delta M/M_\chi = 0.1$ and $\Delta M/M_\chi = 0.5$ cases in all three models, as can be observed comparing the left- and right-hand sides of the figures.

We also note that the dilepton spectrum constraints are stronger when the mass splitting of the mediator and dark matter is small. This is because the monocline is sharper for a degenerate spectrum as demonstrated in Fig. 2.6.. A

mass splitting between ϕ and χ causes a transition from an SM-like spectrum in the IR to the parallel SM+DM-like spectrum in the UV over a larger mass interval. In contrast, searches for mediator pair production in jets+MET events become weaker for smaller M_ϕ/M_χ due to the reduced amount of missing transverse energy. This demonstrates the complementarity of our dilepton spectrum observables to existing DM searches.

In all three models, one finds the jets+MET constraints slightly stronger for $\Delta M/M_\chi = 0.5$ than $\Delta M/M_\chi = 0.1$. The reasons for this behavior are outlined in detail in [69], but we summarize it here as follows. Same-handed squark production, such as in the first Feynman diagram in Fig. 2.8., is absent in the pure Dirac limit, but turns on gradually as we approach the Majorana limit, contributing to the production rates. Hence the jets+MET bounds tighten as we increase $\Delta M/M_\chi$. Once again due to PDF effects this search sets tighter constraints on Model UD than Model U, which in turn are tighter than in Model D. The cuts used in the search get more efficient when the scalar mediator and the LSP are more split in mass. This dependence on the acceptance gives rise to the strengthening of the bounds observed as M_ϕ/M_χ increases. For Model D, the acceptance for a near-degenerate spectrum is poor enough to set no bounds at all in our chosen range of λ for M_ϕ/M_χ. In all the plots, we have assumed that the production of both χ_1 and χ_2 contributes to the MET, while realistically χ_2 would undergo a decay to χ_1 and SM states.

The direct detection limits contain several interesting features. First, the bounds

are identical for either splitting, $\Delta M/M_\chi = 0.1, 0.5$, since for a splitting of more than $\mathcal{O}(100\text{ keV})$, there is insufficient kinetic energy in the nonrelativistic collisions to excite to the heavier state χ_2. Hence, χ_1 behaves entirely Majorana-like for direct detection searches. Next, the spin-independent (SI) scattering bounds (solid green curves) are very similar for Model U and D, but stronger for Model UD since more partons are involved in the scattering in the latter. The spin-dependent (SD) bounds (dashed green curves) differ across all three Models due to the difference in nucleon matrix elements, which are large for down quarks in a neutron and small for up quarks in a neutron (see Appendix C). Moreover, the SI constraints weaken much more rapidly than the SD bounds as we increase in M_ϕ/M_χ (and disappear for $M_\phi/M_\chi = 2$ in the range of our parameter space). This is due to the dominance of the twist-2 operator in SI scattering that scales as $1/M_\phi^8$, as opposed to the $1/M_\phi^4$-dependence of SD scattering. This interplay between the dimensionality of the operator and the relative strengths of the nucleon matrix elements determines whether the SI or the SD direct detection results sets the stronger bounds, that in turn depends on the choice of the Model and M_ϕ/M_χ. In Model U, the SI bounds are stronger than the SD bounds up to $M_\chi \sim 1100$ GeV for $M_\phi/M_\chi = 1.1$ and up to $M_\chi \sim 500$ GeV for $M_\phi/M_\chi = 1.2$; for $M_\phi/M_\chi \geq 1.3$, the SD bounds are stronger. In Model D, the SI bound is stronger up to $M_\chi \sim 600$ GeV for $M_\phi/M_\chi = 1.1$, and the SD bound is uniformly stronger for $M_\phi/M_\chi \geq 1.2$. In Model UD, the SI

bounds are uniformly stronger for $M_\phi/M_\chi \leq 1.3$, stronger than SD bounds up to $M_\chi \sim 400$ GeV for $M_\phi/M_\chi = 1.5$ and weaker (here absent) for $M_\phi/M_\chi = 2$.

The relic density constraints are slightly weaker for Model UD than Models U and D since a pair of χ's can annihilate to two different flavors of quark final states. As M_ϕ/M_χ is increased, the relic density bounds gradually increase in all three Models. This is due to the weak dependence of $\langle \sigma_{\text{eff}} v_{\text{rel}} \rangle$ on M_ϕ/M_χ, as can be seen from Appendix B. The annihilation of Majorana dark matter happens without an s-wave component due to chirality-suppression (see [50]) and hence is less efficient than Dirac dark matter annihilation. For a mixed dark matter candidate like ours, $\Delta M/M_\chi = 0.1$ approximates the Dirac case and $\Delta M/M_\chi = 0.5$ approximates the Majorana case during freeze-out. This is why the thermal relic bounds on the right-hand-side of Figs. 2.11., 2.12. and 2.13. are stronger than those of the left-hand-side.

Finally, we remark on the striking complementarity of the various dark matter probes applied to our model. While it is obvious that the relic constraints bound Models U, D and UD in the low-λ regime, several competing factors determine which of the other experiments – dilepton searches, jets+MET searches, direct detection – set the strongest bound at higher couplings λ. In fact, depending on the Model and choice of parameters, each of these three can give the best bounds in some parameter regime. Since the dependence of each probe on the parameters has been explained in this section, in the following we only briefly describe our findings, as applicable to the high-λ, low-M_χ region.

In Model U, for both $\Delta M/M_\chi = 0.1$ and 0.5, the tightest exclusions come from direct detection for $M_\phi/M_\chi \leq 1.3$, direct detection for $M_\chi \lesssim 450$ GeV and dilepton measurements for $M_\chi \gtrsim 450$ GeV at $M_\phi/M_\chi = 1.5$, and predominantly jets+MET searches at $M_\phi/M_\chi = 2$. In Model D, the tightest exclusions are from direct detection for all M_ϕ/M_χ. In Model UD, direct direction predominantly sets the tightest limits for $M_\phi/M_\chi \leq 1.3$; for $M_\phi/M_\chi = 1.5$, the best bounds are placed by jets+MET searches at $M_\chi \lesssim 500$ GeV for $\Delta M/M_\chi = 0.1$ and at $M_\chi \lesssim 600$ GeV for $\Delta M/M_\chi = 0.5$, and by dilepton measurements at $M_\chi \gtrsim 500$ GeV for $\Delta M/M_\chi = 0.1$; for $M_\phi/M_\chi = 2$, the best bounds are placed by jets+MET searches at $M_\chi \lesssim 500$ GeV and dilepton measurements at $M_\chi \gtrsim 500$ GeV.

Future Projections

We provide in Fig. 2.14. our projections for the sensitivity of the LHC at $\sqrt{s} =$ 14 TeV (left) and for a future proton-proton collider at $\sqrt{s} = 100$ TeV (right) in the dilepton invariant mass spectrum. Here we have chosen $M_\phi/M_\chi = 1.2$ and $\Delta M/M_\chi = 0.1$ for Model U and Model D, for illustration. We expect other choices of parameters to not qualitatively alter the results presented, as may be deduced from the $\Delta\chi^2$ bounds shown across various sets of parameters in Figs. 2.11., 2.12. and 2.13.. The shaded red region corresponds to an overabundance of dark matter ($\Omega_\chi h^2 \gtrsim 0.12$) for $\Delta M/M_\chi = 0.1$. The dashed (solid) curves correspond to an

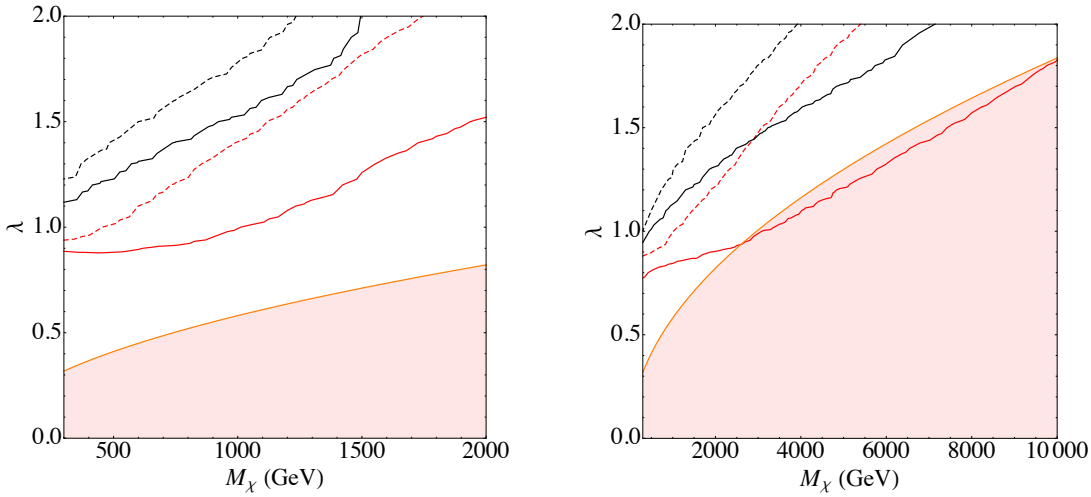

Figure 2.14.: Projections for 95% C.L. sensitivity for the LHC running at $\sqrt{s} =$ 14 TeV (left) and a future $p-p$ collider at $\sqrt{s} = 100$ TeV (right). The red (black) curves denote Model U (D). The dashed (solid) curves correspond to an integrated luminosity of 100fb^{-1}(3000fb^{-1}).

integrated luminosity of 100 fb^{-1}(3000 fb^{-1}); the red (black) curves correspond to Model U (D).

To obtain these plots, leading order cross-sections were computed using MadGraph5 with CTEQ6L1 parton distribution functions and a global K-factor of 1.25 was applied to obtain projected background events. Such a procedure may not capture all the considerations that may go into computing the background for a 100 TeV collider. For a full analysis, for instance, one would need to compute the effects of the double logarithmic contributions of Sudakov electroweak corrections [95], take into account the (modified) running of the standard model

gauge couplings [78], etc. (For additional considerations of dark matter physics at 100 TeV, see for example [96, 97, 98].) Our objective here is to present sensitivity projections that are indicative of what one might expect with extrapolations of what has been done already at the LHC at $\sqrt{s} = 8$ TeV. In particular, a uniform, uncorrelated systematic error of 6% was assumed across all bins. "Signal" events were generated by running 100 pseudo-experiments, applying Poisson fluctuations around the background events. A $\Delta\chi^2$-fit, as defined in Eq. (II.24), was then performed with each pseudo-experiment's results and the arithmetic mean of the $\Delta\chi^2$'s was obtained. 95% C.L. exclusion limits were then set on the $\lambda - M_\chi$ plane.

As one can see, the dilepton spectrum features are significantly more prominent at the LHC at 14 TeV, and even more so at a 100 TeV future collider. This is to be expected since the number of dilepton events increases considerably both by the higher center-of-mass energy and the higher integrated luminosities, thus improving the sensitivity of a shape-fit. For the same reason, the systematic uncertainties, which were smaller than statistical uncertainties in the $\sqrt{s} = 8$ TeV measurements and hence negligible in setting constraints, play a more important role in determining the sensitivities of future colliders.

One also notices the difference in slope between the solid red curves and the others in the left-hand plot, and between solid and dashed curves in the right-hand plot. This is because the contributions to $\Delta\chi^2$ come from a wider range near $m_{\ell\ell} \simeq 2M_\chi$.

We do not attempt to make projections for jets+MET constraints on the model.[5] This is because the exclusion cross-sections obtained by recasting the supersymmetry searches are extremely sensitive to the choice of cuts in the phase space when the LSP and colored scalar are nearly degenerate in mass. We anticipate some complementarity between the jets+MET sensitivity and dilepton sensitivity: as M_ϕ/M_χ is increased, the dilepton monocline signal is suppressed, while the jets+MET signal becomes more easily visible. Where the crossover occurs is undoubtedly highly sensitive to the respective detection search strategies.

In summary, this chapter explored a new signal for detecting dark matter at hadron colliders. In the next chapter, we will use the known properties of and experimental limits on dark matter to constrain a supersymmetric extension of the Standard Model, λ-SUSY.

[5] We are very grateful to Gavin Salam and Andreas Weiler for discussions about the applicability (and difficulties) of using their (awesome) Collider Reach tool [99] for projections in this squeezed scenario.

CHAPTER III

THE 125 GeV FAT HIGGS

This work is previously unpublished material. Arjun Menon initiated the project; Nirmal Raj performed the calculations and produced the plots and tables in this chapter.

Introduction

Weak scale supersymmetry (SUSY) remains a popular and elegant solution to the hierarchy problem of the Standard Model (SM) [100]. It provides a natural means to stabilize the electroweak scale against large quadratic corrections from higher scales. The fact that the Higgs boson was discovered to be light [101, 102], in accordance with SUSY's predictions, encourages us to continue our search for signals of SUSY at the TeV scale.

In the Minimal Supersymmetric extension of the Standard Model (MSSM), the tree-level Higgs quartic couplings are fixed to be the gauge couplings which leads to the tree-level Higgs boson mass that is below that of the Z boson. Therefore, to raise the Higgs boson mass to the observed value of 125 GeV at the LHC [101, 102] requires large corrections due to a heavy stop sector [103, 104, 105, 106, 107, 108, 109, 110, 111, 112, 113]. However, heavy stops lead to large correction to the up-

type soft SUSY breaking Higgs squared mass parameter which in turn leads to a large correction to the electroweak symmetry breaking (EWSB) condition. A delicate cancellation between these corrections and the Higgsino mass parameter is needed to stabilize the electroweak scale, which is generally considered unnatural. Therefore in the MSSM there exists a tension between the observed Higgs mass and the requirement that the model is natural.

The Next-to-Minimal Supersymmetric Standard Model (NMSSM) is the simplest extension of the MSSM that can address this tension. In the NMSSM, the Higgs sector is enlarged to include an extra gauge singlet that couples to the remaining MSSM Higgs doublets through a Yukawa coupling λ. λ contributes to the Higgs quartic at tree-level, and for large enough values, can raise the Higgs mass to the observed 125 GeV. Therefore the stops need not be too heavy, thereby improving the naturalness of the model. Moreover, in the general NMSSM (GNMSSM), an additional tadpole term for the gauge singlet can also facilitate EWSB [114].

For $\lambda \gtrsim 0.7$ at the weak scale, renormalization group (RG) evolution usually leads to this coupling developing a Landau pole below the GUT scale. Refs. [115, 116, 117, 118, 119, 120] have provided explicit UV-completions for such low scale models, which we collectively call Fat Higgs models. Refs. [121, 122, 123, 124, 125, 126, 127, 128, 129, 130, 131, 132, 133] have studied the phenomenological implications of models with such large λ couplings, which we collectively call λ-

SUSY models. For these models, they have found that the Higgs mass can easily be raised to the observed value while still keeping the spectrum natural. These studies have focused on a region of low $\tan\beta$ ($\tan\beta \equiv v_u/v_d$ where v_u and v_d are the vacuum expectation values (VEVs) of the corresponding Higgs doublets) and large λ because these regions were the most natural.

In this chapter, we study the possibility of raising the Higgs mass to 125 GeV in Fat Higgs/λ-SUSY models at *large* $\tan\beta$. As the λ^2-proportional tree-level contribution to the Higgs quartic is suppressed at large $\tan\beta$ the one-loop induced radiative corrections are crucial in raising the Higgs boson mass to its observed value. Similar to the stop-induced corrections that are proportional to $y_t^4 \log(m_{\tilde{t}}^2/Q^2)$ (where y_t is the top Yukawa and $m_{\tilde{t}}$ is the stop mass scale), in Fat Higgs/λ-SUSY models the dominant one-loop corrections are proportional to $\lambda^4 \log(M_A^2/Q^2)$ (where M_A is the scale of the non-standard Higgs bosons). Therefore these corrections are only relevant when $\lambda \gtrsim 1$ and the non-standard Higgs bosons are much heavier than the electroweak scale. The effect of radiative corrections in the NMSSM Higgs sector have been considered before [128, 134]. Ref. [128] focused on the most natural regions in the Scale-Invariant NMSSM, where it was found that these radiative corrections made a negligible contribution. In contrast, we show that at large $\tan\beta$, the λ induced radiative corrections can significantly modify the allowed regions of parameter space. Unlike Refs. [121, 128, 129], we also emphasise that electroweak precision constraints do not put a limit on $\tan\beta$. We

point out that raising the Higgsino mass parameter $\mu_{\rm eff}$ significantly weakens the electroweak precision constraints because the Higgsino component in the lightest neutralino is suppressed. The price of raising $\mu_{\rm eff}$ is a slight increase in the tuning of the EWSB condition. To illustrate these effects in regions of large $\tan\beta$ we also impose constraints from Higgs decay properties, direct dark matter detection experiments, the observed dark matter relic density and the invisible width of the Z boson. In particular, we find that direct dark matter detection experiments place strong limits on many regions of parameter space due to the large λ coupling. We also show that these allowed pockets of parameter space are within the reach of the XENON 1T experiment [135].

This chapter is organized as follows. In Sec. III.2, we set up the theoretical aspects required for the phenomenology of our model. To motivate the sizes of various terms in the Fat Higgs/λ-SUSY model, we present a "toy" high scale model where the fields have canonical mass dimensions in the electric theory. In addition, in this section we also compute the corrections to the Higgs quartic using the one-loop effective potential formalism, discuss the Higgsino contributions to electroweak precision constraints and naturalness in the large $\tan\beta$ regime of the Fat Higgs/λ-SUSY model. In Sec. III.3, we illustrate the impact of the formalism in Sec. III.2 by finding phenomenologically viable scenarios that can be probed at future experiments.

Theoretical Setup

In this section we first motivate the form taken by our superpotential by a simple discussion of the sizes of various terms that can arise in Fat Higgs/λ-SUSY models. In this discussion we assume that any exotic fields are much heavier than the electroweak scale. For the superpotential thus obtained, we present the Higgs potential at the tree level and analytically compute the one-loop corrections to the mass of the SM-like Higgs boson due to heavy non-standard Higgs fields, with special attention to the limit of large λ and $\tan\beta$. In addition we discuss the naturalness of the large $\tan\beta$ regions of the Fat Higgs/λ-SUSY models. We then discuss the reduced couplings of the SM-like Higgs to SM particles, which are constrained by LHC measurements of signal strengths. We end the section with a brief discussion of the neutralino sector with particular attention to electroweak precision observables.

Realizing Low Scale NMSSM with Large λ

The GNMSSM with a large λ at the weak scale implies that some of the Higgs fields are composite states. For example, in the minimal Fat Higgs scenario of Ref. [115], all of the Higgs sector fields are composite, while in Refs. [116, 120] the MSSM Higgs fields are fundamental. For simplicity we will assume that at scales

$\lesssim$10 TeV, the only fields present in the Higgs sector are the $SU(2)_L$ doublets $\hat{H}_u, \hat{H}_d$ and the gauge singlet $\hat{S}$.[1]

The most general superpotential with this particle content (assuming R-parity) has the form [139, 114]

$$\mathcal{W}_{\rm GNMSSM} = \mathcal{W}_{\rm Yukawa} + \lambda \hat{S}\hat{H}_u\hat{H}_d + \frac{1}{3}\kappa\hat{S}^3 + \mu\hat{H}_u\hat{H}_d + \frac{1}{2}\mu'\hat{S}^2 + \xi_F\hat{S}, \quad \text{(III.1)}$$

where λ, κ are dimensionless coupling strengths; μ, μ' are supersymmetric mass terms; ξ_F is a supersymmetric tadpole term of mass dimension 2, and $\mathcal{W}_{\rm Yukawa}$ contains the standard MSSM Yukawa superpotential terms. The corresponding soft SUSY-breaking terms are

$$\begin{aligned} -\mathcal{L}_{\rm soft} &= -\mathcal{L}^{\tilde{f}}_{\rm soft} + m^2_{H_u}|H_u|^2 + m^2_{H_d}|H_d|^2 + m^2_S|S|^2 + \\ &\quad \left(\lambda A_\lambda H_u H_d S + \frac{1}{3}\kappa A_\kappa S^3 + m^2_3 H_u H_d + \frac{1}{2}{m'_S}^2 S^2 + \xi_S S + h.c.\right) \quad \text{(III.2)} \end{aligned}$$

where $\mathcal{L}^{\tilde{f}}_{\rm soft}$ corresponds to the standard MSSM soft SUSY-breaking terms. $m^2_{H_u}, m^2_{H_d}, m^2_S$ are the soft SUSY breaking Higgs squared mass terms and A_λ, A_κ are the soft SUSY breaking trilinear terms. $m^2_3, {m'_S}^2$ are the CP-violating soft SUSY breaking squared mass terms and ξ_S is the dimension-3 soft SUSY breaking term corresponding to ξ_F.

A generic feature of most Fat Higgs/λ-SUSY models is that the Yukawa coupling $\lambda \gtrsim 0.7$ at the TeV scale.[2] Due to its renormalization group (RG) evolution, λ

[1] For more exotic realizations of composite Higgs models, see [117, 118, 136, 137].

[2] For Fat Higgs models that provide an existence proof of gauge coupling unification, see [115, 116].

becomes stronger at higher scales and develops a Landau pole at the compositeness scale Λ_H, where Λ_H is assumed to be lower than the grand unification scale $M_{\rm GUT}$. In the deep IR, much below Λ_H, the magnetic theory of mesons (i.e. the Higgs superfields) is described by the interactions in Eqs. (III.1) and (III.2). In the UV above Λ_H, some or all of the Higgs superfields are revealed to be composite states made up fundamental quarks whose interactions are described by some electric theory.

If the quarks in the electric theory have the canonical mass dimension and all Higgs superfields are composite, then the κ, μ, μ' terms in Eq. (III.1) and their corresponding soft SUSY-breaking terms in Eq. (III.2) are generated by marginal terms in the fundamental theory. For example, in the simplest Fat Higgs model [115], the Higgs superfields in Eq. (III.1) are composite states of the quarks T_i in the electric theory. These quarks are charged under a confining $SU(2)_H$ gauge group, thereby leading to the identification

$$\hat{S} \sim \hat{T}_5 \hat{T}_6; \quad \begin{pmatrix} \hat{H}_u^+ \\ \\ \hat{H}_u^0 \end{pmatrix} \sim \begin{pmatrix} \hat{T}_1 \hat{T}_3 \\ \\ \hat{T}_2 \hat{T}_3 \end{pmatrix}; \quad \begin{pmatrix} \hat{H}_d^0 \\ \\ \hat{H}_d^- \end{pmatrix} \sim \begin{pmatrix} \hat{T}_1 \hat{T}_4 \\ \\ \hat{T}_2 \hat{T}_4 \end{pmatrix}. \tag{III.3}$$

The λ term in Eq. (III.1) is dynamically generated by the Pfaffian of the mesons in the magnetic theory. Naive dimensional analysis (NDA) and canonical

normalization of the fields ($\langle T_i T_j \rangle \to (\Lambda_H/4\pi)\phi_{ij}$) lead to the relations

$$\begin{aligned} \lambda(\Lambda_H) \sim 4\pi; \qquad & \kappa(\Lambda_H) \sim \left(\frac{\Lambda_H}{4\pi\Lambda_0}\right)^3 \\ \mu \sim \frac{\Lambda_H^2}{(4\pi)^2\Lambda_0} \sim \mu'; \qquad & \xi_F \sim \frac{m\Lambda_H}{4\pi}, \end{aligned} \tag{III.4}$$

where m and Λ_0 are parameters in the electric superpotential given by

$$\begin{aligned} \mathcal{W}_{\text{electric}} \simeq\ & m\hat{T}_5\hat{T}_6 + \frac{y}{\Lambda_0}\left(\hat{T}_5\hat{T}_6\right)^2 + \frac{y'}{\Lambda_0}\left[\left(\hat{T}_1\hat{T}_3\right)\left(\hat{T}_2\hat{T}_4\right) - \left(\hat{T}_1\hat{T}_4\right)\left(\hat{T}_2\hat{T}_3\right)\right] + \\ & \frac{y''}{\Lambda_0^3}(T_5T_6)^3. \end{aligned} \tag{III.5}$$

The couplings y, y', y'', in the above equation, need not be $\mathcal{O}(1)$ numbers because Λ_0 is just a generic scale used to parameterize the mass dimension of each of these operators.

Eq. III.4 gives us a definition of Λ_H: it is the scale at which the size of λ is 4π. Using this definition, we can then estimate the size of the other parameters at the weak scale from their RG evolution. In determining Λ_H, we also account for the effects of the SM Yukawa couplings using the renormalization group equations (RGEs) in Ref. [139]. Having estimated the NMSSM parameters at the scale Λ_H using Eq. III.4, we run them down to the TeV scale by solving the RGEs and find that they *decrease* with decreasing scale. This running behavior has two important implications for our model:

1. Eq. (III.4) implies $\kappa(\Lambda_H) \ll \mathcal{O}(1)$. Run down to a renormalization scale $Q = \mathcal{O}(\text{TeV})$, we expect κ to be quickly suppressed due to the contribution of λ to its running. This suppression is illustrated in Fig. 3.1.(a), where we plot κ at

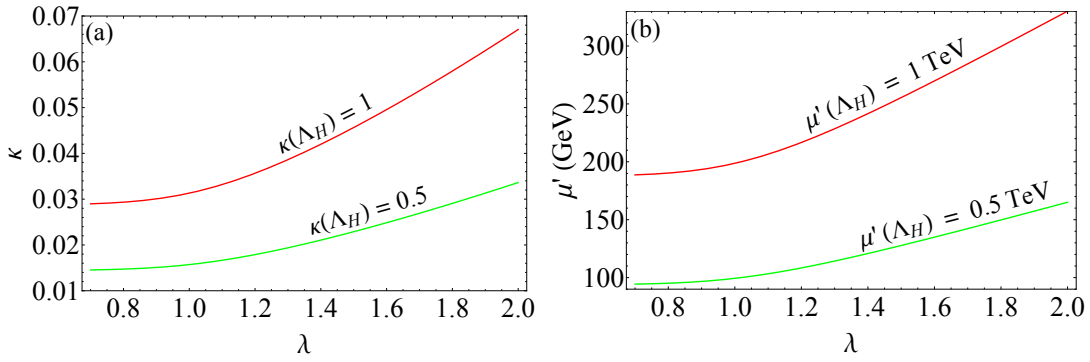

Figure 3.1.: (a): κ as a function of λ at the scale $Q = M_Z$, obtained by fixing κ at the scale Λ_H and then evolving it down with RGEs. The red (green) curve corresponds to $\kappa(\Lambda_H) = 1(0.5)$. (b): μ' as a function of λ at the scale $Q = M_Z$, obtained in a manner analogous to (a). The red (green) curve corresponds to $\mu'(\Lambda_H) = 1(0.5)$ TeV. In both plots we set $\tan\beta = 50$. See text for details of their behavior.

$Q = M_Z$ as a function of λ at $Q = M_Z$, setting $\tan\beta = 50$. These curves were obtained by first running $\lambda(Q = M_Z)$ up to determine Λ_H, then setting $\kappa(Q = \Lambda_H)$ to different values ≤ 1, and finally running κ down to $Q = M_Z$. We checked that the running of λ is insensitive to κ for these sizes of κ. The red curve corresponds to $\kappa(\Lambda_H) = 1$ and the green curve to $\kappa(\Lambda_H) = 0.5$. As expected from the RG running, smaller values of $\kappa(\Lambda_H)$ result in smaller values of $\kappa(Q = M_Z)$.

A larger λ implies a Landau pole at a lower scale. Therefore, Λ_H is closer to the electroweak scale for larger values of λ, which in turn weakens the suppression of κ as it runs down from Λ_H to M_Z. This is why κ is an increasing function of

λ in Fig. 3.1.(a). From the plot, we infer that for $\kappa(\Lambda_H) \leq 1$, the size of κ at the weak scale is suppressed by at least an order of magnitude. The implication of this suppression is that we can consistently neglect the effects of κ in our TeV-scale phenomenology. Therefore, for the rest of this chapter we will take $\kappa = 0$.

2. As compared to κ, μ' is only suppressed by an $\mathcal{O}(1)$ number when it is run down from $Q = \Lambda_H$ and $Q = M_Z$. This difference between values of μ' and κ can be understood from their β-function dependences. Using their one-loop β-functions in Ref. [139] we find

$$\frac{\kappa(Q)}{\kappa(\Lambda_H)} = \left(\frac{\mu'(Q)}{\mu'(\Lambda_H)}\right)^3. \tag{III.6}$$

We check this by determining $\mu'(Q = M_Z)$ as a function of $\lambda(Q = M_Z)$ in a manner analogous to the determination of $\kappa(Q = M_Z)$ above. Our results are shown in Fig. 3.1.(b), where the red (green) curve corresponds to $\mu'(\Lambda_H) = 1(0.5)$ TeV, with $\tan\beta = 50$. We see that $\mu'(\Lambda_H)$ is suppressed at the electroweak scale by at most a factor of 5. Hence $\mu'(M_Z)$ that can be of the size of the electoweak scale. Similarly, the Higgsino mass parameter μ and the tadpole term $\xi_F^{1/2}$ can also be the size of the electroweak scale.

We can now write down our low energy superpotential below the scale Λ_H:

$$\mathcal{W}^{\text{eff}}_{\text{NMSSM}} = \mathcal{W}_{\text{Yukawa}} + \lambda\hat{S}\hat{H}_u\hat{H}_d + \frac{1}{2}\mu'\hat{S}^2 + \xi_F\hat{S} \tag{III.7}$$

The associated soft-SUSY breaking potential is

$$\begin{aligned} -\mathcal{L}_{\rm soft}^{\rm eff} &= -\mathcal{L}_{\rm soft}^{\tilde{f}} + m_{H_u}^2|H_u|^2 + m_{H_d}^2|H_d|^2 + m_S^2|S|^2 \\ &\quad + \left(\lambda A_\lambda S H_u H_d + m_3^2 H_u H_d + \frac{1}{2}m_S'^2 + \xi_S S + \text{h.c.}\right). \end{aligned} \tag{III.8}$$

We have redefined the singlet chiral superfield, $\hat{S} \to \hat{S} - \mu$, to remove the μ term in the superpotential. In general, the associated soft term m_3^2 cannot be absorbed into A_λ simultaneously. Eqs. (III.7) and Eq. (III.8) constitute all the parameters treated in the rest of this article.

Higgs Sector

Tree level

At the tree level, the Higgs potential is given by

$$V_{\rm Higgs}^{\rm tree} = V_F + V_D + V_S \tag{III.9}$$

where

$$\begin{aligned} V_F &= \left|\lambda\left(H_u^+ H_d^- - H_u^0 H_d^0\right) + \mu' S + \xi_F\right|^2 + |\lambda S|^2 \ (|H_u|^2 + |H_d|^2), \\ V_D &= \frac{g^2}{8}\left(\left|H_u^0\right|^2 + \left|H_u^+\right|^2 - \left|H_d^0\right|^2 - \left|H_d^-\right|^2\right) + \frac{g^2}{2}\cos^2\theta_W \left|H_u^+ H_d^{0*} + H_u^0 H_d^-\right|^2, \\ V_S &= m_{H_u}^2|H_u|^2 + m_{H_d}^2|H_d|^2 + m_S^2|S|^2 + \\ &\quad (\lambda A_\lambda (H_u^+ H_d^- - H_u^0 H_d^0) S + m_3^2 (H_u^+ H_d^- - H_u^0 H_d^0) + \frac{1}{2}m_S'^2 S^2 + \xi_S S + \text{h.c.}), \end{aligned} \tag{III.10}$$

$H_u = (H_u^+, H_u^0)$, $H_d = (H_d^0, H_d^-)$, $g^2 \equiv g_1^2 + g_2^2$ and θ_W is the weak mixing angle. After electroweak symmetry breaking we can expand the Higgs fields in terms of the

CP-even fields (h_u^0, h_d^0, h_s^0), the CP-odd fields (A_D^0, A_S^0), the charged Higgs bosons $H^\pm$ and the Goldstone bosons $(G^\pm, G^0)$:

$$\begin{aligned} H_u &= \begin{pmatrix} G^+ s_\beta + H^+ c_\beta \\ \\ v s_\beta + \frac{1}{\sqrt{2}}[(h_u^0 + i(G^0 s_\beta - A_D^0 c_\beta)] \end{pmatrix}, \\ H_d &= \begin{pmatrix} v c_\beta + \frac{1}{\sqrt{2}}[(h_d^0 + i(-G^0 c_\beta + A_D^0 s_\beta)] \\ \\ -G^- c_\beta + H^- s_\beta \end{pmatrix}, \\ S &= \frac{1}{\sqrt{2}}(s + h_s^0 + i A_S^0), \end{aligned} \tag{III.11}$$

where $v \simeq 174$ GeV is the VEV of EWSB, $s_\beta \equiv \sin\beta$, $c_\beta \equiv \cos\beta$ and $s \equiv \langle S \rangle$. Expanding the potential about the minimum at $v_i \equiv (v_u, v_d, s)$, we can find the tree-level tadpole terms

$$T_j^{\text{tree}} \equiv \left. \frac{\partial V_{\text{Higgs}}^{\text{tree}}}{\partial \phi_j} \right|_{\{v_i\}} \tag{III.12}$$

where $\phi_j = (H_u^0, H_d^0, S)$. We can then solve for the soft squared masses $m_{H_u}^2, m_{H_d}^2, m_S^2$ by setting each $T_j^{\text{tree}} = 0$. Substituting these masses into the second order derivatives of the Higgs potential and neglecting CP-violating effects, we obtain the following tree-level CP-even Higgs mass matrix in the basis (h_u^0, h_d^0, h_s^0).

$$\begin{aligned} \left(M_H^2\right)_{11} &= M_Z^2 s_\beta^2 + r\ t_\beta^{-1}; & \left(M_H^2\right)_{12} &= (2\lambda^2 v^2 - M_Z^2) s_\beta c_\beta - r; \\ \left(M_H^2\right)_{22} &= M_Z^2 c_\beta^2 + r\ t_\beta; & \left(M_H^2\right)_{13} &= \lambda v (2\mu_{\text{eff}} s_\beta - (A_\lambda + \mu') c_\beta); \\ \left(M_H^2\right)_{23} &= \lambda v (2\mu_{\text{eff}} c_\beta - (A_\lambda + \mu') s_\beta); & \left(M_H^2\right)_{33} &= \left(\lambda v^2 (A_\lambda + \mu') - (\xi_S + \xi_F \mu')\right)/s, \end{aligned} \tag{III.13}$$

where $\mu_{\rm eff} \equiv \lambda s,\ t_\beta \equiv \tan\beta$ and $r \equiv \mu_{\rm eff}(A_\lambda + \mu') + m_3^2 + \lambda\xi_F$. The CP-odd Higgs mass matrix in the basis (A_D^0, A_S^0) is given by

$$\begin{aligned} \left(M_A^2\right)_{11} &= 2r/s_{2\beta}; \qquad \left(M_A^2\right)_{12} = \lambda v(A_\lambda - \mu'); \\ \left(M_A^2\right)_{22} &= \frac{1}{s}\left(\lambda v^2(A_\lambda + \mu')s_\beta c_\beta - (\xi_F\mu' + \xi_S)\right) - 2m_S'^2, \end{aligned} \tag{III.14}$$

and the charged Higgs mass is

$$M_\pm^2 = 2r/s_{2\beta} - (\lambda^2 - g_2^2/2)v^2. \tag{III.15}$$

We point out two features of the tree level masses that will be important in our discussion of the one-loop corrected Higgs mass. The first feature is the correlation among the scalar masses in the limit where A_λ and μ' are small compared to the heavy Higgs masses. This is best seen by setting $\left(M_A^2\right)_{12} = 0$ in Eq. (III.14) (which can be obtained by choosing $A_\lambda = \mu'$). Then the CP-odd eigenmasses are identified as $M_{A_D}^2 = \left(M_A^2\right)_{11}$ and $M_{A_S}^2 = \left(M_A^2\right)_{22}$. In this limit, by inspecting the matrix elements in Eqs. (III.13)–(III.15), we find that the CP-even, CP-odd and charged Higgs eigenstates arising from the $SU(2)$ doublet sector are nearly degenerate in mass, a feature well-known in the MSSM. Their mass splittings $\sim v^2$. These three fields then have a mass $\sim M_{A_D}$ in the limit $M_{A_D}^2 \gg v^2, A_\lambda^2, \mu'^2$, where M_{A_D} denotes the corresponding CP-odd eigenmass. Likewise, the CP-even and CP-odd Higgs eigenstates arising from the $SU(2)$ singlet are nearly degenerate, with mass splitting $\sim s^2$. Therefore, these two fields have a mass $\sim M_{A_S}$ in the limit $M_{A_S}^2 \gg s^2, A_\lambda^2, \mu'^2$.

The second feature is the decoupling of heavy states. Raising $M_{A_D}^2$ and $M_{A_S}^2$

decreases their impact on the mass of the lightest CP-even state, effectively making it more SM-like. A simple way to see this decoupling behavior is to rotate the CP-even mass matrix into the basis

$$h^0 = h_u^0 s_\beta + h_d^0 c_\beta,\ H^0 = h_u^0 c_\beta - h_d^0 s_\beta,\ h_s^0 = h_s^0 \tag{III.16}$$

which leads to the CP-even mass matrix

$$\begin{aligned}
\left(M_H^2\right)_{hh} &= M_Z^2 c_{2\beta}^2 + \lambda^2 v^2 s_{2\beta}^2; & \left(M_H^2\right)_{hH} &= (\lambda^2 v^2 - M_Z^2) s_{4\beta}/2; \\
\left(M_H^2\right)_{HH} &= M_{A_D}^2 - (\lambda^2 v^2 - M_Z^2) s_{2\beta}^2; & \left(M_H^2\right)_{hS} &= 2\lambda v(\mu_{\rm eff} - A_\lambda s_{2\beta}); \\
\left(M_H^2\right)_{HS} &= -2\lambda v A_\lambda c_{2\beta}; & \left(M_H^2\right)_{SS} &= M_{A_S}^2 + 2{m'_S}^2 + \frac{\lambda^2 v^2}{\mu_{\rm eff}} A_\lambda (2 - s_{2\beta} c_\beta),
\end{aligned} \tag{III.17}$$

Notice that ξ_F, ξ_S and m_3^2 are absorbed into our definition of $M_{A_D}^2$ and $M_{A_S}^2$. For large $\tan\beta$, $M_{A_D}^2$ and $M_{A_S}^2$, h^0 is identified with the SM Higgs, and H^0 and h_s^0 with non-standard Higgs bosons. This decoupling feature should be preserved after the inclusion of radiative corrections to the lightest CP-even Higgs mass, which is a non-trivial check of this computation.

Radiative corrections

The mass of the lightest Higgs boson can be significantly modified by one-loop corrections. The largest contributions to the Higgs potential at one-loop level are from the Higgs bosons, third generation squarks, charginos and neutralinos. Thus we have

$$\Delta V \ = \ \frac{1}{32\pi^2}\left(3\Delta V^{\tilde{t}} - 6\Delta V^t - \Delta V^{\chi^\pm} - 2\Delta V^{\chi^0} + \frac{1}{2}\Delta V^H + \frac{1}{2}\Delta V^A + \Delta V^{H^\pm}\right), \tag{III.18}$$

where for the a^{th} sector in the $\overline{\text{MS}}$ scheme,

$$\Delta V^a = \sum_i \left(M_{ia}^2(\phi_k)\right)^2 \left(\log \frac{M_{ia}^2(\phi_k)}{Q^2} - \frac{3}{2}\right) \approx \sum_{i=\text{heavy}} \left(M_{ia}^2(\phi_k)\right)^2 \left(\log \frac{M_{ia}^2}{Q^2} - \frac{3}{2}\right) \quad \text{(III.19)}$$

$M_{ia}^2(\phi_k)$ is the field-dependent mass eigenvalue for i^{th} contribution, M_{ia}^2 is the corresponding field-independent tree-level eigenvalue and the renormalization scale $Q \sim m_h = 125$ GeV. The approximation in Eq. (III.19) holds because we are interested in large corrections to the lightest Higgs mass due to states much heavier than the electroweak scale. Also, the field dependences inside log terms are neglected since they only induce higher order field-dependent terms.

The dominant contributions to ΔV in our scenario are due to heavy Higgs scalars coupling to the light Higgs boson with strengths proportional to powers of λ. The effects of the top quarks and the scalar tops on the Higgs potential have been studied in great detail in Refs. [103, 104, 105, 106, 107, 108, 109, 110, 111, 112, 113]. To highlight the effect of large λ corrections, we suppress the contribution of scalar tops to ΔV by choosing their masses close to the electroweak scale while still being compatible with ATLAS and CMS bounds [143, 144, 145]. The contributions of charginos and neutralinos to ΔV are typically small. The Higgs couples to the bino and the wino triplet with electroweak strength, whereas the λ-dependent coupling to the Higgsinos and singlino is typically suppressed due to neutralino mixing. In addition, the masses of the Higgsinos and singlino $\lesssim$ 1 TeV in our phenomenology while $M_A \in [4, 8]$ TeV. We therefore neglect corrections from the chargino-neutralino sector in the remainder of this article.

In order to compute the one-loop corrections to the Higgs potential in Eq. (III.19) due to the heavy CP-even, CP-odd and charged Higgs bosons, we must determine the field-dependent eigenvalues of each of the respective matrices. When expressed in terms of the matrix elements these field-dependent eigenvalues can in general be quite complicated. The calculation can nevertheless be simplified if we expand the eigenvalues as a Taylor series in the tree-level masses:

$$M_i^2(\phi_k) = M_{i,\text{tree}}^2 + \hat{b}_i(\phi_k) + \frac{\hat{c}_i(\phi_k)}{M_{i,\text{tree}}^2} + \mathcal{O}\left(\frac{1}{M_{i,\text{tree}}^4}\right), \tag{III.20}$$

where the coefficients $\hat{b}_i(\phi_k)$ and $\hat{c}_i(\phi_k)$ are at most quadratic and quartic in the fields respectively. Furthermore, when evaluated at the tree-level VEVs, the coefficients satisfy the condition $\hat{b}(\{v_k\}) = 0 = \hat{c}(\{v_k\})$.

In practice, we expand the eigenvalues as a Taylor series in the pseudoscalar masses $M_{A_D}^2$ and $M_{A_S}^2$. Using these approximations the one-loop effective potential due to the heavy Higgs scalars now evaluates to

$$\Delta V \propto \sum_i \left[a_i M_{A,i}^4 + 2b_i M_{A,i}^2 + (b_i^2 + 2c_i)\right]\left(\log\frac{M_{A,i}^2}{Q^2} - \frac{3}{2}\right) \tag{III.21}$$

where a_i are constants and the field-dependent coefficients b_i and c_i are obtained from the hatted coefficients in Eq. (III.20). Reducing ΔV to this form considerably simplifies the calculation of Higgs mass corrections. ΔV as presented here must also ensure that the decoupling behavior discussed in the previous subsection is preserved at one-loop order. This result is demonstrated in Appendix D.

The full details of our computation and the corresponding results are presented

in Appendix E, where two cases satisfying the condition $\left(M_A^2\right)_{12} = 0$ in Eq. (III.14) were considered. In the first case, which we call Case (A), we assume that the one-loop corrections arise from a single heavy scale $M_A = M_{A_D} = M_{A_S}$. The results from this case will be used in our discussion of phenomenology in Section III.3. In the second case, which we call Case (B), we show the effect of splitting the CP-odd Higgs masses, thereby obtaining corrections from two heavy scales. In this case we set the terms $A_\lambda, \mu', A_\kappa, m_3, m_S'$ to zero for simplicity. Further, we ignored corrections that depend on electroweak couplings since we are interested in the limit $\lambda \gg g$. It is important to note that Cases (A) and (B) pertain not only to different limits of the mass spectra of the CP-odd scalars, but also to somewhat different regions of the Lagrangian parameters. In Case (A), the parameters $A_\lambda, \mu', A_\kappa, m_3, m_S'$ can be non-zero in general, with the condition $\left(M_A^2\right)_{12} = 0$ imposing $A_\lambda = \mu'$. On the other hand, Case (B) explicitly sets them all to zero.

For Case B, the one-loop corrections obtained in the basis (h_u^0, h_d^0, h_s^0) are

$$
\begin{aligned}
\Pi_{11} &= \frac{\lambda^4 v^2}{16\pi^2} s_\beta^2 \left[-(4c_{2\beta} + c_{4\beta} + 1) \log\left(\frac{M_{A_D}^2}{M_Z^2}\right) + 2\log\left(\frac{M_{A_S}^2}{M_Z^2}\right) \right], \\
\Pi_{12} &= \frac{2\lambda^4 v^2}{16\pi^2} s_\beta c_\beta (2 + c_{4\beta}) \log\left(\frac{M_{A_D}^2}{M_Z^2}\right), \\
\Pi_{22} &= \frac{\lambda^4 v^2}{16\pi^2} c_\beta^2 \left[-(-4c_{2\beta} + c_{4\beta} + 1) \log\left(\frac{M_{A_D}^2}{M_Z^2}\right) + 2\log\left(\frac{M_{A_S}^2}{M_Z^2}\right) \right], \\
\Pi_{13} &= \frac{\lambda^3 v \mu_{\text{eff}}}{16\pi^2} s_\beta \left[-(1 + 3c_{2\beta}) \log\left(\frac{M_{A_D}^2}{M_Z^2}\right) + 4\log\left(\frac{M_{A_S}^2}{M_Z^2}\right) \right], \\
\Pi_{23} &= \frac{\lambda^3 v \mu_{\text{eff}}}{16\pi^2} c_\beta \left[-(1 - 3c_{2\beta}) \log\left(\frac{M_{A_D}^2}{M_Z^2}\right) + 4\log\left(\frac{M_{A_S}^2}{M_Z^2}\right) \right], \\
\Pi_{33} &= \frac{4\lambda^2 \mu_{\text{eff}}^2}{16\pi^2} \log\left(\frac{M_{A_D}^2}{M_Z^2}\right).
\end{aligned}
$$

When these contributions are rotated into the basis of Eq. (III.16), we get the (1, 1) element of the self-energy corrections as

$$\Pi_{hh} = \frac{\lambda^4 v^2 s_\beta}{16\pi^2}\left[\left(c_\beta^2(2+c_{4\beta}) - s_\beta^2(1+c_{4\beta}+4c_{2\beta})\right)\log\left(\frac{M_{A_D}^2}{M_Z^2}\right) + 2s_\beta^2\log\left(\frac{M_{A_S}^2}{M_Z^2}\right)\right]. \tag{III.22}$$

This is a good approximation for the Higgs mass correction when the mixing between the $SU(2)$ Higgs doublets and the singlet is negligible. At large $\tan\beta$, Eq. (III.22) further simplifies to

$$\Pi_{hh} \xrightarrow{\text{large}\tan\beta} \frac{\lambda^4 v^2}{16\pi^2}\left[2\log\left(\frac{M_{A_D}^2}{M_Z^2}\right) + 2\log\left(\frac{M_{A_S}^2}{M_Z^2}\right)\right]. \tag{III.23}$$

We could gain an intuitive understanding of our results by qualitatively estimating the size of the one-loop radiative corrections without recourse to the effective potential. Such an estimate would serve as a useful cross-check of the results obtained from ΔV. We do this by the following argument in our limit of interest, $\tan\beta \gg 1$ and $\lambda \gg g$. In this limit, we identify the real scalars $h_u^0 \to h,\ h_d^0 \to H,\ h_s^0 \to h_s^0$, where h is the SM Higgs boson, and H and h_s^0 are non-standard Higgses. The Standard Model Higgs and the Goldstone bosons reside mostly in H_u and the non-standard CP-even and CP-odd Higgses in H_d and S.

For $\lambda \gg g$, the most important quartic terms at tree-level are those proportional to λ^2. Before EWSB, we can read them off from Eq. (III.10) as the terms $|H_u^0|^2|H_d^0|^2$, $H_u^0 H_d^0 H_u^+ H_d^-$, $|H_u^0|^2|S|^2$ and $|H_d^0|^2|S|^2$. After EWSB, we can expand H_u, H_d, S using

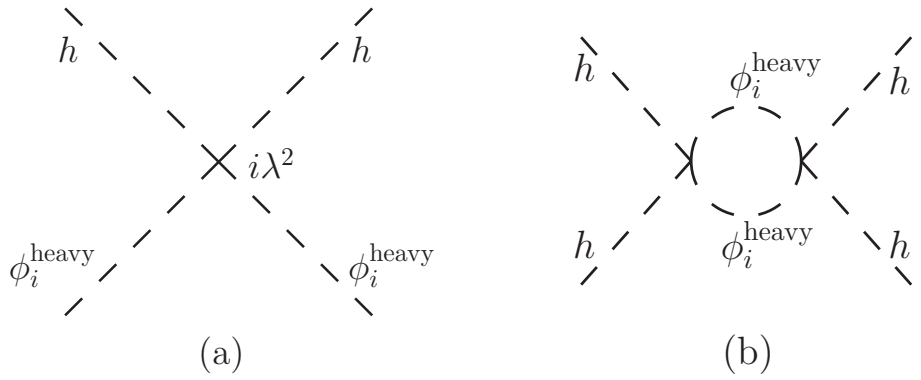

Figure 3.2.: (a): Tree level quartic vertices involving at least two h fields with vertex factors $\propto \lambda^2$, in the limit $\tan\beta \gg 1$. In this limit, $h_u^0 \to h, h_d^0 \to H, h_s^0 \to h_s^0$. No h^4 quartic terms at formed at tree level. ϕ_i correspond to the heavy fields H, h_s^0, A_D^0, A_S^0. (b): One-loop quartic vertices with four h legs, formed from the tree level vertices in (a). These are $\propto \lambda^4$ and account for most of the radiative corrections to the Higgs mass in our model.

Eq. (III.11) to obtain various quartic vertices in terms of the real and charged scalars.

Fig. 3.2.(a) shows all the tree-level quartic vertices that involve at least two h fields. Recall that the SM Higgs mass is set by the coupling strength of the quartic term h^4 in the scalar potential. The tree-level λ-dependent quartic h^4 terms are suppressed at large $\tan\beta$. However, using the vertices in Fig. 3.2.(a), we can construct four one-loop level quartic vertices proportional to h^4, as shown in Fig. 3.2.(b)[3]. Each of these diagrams is proportional to $\lambda^4 \log(M_{A_i}^2/M_Z^2)$, where

[3]We could also construct one-loop box diagrams with four external h fields using tree

$M^2_{A_i}$ is the mass scale of the heavy field running in the loop. Two diagrams each correspond to $M^2_{A_D}$ and $M^2_{A_S}$ respectively. Since the internal propagators are identical, each diagram comes with a factor of 2. Canonical normalization of the mass term of a real scalar implies an additional factor of 1/2. Finally, including the loop factor $1/16\pi^2$, we find the approximate correction to the lightest CP-even eigenstate to be

$$\Pi_{hh} \approx \frac{1}{2} \cdot \frac{2 \cdot 2 \cdot \lambda^4}{16\pi^2} \left[\log\left(\frac{M^2_{A_D}}{M^2_Z}\right) + \log\left(\frac{M^2_{A_S}}{M^2_Z}\right) \right], \tag{III.24}$$

which agrees with Eq. (III.23).

It would be interesting to compare the Higgs mass corrections obtained from the heavy Higgs fields and those obtained from top squarks. For simplicity, let us set the pseudoscalar masses equal, $M_A = M_{A_D} = M_{A_S}$, and obtain

$$\Pi^{\text{higgs}}_{hh} = \frac{\lambda^4}{4\pi^2} v^2 \log\left(\frac{M^2_A}{M^2_Z}\right). \tag{III.25}$$

Again for simplicity, we can assume the top squarks are degenerate ($m_{\tilde{t}} = m_{\tilde{t}_1} = m_{\tilde{t}_2}$). Then we obtain [139]

$$\Pi^{\text{stops}}_{hh} = \frac{3y_t^4}{4\pi^2} v^2 \log\left(\frac{m^2_{\tilde{t}}}{M^2_Z}\right). \tag{III.26}$$

The factor of 3 arises from the three QCD colors. If the pseudoscalars and the top squark are degenerate ($M_A = m_{\tilde{t}}$), we find from Eqs. (III.25) and (III.26) that $\Pi^{\text{higgs}}_{hh} \gtrsim \Pi^{\text{stops}}_{hh}$ for $\lambda \gtrsim 3^{1/4} y_t$. Since $y_t = m_t/v \simeq 1$, we have $\Pi^{\text{higgs}}_{hh} \gtrsim \Pi^{\text{stops}}_{hh}$ for $\lambda \gtrsim 1.3$.

level trilinear vertices, but these evaluate to finite amplitudes and do not contribute to the renormalization of the Higgs mass.

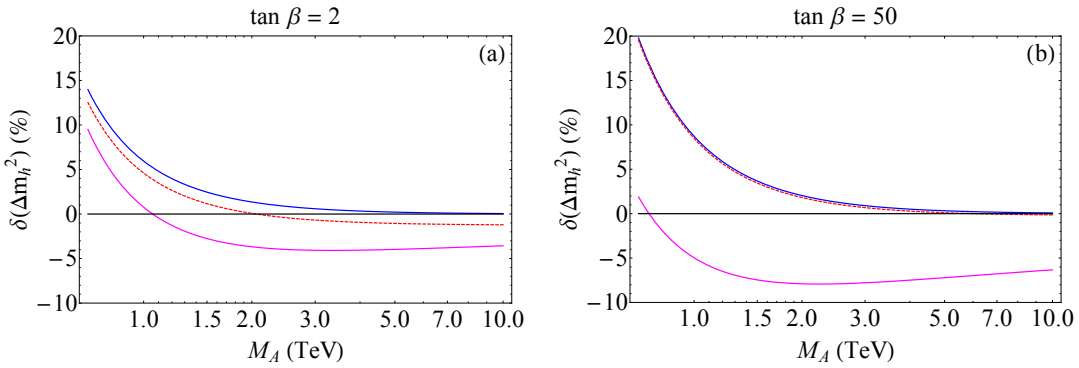

Figure 3.3.: Discrepancies between the Higss mass radiative corrections obtained from our one-loop effective potential in Eq. (III.22) and those obtained by other means, as a function of the mass M_A of degenerate pseudoscalars. The blue, dashed red and magenta curves represent corrections obtained from Eq. (III.22), Eq. (III.24) and Ref. [134] respectively. (a) corresponds to $\tan\beta = 2$, (b) corresponds to $\tan\beta = 50$. See text for details of the behavior of the curves.

In the discussion of our model's phenomenology, we set $m_{\tilde{t}} = 800$ GeV while M_A ranges between 4 TeV and 8 TeV; therefore, the one-loop corrections from the Higgs sector dominate those from the stops. Hence, throughout our analysis, the effect of the top squark correction to the SM Higgs mass is neglected.

We can now quantify the discrepancies between the results obtained by a full one-loop effective potential calculation and those obtained by other means. To do so, first we compute the correction to the Higgs squared mass obtained from Eq. (III.22), and denote it by Δm_h^2. For the same set of parameters, we compute $(\Delta m_h^2)_i$ for each alternative approximation labelled by i. We then take the difference

and normalize it to Δm_h^2 and define the discrepancy as

$$\delta(\Delta m_h^2) = \frac{(\Delta m_h^2)_i - \Delta m_h^2}{\Delta m_h^2}, \tag{III.27}$$

which is then expressed as a percentage. This approach eliminates the λ-dependence of the discrepancies and allows us to focus on their behavior with respect to $\tan\beta$ and the heavy (pseudo)scalar masses.

Assuming for simplicity that the CP-odd scalars are degenerate, we depict in Fig. 3.3. the discrepancies as a function of M_A. Figs. 3.3.(a) and 3.3.(b) correspond to $\tan\beta = 2$ and $\tan\beta = 50$ respectively. The blue curve denotes $(\Delta m_h^2)_i$ obtained from the approximation in Eq. (III.22). Since this approximation neglects doublet-singlet mixing, it tends to overestimate the correction, i.e., $\delta(\Delta m_h^2) > 0$ as observed in the plot. The discrepancy is also seen to asymptote to zero at large M_A, where the CP-even singlet Higgs decouples from the SM Higgs. The dashed red curve is $(\Delta m_h^2)_i$ obtained from our qualitative diagrammatic estimate (Eq. (III.23)). Since the estimate is designed for large $\tan\beta$ it disagrees with the blue curve at $\tan\beta = 2$, but coincides with it very well at $\tan\beta = 50$. The magenta curve depicts $(\Delta m_h^2)_i$ obtained from NMSSMTools 4.5.1 [134, 139], which also computes the one-loop radiative corrections from the effective potential, albeit under a different set of approximations. We find an interesting discrepancy here, to which we now turn.

The eigenvalues of the CP-odd mass matrix in Eq. (III.14) are given by

$$E_\pm^2 = \frac{1}{2}\left(T \pm \sqrt{T^2 - 4D}\right), \tag{III.28}$$

where $T = \left(M_A^2\right)_{11} + \left(M_A^2\right)_{22}$ is the trace and $D = \left(M_A^2\right)_{11}\left(M_A^2\right)_{22} - \left(M_A^2\right)_{12}^2$ is the determinant of the mass matrix. In Ref. [134], it is assumed that $D \ll T^2$, so that the eigenmasses are obtained as $E_+^2 \simeq T,\ E_-^2 \simeq D/T$. This always leads to a hierarchy between the pseudoscalar masses. In contrast, our approach sets the off-diagonal element $\left(M_A^2\right)_{12}$ to zero so that the eigenmasses are $E_+^2 = M_{A_D}^2 = \left(M_A^2\right)_{11},\ E_-^2 = M_{A_S}^2 = \left(M_A^2\right)_{22}$. Therefore, our approach allows for a variety of mass splittings. Hence the discrepancy between us and Ref. [134] is expected to be maximum when the CP-odd Higgses are degenerate, and minimum when these masses are well split. We illustrate this effect in Fig. 3.4.. Since $\left(M_A^2\right)_{12} = 0$ in our approach, we set $\left(M_A^2\right)_{12}$ to zero in the expression of Ref. [134] as well, in order to make an "apples-to-apples" comparison. We then plot $\delta(\Delta m_h^2)$ as a function of M_{A_D}/M_{A_S}, where we have taken $\lambda = 1.25$, $\tan\beta = 50$ and $\mu_{\text{eff}} = 110$ GeV. The red and blue curves depict $M_{A_S} = 1$ TeV and $M_{A_S} = 2$ TeV respectively. As expected, we find the discrepancy at its greatest at $M_{A_D}/M_{A_S} = 1$, which can reach upto $\sim 15\%$. Observe also that $\delta(\Delta m_h^2) < 0$, implying that Ref. [134] underestimates the one-loop contribution to the Higgs mass in the region around $M_{A_D}/M_{A_S} = 1$. As we raise M_{A_D}/M_{A_S}, the discrepancy drops quickly and our results concur.

The results of Ref. [134] were originally used in the code of NMSSMTools 4.5.1 [139]. Since our phenomenology in Section III.3 assumes $M_{A_D} = M_{A_S}$, we replaced the code in NMSSMTools 4.5.1 with the expressions that we derived in Appendix E.

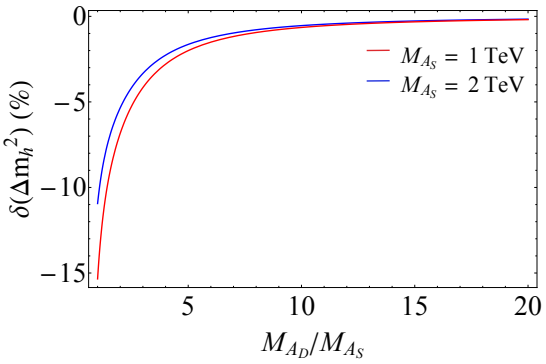

Figure 3.4.: The discrepancy between Higgs mass corrections obtained by Ref. [134] (which were used in the original code of NMSSMTools 4.5.1) and by us, as a function of the ratio of the heavy CP-odd Higgs masses. The red (blue) curve corresponds to $M_{A_S} = 1(2)$ TeV. The discrepancy arises due to an approximation assumed by Ref. [134], namely, that a hierarchy exists in the pseudoscalar spectrum. It is seen that our results agree when there is indeed a hierarchy. See text for more details.

Stability of the electroweak scale

The minimization conditions of the tree level Higgs potential in Eq. (III.9) lead to the same relation between the electroweak scale and the SUSY parameters seen in the MSSM. In particular, the EWSB condition is [140]

$$M_Z^2 = \frac{t_\beta^2 + 1}{t_\beta^2 - 1}\left(m_{H_d}^2 - m_{H_u}^2\right) - \left(m_{H_u}^2 + m_{H_d}^2\right) - 2\left|\mu_{\text{eff}}\right|^2, \tag{III.29}$$

which at large $\tan\beta$ reduces to

$$\frac{1}{2}M_Z^2 \approx -m_{H_u}^2 - \left|\mu_{\text{eff}}\right|^2, \tag{III.30}$$

where the $m_{H_d}^2$ terms are suppressed by t_β^{-1}. With this result we can now quantify the relative importance of different contributions (denoted by a) to the EWSB scale $(M_Z^2/2)$ as

$$\Delta(a^2) = \left| \frac{a^2}{M_Z^2/2} \right|. \tag{III.31}$$

The tree-level and one-loop corrections are the same as in the MSSM and are well-known [141]. For instance, the tree-level contribution due to $\mu_{\text{eff}} \lesssim 350$ GeV is equivalent to the one-loop contribution of stops at $m_{\tilde{t}} \lesssim 800$ GeV [142]. Hence the regions we are considering in this article are typically as tuned as regions of the MSSM with a light stop.

Higgs couplings to SM particles

LHC measurements of signal strengths (production rate $\times$ branching ratio) can potentially constrain the properties of the Higgs sector. Mixing among the Higgs fields can in principle alter the lightest Higgs boson's SM-like behavior. We follow the analysis of Ref. [129] to apply the relevant limits.

After including the one-loop self-energy corrections, we rotate the Higgs fields (h_u^0, h_d^0, h_s^0) into the mass eigenbasis (h_1, h_2, h_3) and identify the lightest scalar as

$$h_1 = (-h_u^0 \ \sin\alpha + h_d^0 \ \cos\alpha)\cos\gamma + h_s^0 \ \sin\gamma, \tag{III.32}$$

where the angles α is the usual MSSM CP-even mixing angle that characterizes doublet-doublet mixing and γ characterizes the doublet-singlet mixing. We can

then write down the reduced couplings of h_1 to pairs of fermions and vector bosons as

$$\begin{aligned}
\frac{g_{tth_1}}{g_{tth_{\rm SM}}} &= \cos\gamma\left(\cos\delta + \frac{\sin\delta}{\tan\beta}\right), \\
\frac{g_{bbh_1}}{g_{bbh_{\rm SM}}} &= \cos\gamma(\cos\delta - \sin\delta\tan\beta), \\
\frac{g_{VVh_1}}{g_{VVh_{\rm SM}}} &= \cos\gamma\cos\delta,
\end{aligned} \tag{III.33}$$

where $\delta = \alpha - \beta + \pi/2$.

If we inspect the off-diagonal entries of Eq. (III.17), we see that for $A_\lambda \ll M_A$ and large $\tan\beta$, $\left(M_H^2\right)_{hH} < \left(M_H^2\right)_{hS}$. Thus as we raise M_A, the heavy doublet Higgs (identified as h_3) generally decouples faster than the heavy singlet (identified as h_2), as noted by Refs. [124, 130] In dealing with the phenomenological consequences of our model, we focus exactly on the region of $A_\lambda \ll M_A$ and large $\tan\beta$. Therefore for the rest of this analysis we assume h_3 is decoupled from the spectrum and h_2 is not. In this limit, the mixing angle γ is given by

$$\sin^2\gamma = \frac{m_{hh}^2 - m_{h_1}^2}{m_{h_2}^2 - m_{h_1}^2}, \tag{III.34}$$

where $m_{hh}^2 = \lambda^2 v^2 \sin^2 2\beta + M_Z^2 \cos^2 2\beta$, and the Higgs couplings to fermions and vector bosons become

$$\frac{g_{tth_1}}{g_{tth_{\rm SM}}} = \frac{g_{bbh_1}}{g_{bbh_{\rm SM}}} = \frac{g_{VVh_1}}{g_{VVh_{\rm SM}}} = \cos\gamma. \tag{III.35}$$

Using these relations Ref. [129] performed a universal fit on the LHC signal strength measurements and found that $\sin^2\gamma \leq 0.23$ at 95% C.L. This result was

obtained using tree level relations for the reduced couplings. When we include our one-loop corrections, we find that the reduced couplings are modified by less than 1%. Therefore, in the discussion of our model's phenomenology in Section III.3 we will simply use the results of Ref. [129] to constrain the Higgs couplings with LHC measurements.

Neutralino Sector

The composition of the lightest neutralino and its couplings to the Higgs sector is central to the dark matter phenomenology of our model. The neutralino mass matrix in the basis $(\widetilde{B}, \widetilde{W}, \widetilde{\psi}_d^0, \widetilde{\psi}_u^0, \widetilde{\psi}_s^0)$ is given by

$$\mathcal{M}_{\rm neut} = \begin{pmatrix} M_1 & 0 & -g_1 v\cos\beta/\sqrt{2} & g_1 v\sin\beta/\sqrt{2} & 0 \\ 0 & M_2 & g_2 v\cos\beta/\sqrt{2} & -g_2 v\sin\beta/\sqrt{2} & 0 \\ -g_1 v\cos\beta/\sqrt{2} & g_2 v\cos\beta/\sqrt{2} & 0 & -\mu_{\rm eff} & -\lambda v\sin\beta \\ g_1 v\sin\beta/\sqrt{2} & -g_2 v\sin\beta/\sqrt{2} & -\mu_{\rm eff} & 0 & -\lambda v\cos\beta \\ 0 & 0 & -\lambda v\sin\beta & -\lambda v\cos\beta & \mu' \end{pmatrix} \tag{III.36}$$

Notice that when $\mu' \ll M_1, M_2, \mu_{\rm eff}$, large λ couplings imply a large Higgsino component in the lightest neutralino. This feature has many unique consequences for the dark matter phenomenology discussed in Sec. III.3. As we shall see, the Higgs-$\widetilde{\chi}_1^0$-$\widetilde{\chi}_1^0$ coupling strengh plays an important role in constraining our model

with dark matter experiments. This coupling, denoted hereafter by $g_{h\chi\chi}$, is obtained as

$$g_{h\chi\chi} = \frac{\lambda}{\sqrt{2}}(\zeta_{H_u} N_{\widetilde{\psi}_d^0} N_{\widetilde{\psi}_s^0} + \zeta_{H_d} N_{\widetilde{\psi}_u^0} N_{\widetilde{\psi}_s^0} + \zeta_S N_{\widetilde{\psi}_u^0} N_{\widetilde{\psi}_d^0}) - \frac{g_1}{2} N_{\widetilde{B}} (\zeta_{H_u} N_{\widetilde{\psi}_d^0} - \zeta_{H_d} N_{\widetilde{\psi}_u^0}), \tag{III.37}$$

where the N_i and ζ_j are the appropriate components of the lightest neutralino and the SM-like Higgs respectively. In terms of the rotation angles in Eq. (III.32), we can read off

$$\zeta_{H_u} = -\sin\alpha\cos\gamma, \quad \zeta_{H_d} = \cos\alpha\cos\gamma, \quad \zeta_S = \sin\gamma.$$

The dominant channel for $\widetilde{\chi}_1^0$-nucleon scattering is through a t-channel Higgs. Therefore, dark matter direct detection experiments, as well as limits on the invisible decay width of the Higgs, apply strong contraints on the coupling $g_{h\chi\chi}$. A suppressed $g_{h\chi\chi}$ can occur in our model either when the Higgsino content is suppressed or when there is a delicate cancellation between the various terms in Eq. III.37. We illustrate this point in more detail in Sec. III.3.

Electroweak precision limits

Due to mixing between the Higgsinos and the singlino induced by large λ in certain regions, constraints from electroweak precision experiments can be strong in Fat Higgs/λ-SUSY models [121, 123]. In particular, the T parameter can get large contributions from the neutralino sector, denoted hereafter by T_χ. This

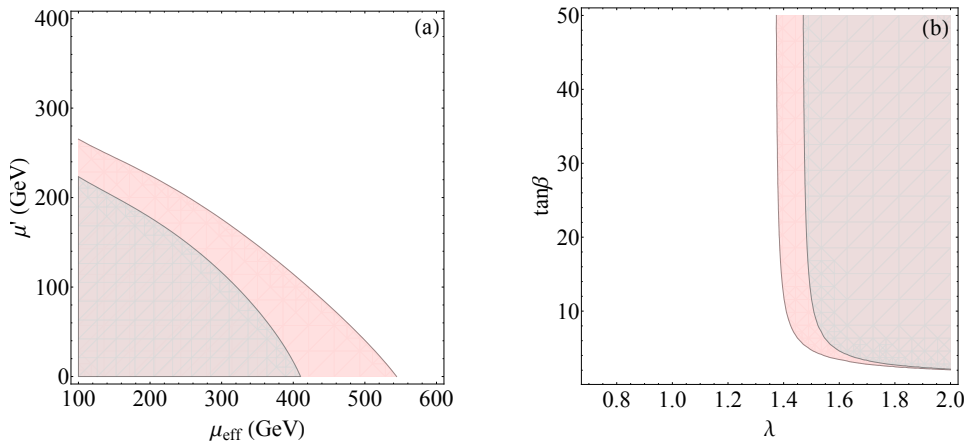

Figure 3.5.: Limits from electroweak precision parameter T on the neutralino sector of our model. The shaded regions are where $T_\chi > 0.15$ and therefore excluded at 95% C.L. Regions shaded gray correspond to the wino decoupled from the spectrum ($M_{\tilde{W}} = 10$ TeV) and regions shaded red to $M_{\tilde{W}} = 200$ GeV. In (a), $\lambda = 1.25$ and $\tan\beta = 5$ and in (b), $\mu_{\rm eff} = \mu' = 300$ GeV. See text for details of the behavior of these curves.

phenomenon is understood easily in the limit where the electroweak gauginos $\widetilde{B}$ and $\widetilde{W}$ decouple from the spectrum, i.e., M_1, M_2 are very large. This leaves us with three mass scales $\mu_{\rm eff}, \mu'$ and λv, which set the mass of the lightest neutralino, $M_{\tilde{\chi}^0_1}$. The lightest chargino is mostly Higgsino with a mass $\mu_{\rm eff}$. In this limit, T_χ is large when $M_{\tilde{\chi}^\pm_1} - M_{\tilde{\chi}^0_1}$ is large and when there is as a significant Higgsino component in $\widetilde{\chi}^0_1$. For simplicity, let us work in the limit where $\tan\beta$ is large. Then the neutralino

mass matrix in Eq. (III.36) is simply

$$\mathcal{M}_{\rm neut} \sim \begin{pmatrix} 0 & -\mu_{\rm eff} & -\lambda v \\ -\mu_{\rm eff} & 0 & 0 \\ -\lambda v & 0 & \mu' \end{pmatrix}. \tag{III.38}$$

T_χ is suppressed either when $\mu' \sim \mu_{\rm eff} \sim \lambda v$, where $M_{\tilde{\chi}_1^\pm} - M_{\tilde{\chi}_1^0}$ is small, or when $\mu_{\rm eff} \gg \mu' \sim \lambda v$, where the Higgsino component in $\widetilde{\chi}_1^0$ is suppressed. For $\mu' \ll \mu_{\rm eff} \sim \lambda v$, where both $M_{\tilde{\chi}_1^\pm} - M_{\tilde{\chi}_1^0}$ and the Higgsino component in $\widetilde{\chi}_1^0$ are large, constraints from T_χ can be strong.

Lowering the mass of the wino triplet M_2 to $\sim \mu_{\rm eff} \sim \lambda v$ can have a significant impact on T_χ. This is because the wino would mix with the light neutralinos and charginos. Lowering the bino mass M_1, on the other hand, gives only a negligible contribution to T_χ. This is because the bino mixing with the rest of the neutralinos is only proportional to g_1.[4]

In Fig. 3.5. we present the T-parameter contributions from the charginos and neutralinos, which were computed using the general expressions provided in Ref. [146]. In Fig. 3.5.(a), we take $\lambda = 1.25$ and $\tan\beta = 5$ and show our results in the $\mu_{\rm eff} - \mu'$ plane. The shaded regions denote where T_χ is not within the 95% C.L range $[-.01, 0.15]$ set by the Particle Data Group [147]. The gray

[4]It must be remembered that relative minus signs between $\mu_{\rm eff}, \mu'$ and $M_{\tilde{W}}$ would introduce quantitative changes in the picture owing to new phases in the neutralino mixing angles. We will not include these relative signs in our discussion.

region corresponds to large gaugino masses $(M_1, M_2) = (10\text{ TeV}, 10\text{ TeV})$ while the red region corresponds to a light wino with $(M_1, M_2) = (10\text{ TeV}, 0.2\text{ TeV})$. As discussed above, lowering the wino mass can lead to a larger T_χ. For small μ', T_χ decreases as μ_{eff} increases due to a reduction in the Higgsino component of the lightest neutralino. Similarly, raising μ' has the effect of reducing the splittings between the neutralinos and charginos which also leads to a smaller T_χ.

The effects of varying λ and $\tan\beta$ on T_χ are presented in Fig. 3.5.(b). Here we fix $\mu_{\text{eff}} = \mu' = 300$ GeV. The colored regions have the same definition as those in Fig. 3.5.(a). Since the elements of $\mathcal{M}_{\text{neut}}$ quickly asymptote to fixed values as a function of $\tan\beta$, it can be seen that T_χ is insensitive to large $\tan\beta$. This insensitivity to large $\tan\beta$ is clear in the relation derived in Ref. [121]

$$T_\chi \approx \left(\frac{t_\beta^2 - 1}{t_\beta^2 + 1}\right)^2 F(\mu_{\text{eff}}, \mu', \lambda), \tag{III.39}$$

where $F(\mu_{\text{eff}}, \mu', \lambda)$ is some function of these variables. This relation also shows that T_χ is suppressed as t_β approaches 1, thereby allowing for larger values of λ. As stated before, lowering M_2 typically increases the neutralino and chargino contributions to the T-parameter. However, it is important to emphasize that increasing either μ_{eff} or μ' can significantly lower the electroweak precision constraints even for large $\tan\beta$. A large μ_{eff} comes at the cost of a slight increase in electroweak fine-tuning, but can greatly weaken T-parameter constraints.

Finally, we make two remarks. First, the S-parameter was not discussed here. This is because the contributions of our model to S are very small in our regions of

interest and hence the constraints are much weaker than those on the T-parameter. Second, the T-parameter receives a stop-sbottom contribution, as discussed in Ref. [121]. In the limit of zero left-right mixing, this is given by

$$T_{\text{st}-\text{sb}} \approx 0.05 \left(\frac{500 \text{ GeV}}{m_{\tilde{t}_L}} \right)^2 \tag{III.40}$$

In our phenomenological discussions, we will choose $m_{\tilde{t}_L} = 800$ GeV to suppress this contribution.

Phenomenology

In this section we study the phenomenological constraints on the large $\tan\beta$ regions of the Fat Higgs/λ-SUSY models. In addition to the constraints arising from Higgs corrections discussed in the previous section, we also include limits from dark matter experiments, most importantly those set by the LUX experiment [18]. In particular, the mass and couplings of the lightest neutralino $\widetilde{\chi}_1^0$ can put strong constraints on our parameter space.

In order find phenomenologically viable regions, we modified NMSSMTools 4.5.1 [139] to include the Higgs mass corrections we computed in Sec. III.2.2. We then made the following simplifying assumptions:

- In the Higgs sector, we take the pseudoscalars to be degenerate, with $M_{A_D} = M_{A_S} = M_A$. Furthermore we assume that $m'_S = m_3 = 0$, so that the heavy CP-even Higgs bosons are also (nearly) degenerate. The condition that the

CP-odd masses are degenerate requires that $\left(M_A^2\right)_{12} = 0$ in Eq. III.14, which implies $A_\lambda = \mu'$. Therefore, both μ' and $\mu_{\rm eff}$ control the amount of doublet-singlet mixing in Eq. (III.13). The only independent parameters in the Higgs sector are then: $\lambda, \mu_{\rm eff}, \mu', \tan\beta$ and M_A.

- In order to be safe from electroweak precision bounds, we decouple the winos at $M_2 = 10$ TeV, leading to an effective theory for the neutralino system with five free parameters : M_1, $\mu_{\rm eff}$, μ', λ and $\tan\beta$.

- We require $\mu_{\rm eff} > 104$ GeV to evade the LEP II bound on charged Higgsinos [148].

- The sleptons and the first two generations of squarks are decoupled from the low energy phenomenology and their masses set at 5 TeV, unless stated otherwise. The top squark parameters are set at $m_{\tilde{Q}_3} = m_{\tilde{U}_3} = 800$ GeV and $A_t = 0$, thereby making the stop contributions to the Higgs mass and the electroweak symmetry breaking condition in Eq. (III.30) small. This choice of stop masses also avoids constraints from collider searches [143, 144, 145] and, as mentioned in Sec. III.2.3, from electroweak precision tests.

- We choose to require the conventional upper limit $\tan\beta \leq 60$, so that $y_b \leq 1$ at the weak scale. Larger values of y_b may be allowed as long they do not develop a Landau pole at a scale below that of λ.

These assumptions reduce the number of independent SUSY parameters to

$$\lambda,\ \tan\beta,\ M_A,\ \mu_{\rm eff},\ \mu',\ M_1\ .$$

As discussed in Sec. III.2.3, precision electroweak constraints are weak when either the Higgsinos decouple ($\mu', \mu_{\rm eff} \gtrsim \lambda v$) at any value of $\tan\beta$, or when $\mu' \ll \lambda v \sim \mu_{\rm eff}$ at low $\tan\beta$. In these regions, $g_{h\chi\chi}$ (as defined in Eq. III.37) is suppressed in the following two scenarios that lead to suppressed rates of DM-nucleon scattering.

(a) **Large** $\tan\beta$ **and** $\mu' \sim \lambda v \sim \mu_{\rm eff}$.

$\widetilde{\chi}_1^0$ is an admixture of singlino and bino, such that the Higgsino content is suppressed [126]. We will show that, when the one-loop Higgs mass corrections are taken into account, this dark matter scenario is compatible with all constraints for $\tan\beta \leq 60$, thus opening the window to viable pockets of parameter space at very large $\tan\beta$. The focus of this section will be on this case.

(b) **Low** $\tan\beta$ **and** $\mu' \ll \lambda v \sim \mu_{\rm eff}$.

$\widetilde{\chi}_1^0$ is an admixture of bino, Higgsino and singlino. This is an example of the well-known "well-tempered" dark matter [150], which works in our model for $\tan\beta \lesssim 3$. Since the emphasis of this chapter is on opening up large $\tan\beta$, we discuss this case only briefly.

In each of these regions, constraints from the Higgs boson mass, direct detection experiments, the dark matter relic abundance and the invisible decay width of the Z and Higgs boson are crucial in determining viable parametric scenarios.

Large $\tan\beta$ *and* $\mu' \sim \lambda v \sim \mu_{eff}$*: Bino and Singlino Dark Matter*

Large λ and large $\tan\beta$ are a new region of parameter space that have not been emphasized in the literature before. We showed in Sec. III.2.2 that this region can be compatible with the mass of the SM Higgs boson because one-loop radiative corrections to the Higgs mass are insensitive to $\tan\beta$ at large values, and are set solely by λ and M_A. We also showed that precision electroweak constraints can be weak in this region. We now show that this region is also compatible with constraints from dark matter.

As mentioned in Sec. III.2.3, it can be seen from Eq. (III.37) that $g_{h\chi\chi}$ is suppressed when $\widetilde{\chi}_1^0$ is an admixture of bino and singlino such that $N_{\widetilde{B}}^2 + N_{\widetilde{\psi}_s^0}^2 \simeq 1$. This is possible when M_1 and/or μ' are small relative to the other mass parameters. For simplicity, we illustrate this scenario for a bino-like ($N_{\widetilde{B}}^2 \simeq 1$) or singlino-like ($N_{\widetilde{\psi}_s^0}^2 \simeq 1$) dark matter candidate. The self-annihilation of $\widetilde{\chi}_1^0$ into SM fields in the early universe is generally inefficient, since its tiny Higgsino content suppresses both the Z- and h-mediated channels. This typically leads to the model predicting relic abundances that exceed the observed value, $\Omega_\chi h^2 \simeq 0.12$. However, a viable relic abundance of $\Omega_\chi h^2 \leq 0.12$ can be accomplished by means of two exceptions to the standard freeze-out mechanism resonant annihilation and co-annihilation [152].

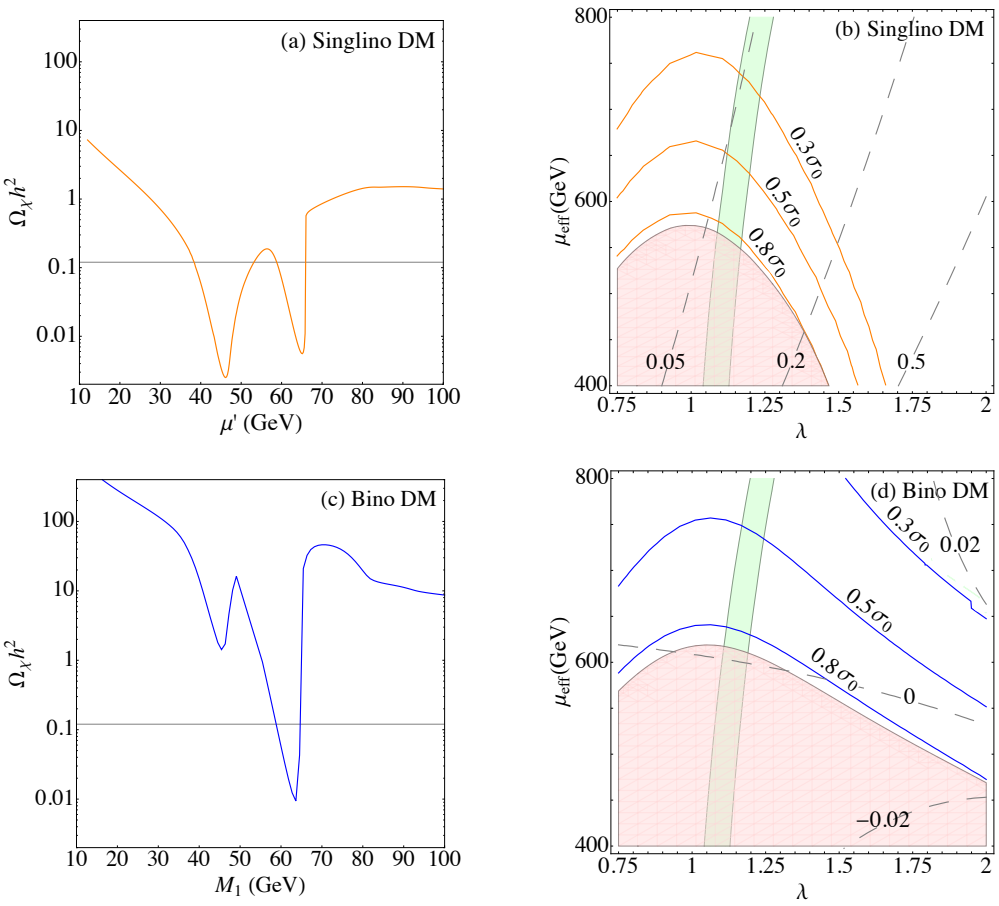

Figure 3.6.: Scenarios where resonant annihilation in the early universe leads to $\Omega_\chi h^2 \leq 0.12$. (a): Relic abundance as a function of $\mu' \simeq M_{\tilde{\chi}_1^0}$ for singlino dark matter. The dips at $\mu' \simeq 45$ GeV and $\mu' \simeq 62$ GeV correspond to resonant annihilation via an s-channel Z and h respectively. (b): Contours of DM-nucleon scattering cross-section for singlino DM in units of $\sigma_0 = 10^{-45}$ cm^2, fixing $\mu' = 62.5$ GeV. The region shaded red is excluded by LUX and the region shaded green corresponds to 120 GeV $< m_h <$ 130 GeV. The dashed lines are contours of T_χ. (c) and (d) are the same as (a) and (b), but for bino dark matter.

Resonant Annihilation Region

If $M_{\tilde{\chi}_1^0}$ happens to be close to $m_h/2$, it can undergo resonant annihilation through an s-channel Higgs. Fig. 3.6. illustrates this scenario. Fig. 3.6.(a) shows $\Omega_\chi h^2$ as a function of $\mu' \simeq M_{\tilde{\chi}_1^0}$ for a singlino-like LSP, where we decouple the Higgsinos and the bino by setting $\mu_{\rm eff} = 800$ GeV and $M_1 = 1$ TeV, and obtain $m_h = 125$ GeV by setting $\lambda = 1.25, \tan\beta = 50$ and $M_A = 4$ TeV. We notice two dips at $\mu' \simeq 45$ GeV and $\mu' \simeq 62$ GeV, corresponding to resonant annihilation through an s-channel Z and h respectively. The dip near $\mu' \simeq 62$ GeV falls below $\Omega_\chi h^2 = 0.12$, making it a cosmologically viable region. The orange curves in Fig. 3.6.(b) depict contours of the LSP-nucleon scattering rates, $\sigma_{\rm SI}$ (in units of $\sigma_0 = 10^{-45}$ cm^2), in the $\lambda - \mu_{\rm eff}$ plane. Here we fix $\mu' = 62.5$ GeV while the rest of the parameters are as in Fig. 3.6.(a). Regions shaded red are excluded by LUX at 90% C.L., and the band shaded green corresponds to 120 GeV $\leq m_h \leq$ 130 GeV. Contours of T_χ are denoted by dashed curves. Figs. 3.6.(c) and 3.6.(d) depict the same features as Figs. 3.6.(a) and 3.6.(b) respectively, but for a bino-like LSP. All the parameters are the same as before, but with $M_1 \leftrightarrow \mu'$.

In both Figs. 3.6.(b) and 3.6.(d), the dark matter-nucleon scattering rates are seen to decrease as we decouple the Higgsinos by increasing $\mu_{\rm eff}$. In Fig. 3.6.(b), T_χ is observed to rise with increasing λ due to an increase in mixing between the Higgsinos and singlino. The region around $m_h \sim 125$ GeV corresponds to $T_\chi \sim 0.05$, safe from electroweak precision constraints. In contrast to singlino

dark matter, $T_\chi \sim 0$ for bino dark matter throughout the plot in Fig. 3.6.(b), a result of decoupling both the singlino and the Higgsinos. The regions described in Figs. 3.6.(b) and 3.6.(d) are also safe from invisible Higgs decay bounds since the process $h \to \widetilde{\chi}_1^0 \widetilde{\chi}_1^0$ is phase space suppressed.

Co-annihilation Region

If the mass spectrum is such that one or more sleptons are nearly degenerate with $\widetilde{\chi}_1^0$, dark matter annihilation could be assisted by the sleptons through co-annihilation effects, leading to a small relic abundance. Bounds from LEP on charged sleptons [149] would then imply that $M_{\tilde{\chi}_1^0} > 104$ GeV.

We investigate this in Fig. 3.7.. Shown with orange curves in Fig. 3.7.(a) are contours of $\sigma_{\rm SI}$ (in units of $\sigma_0 = 10^{-45}$ cm^2) on the $\mu_{\rm eff} - \mu'$ plane, for singlino dark matter at $\lambda = 1.25$ and $\tan\beta = 50$. Here we have taken $M_1 = 1$ TeV and $M_A = 8$ TeV. The region shaded red is excluded by LUX at 90% C.L. The vertical bands capture $m_h \in [120, 130]$ GeV, where the band shaded green (gray) corresponds to $\lambda = 1.1(1.25)$. The effect of varying λ on $\sigma_{\rm SI}$ is not shown since the scattering cross-section is insensitive to it due to the large values of $\mu_{\rm eff}$. Fig. 3.7.(b) represents a similar scenario for bino dark matter, with blue curves depicting contours of $\sigma_{\rm SI}$ in units of $\sigma_0 = 10^{-45}$ cm^2. All parameters are the same as before, but with $M_1 \leftrightarrow \mu'$.

In both plots in Fig. 3.7., we find a decrease in $\sigma_{\rm SI}$ with $\mu_{\rm eff}$, which is an effect of decoupling the Higgsinos that results in the diminution of $g_{h\chi\chi}$. We also find an

increase in $\sigma_{\rm SI}$ with μ' or M_1, which is the opposite effect. Raising μ' or M_1 leads to more mixing with the Higgsinos, thereby bolstering $g_{h\chi\chi}$. Comparing across the plots, we immediately notice that $\sigma_{\rm SI}$ is greater for singlino DM than for bino DM for the same $M_{\tilde{\chi}_1^0}$ (set by μ' and M_1 respectively). This is of course because the singlino mixes with the Higgsinos more than the bino does, as can be inferred from the corresponding off-diagonal entries in Eq. (III.36).

The relatively large size of $\mu_{\rm eff}$ and μ' here suppress the Higgsino sector contributions to the T parameter. For regions where $m_h \sim 125$GeV, we find that $T_\chi < 0.03$ for singlino dark matter and $T_\chi \sim 0$ for bino dark matter.

Future prospects

In this region (large $\tan\beta$ with $\mu' \sim \lambda v \sim \mu_{\rm eff}$), the non-standard Higgs scalars are heavy with M_A between $4-8$ TeV. Therefore the doublet-singlet mixing in the Higgs sector is very small leading to a 1% deviation in the Higgs signal strengths from the SM. Such deviations are much below the sensitivity of the LHC at present and future runs, and can only be tested at a future "Higgs factory". However, this region can be probed by future dark matter direct detection experiments. In particular, the projected reach of the XENON1T experiment [135] corresponds to $\sigma_{\rm SI} \approx 10^{-47} - 10^{-46}$ cm^2 for dark matter masses between 50 GeV and 500 GeV. Since the DM-nucleon scattering cross-sections in our viable regions in Figs. 3.6.

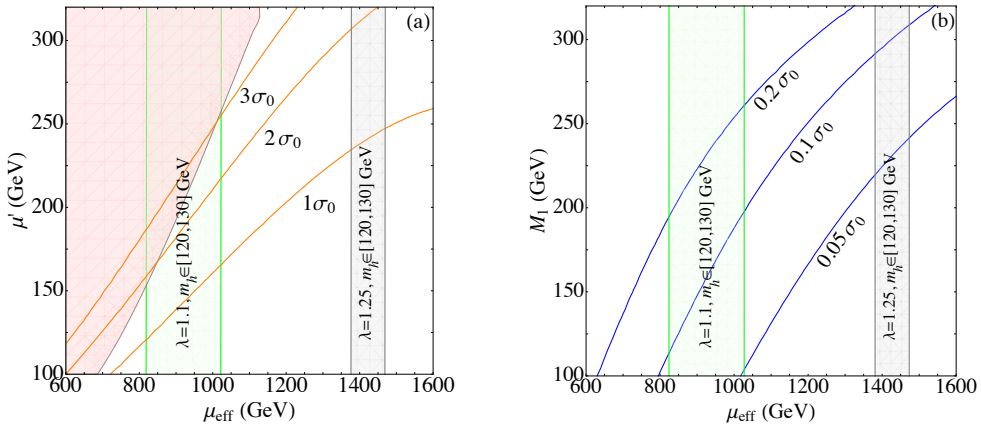

Figure 3.7.: Scenarios where co-annihilation with sleptons leads to $\Omega_\chi h^2 \leq 0.12$. (a): Singlino dark matter, with orange curves depicting contours of LSP-nucleon scattering cross-section in units of $\sigma_0 = 10^{-45}$ cm^2. The region shaded red is excluded by LUX. (b): Bino dark matter, with blue curves depicting contours of LSP-nucleon scattering cross-section in units of $\sigma_0 = 10^{-45}$cm^2. In both plots, the green and gray shaded regions correspond to 120 GeV $< m_h <$ 130 GeV for $\lambda = 1.1$ and $\lambda = 1.25$ respectively. More details are presented in the text.

and 3.7. vary from $\sim 10^{-46} - 10^{-45}$ cm^2, these regions can be completely probed at the XENON1T experiment.

Low $\tan\beta$ *and* $\mu' \ll \lambda v \sim \mu_{eff}$*: Well-tempered Dark Matter*

In the limit where $\mu' \ll \mu_{\rm eff}, M_1$, precision electroweak contraints can be evaded by raising $\mu_{\rm eff}$ and decoupling the Higgsinos. However, this would introduce constraints from limits on the invisible decay of the Z boson. We can see this by inspecting the mass of the lightest neutralino in this limit,

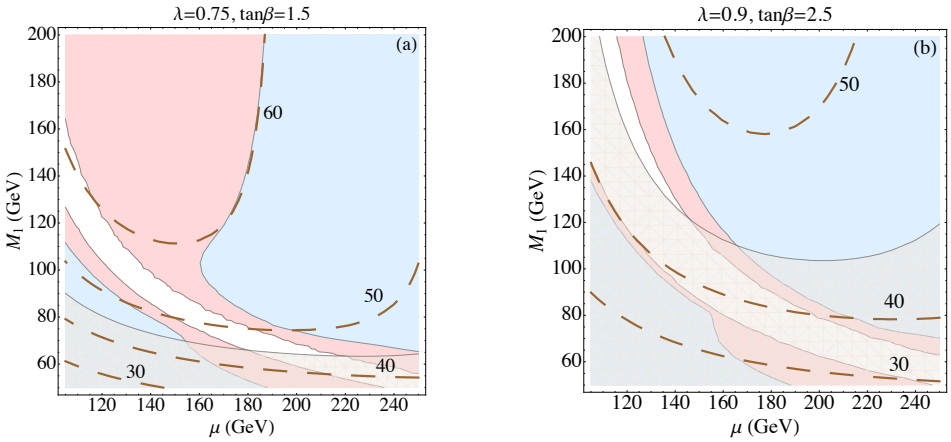

Figure 3.8.: The well-tempered scenario at low $\tan\beta$, with $\widetilde{\chi}_1^0$ an admixture of bino, Higgsino and singlino. In (a), $\lambda = 0.75$, $\tan\beta = 1.5$ and in (b), $\lambda = 0.9$, $\tan\beta = 2.5$. The heavy Higgs states are decoupled at $M_A = 5$ TeV. This choice of parameters fixes $m_h \sim 125$ GeV. Regions shaded red are excluded by LUX at 90% C.L., blue by $h \to \widetilde{\chi}_1^0\ \widetilde{\chi}_1^0$ bounds and gray by $Z \to \widetilde{\chi}_1^0\ \widetilde{\chi}_1^0$ bounds. These constraints leave a small patch of parameter space that are still viable, the "blind spots". The dashed lines are contours of $M_{\widetilde{\chi}_1^0}$ in GeV. More details are presented in the text.

$M_{\widetilde{\chi}_1^0} \approx \mu' + \lambda^2 v^2 \mu_{\rm eff} s_{2\beta}/(\mu_{\rm eff}^2 + \lambda^2 v^2)$. Raising $\mu_{\rm eff}$ has the effect of lowering $M_{\widetilde{\chi}_1^0}$, which may push it below $M_Z/2$. We also see that large $\tan\beta$ can lower $M_{\widetilde{\chi}_1^0}$ and bring the $Z \to$ invisible limits into play. Therefore, for this scenario to be viable, we require $\mu_{\rm eff} \sim \lambda v$ and small $\tan\beta$. In this region, $g_{h\chi\chi}$ is supppressed when $\widetilde{\chi}_1^0$ is an admixture of $\widetilde{B}$, $\widetilde{\psi}_u^0$, and $\widetilde{\psi}_s^0$ such that they lead to "blind spots" in parameter

space [138] – regions that are compatible with current experiment. For illustration, we have consistently set $\mu' = 0$ in this section.

We illustrate these blind spots in Fig. 3.8., which shows constraints on the LSP in the $M_1 - \mu_{\text{eff}}$ plane. Fig. 3.8.(a) corresponds to $\tan\beta = 1.5$ and Fig. 3.8.(b) to $\tan\beta = 2.5$. To fix $m_h \sim 125$ GeV, we take $\lambda = 0.75$ and $\lambda = 0.9$ respectively and decouple the heavy Higgses with $M_A = 5$ TeV. The regions shaded red are excluded by LUX at 90% C.L. Regions shaded blue are excluded by the latest limit on the invisible decay of the Higgs, $\mathcal{B}.\mathcal{R}.(h \to \widetilde{\chi}_1^0\widetilde{\chi}_1^0) < 0.4$ [151]. The gray region is excluded by limits from the invisible decay of the Z. The dashed curves represent contours of $M_{\widetilde{\chi}_1^0}$ in GeV. This range of parameters is cosmologically viable with $\Omega_\chi h^2 < 0.12$, where the dominant primordial annihilation of $\widetilde{\chi}_1^0$ is through an s-channel Z.

A comparison across the plots informs us that an increase in $\tan\beta$ strengthens the constraints from $Z, h \to \widetilde{\chi}_1^0\widetilde{\chi}_1^0$, which is due to the decrease in $M_{\widetilde{\chi}_1^0}$, as discussed earlier. We also notice that the LUX constraints are consistently stronger than $h \to \widetilde{\chi}_1^0\widetilde{\chi}_1^0$ bounds. Therefore, the blind spots (unshaded regions) are determined in this case by limits from LUX and invisible Z decays alone. As mentioned in Sec. III.2.3, larger values of λ contribute more to T_χ. For Fig. 3.8.(a) and Fig. 3.8.(b), $T_\chi < 0.02$ (completely safe) and $T_\chi < 0.11$ (marginally safe) in the blind spots. Unlike the large μ' scenario, the future dark matter detection experiment XENON1T will only

be able to probe some of the allowed regions because $g_{h\chi\chi}$ in this scenario can be arbitrarily small.

In summary, this chapter investigated the viability of a supersymmetric extension of the Standard Model, λ-SUSY. In the next chapter, we will continue our study of such supersymmetric extensions. Specifically, we will inspect the production of colored scalars under a certain assumption of supersymmetry breaking, to wit, one that gives both Dirac and Majorana masses to gauge superpartners.

CHAPTER IV

MIXED GAUGINOS

This work was published in Volume 86 of *Physical Review D* in March 2014. Graham Kribs initiated the project; Nirmal Raj performed the calculations and produced the plots and tables in this chapter.

Introduction

The strongest constraints on weak scale supersymmetry from the LHC are on first generation squarks and the gluino [157, 158]. First generation squark production proceeds through $pp \to \tilde{q}\tilde{q}$ that is dominated by t-channel exchange of a gluino that acquires a Majorana mass ("Majorana gluino") using valence quarks from the proton. Not surprisingly, the largest contributions come from sub-processes involving a chirality flip in the t-channel gluino exchange diagram which is a comparatively unsuppressed dimension-5 interaction. The bounds on first generation squarks, typically combined with the second generation in a simplified model involving $M_{\tilde{q}}$ and $M_{\tilde{g}}$, are currently $M_{\tilde{q}} > 1.8$ TeV for $M_{\tilde{g}} \simeq M_{\tilde{q}}$ [157].

The authors of [159] showed that the presence of a gluino that acquires a Dirac mass (referred to as a "Dirac gluino") – instead of a Majorana mass – significantly weakens these collider constraints. This was due to three reasons:

first, a Dirac gluino can be significantly heavier than a Majorana gluino, with respect to fine-tuning of the electroweak symmetry-breaking scale. This is because a Dirac gluino yields one-loop *finite* contributions to squark masses [160]. Second, no "chirality-flipping" Dirac gluino t-channel exchange diagrams exist, and thus several subprocesses for squark production simply vanish. Third, the remaining squark production subprocess amplitudes are suppressed by $|p|/M_{\tilde{g}}^2$, where $|p|$ is the typical momentum exchanged through the Dirac gluino. For a heavier Dirac gluino ($M_{\tilde{g}} \gtrsim$ 2-3 TeV), this significantly suppresses t-channel gluino exchange to the point where it is subdominant to the gluino-independent squark–anti-squark production processes [159].

Dirac gaugino masses have been considered long ago [161, 162, 163] and have inspired more recent model building [160, 164, 165, 166, 167, 168, 169, 170, 171, 172, 173, 174, 175, 176, 177, 178, 179, 180] and phenomenology [181, 182, 183, 184, 185, 186, 187, 188, 189, 190, 191, 192, 193, 194, 195, 196, 197, 199, 198, 200, 201, 202, 203, 204, 205, 159, 206, 207, 208, 209, 210, 211, 212, 213, 214]. As beautiful as Dirac gauginos may be, there are two objections that are sometimes raised:

- Supersymmetry-breaking sectors do not generically have F-terms much smaller than D-terms. In the absence of a specialized mediation sector that sequesters the F-term contributions [165], we might expect both Dirac and Majorana masses to be generated (for example, [175]). Moreover, even

if F-term mediation is sequestered, gauginos do acquire Majorana masses through anomaly-mediation [215, 216].

- In the presence of a pure Dirac wino and bino, the usual tree-level D-term quartic coupling for the Higgs potential is not generated [160]. This requires additional couplings to regenerate the quartic coupling. While there are mechanisms to generate a quartic in models with a pure Dirac gaugino mass (see [207] in the context of R-symmetric supersymmetry), it is obviously of interest to understand the impact of electroweak gauginos acquiring Majorana masses on squark production cross section limits.

In this context, we consider two generalizations of Ref. [159]: (i) models with a "Mixed Gluino" that acquires both Dirac and Majorana masses, and (ii) models in which the electroweak gauginos acquire purely Majorana masses, and contribute to squark production. As we will see, both cases have surprising outcomes.

Our primary interest is to compare squark production cross sections with mixed gauginos against the pure Dirac and pure Majorana cases. Mixed gauginos were also considered in [185], where the main emphasis was on distinguishing the different types of gaugino masses well before the strong bounds on colored superpartner production were set by the LHC collaborations. Our interest in this chapter is largely orthogonal, examining in detail the modifications to squark production when the gaugino is *heavy*. We used MadGraph5 [217] to simulate squark production at leading order (LO) for the LHC operating at a center-

of-mass energy of 8 TeV and 14 TeV using the CTEQ6L1 parton distribution functions (PDFs). We modified the existing minimal supersymmetric standard model (MSSM) model files to incorporate the effects of mixed gluinos. We did not, however, incorporate next-to-leading-order (NLO) corrections in our cross sections, for several reasons: first, in some cases there is a large range of scales between the squark mass and the gaugino mass, and unfortunately existing codes (Prospino 2.1 [218] and [219]) are not designed to handle this. Second, to the best of our knowledge, the NLO corrections for a Dirac gaugino as well as a mixed gaugino have not been computed. This is an important outstanding problem, but it is not the primary interest of this chapter. In much of the results presented below, we consider *ratios* of production cross sections, where most of the large NLO corrections are expected to cancel. We do show some LO cross sections as a function of gaugino mass, to better explain our results, however, in these cases we are generally interested in the trend as a function of the gaugino mass rather than the precise cross section values. The full NLO calculation would be interesting to compute, but it is beyond the scope of this dissertation.

Mixed Gauginos

"Mixed Gauginos" are, by definition, the Majorana mass eigenstates of gauginos that acquire both a Dirac mass with an adjoint fermion partner as well as Majorana masses for the gluino, the adjoint fermion, or both. This occurs when

the supersymmetry-breaking hidden sector contains superfields that acquire both F-type and D-type supersymmetry-breaking vacuum expectation values. Let us first write the operators that lead to these contributions to the gaugino masses, using the spurions $X \equiv F\theta^2$ and $W'_\alpha \equiv D'\theta_\alpha$. A Majorana mass arises from the usual operator

$$c_m \int d^2\theta \frac{X}{M} W^\alpha W_\alpha \tag{IV.1}$$

and a Dirac mass from [160]

$$c_d \int d^2\theta \sqrt{2} \frac{W'_\alpha}{M} W_j^\alpha A_j \,, \tag{IV.2}$$

where M is the mediation scale and A_j is a chiral superfield in the adjoint representation of the relevant gauge group of the Standard Model. Whether a gaugino acquires a Dirac mass obviously depends on the existence of a chiral adjoint to pair up with. There are additional operators that can contribute to gaugino masses. The chiral adjoint can acquire a Majorana mass through

$$c_{m'} \int d^4\theta \frac{1}{2} \frac{X^\dagger}{M} \mathrm{tr} A_j A_j + \mathrm{h.c.} \,, \tag{IV.3}$$

familiar from the Giudice-Masiero mechanism for generating μ in the MSSM. Here we are assuming that the adjoint fermion only acquires mass after supersymmetry breaking, i.e., there is no "bare" contribution to its mass in the superpotential.

Scalar masses can be generated by contact interactions

$$\int d^4\theta \frac{X^\dagger X}{M^2} Q^\dagger Q \,,$$

at the messenger scale, as well as the "soft" and "supersoft" contributions from Majorana and Dirac gauginos, respectively. In this chapter, we neglect flavor mixing among the squarks, since the existence of sizable Majorana masses means we do not have R-symmetry to protect us against flavor-changing neutral currents [170].

Renormalization group evolution from the messenger scale to the weak scale affects the relative size of the Dirac and Majorana masses. Let us first define the Dirac mass, the Majorana gaugino mass, and the Majorana adjoint mass as

$$\begin{aligned} M_d &= c_d \langle D' \rangle / M \\ M_m &= c_m \langle F \rangle / M \\ M'_m &= c_{m'} \langle F^\dagger \rangle / M \,. \end{aligned} \tag{IV.4}$$

All of these quantities are generated at the messenger scale (possibly with additional hidden sector renormalization [220]). For a gauge group i with beta function coefficient b_i and quadratic Casimir of the adjoint c_i, the Dirac operator receives significant RG effects (neglecting Yukawa couplings) [160, 175]

$$M_d(\mu) = M_d(M) \times \begin{cases} \left(\dfrac{\mu}{M}\right)^{-c_i \alpha_i/(2\pi)} & \text{for} \quad b_i = 0 \\ \left(\dfrac{\alpha_i(\mu)}{\alpha_i(M)}\right)^{(b_i - 2c_i)/(2b_i)} & \text{for} \quad b_i \neq 0 \,. \end{cases} \tag{IV.5}$$

We calculated the RG evolution of the Majorana adjoint mass to be (again

neglecting Yukawa couplings)

$$M_{m'}(\mu) = M_{m'}(M) \times \begin{cases} \left(\frac{\mu}{M}\right)^{-c_i \alpha_i/\pi} & \text{for} \quad b_i = 0 \\ \left(\frac{\alpha_i(\mu)}{\alpha_i(M)}\right)^{-2c_i/b_i} & \text{for} \quad b_i \neq 0 \end{cases} \tag{IV.6}$$

which can be obtained directly from the wavefunction renormalization of the superpotential (and agrees with resuming the RG equation given in Ref. [221] without Yukawa couplings). The size of the RG evolution can be substantial [175], but depends heavily on several assumptions about the mediation as well as the particle content of the model above the electroweak scale. These "ultraviolet" (UV) issues will not be discussed further in this chapter.

Mixed Gluino

Let us now specialize our discussion to a gluino that acquires a Dirac and Majorana mass. All of what we say below can also be straightforwardly applied to the electroweak gauginos.[1] Using Eq. (IV.4), the resulting mass terms for the gaugino and adjoint superfield are (in 2-component language)

$$\mathcal{L}_{\tilde{g}\,\text{mass}} = \begin{pmatrix} g & \psi \end{pmatrix} \begin{pmatrix} M_m & M_d \\ M_d & M'_m \end{pmatrix} \begin{pmatrix} g \\ \psi \end{pmatrix} + \text{h.c.} \tag{IV.7}$$

[1] There is an amusing subtlety involving charginos that acquire "Dirac" masses (by this we mean charginos that acquire Dirac masses by pairing up with additional fermions in the triplet representation of $SU(2)_W$), that we relegate to App. G.

where we have suppressed the $SU(3)_c$ color indices on the fields. The relative size of the Dirac and Majorana contributions are set by the coefficients of the operators (evaluated at the weak scale). While we take the coefficients to be arbitrary, our main phenomenological interest is the range $M_d \gg M_m, M'_m$ to $M_d \gtrsim M_m, M'_m$.

From Eq. (IV.7), the 2-component fermions g and ψ mix, giving us the mass eigenstates of the gluino

$$\begin{pmatrix} g_1 \\ \\ g_2 \end{pmatrix} = \begin{pmatrix} \cos\theta_{\tilde{g}} & \sin\theta_{\tilde{g}} \\ \\ -\sin\theta_{\tilde{g}} & \cos\theta_{\tilde{g}} \end{pmatrix} \begin{pmatrix} \psi \\ \\ g \end{pmatrix}, \tag{IV.8}$$

where the mixing angle is given by

$$\cos\theta_{\tilde{g}} \;=\; \sqrt{\frac{1}{2}}\left(1 + \frac{M_m - M'_m}{\sqrt{(M_m - M'_m)^2 + 4M_d^2}}\right)^{1/2}. \tag{IV.9}$$

Diagonalizing the Lagrangian, Eq. (IV.7), gives the two eigenvalues that we write as $-M_{\tilde{g}1}$ and $M_{\tilde{g}2}$ respectively,

$$\begin{aligned} -M_{\tilde{g}1} &= \frac{1}{2}\left(M_m + M'_m - \sqrt{(M_m - M'_m)^2 + 4M_d^2}\right) \\ M_{\tilde{g}2} &= \frac{1}{2}\left(M_m + M'_m + \sqrt{(M_m - M'_m)^2 + 4M_d^2}\right) \end{aligned} \tag{IV.10}$$

We have chosen to define $M_{\tilde{g}1}$ to be the negative of the eigenvalue of the mass matrix so that when $M_d^2 > M_m M'_m$, both $M_{\tilde{g}1}$ and $M_{\tilde{g}2}$ are positive. We could have instead redefined the eigenstates to absorb this sign, however this would lead to proliferation of i's in the following, that we prefer to avoid.

The two familiar limits of these equations are now evident: For a pure Dirac gluino ($M_m = M'_m = 0$), $M_{\tilde{g}1} = M_{\tilde{g}2} = M_d$, the mixing angle $\theta_{\tilde{g}} = \pi/4$, and then the gluino eigenstates are $g_{1,2} = (g \pm \psi)/\sqrt{2}$. For a pure Majorana gluino ($M_d = 0$), the mixing angle $\theta_{\tilde{g}} = 0$, which means the gluino and its adjoint fermion partner do not mix, i.e., $g_1 = g$, $g_2 = \psi$. Consequently, $M_{\tilde{g}1} = M_m$ and $M_{\tilde{g}2} = M'_m$.

The quark-gluino-squark interactions are given by

$$\begin{aligned}\mathcal{L}_{int} \; = \\ & - \sqrt{2} g_s \big(\tilde{u}^*_{L,i} \; t^a \; g_a \; u_{L,i} + \tilde{d}^*_{L,i} \; t^a \; g_a \; d_{L,i} \\ & - \tilde{u}^*_{R,i} \; t^a \; g_a u_{R,i} - \tilde{d}^*_{R,i} \; t^a \; g_a \; d_{R,i} \big) + \text{h.c.}\end{aligned} \tag{IV.11}$$

where g_s is the strong coupling and t_a's are the $SU(3)$ generators. The index i runs over each quark generation and the squark color indices have been suppressed. Expanding using Eq. (IV.8), this becomes

$$\begin{aligned}-\mathcal{L}_{int}/\sqrt{2} g_s \; = \\ & + \tilde{u}^*_{L,i} \; t^a \; g_{1,a} \cos\theta_{\tilde{g}} \; u_{L,i} + \tilde{u}^*_{L,i} \; t^a \; g_{2,a} \sin\theta_{\tilde{g}} \; u_{L,i} \\ & + \tilde{d}^*_{L,i} \; t^a \; g_{1,a} \cos\theta_{\tilde{g}} \; d_{L,i} + \tilde{d}^*_{L,i} \; t^a \; g_{2,a} \sin\theta_{\tilde{g}} \; d_{L,i} \\ & - \tilde{u}^*_{R,i} \; t^a \; g_{1,a} \cos\theta_{\tilde{g}} \; u_{R,i} - \tilde{u}^*_{R,i} \; t^a \; g_{2,a} \sin\theta_{\tilde{g}} \; u_{R,i} \\ & - \tilde{d}^*_{R,i} \; t^a \; g_{1,a} \cos\theta_{\tilde{g}} \; d_{R,i} - \tilde{d}^*_{R,i} \; t^a \; g_{2,a} \sin\theta_{\tilde{g}} \; d_{R,i} \\ & + \; \text{h.c.}\end{aligned} \tag{IV.12}$$

This is the form of the interaction Lagrangian most useful for our phenomenological study.

In order to understand the implications of a mixed gluino arising from both a Dirac and a Majorana mass, we first need to parameterize the mixing in a way relevant to our collider study. There are two distinct effects when simultaneously varying M_d, M_m, and M'_m: the coupling constants to the squarks and quarks change, according to Eq. (IV.12), and the masses of the gluino eigenstates change, according to Eq. (IV.10). This leads to changes in both the *dynamics* (the coupling constants) and the *kinematics* (the gluino masses) of the squark production cross sections. We are interested in separating these effects, to the extent possible.

Review of Pure Dirac Gluinos

Before embarking on our study of mixed gluinos, we first want to review the effects of a pure Dirac gluino on the various squark production processes. The relevant squark production processes include[2] $pp \to \tilde{q}_{L,R}\tilde{q}_{L,R}$ and $pp \to \tilde{q}_{L,R}\tilde{q}^*_{L,R}$. Fig. 4.1. shows the relative contributions of these two production modes for different (pure Dirac) gluino masses, depicted by the solid curves. The dominant effects of t-channel gluino exchange impact just the first generation of squarks. However, since a common simplified model that ATLAS and CMS use in quoting bounds is to sum over all squarks of the first two generations assuming the flavors and chiralities are degenerate in mass, we do this also. The lightest supersymmetric particle (LSP) is taken to be a neutral particle odd under R-parity. The gravitino is one possibility, though as we will see, a Majorana bino is another distinct possibility.

[2]The third combination, antisquark-antisquark production, can be ignored since its rate is highly suppressed by PDFs.

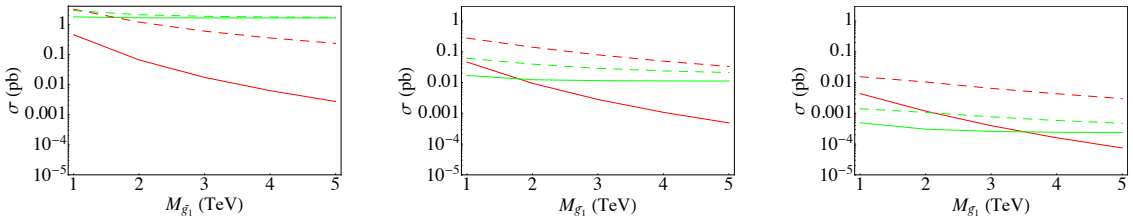

(a) $M_{\tilde{q}} = 400$ GeV (b) $M_{\tilde{q}} = 800$ GeV (c) $M_{\tilde{q}} = 1200$ GeV

Figure 4.1.: Comparing the squark pair production cross section (red) against squark–anti-squark production cross section (green) summing over the first two generations of squarks with masses of 400, 800 and 1200 GeV. The solid lines denote the case in which the Majorana masses vanish ($M_m = M'_m = 0$), so the x-axis corresponds to a pure Dirac gluino mass. At low squark masses, squark-anti-squark production through an s-channel gluon that dominates over the t-channel gluino-mediated squark-squark production. However, for $m_{\tilde{q}} = 800, 1200$ GeV we find that squark-squark production dominates up to $M_d \simeq 2, 3.5$ TeV. The dotted lines depict the behavior when the Dirac mass vanishes ($M_d = 0$), with the x-axis corresponding to a pure Majorana mass. Only at a very low squark mass of 400 GeV does squark–anti-squark production dominate. For higher squark masses 800 and 1200 GeV, squark pair production dominates for all gluino masses. This is due to t-channel mediated *same-handed* squark production, which was absent in the case of a pure Dirac gluino.

At low squark masses, 400 GeV (Fig. 4.1.a), the production cross section is heavily dominated by squark-antisquark production with quarks or gluons in the initial state. This is because squark pair production through t-channel (Dirac) gluino exchange can only yield $pp \to \tilde{q}_L \tilde{q}_R$; the other processes ($LL, RR$) are absent. As the squark mass is increased, the modes $\tilde{q}_{L/R}, \tilde{q}^*_{L/R}$ and $\tilde{q}_L, \tilde{q}_R$ become comparable to each other. For $M_{\tilde{q}} = 800$ GeV, this occurs for Dirac gluino masses near $\simeq 2$ TeV, as shown in Fig. 4.1.b. In other words, the gluino t-channel exchange diagrams of squark pair production are not as suppressed in this range. Considering even larger squark masses, $M_{\tilde{q}} = 1200$ GeV, we find squark pair production becomes comparable to squark–anti-squark production for a (Dirac) gluino mass $\simeq 4$ TeV, shown in Fig. 4.1.c.

The dashed lines in Fig. 4.1. depict the two production modes for a pure Majorana gluino. At a low squark mass of 400 GeV, squark–anti-squark production dominates the cross section for gluino masses greater than ~ 2 TeV, while for $M_{\tilde{q}} = 800$ GeV and $M_{\tilde{q}} = 1200$ GeV, squark pair production dominates for all gluino masses shown in the figures. This is because t-channel production of same-handed squark production is the dominant production mode for these masses and energies with a Majorana gluino.

Case I: $M'_m = 0$

First, we consider the scenario $M'_m = 0$, $M_m \lesssim M_d$. In this Case, we can simplify

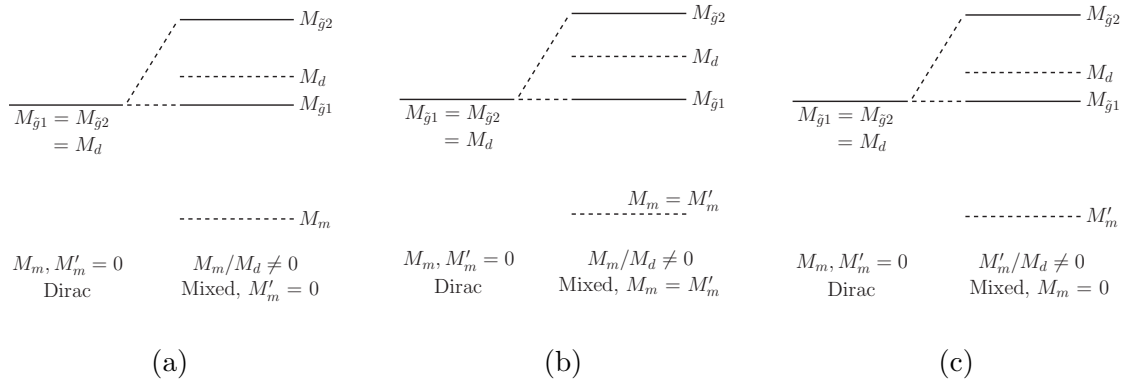

Figure 4.2.: The method we employ for adding Majorana masses M_m, M'_m to the supersoft Dirac mass M_d of a gaugino. The lower eigenvalue $M_{\tilde{g}1}$ is kept constant as M_m/M_d or M'_m/M_d is varied.

the expressions for the masses and mixing angle of the mixed gluino:

$$-M_{\tilde{g}1} = \frac{1}{2}\left(M_m - \sqrt{M_m^2 + 4M_d^2}\right) \tag{IV.13}$$

$$M_{\tilde{g}2} = \frac{1}{2}\left(M_m + \sqrt{M_m^2 + 4M_d^2}\right) \tag{IV.14}$$

$$\cos\theta_{\tilde{g}} = \sqrt{\frac{M_{\tilde{g}2}}{M_{\tilde{g}2} + M_{\tilde{g}1}}}\,. \tag{IV.15}$$

Next, to separate the "kinematics" from the "dynamics", we take the parameterization where we hold the mass eigenvalue of the lightest gluino, $M_{\tilde{g}1}$, fixed, while varying the ratio $x \equiv M_m/M_d$. This gives two Majorana gluinos with masses $M_{\tilde{g}1}$ and $M_{\tilde{g}2}$ with mass difference given by $M_{\tilde{g}2} - M_{\tilde{g}1} = M_m$. In the case $x < 1$, the mixing angle is in the range $1/\sqrt{2} < \cos\theta_{\tilde{g}} \lesssim 0.85$. The mass spectrum is illustrated in Fig. 4.2.a.

To explore a wider range of mixing angles, $0.85 \lesssim \cos\theta_{\tilde{g}} \leq 1$, the parameter

$x \gg 1$, that corresponds to $M_m \gg M_d$. In this regime, we get the usual see-saw formula, familiar from neutrino physics, for the mass of the lightest gluino eigenstate, $\simeq M_d^2/M_m$. Here, however, the lighter mass eigenstate decouples from squarks and quarks, while it is the heavier nearly pure Majorana gluino eigenstate that maximally couples. Without adjusting our basic premise – hold the kinematics constant – there is no way to enter this regime of parameters without taking the Majorana mass for the gluino unnaturally large.

Cross sections across parameter space

Our first foray into the behavior of the squark cross sections is shown in Fig. 4.3. that contains contour plots in the ($M_{\tilde{g}1}$, $x\,(=\,M_m/M_d)$) space. On the x-axis is the eigenvalue of the lighter of the gluino eigenstates, and on the y-axis is the mixed nature of the gauginos, parameterized by M_m/M_d. The contours on the right show the production cross sections summing over all combinations of squarks and antisquarks of the first and second generations, and the contours on the left show the ratios of these cross sections to their equivalents in the scenario of a Majorana gluino with the same mass as $M_{\tilde{g}1}$. To illustrate the differences as the squark mass is increased, the three pairs of plots show three different squark masses: 400, 800 and 1200 GeV.

There are several interesting features shown in Fig. 4.3.. Holding the lightest gluino eigenmass constant, we see that the squark production cross section *decreases*

as a Majorana mass M_m is introduced. This we explore in detail below. Next, we see distinctly different rates of variation in the cross sections across the three plots. At $M_{\tilde{q}} = 1200$ GeV (Fig. 4.3.f) the cross section falls by an order of magnitude as $M_{\tilde{g}1}$ goes from 1 to 4 TeV, after which it is roughly constant, whereas for squark masses 400 GeV (Fig. 4.3.b) and 800 GeV (Fig. 4.3.d) we find much less variation: the cross section drops by a factor of a few as $M_{\tilde{g}1}$ is increased from 1 to 2 TeV, and then asymptotes to a fixed value. The larger variation is present because, as we saw earlier, for larger squark masses, the s-channel squark—anti-squark cross section becomes more competitive with the t-channel gluino exchange induced squark-squark production processes. It is this competition between the two leading modes for gluino masses below ~ 4 TeV that results in the larger rate of variation of the cross section in that region in Fig. 4.3.f. The domination of squark-antisquark production for gluino masses above 4 TeV results in the constancy of the cross section observed in the right end of the plot.

Figure 4.3.: (next page) Plots illustrating Case I. LEFT: Contours of the ratios of the total production cross-section of the first two squark generations at LHC with $\sqrt{s} = 8$ TeV of our model to the cross-section in MSSM. RIGHT: Contours of the cross sections themselves (at leading order), in pb, at LHC with $\sqrt{s} = 8$ TeV. The details of the critical features are explained in the text.

(a) $M_{\tilde{q}} = 400$ GeV: ratios

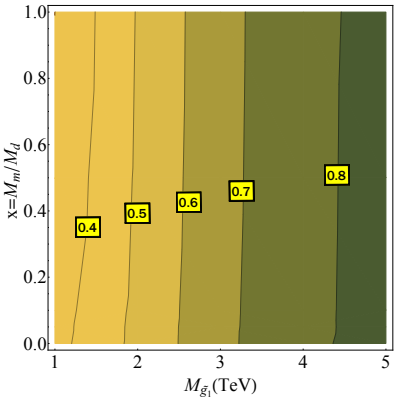

(b) $M_{\tilde{q}} = 400$ GeV: $d\sigma$

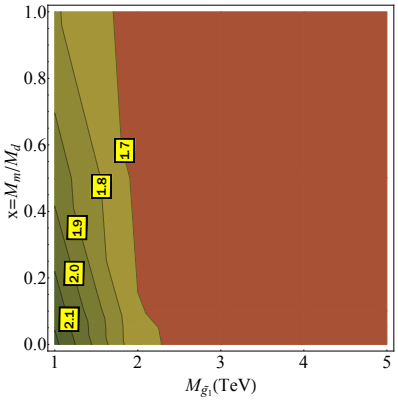

(c) $M_{\tilde{q}} = 800$ GeV: ratios

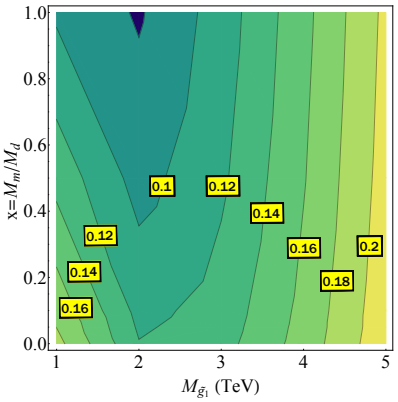

(d) $M_{\tilde{q}} = 800$ GeV: $d\sigma$

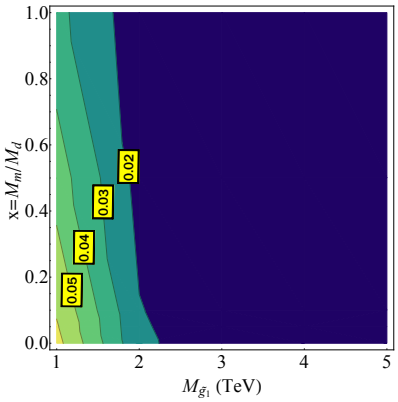

(e) $M_{\tilde{q}} = 1200$ GeV: ratios

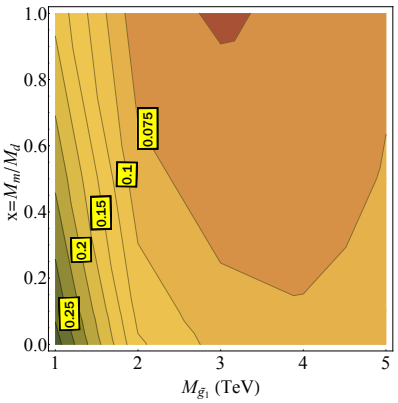

(f) $M_{\tilde{q}} = 1200$ GeV: $d\sigma$

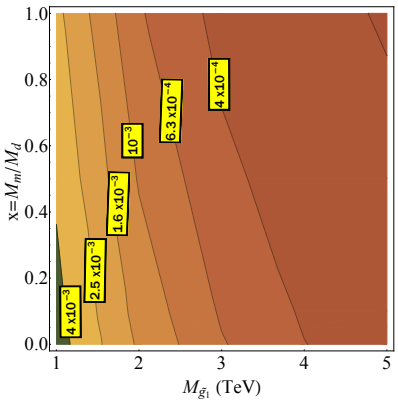

We now turn our attention to the plots on the left, depicting contours of the ratios of the corresponding cross sections on the right to those of a pure Majorana gluino with a mass the same as $M_{\tilde{g}1}$. To understand the features of these plots, we will have to consider the competition between three different modes: squark–anti-squark production, *same-handed* squark pair production and *opposite-handed* squark pair production. Two distinctive features seen here are (i) at a low squark mass of 400 GeV, the ratio increases as we move horizontally to the right, as shown in Fig. 4.3.a, (ii) at higher squark masses of 800 and 1200 GeV, the ratio first decreases and then increases as we move in the horizontal direction, with the local minimum shifting to the right as $M_{\tilde{q}}$ is increased, as shown in Figs. 4.3.c and 4.3.e.

The first feature is a result of the same mechanism that results in the lack of variation in Fig. 4.3.b. The squark–anti-squark production dominates over squark-squark production for a large range of gluino masses at $M_{\tilde{q}} = 400$ GeV, and as $M_{\tilde{g}1}$ is increased, this domination increases for both a Majorana and a mixed gluino (with the domination in the Majorana case weaker) as we saw earlier in Fig. 4.1.a. Hence we observe a uniform increase in the ratio, seen to approach unity. The second feature can be understood in terms of Figs. 4.1.b and 4.1.c. In Fig. 4.1.b, we notice that near $M_{\tilde{g}1} \sim 1$ TeV, the Majorana rate is dominated by squark pair production and the Dirac rate gets comparable contributions from both squark–anti-squark and squark pair production.

Near the right extreme ($M_{\tilde{g}1} \sim 5$ TeV), the dominant mode of Majorana cross

section has fallen and the total cross section has near-equal contributions from both modes, while the Dirac cross section, dominated strongly by squark–anti-squark production, is now comparable to either mode of the Majorana case. At either extreme, the total Dirac cross section is able to catch up to an extent with the total Majorana cross section, for different reasons. In the intermediary mass range, however, the Dirac cross section, dominated by only squark–anti-squark production, is much smaller than the Majorana case. This argument can be extended to mixed gluinos as well, and hence the local minimum observed in Fig. 4.3.c. The above discussion applies also to Fig. 4.3.e, except that, as seen in Fig. 4.1.c, the Dirac cross section catches up with the Majorana at even higher gluino masses. This results in the rightward shift compared to the $M_{\tilde{q}} = 800$ GeV case in the local minimum.

If we now move vertically anywhere in Fig. 4.3.f, or for gluino masses below 2 TeV in Figs. 4.3.b and 4.3.d, we observe a drop in cross section. We notice the same for the contours of the ratios of cross sections, i.e., Figs. 4.3.a, 4.3.c and 4.3.e. This may seem counter to what we would expect when increasing the Majorana content of the model. The reasons for the reduction would become clear were we to investigate the physics of each individual subprocess separately.

Individual modes

Let us now consider primarily the gluino t-channel pair-production of squarks with quarks in the initial state. A Feynman diagram depicting this channel is shown in Fig. 4.4.. No arrows and labels are shown, which allows us to keep the discussion as generic as possible at this point. Let us first divide pair production into six

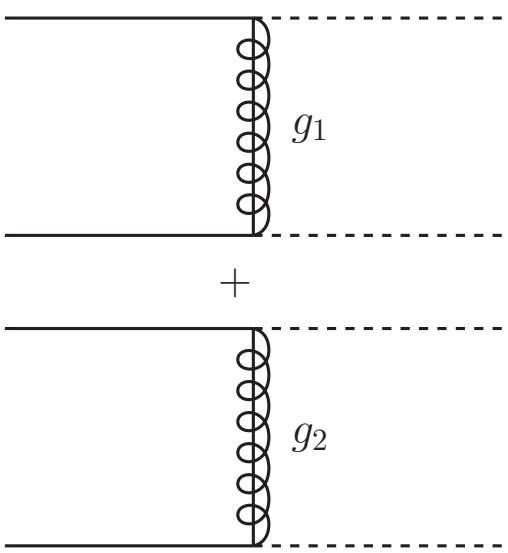

Figure 4.4.: General Feynman diagrams (without arrows) for t-channel gluino-mediated squark production. The solid lines (initial state) may be labeled with all combinations from the quark fields $q_L, q_L^\dagger, q_R, q_R^\dagger$, and the dashed lines (final state) with the corresponding squark fields $\tilde{q}_L, \tilde{q}_L^*, \tilde{q}_R, \tilde{q}_R^*$.

distinct possibilities:

$$
\begin{aligned}
(i) \qquad & \tilde{q}_L, \tilde{q}_L \text{ or } \tilde{q}_R, \tilde{q}_R \\
(ii) \qquad & \tilde{q}_L^*, \tilde{q}_L \text{ or } \tilde{q}_R^*, \tilde{q}_R \\
(iii) \qquad & \tilde{q}_L^*, \tilde{q}_L^* \text{ or } \tilde{q}_R^* \tilde{q}_R^* \\
(iv) \qquad & \tilde{q}_L, \tilde{q}_R \\
(v) \qquad & \tilde{q}_L, \tilde{q}_R^* \text{ or } \tilde{q}_R, \tilde{q}_L^* \\
(vi) \qquad & \tilde{q}_L^*, \tilde{q}_R^*
\end{aligned}
$$

In Fig. 4.5., we illustrate the physics behind each of these modes with a single flavor: up squarks. Here the squark mass is taken as 1200 GeV and the absolute mass of the lighter gluino eigenstate $|M_{\tilde{g}1}| = 5$ TeV while the heavier eigenvalue, $M_{\tilde{g}2}$, is varied. These are illustrative values, to gain intuition for the effects of varying $x = M_m/M_d$ on the cross sections of the individual modes. In this section, we state the results obtained, leaving the detailed behavior of the analytic expressions of certain amplitudes to App. F.

(i) $\tilde{u}_L, \tilde{u}_L$

The cross section increases from zero and saturates at a value far below the Majorana cross section as $x = M_m/M_d$ is increased, as shown in Fig. 4.5.a. The amplitude is written in App. F, where we find that it is suppressed by $p^2/M_{\tilde{g}1}^3$ (times a function of x that becomes just one power of x for small values), considerably smaller than the naive result of $1/M_{\tilde{g}1}$. Moreover, at larger $x \simeq 1$, the amplitude

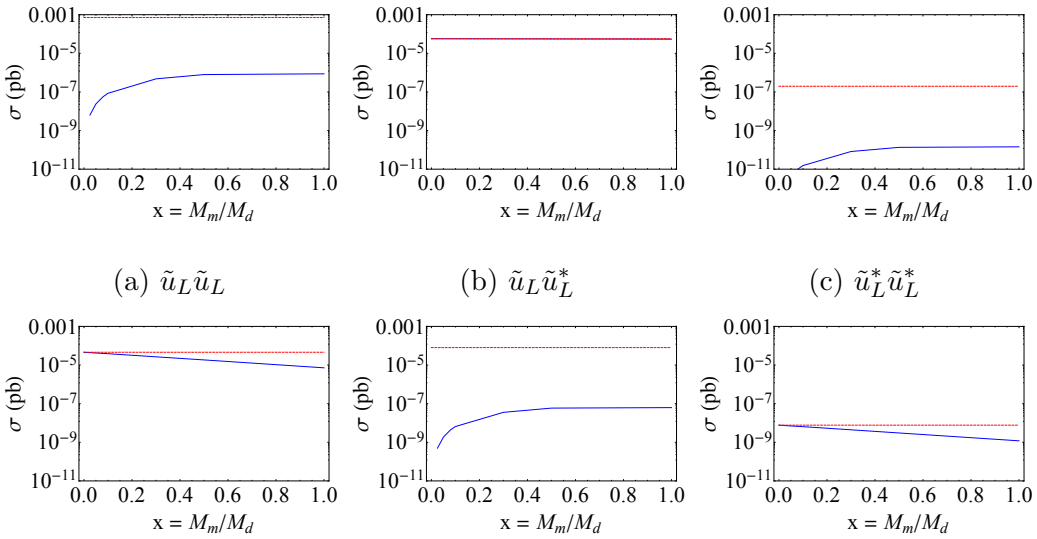

(a) $\tilde{u}_L\tilde{u}_L$ (b) $\tilde{u}_L\tilde{u}_L^*$ (c) $\tilde{u}_L^*\tilde{u}_L^*$

(d) $\tilde{u}_L\tilde{u}_R$ (e) $\tilde{u}_L\tilde{u}_R^*$ (f) $\tilde{u}_L^*\tilde{u}_R^*$

Figure 4.5.: Cross sections of the various unique modes that constitute up squark production when M_m' is set to zero. The blue curves show these as a function $x = M_m/M_d$, while the dashed red horizontal lines denote the corresponding cross section for the case of a pure Majorana gluino of the same mass as $M_{\tilde{g}1}$. Here the squark mass $M_{\tilde{u}}$ is 1200 GeV and the mass of the lighter gluino eigenstate $M_{\tilde{g}1}$ is 5 TeV.

is not scaling with x. This is due to the lightest gaugino eigenstate becoming increasingly the adjoint fermion, which does not couple to quarks and squarks.

(*ii*) $\tilde{u}_L^*, \tilde{u}_L$

The dominant contribution to this diagram is production via an s-channel gluon. In Fig. 4.5.b we see a nearly unvarying cross section as we increase x as shown by

the the blue line. Since the sub-dominant t-channel gluino diagram is negligible, we find that the cross section values nearly coincides with the pure Majorana case.

(iii) $\tilde{u}_L^*, \tilde{u}_L^*$

The physical principles are the same as (i), hence the similar trends observed in Fig. 4.5.c. However, the cross section values are much smaller since the PDF effects of anti-up quarks cause to suppress this mode.

(iv) $\tilde{u}_L, \tilde{u}_R$

The amplitude, and hence the cross section, turns out to be numerically the same for the cases of pure Majorana and pure Dirac gluinos. This is reflected in Fig. 4.5.d, where the blue and red curves intersect at $x = 0$. As x is increased to 1, however, the cross section decreases to roughly 1/13 of the cross section of the pure Majorana case. This is evident in the form of the amplitude shown analytically in App. F. As we will see shortly, this is important in understanding the features of Fig. 4.3..

(v) $\tilde{u}_L, \tilde{u}_R^*$

The physics here is identical to cases (i) and (iii), except for the suppressing effect of excavating a sea antiquark from one of the protons. The effect is a decreased cross section as reflected in Fig. 4.5.e.

(vi) $\tilde{u}_L^*, \tilde{u}_R^*$

Conceptually similar to case (iv), this production mode suffers from PDF

suppression, resulting in the lowered cross sections seen in Fig. 4.5.f.

We can now answer the question posed at the end of Sec. IV.3.1, on why the total cross section of squark production declines despite an addition of Majorana content. We find that an increase in cross section of the pairs $(\tilde{q}_L, \tilde{q}_L), (\tilde{q}_R, \tilde{q}_R), (\tilde{q}_L, \tilde{q}_R^*), (\tilde{q}_R, \tilde{q}_L^*), (\tilde{q}_L^*, \tilde{q}_L^*)$, – as expected when departing from a pure Dirac scenario – is less relevant in comparison to the decrease in the cross section of $(\tilde{q}_L, \tilde{q}_R), (\tilde{q}_L^*, \tilde{q}_R^*)$ and the approximately constant cross section of $(\tilde{q}_L, \tilde{q}_L^*), (\tilde{q}_R, \tilde{q}_R^*)$ – due to various kinds of kinematic suppression as discussed in this section.

The analysis above shows that in addition to the suppression from the operator dimension (relative dominance of dim-5 or dim-6) and the kinematics, the third factor that is essential to determine the cross section trends is the PDFs. Thus the trends for individual modes would be identical for down squarks except for the effects of PDF suppression. As for the second generation of squarks, the far smaller PDFs of the corresponding second generation quarks in the proton render most modes negligible, with the only sizeable contribution coming from $(\tilde{q}_L, \tilde{q}_L^*)$ and $(\tilde{q}_R, \tilde{q}_R^*)$, which proceed through an s-channel gluon. Therefore we see that the principal difference between the first and second generations is that t-channel gluino mediation exhibits non-trivial behavior in the former, while it is practically absent in the latter.

Case II: $M_m = M'_m,\ x = 2M_m/M_d = 2M'_m/M_d$

In this scenario (Fig. 4.2.b), the two gluino mass eigenstates have masses $-M_{\tilde{g}1} = M_m - M_d$, $M_{\tilde{g}2} = M_m + M_d$, and the mixing between the states is maximal ($\cos\theta_{\tilde{g}} = 1/\sqrt{2}$) independent of M_m, M'_m and M_d. We consider the modification resulting from the Majorana content of gluino in the same way as the previous section, with the corresponding results shown in Fig. 4.6.. However, since both Majorana masses are nonzero, the difference between the eigenvalues $M_{\tilde{g}2} - M_{\tilde{g}1} = 2M_m$ (as opposed to just $M_{\tilde{g}2} - M_{\tilde{g}1} = M_m$ in Case I and $M_{\tilde{g}2} - M_{\tilde{g}1} = M'_m$ in Case III). In order to make an direct comparison of the mixing effects to Cases I and III, while holding the kinematics approximately equivalent, we define x as $x = 2M_m/M_d = 2M'_m/M_d$.

The features shown in Fig. 4.6. are in many ways similar to those of Case I. For instance, in the cross section contours on the right, we see little variation moving horizontally direction at high $M_{\tilde{g}1}$ for squark masses 400 and 800 GeV (Figs. 4.6.b

---

Figure 4.6.: (next page) Plots illustrating Case II. LEFT: Contours of the ratio of the total production cross section of the first two generations of squarks at LHC with $\sqrt{s} = 8$ TeV in our model to the cross sections in MSSM. RIGHT: Contours of the cross sections themselves (at leading order), in pb, at LHC with $\sqrt{s} = 8$ TeV. The critical features are explained in the text.

(a) $M_{\tilde{q}} = 400$ GeV: ratios

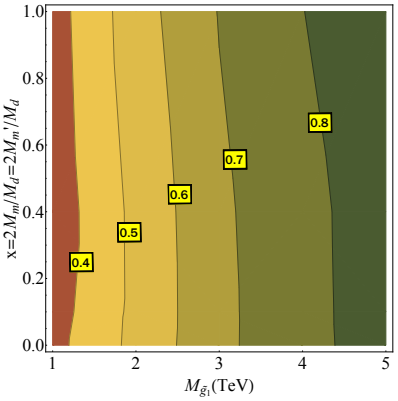

(b) $M_{\tilde{q}} = 400$ GeV: $d\sigma$

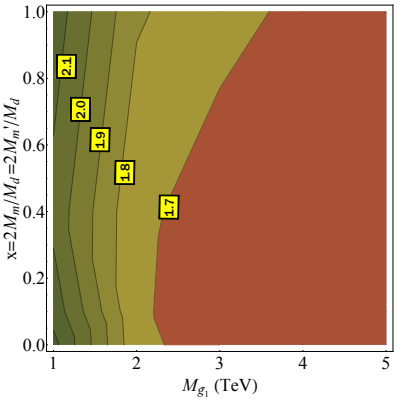

(c) $M_{\tilde{q}} = 800$ GeV: ratios

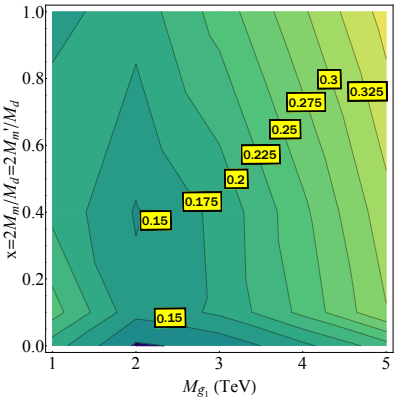

(d) $M_{\tilde{q}} = 800$ GeV: $d\sigma$

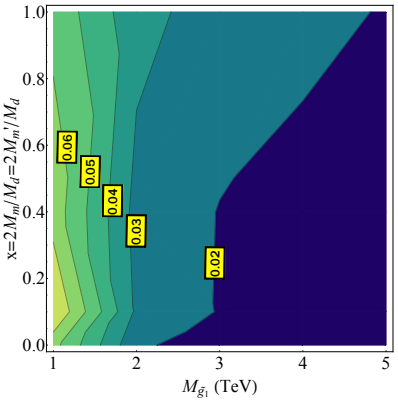

(e) $M_{\tilde{q}} = 1200$ GeV: ratios

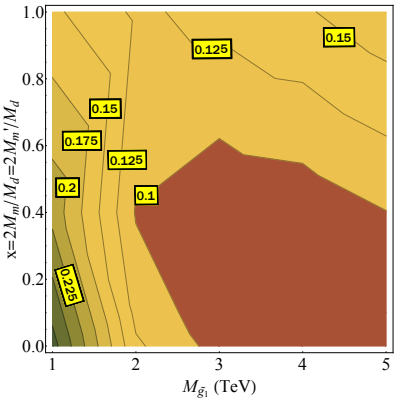

(f) $M_{\tilde{q}} = 1200$ GeV: $d\sigma$

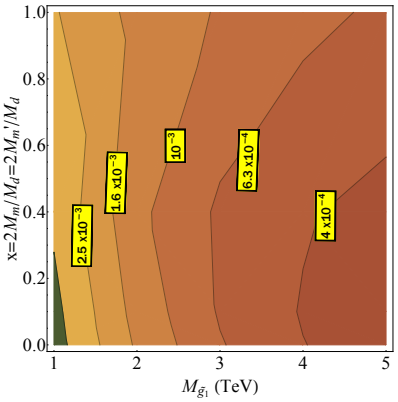

and 4.6.d), for the same reasons as before. We also notice the local minimum in Figs. 4.6.c and 4.6.e shifts to the right as we go from $M_{\tilde{q}} = 800$ GeV to $M_{\tilde{q}} = 1200$ GeV. Notice that, in all the plots, the values of the cross sections and ratios are identical to Case I along x=0, since they correspond to a pure Dirac gluino in either case.

The main differences between Cases I and II are seen when we move vertically in the contour plots. Whereas previously the cross section was seen to uniformly decrease as $x = M_m/M_d$ was increased, we now notice that it first decreases and then increases, a trend particularly pronounced for $M_{\tilde{q}} = 800$ GeV and 1200 GeV, as seen in Figs. 4.6.c-4.6.f. This feature can again by understood in terms of the individual subprocesses, which are given in the plots of Figs. 4.7..

In Case I, we saw that the subprocess setting the total cross section was the production mode $\tilde{q}_L\tilde{q}_R$, which decreased by roughly an order of magnitude as x was increased from 0 to 1. Even though the modes ($\tilde{q}_L\tilde{q}_L$, $\tilde{q}_R\tilde{q}_R$, $\tilde{q}_L\tilde{q}_R^*$) increased in the same range, their values never caught up with the opposite-handed squark pair production. This is not the situation here. Figs. 4.7.a and 4.7.e show that although the same-handed modes begin at zero cross section, they overtake opposite-handed modes at around $x = 0.2$, bolstering the total production.

Case III: $M_m = 0,\ x' = M'_m/M_d$

Lastly, we consider the scenario $M_m = 0$, $M'_m \lesssim M_d$ (Fig. 4.2.c). In this Case, the simplified expressions for the masses in Eqs. (IV.13)-(IV.14) carry over here with the

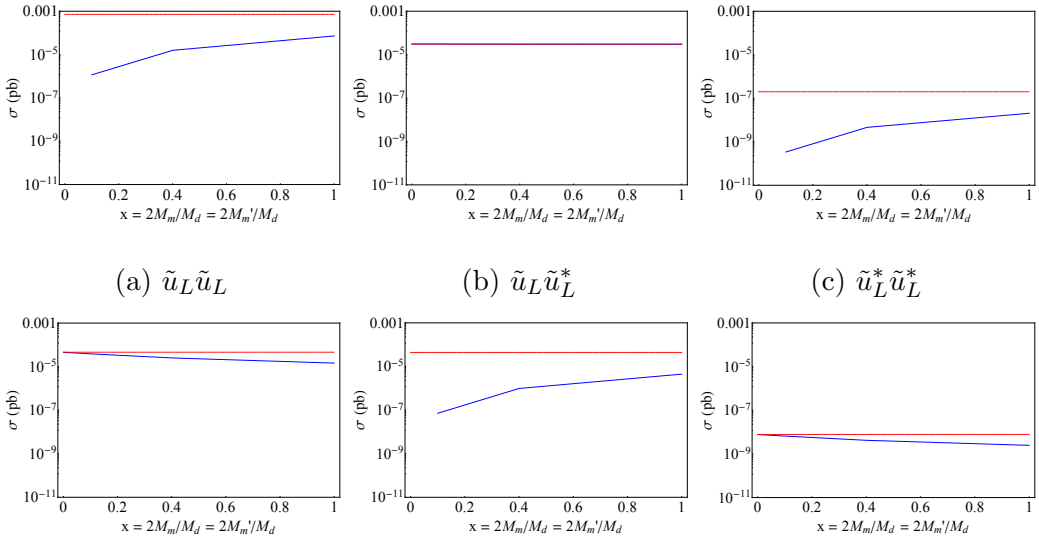

(a) $\tilde{u}_L\tilde{u}_L$ (b) $\tilde{u}_L\tilde{u}_L^*$ (c) $\tilde{u}_L^*\tilde{u}_L^*$

(d) $\tilde{u}_L\tilde{u}_R$ (e) $\tilde{u}_L\tilde{u}_R^*$ (f) $\tilde{u}_L^*\tilde{u}_R^*$

Figure 4.7.: Cross sections of the various unique modes that constitute up squark production when M_m' and M_m are set equal. The blue curves show these as a function $x = 2M_m/M_d = 2M_m'/M_d$, while the dashed red horizontal lines denote the corresponding cross section for the case of a pure Majorana gluino of the same mass as $M_{\tilde{g}1}$. Here the squark mass $M_{\tilde{u}}$ is 1200 GeV and the mass of the lighter gluino eigenstate $M_{\tilde{g}1}$ is 5 TeV.

replacement $M_m \leftrightarrow M_m'$, while the mixing angle is $\cos\theta_{\tilde{g}} = \sqrt{M_{\tilde{g}1}/(M_{\tilde{g}1} + M_{\tilde{g}2})}$. This means that the relevant mixing angle ranges are switched, with $\cos\theta_{\tilde{g}}$ varying from $1/\sqrt{2}$ to 0.53 and $\sin\theta_{\tilde{g}}$ from $1/\sqrt{2}$ to 0.85 as $x' = M_m'/M_d$ is varied from 0 to 1. Hence the lighter eigenstate is more of the gluino, and the heavier eigenstate more of the adjoint fermion. If x' were to be taken to infinity, $\cos\theta_{\tilde{g}} \to 0$ and the heavier eigenstate decouples, recovering the MSSM pure Majorana gluino limit.

Therefore, we expect the cross section to increase as x' is increased from 0 to 1. This is exactly the trend we notice in the plots of Fig. 4.8., corresponding to this case. The features of the contours here are very similar to those of Case II when we move horizontally across the plots, and the physical reasons are the same. The difference is in the variation in the vertical direction; the cross sections uniformly increase whereas previously there was a decrease followed by an increase.

Once again we may understand such a trend by inspecting the individual production modes, shown in Fig. 4.9.. The same-handed squark pair production modes catch up with and overtake their opposite-handed equivalents at small x', while the $\tilde{q}_L\tilde{q}_R$ cross section remains nearly constant.

Mixed Electroweak Gauginos

We now turn to the effects of electroweak gauginos on squark production. We assume Higgsino-quark-squark couplings are negligible and thus can ignore

---

Figure 4.8.: (next page) Plots illustrating Case III. LEFT: Contours of the ratio of the total production cross section of the first two generations of squarks at LHC with $\sqrt{s} = 8$ TeV in our model to the cross sections in MSSM. RIGHT: Contours of the cross sections themselves (at leading order), in pb, at LHC with $\sqrt{s} = 8$ TeV. The critical features are explained in the text.

(a) $M_{\tilde{q}} = 400$ GeV: ratios

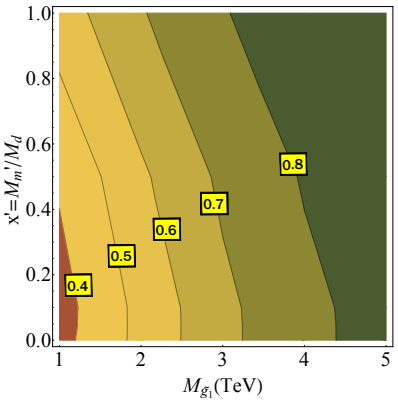

(b) $M_{\tilde{q}} = 400$ GeV: $d\sigma$

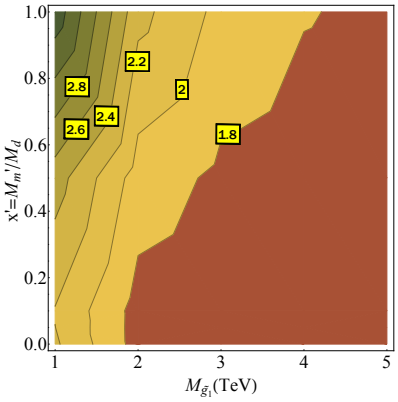

(c) $M_{\tilde{q}} = 800$ GeV: ratios

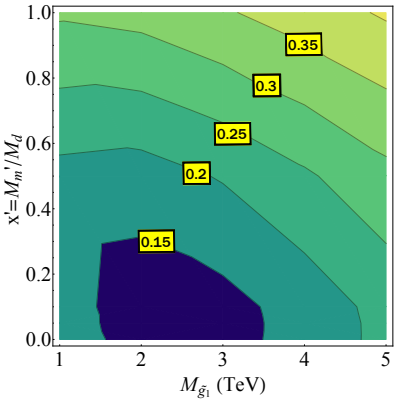

(d) $M_{\tilde{q}} = 800$ GeV: $d\sigma$

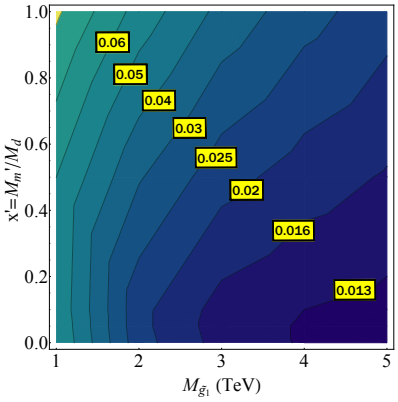

(e) $M_{\tilde{q}} = 1200$ GeV: ratios

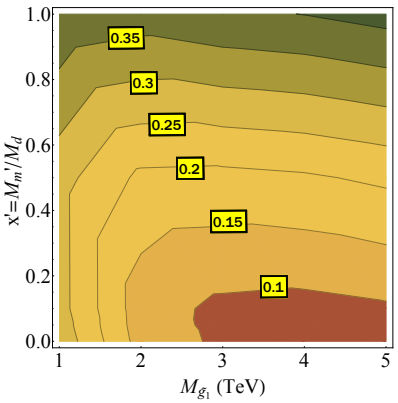

(f) $M_{\tilde{q}} = 1200$ GeV: $d\sigma$

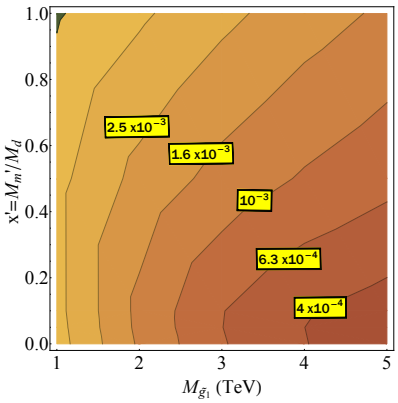

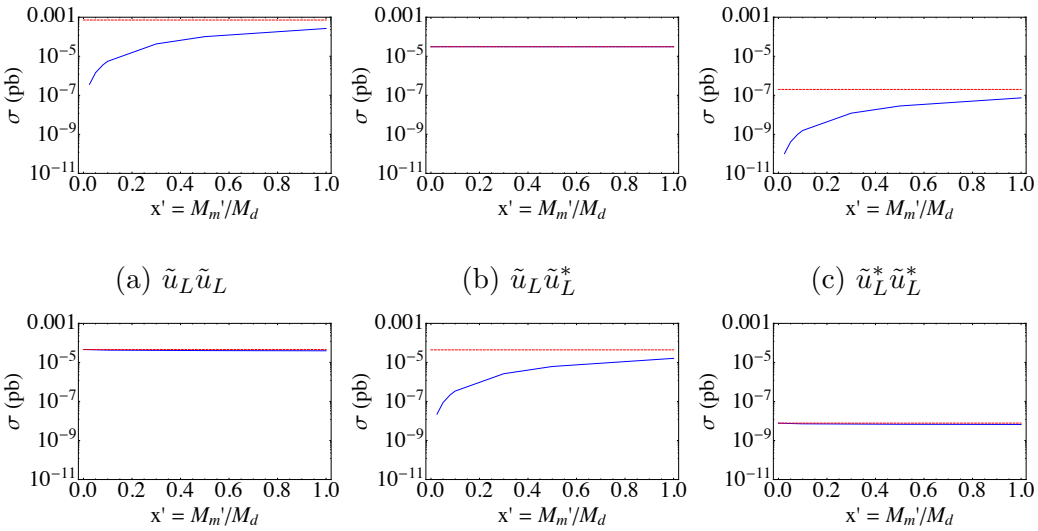

(a) $\tilde{u}_L\tilde{u}_L$ (b) $\tilde{u}_L\tilde{u}_L^*$ (c) $\tilde{u}_L^*\tilde{u}_L^*$

(d) $\tilde{u}_L\tilde{u}_R$ (e) $\tilde{u}_L\tilde{u}_R^*$ (f) $\tilde{u}_L^*\tilde{u}_R^*$

Figure 4.9.: Cross sections of the various unique modes that constitute up squark production when M_m is set to zero. The blue curves show these as a function $x = M_m/M_d$, while the dashed red horizontal lines denote the corresponding cross section for the case of a pure Majorana gluino of the same mass as $M_{\tilde{g}1}$. Here the squark mass $M_{\tilde{u}}$ is 1200 GeV and the mass of the lighter gluino eigenstate $M_{\tilde{g}1}$ is 5 TeV.

t-channel Higgsino mediation of squark production. This leaves us with only winos and binos, specifically two neutralinos and one chargino. The particle content and the effects on the squark cross sections depend on whether the electroweak gauginos acquire Dirac, Majorana, or mixed gaugino masses.

With charged gauginos, there is one additional Feynman diagram (Fig. G.1) that contributes to the squark production subprocess $pp \to \tilde{u}_L\tilde{d}_L$. Of course regardless

of the "mixed" nature of the winos, the chargino is obviously a Dirac fermion. This particular subprocess is absent in pure supersoft models, and we have provided a discussion of this in App. G.

For general mixed (Dirac and Majorana) neutralinos and a mixed chargino, there is a large parameter space that could be considered. In this section, we focus on *just* the effects of electroweakinos, and assume the gluino is decoupled. For a Dirac gluino, effective decoupling occurs once $M_{\tilde{g}} \gtrsim$ 1-3.5 TeV for squark mass 400-1200 GeV, as shown in Fig. 4.1.. Earlier work on electroweak contributions to squark production in the MSSM can be found in Ref. [223, 222], however the benchmark spectra considered there included contributions from a (Majorana) gluino comparable in mass to the squarks.

We further specialize to pure Majorana masses for the wino and bino. This is for two reasons. First, we expect that purely Majorana electroweakino masses will yield the largest effects on first generation squark production cross sections, and thus bound what can happen in a general model. Second, as pointed out in [160], if $U(1)$ and $SU(2)$ gauginos acquire pure Majorana masses, there is no suppression of the quartic coupling of the Higgs potential. Generating this unusual spectrum of gaugino masses is an interesting model-building issue, however the absence of Dirac masses for the bino and wino occurs automatically if no chiral superfields in the adjoint (triplet and singlet) representation exist in the low energy theory.

We are primarily interested in bino and/or wino masses at which there is a

noticeable departure from the "QCD-only" (i.e., mediated by gluons) cross section, σ_{QCD}. We characterize this by finding the total cross section for a given squark mass within a range of bino and wino masses. We find that the largest effect of electroweakinos on the total squark production cross section occurs when the squark mass is near the Majorana electroweakino mass. The explanation becomes apparent when we consider these two observations:

1. We expect t-channel exchange of Majorana electroweakinos will lead to significant contributions to squark-squark production in the same kinematic regime as occured for a mixed or pure Dirac gluino. That is, the dominant contributions to total squark production change from $q\bar{q}, gg \to \tilde{q}\tilde{q}^*$ (s-channel gluon-mediated processes) at lower squark masses to $qq \to \tilde{q}\tilde{q}$ (t-channel gaugino-mediated processes) at higher squark masses.

2. As we know from the discussion under (i) in Sec. IV.3.2, the coefficient of the Weyl spinors in the amplitude for a t-channel exchange diagram for same-handed squark production is

$$g_f^2 \frac{M_f}{t - M_f^2}$$

where M_f and g_f are the mass and chargino-squark-quark coupling of the fermion (gaugino) respectively. One can see that, as a function of M_f, the absolute value of this expression is at its maximum when $M_f^2 = -t$, where it

becomes

$$g_f^2 \frac{-1}{2\sqrt{-t}}$$

Moreover, if β is an arbitrary real number, both $M_f = \beta\sqrt{-t}$ and $M_f = \beta^{-1}\sqrt{-t}$ are fermion masses that confer the same value to the amplitude,

$$g_f^2 \frac{\beta}{1+\beta^2} \frac{-1}{\sqrt{-t}}$$

This leads to an effect on the cross section that is symmetric with respect to $M_f \to 1/M_f$, as we will see.

Opposite-handed squark production, however, has a different expression for the co-efficient of the spinors in the amplitude:

$$g_f^2 \frac{p \cdot \sigma}{t - M_f^2}$$

where the spinor indices are suppressed. The maximum of *this* expression is achieved when $M_f \to 0$, at which point it tends to $g_f^2 \ (p \cdot \sigma)/t$.

One might be concerned about the possible existence of a t-channel pole if t were to approach M_f^2. However, upon integrating the total cross section between $-1 < \cos\theta < 1$, corresponding to t over the range

$$\begin{aligned} t_- \ &< \ t \ < \ t_+ \\ t_\pm \ &= \ \frac{1}{2}\left(-s \pm \sqrt{s^2 - 4sM_{\tilde{q}}^2}\right) + M_{\tilde{q}}^2 \,. \end{aligned} \tag{IV.16}$$

It is clear that t is negative definite, and moreover, approaches a small (negative) value only when s is large. The required large s means there is substantial

suppression of the integrated cross section in the integration region where $t \simeq t_+$ is small. Hence, the case of $M_f \to 0$ does not lead to a divergent contribution to the squark production rate.

Now these observations can be put together when reflecting on what happens when Majorana winos and/or binos are turned on. We define σ_{QCD} as the total cross section when squark production is QCD-only and σ_{QECD} as the cross section when it is mediated by winos, binos, and gluinos. Table 4.1. provides information on the electroweakino mediation of the individual modes.

Maximal Electroweakino Impact (MEI)

The cross section for $\tilde{q}_L\tilde{q}_L$ production reaches its maximal value when the wino, which couples only to left-handed squarks, has a mass $M_{\tilde{W}} = M_{\tilde{q}}$, since the characteristic $\sqrt{-t}$ of the t-channel subprocess is $M_{\tilde{q}}$. Similarly, the cross section of $\tilde{q}_R\tilde{q}_R$ production reaches its maximal value when the mass of the bino is also at $M_{\tilde{B}} = M_{\tilde{q}}$. If these sub-processes dominate over the QCD-only squark production, we may have a significant increase in σ_{QECD}. We call this Maximal Electroweak Impact (MEI). Indeed, these two individually overtake $\tilde{q}_L\tilde{q}_R$ production, which is the leading sub-process at high squark masses in a QCD-only picture. The enhancement to $\tilde{q}_L\tilde{q}_L$ is larger than $\tilde{q}_R\tilde{q}_R$ since the wino couples more strongly to quarks and squarks than the bino.

In Fig. 4.10., we show the maximum deviation from σ_{QCD}, represented by the ratio $\sigma_{QECD}/\sigma_{QCD}$, when both the bino and wino have masses at their $M_{\tilde{q}}$-

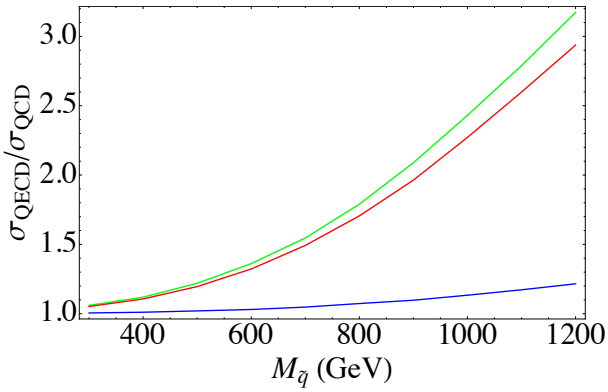

Figure 4.10.: Impact of electroweakinos at their maximal electroweakino impact (MEI) values, where the Majorana wino mass is equal to the squark mass. The MEI value establishes the upper bound in cross section from the impact of electroweakinos versus the QCD-only scenario (pure s-channel gluon-mediated squark–anti-squark production). In this plot, green: both electroweakinos are at their MEI values, red: the wino is pure Majorana with $M_{\tilde{W}} = M_{\tilde{q}}$, blue: the bino is pure Majorana with $M_{\tilde{B}} = M_{\tilde{q}}$. These curves show that at the MEI values, the wino is more responsible than the bino for maximizing the cross section by virtue of its stronger couplings.

dependent MEI values. As expected, the greatest departures are observed at high squark masses. Two other scenarios are also shown: (*i*) a Majorana bino at the MEI value with a Dirac wino (blue), (*ii*) a Majorana wino at the MEI value with a Dirac bino (red). From these we see that the wino, despite coupling only to left-handed squarks, dominates the increase in the total cross section.

The contour plot in Fig. 4.11. shows ratios of the cross sections with and

	wino	bino
$u_{i,L}; \tilde{u}_{i,L}$	$g/\sqrt{2}$	$g'/3\sqrt{2}$
$d_{i,L}; \tilde{d}_{i,L}$	$-g/\sqrt{2}$	$g'/3\sqrt{2}$
$u_{i,R}; \tilde{u}_{i,R}$	0	$-4g'/3\sqrt{2}$
$d_{i,R}; \tilde{d}_{i,R}$	0	$2g'/3\sqrt{2}$

Mode	Wino	Bino
$\tilde{q}_L\tilde{q}_L$	✓	✓
$\tilde{q}_R\tilde{q}_R$	X	✓
$\tilde{q}_L\tilde{q}_L^*$	✓	✓
$\tilde{q}_R\tilde{q}_R^*$	X	✓
$\tilde{q}_L^*\tilde{q}_L^*$	✓	✓
$\tilde{q}_R^*\tilde{q}_R^*$	X	✓
$\tilde{q}_L\tilde{q}_R$	X	✓
$\tilde{q}_L\tilde{q}_R^*$	X	✓
$\tilde{q}_L^*\tilde{q}_R$	X	✓
$\tilde{q}_L^*\tilde{q}_R^*$	X	✓

Table 4.1.: (a) Quark-squark-electroweakino couplings of the wino and the bino for different chiralities. The index i runs over quark generation; (b) Categorizing the distinct individual subprocesses of squark production mediated by the wino and bino. The wino participates in only the left-handed (anti-)squark production, yet dominates the increase in the total cross section.

without electroweakino impact, $\sigma_{QECD}/\sigma_{QCD}$, and spans the parameter space in its most interesting district, that is, where the masses of the bino and wino are in the neighborhood of the squark mass. Specifically, we vary the neutralino or chargino mass in the range $\{0.1M_{\tilde{q}}, 10M_{\tilde{q}}\}$. The symmetry spoken of in our second observation, namely, the amplitudes for same-handed squark production are identical when $M_f/M_{\tilde{q}}$ is the same as $M_{\tilde{q}}/M_f$, is reflected in the near-mirror symmetry of the contours in Fig. 4.11..

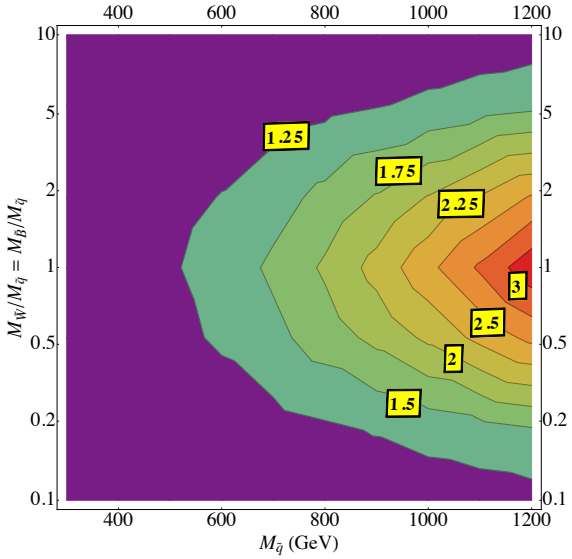

Figure 4.11.: Contours showing the impact of electroweak gauginos when both the Majorana wino and Majorana bino masses are within an order of magnitude of their MEI values. The peaks are values of $\sigma_{QECD}/\sigma_{QCD}$. The gluino mass here is 5 TeV.

Once again we perceive that the region where the squark mass is high and the electroweak gaugino masses are close to the squark mass (by a factor of 2) is where the colored superpartner production cross section is most enhanced compared to a pure Dirac gluino. Different regions of the contour plot of Fig. 4.11. are dominated in cross section by the production of different final states. Fig. 4.12. is a representation of these relative effects. The ratio $\sigma(\text{mode})/\sigma(\text{total})$ is plotted against squark mass for three different kinds of final state modes: (i) same-handed squark-antisquark (solid lines), (ii) same-handed squark-squark (dotted), and (iii)

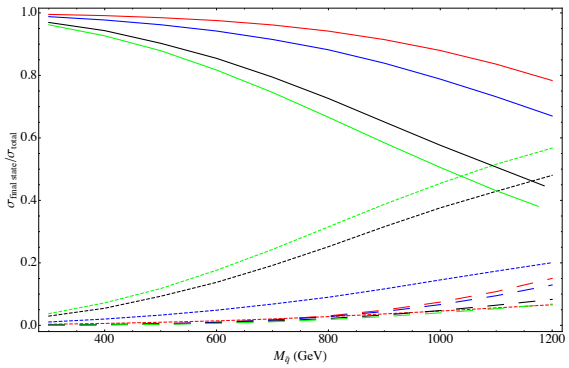

Figure 4.12.: Regions of domination: a different look at the plot in Fig. 4.11.. The ratio $M_{\tilde{W}}/M_{\tilde{q}} = M_{\tilde{B}}/M_{\tilde{q}}$ is represented by the colors and the code is (green: 1; black: 0.5; blue: 0.2; red: 0.1). The final state of production is given by the constitution of the line, the code being (solid: $\tilde{q}_{i,L}, \tilde{q}^*_{i,L}$ and $\tilde{q}_{i,R}, \tilde{q}^*_{i,R}$; dotted: $\tilde{q}_{i,L}, \tilde{q}_{j,L}$ and $\tilde{q}_{i,R}, \tilde{q}_{j,R}$; dashed: $\tilde{q}_{i,L}, \tilde{q}_{j,R}$). The gluino mass here is 5 TeV.

opposite-handed squark-squark (dashed). The color code is (green, black, blue, red) = (1, 0.5, 0.2, 0.1) where the numbers on the RHS are the ratios of the weak gaugino mass to the squark mass. The green curves show that as the squark mass exceeds a TeV, the contribution of the same-handed squark production surpasses the same-handed squark-antisquark production. As $M_{\tilde{W}} = M_{\tilde{B}}$ is lowered (that is, as red is approached), the final states $\tilde{q}_L\tilde{q}^*_L$ and $\tilde{q}_R\tilde{q}^*_R$ dominate the cross section irrespective of the squark mass. These subprocesses, as seen before, occur chiefly through an s-channel gluon with the initial state as two gluons or a quark and an antiquark.

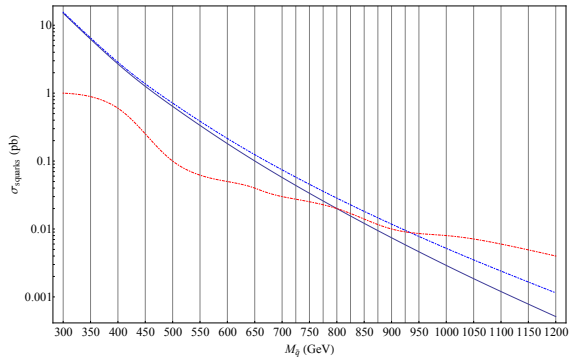

Figure 4.13.: The 8 TeV cross sections at leading order of scenarios with a pure Dirac gluino (black) and electroweakinos at their MEI values (blue) intersect with the exclusion cross section set by the multijet plus missing energy search (red) [158], which gives us bounds on the squark mass. The gluino mass is taken as 5 TeV.

We now consider what our results imply for the supersymmetry search strategies at LHC. The CMS collaboration has provided exclusion cross section limits on pair-produced first and second generation squarks with the gluino decoupled at $\sqrt{s} = 8$ TeV with 19.5 fb^{-1} of data in their "T2qq" simplified model [158]. A similar simplified model, with the gluino decoupled, has been subjected to a multijet plus missing energy search analysis by the ATLAS collaboration [157] obtaining similar bounds. We omit this from our discussion since the CMS results provided rate bounds throughout the $M_{\tilde{q}}$-$M_{\rm LSP}$ plane. Here we focus on the bounds when the LSP is massless, to compare with our earlier results.

The various cross sections obtained in our model are compared against the

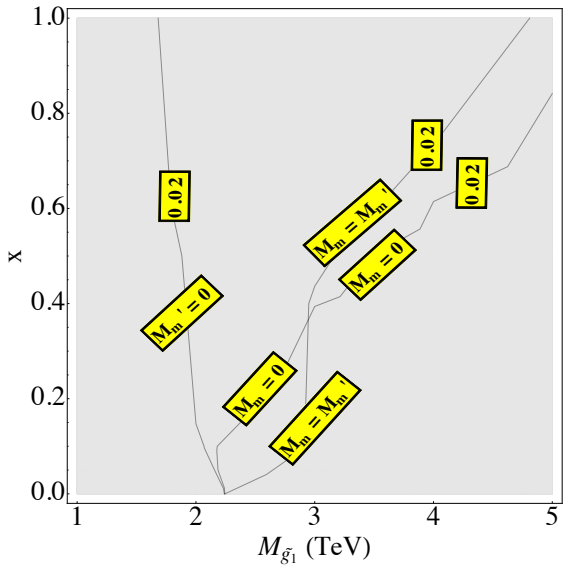

Figure 4.14.: Constraints set by the multi-jet plus missing energy search on the parameter space of our model. Since we find in Fig. 4.13. that that the bound is set at $M_{\tilde{q}} \approx 800$ GeV at an exclusion cross section ≈ 0.02 pb (at leading order), we have included the contour of that value for that squark mass. All three scenarios we have considered are shown, using the appropriate contours from Figs. 4.3.d, 4.6.d and 4.8.d, and the space to the left of each contour is excluded for the corresponding scenario. Depending on the contour, the y-axis is interpreted as $x = M_m/M_d$ or $x = 2M_m/M_d = 2M'_m/M_d$ or $x' = M'_m/M_d$.

exclusion cross sections of CMS searches that were based on the search for new physics in multijets and missing momentum final state at $\sqrt{s} = 8$ TeV and $\mathcal{L} = 19.5$ fb^{-1} [158]. Note however that the CMS exclusion cross sections are computed at NLO+NLL, while the cross sections computed here are at leading order.

The CMS "T2qq" simplified model exclusion cross section limits can be re-interpreted to a model with a mixed gluino. Here we assume the gluino itself is not pair-produced or produced in association with a squark, and only consider its effects through modifications to squark production (since this is what can be easily bounded using the CMS simplified model). We obtain $M_{\tilde{q}} \geq 800$ GeV for a Dirac-gluino-only scenario and $M_{\tilde{q}} \geq 925$ GeV when both the electroweakinos are at their MEI values, with the gluino mass taken as 5 TeV. Fig. 4.13. shows the predictions for the leading order cross sections in these two cases, and the bound we have extracted from [158]. We note that the bound we obtain for a pure Dirac gluino is $M_{\tilde{q}} \geq 800$ GeV, whereas the CMS collaboration obtained $M_{\tilde{q}} \geq 840$ GeV for a decoupled gluino. In principle these should match precisely, though given the comparison is made in a plot spanning four orders of magnitude (like Fig. 4.13.), we believe this difference is not significant, and represents the error of our reinterpretation.

The pure Dirac gluino bound also enables us to set constraints on the parameter space of mixed gluinos. Since the exclusion cross section at $M_{\tilde{q}} = 800$ GeV is ~ 0.02 pb (at leading order), we can overlay the contours of different mixed gluino

scenarios corresponding to that cross section. Fig. 4.14. shows this superimposition, and for each scenario the parameter space to the left of the corresponding contour is excluded.

CHAPTER V

CONCLUSIONS

In Chapter II, we presented a simple but realistic model of pseudo-Dirac fermionic dark matter that results in a qualitatively new signal in the form of kinematical and angular features in dilepton production at the LHC. The most spectacular feature is the "monocline", a step-like feature with a sharp rise in the differential cross section for dilepton production occurring for a dilepton invariant mass near the sum of the dark fermion masses, $m_{\ell\ell} \sim M_1 + M_2$, with a subsequent gradual falloff. If discovered, this signal provides an immediate target of opportunity given that the putative dark matter particle's mass is bounded (namely, $m_{\rm DM} \lesssim m_{\ell\ell}/2$ for a monocline feature at $m_{\ell\ell}$). Of course observing the feature consistent with a radiative correction from a box of new particles with masses $\sim m_{\ell\ell}/2$ does not immediately imply these particles are dark matter. Nevertheless, knowing the scale is immensely useful when applied to direct and indirect detection experiments, as well as traditional signals at colliders of both the dark matter (e.g., mono-X + MET signals) as well as the scalar mediators (e.g., jets + MET for the scalar mediator). We also note that our monocline signal is most powerful when the spectrum of dark matter and its mediator is nearly degenerate. This strategy is thus complementary to MET-based searches.

Pseudo-Dirac dark matter, that we have shown leads to interesting signals in dilepton production, is also well-motivated and predictive. Pseudo-Dirac fermions could arise naturally when an accidental $U(1)$ symmetry that gives a Dirac mass to the fermions is broken at loop level [224]. Since a Dirac fermion can be thought of as two degenerate Majorana eigenstates, the effect of the small Majorana mass is to introduce a splitting in the eigenmasses. If the splitting is of the order of a few GeV, we obtain several desirable features. Among these is that since the momentum transfer scale of direct detection experiments is 10-100s of keV, such experiments are only sensitive to the lighter eigenstate; thus, the pseudo-Dirac fermion with a few-GeV-splitting can be treated as a Majorana fermion for direct detection. In addition, efficient s-wave coannihilation between the two eigenstates would result in a relic abundance that does not overclose the universe even for small couplings. The heavier eigenstate produced in a collider can decay to the lighter one with a displaced vertex that is measurable at the LHC. By studying the dilepton spectrum in this decay, the mass splitting can be directly measured. The decay length can also predict the mass of the lighter state if the model's relic abundance is matched with the observed value and if the mediators are heavy [196].

The model as presented is renormalizable, and thus in principle UV complete. However, we have considered relatively large (though perturbative) λ couplings between the dark fermion, the scalar mediator, and a Standard Model quark or lepton. These couplings, when RG evolved to higher scales, may develop Landau

poles. This is not in itself a concern for us since we have focused on the physics of the new particles near to their threshold production at the LHC. Larger λ couplings could arise from several sources. The most logical possibility is that there is a larger set of scalar mediators, for instance scalar quark mediators that couple to the left-handed quarks, that, when summed into the box contributions, masquerade as a larger effective λ coupling with fewer mediators. Another possibility is that the pseudo-Dirac fermionic partner χ_A couples to the scalar mediators and quarks, also effectively increasing the strength of the λ couplings.

The model has unmistakable similarities to simplified supersymmetric models with a bino or neutral wino as the dark matter, with the squarks and sleptons are the scalar mediators. Indeed, the supersymmetric limit is interesting, since several of our otherwise arbitrary assumptions (coupling of just χ_B to the scalar mediator and quarks) could arise naturally in a supersymmetric context. The main impediment is that an observable feature in dilepton production requires $\lambda \gtrsim g$ by a factor of perhaps 1.5 – 3 times what would have otherwise been required by (at least unbroken) supersymmetry. This is intriguingly reminiscent of the Higgs quartic coupling, which is related to the electroweak couplings at tree-level, but in fact must be significantly larger to accommodate the observed value of 125 GeV. An interesting question for future exploration is to understand what could be possible from supersymmetry breaking corrections to increase the size of the quark-squark-neutral gaugino coupling.

We have not considered flavor-violation in the model, but this too could be interesting, especially if the dilepton signal was also accompanied by some fraction of $e^{\pm}\mu^{\mp}$ events (that would also exhibit a feature in their $m_{\ell\ell}$ spectrum). We did not consider flavor-violation in this chapter for two reasons: one is that it obviously would not interfere with SM Drell-Yan production, which was our primary motivation. Second, we would necessarily be forced into considering additional lepton-flavor-violating constraints, which are likely to be highly constraining. For a discussion of quark flavor constraints on models similar to ours see [76].

The scalar quark mediator will necessarily have box contributions to the dijet signal as well. Unfortunately, our estimates of the size of this radiative correction are that it is much too small to lead to an observable monocline signal in the dijet spectrum. This is because the box contribution arises in the partonic process $q\bar{q} \to q\bar{q}$ whereas the dominant dijet production involves $qq \to qq$ as well as gluon mediated processes, which are much more significant given the associated PDF enhancements. To get a signal that could compete with QCD strength would require λ couplings much larger than required for dilepton production, and this suggests that a perturbative analysis is no longer possible.

In summary, we encourage ATLAS and CMS to explore the sensitivity of features in the dilepton kinematic and angular spectrum for extracting dark matter signals!

In Chapter III we investigated the viability of regions of large $\tan\beta$ in the

frame of Fat Higgs/λ-SUSY models. In the "toy" model we constructed we showed that the singlet cubic term is suppressed while the the tadpole and singlino mass parameter term were allowed. Within this framework we showed that there are regions of large $\tan\beta$ that are phenomenologically viable.

We computed the one-loop effective potential and showed that the $\tan\beta$-independent contributions to the Higgs quartic are crucial in raising the Higgs mass to the observed value of 125 GeV. We have also shown that non-standard Higgs bosons of the same mass as the stops will give comparable contributions to the Higgs quartic when $\lambda \simeq \sqrt{3} y_t$. In the region of degenerate non-standard Higgs boson masses, the corrections are larger than those estimated in Ref. [134, 139]. This discrepancy is purely due to the assumptions made in Ref. [134, 139] that lead to a split heavy CP-even and CP-even spectrum.

Furthermore, we pointed out that contributions of the neutralino and charginos to electroweak precison observables are small even for large $\tan\beta$ when $\mu_{\text{eff}} \simeq 500$ GeV and $\mu' \gtrsim 100$ GeV. Such large values of μ_{eff} make this region Fat Higgs/λ-SUSY parameter space slightly more unnatural than the low $\tan\beta$ region considered in Ref. [121, 122, 123, 124, 125, 126, 127, 128, 129, 130, 131, 132, 133]. Additionally, this scenario corresponds to the decoupling limit where the mixing between the heavy Higgs states and the SM-like Higgs is suppressed. Therefore SM-like Higgs decay properties are with 1% of their corresponding Standard Model values. Therefore detecting this scenario at the LHC will be challenging.

We also found regions of large $\tan\beta$ in Fat Higgs/λ-SUSY models that satisfy all the above constraints and provide a viable dark matter candidate, namely, a bino/singlino admixture. If we were to impose thermal freezeout constraints, the dark matter mass must be either at the pole of annihilation (half the Higgs boson mass) or above 104 GeV for the relic abundance to be set by coannihilation effects from a possible compressed slepton spectrum. The regions satisfying this hypothesis can completely be probed by the future XENON1T experiment.

In Chapter IV, we found that a mixed gluino that acquires both a Dirac mass and a Majorana mass solely for its gaugino component ($M_m \neq 0,\ M'_m = 0$), is *less* constrained from LHC searches than a pure Dirac gluino. This is because the lightest gluino eigenstate contains more of the adjoint fermion partner that does not couple to quarks and squarks, and thus further suppresses squark production through t-channel exchange. This was shown in detail by examining the individual squark production sub-processes as a function of the Majorana mass.

A mixed gluino that acquires both a Dirac mass and a Majorana mass for its adjoint fermion component ($M_m = 0,\ M'_m \neq 0$), or for both of its components ($M_m \neq 0,\ M'_m \neq 0$), is more constrained from LHC searches than a pure Dirac gluino. This is because the lightest gluino eigenstate contains more of the gaugino that does couple to quarks and squarks. However, the effect is not significant when the Majorana masses are small compared with the Dirac mass, roughly

$M_m, M'_m \lesssim \mathcal{O}(0.1) M_d$. Again, this was shown in detail by examining the individual squark production sub-processes as a function of the Majorana mass(es).

A model with a Dirac gluino and Majorana electroweak gauginos that both contribute to squark production can have modifications from the gluino-only cross section by a factor of a few. The largest effect occurs at the "maximal electroweakino impact" mass values of $M_1, M_2 \simeq M_{\tilde{q}}$. As the electroweak gauginos become larger or smaller than this value, their effect on squark production becomes suppressed.

New candidates for the LSP are one of the consequences of finding that light Majorana electroweak gauginos not significantly affecting cross sections. In addition to a gravitino LSP, we showed that a Majorana bino is also perfectly viable since it does not significantly increase squark production cross sections. One could also contemplate a light Majorana wino, however this would introduce new branching fractions of left-handed squarks to winos.

The results in the chapter focused on the LHC operating at 8 TeV; to illustrate what happens at the LHC operating at 14 TeV, we have extended some of the results for both the mixed gluino as well as Majorana electroweakinos in Appendix H. We conclude by considering several new simplified models could be studied and constrained (by the experimental collaborations) that would capture the essentials of these scenarios with mixed gauginos and electroweakinos. It would be particularly insightful to study the simplified models when not only the squarks

but also the gluino is relatively light, while the LSP mass is allowed to vary. Here are several proposals:

1) **Dirac gluino, several choices of LSP mass**: Cross section bounds in $M_{\tilde{q}} - M_D$ plane; $M_{\rm LSP} = 0, 200, 400$ GeV.

2) **Dirac gluino, several choices of gluino mass**: Cross section bounds in $M_{\tilde{q}} - M_{\rm LSP}$ plane M_D = 1-3 TeV in steps of 0.5 TeV.

3) **Mixed gluino, several choices of squark mass**: Cross section bounds in $M_{\tilde{g}1} - x$ plane for Cases I,II,III; $M_{\tilde{q}}$ = 500-1000 GeV in steps of 100-250 GeV, with a massless LSP.

4) **Mixed gluino, several choices of LSP mass**: Cross section bounds in $M_{\tilde{g}1} - x$ plane for Cases I,II,III; $M_{\tilde{q}} = 500$, $M_{\rm LSP} = 0, 200, 400$ GeV.

5) **Dirac gluino with Majorana electroweakinos, several choices of LSP mass**: Cross section bounds in $M_{\tilde{q}} - M_{\tilde{W},\tilde{B}}/M_{\tilde{q}}$ plane; take $M_{\tilde{W}} = M_{\tilde{B}}$ and $M_{\tilde{W}} = 2M_{\tilde{B}}$; $M_{\rm LSP} = 0, 200, 400$ GeV.

APPENDIX A

PARTON LEVEL CROSS-SECTIONS

In this appendix, we provide expressions for the new physics box contributions to the parton level $q\bar{q} \to \ell^+\ell^-$ cross-sections that are then convoluted with parton distribution functions to obtain the proton-level differential cross-sections $d\sigma/dm_{\ell\ell}$.

We define the following short hand notation for 4-point loop functions

$$\begin{aligned} D_i &\equiv D_i[m_q^2, m_q^2, m_l^2, m_l^2, s, t, \mu_1^2, M_\phi^2, \mu_2^2, M_\phi^2] \ , \\ \tilde{D}_i &\equiv D_i[m_q^2, m_q^2, m_l^2, m_l^2, s, t, \mu_3^2, M_\phi^2, \mu_4^2, M_\phi^2] \ , \\ \bar{D}_i &\equiv D_i[m_q^2, m_q^2, m_l^2, m_l^2, s, u, \mu_1^2, M_\phi^2, \mu_2^2, M_\phi^2] \ , \\ \tilde{\bar{D}}_i &\equiv D_i[m_q^2, m_q^2, m_l^2, m_l^2, s, u, \mu_3^2, M_\phi^2, \mu_4^2, M_\phi^2] \ , \end{aligned} \tag{A.1}$$

with the conventions for 4-point functions as in [225].

To incorporate the mixing of the dark fermions, we define the function

$$\vartheta[x] \equiv 1 - \frac{x}{M_1 + M_2} \ , \tag{A.2}$$

so that $\vartheta[M_1] = \cos^2\theta$ and $\vartheta[M_2] = \sin^2\theta$. Here, θ is the mixing angle introduced in Eq. (IV.8). In the following, $c = 2/3$ for up quarks in the initial state and $c = -1/3$ for down quarks in the initial state.

The interference of the tree-level s-channel photon-mediated diagram with

(i) any direct box diagram is given by

$$d\tilde{\sigma}_{\gamma-\mathrm{box}}[\mu_1,\mu_2] = -\vartheta[\mu_1]\vartheta[\mu_2]\frac{ce^2|\lambda_{\tilde{q}}|^2|\lambda_{\tilde{\ell}}|^2}{256\pi^3}$$
$$\times 2\mathrm{Re}\left\{\frac{(s+t)^2}{s^2}(2D_{00}+(D_2+D_{12}+D_{22}+D_{23})s)\right\} \ ;$$

(ii) any crossed box diagram is given by

$$d\tilde{\sigma}_{\gamma-\mathrm{xbox}}[\mu_1,\mu_2] = -\vartheta[\mu_1]\vartheta[\mu_2]\frac{ce^2|\lambda_{\tilde{q}}|^2|\lambda_{\tilde{\ell}}|^2}{256\pi^3}$$
$$\times\ 2\mathrm{Re}\left\{\frac{(s+t)^2}{s^2}(\mu_1\mu_2\bar{D}_0)\right\} \ .$$

The interference of the tree-level s-channel Z-mediated diagram with

(i) any direct box diagram is given by

$$d\tilde{\sigma}_{Z-\mathrm{box}}[\mu_1,\mu_2] = -\vartheta[\mu_1]\vartheta[\mu_2]\frac{ce^2t_W^2|\lambda_{\tilde{q}}|^2|\lambda_{\tilde{\ell}}|^2}{256\pi^3}$$
$$\times 2\mathrm{Re}\left\{\frac{(s+t)^2}{s(s-M_Z^2)}(2D_{00}+(D_2+D_{12}+D_{22}+D_{23})s)\right\} \ ;$$

(ii) any crossed box diagram is given by

$$d\tilde{\sigma}_{Z-\mathrm{xbox}}[\mu_1,\mu_2] = -\vartheta[\mu_1]\vartheta[\mu_2]\frac{ce^2t_W^2|\lambda_{\tilde{q}}|^2|\lambda_{\tilde{\ell}}|^2}{256\pi^3}$$
$$\times\ 2\mathrm{Re}\left\{\frac{(s+t)^2}{s(s-M_Z^2)}(\mu_1\mu_2\bar{D}_0)\right\} \ ,$$

where $t_W = \tan\theta_W$ and θ_W is the weak mixing angle.

Thus, the interference between the all the tree diagrams and any direct box diagram is

$$d\tilde{\sigma}_{\mathrm{tree-box}}[\mu_1,\mu_2] =$$
$$d\tilde{\sigma}_{\gamma-\mathrm{box}}[\mu_1,\mu_2] + d\tilde{\sigma}_{Z-\mathrm{box}}[\mu_1,\mu_2] \ , \qquad \text{(A.3)}$$

and the interference between all the tree diagrams and any crossed box diagram is

$$d\tilde{\sigma}_{\rm tree-xbox}[\mu_1,\mu_2] =$$
$$d\tilde{\sigma}_{\gamma-{\rm xbox}}[\mu_1,\mu_2] + d\tilde{\sigma}_{Z-{\rm xbox}}[\mu_1,\mu_2]\ . \tag{A.4}$$

The interference between any two direct box diagrams is given by

$$\begin{aligned} d\tilde{\sigma}_{\rm box^2}[\mu_1,\mu_2,\mu_3,\mu_4] =& \\ &\vartheta[\mu_1]\vartheta[\mu_2]\vartheta[\mu_3]\vartheta[\mu_4]\frac{|\lambda_{\tilde{q}}|^4|\lambda_{\tilde{\ell}}|^4}{2048\pi^5 s}(s+t)^2 \\ \times 2{\rm Re}\Big\{&(2D_{00}+(D_2+D_{12}+D_{22}+D_{23})s) \\ &\times(2\tilde{D}^*_{00}+(\tilde{D}^*_2+\tilde{D}^*_{12}+\tilde{D}^*_{22}+\tilde{D}^*_{23})s)\Big\}\ . \end{aligned} \tag{A.5}$$

The interference between any two crossed box diagrams is given by

$$\begin{aligned} d\tilde{\sigma}_{\rm xbox^2}[\mu_1,\mu_2,\mu_3,\mu_4] =& \\ &\vartheta[\mu_1]\vartheta[\mu_2]\vartheta[\mu_3]\vartheta[\mu_4]\frac{|\lambda_{\tilde{q}}|^4|\lambda_{\tilde{\ell}}|^4}{2048\pi^5 s}(s+t)^2 \\ &\times 2{\rm Re}\Big\{(\mu_1\mu_2\mu_3\mu_4\bar{D}_0\tilde{\bar{D}}^*_0)\Big\}\ . \end{aligned} \tag{A.6}$$

The interference between any direct box diagram and any crossed box diagram is given by

$$\begin{aligned} d\tilde{\sigma}_{\rm box-xbox}[\mu_1,\mu_2,\mu_3,\mu_4] =& \\ &\vartheta[\mu_1]\vartheta[\mu_2]\vartheta[\mu_3]\vartheta[\mu_4]\frac{|\lambda_{\tilde{q}}|^4|\lambda_{\tilde{\ell}}|^4}{2048\pi^5 s}(s+t)^2 \\ \times 2{\rm Re}\Big\{&((2D_{00}+(D_2+D_{12}+D_{22}+D_{23})s) \\ &\times\mu_3\mu_4\tilde{\bar{D}}^*_0)\Big\}\ . \end{aligned} \tag{A.7}$$

We can now write down the total cross-sections using the expressions above. From Eq. (A.3), the interference between all the tree diagrams and all the direct box diagrams is obtained as

$$d\sigma_{\rm tree-box} = \sum_{a,b=1,2} d\tilde{\sigma}_{\rm tree-box}[M_a, M_b] \ .$$

From Eq. (A.4), the interference between all the tree diagrams and all the crossed box diagrams is obtained as

$$d\sigma_{\rm tree-xbox} = \sum_{a,b=1,2} d\tilde{\sigma}_{\rm tree-xbox}[M_a, M_b] \ .$$

From Eq. (A.5), the total interference between a pair of direct boxes (including box^2 pieces) is given by

$$d\sigma_{\rm box^2} = \frac{1}{2} \sum_{a,b,c,d=1,2} d\tilde{\sigma}_{\rm box^2}[M_a, M_b, M_c, M_d] \ .$$

From Eq. (A.6), the total interference between a pair of crossed boxes (including crossed box^2 pieces) is given by

$$d\sigma_{\rm xbox^2} = \frac{1}{2} \sum_{a,b,c,d=1,2} d\tilde{\sigma}_{\rm xbox^2}[M_a, M_b, M_c, M_d] \ .$$

Finally, from Eq. (A.7), the total interference between direct and crossed boxes is given by

$$d\sigma_{\rm box-xbox} = \sum_{a,b,c,d=1,2} d\tilde{\sigma}_{\rm box-box}[M_a, M_b, M_c, M_d] \ .$$

APPENDIX B

CALCULATION OF $a_{\rm eff}$ AND $b_{\rm eff}$

In this appendix we describe the calculation of $a_{\rm eff}$ and $b_{\rm eff}$, which characterize the $s-$wave and $p-$wave contributions to the effective annihilation cross-section $\langle\sigma_{\rm eff}v_{\rm rel}\rangle$ of pseudo-Dirac dark matter.

Consider the annihilation process $\chi_1\chi_2 \to f\bar{f}$, which proceeds through the t and u channels. Here χ_1 and χ_2 are two Majorana fermions with masses μ_1 and μ_2 respectively, and f is an SM fermion taken to be massless for simplicity. Taylor-expanding in v to write $\langle\sigma v\rangle = a[\mu_1,\mu_2] + b[\mu_1,\mu_2]v^2 + \mathcal{O}(v^4)$, we get

$$\begin{aligned}
a[\mu_1,\mu_2] &= \frac{\lambda^4 d^2(|p|-p)}{16\pi|p|(|p|+M_\phi^2)^2}\ , \\
b[\mu_1,\mu_2] &= \frac{\lambda^4 \mathrm{sgn}(p)}{96\pi(|\mu_1|+|\mu_2|)(|p|+M_\phi^2)^4} \\
&\times \Big\{4|p|[4p^2q + p(4M_\phi^4 - q^2) + 3M_\phi^2 d^2 q] \\
&\quad + p^2[4(p-q)^2 + 3q^2] + M_\phi^4[3q^2 + 8qp - 12p^2] \\
&\quad - 2pM_\phi^2 d^2[5q - 2p]\Big\}\ ,
\end{aligned} \tag{B.1}$$

where $d = \mu_1 - \mu_2$, $p = \mu_1\mu_2$ and $q = \mu_1^2 + \mu_2^2$. The expressions above hold for annihilation into leptons. For annihilation into quarks, the expressions must be multiplied by a color factor of 3. We recover the Majorana limit by setting

$\mu_1 = \mu_2 = M_\chi$

$$\begin{aligned} a_{\rm Maj} &= 0 \ , \\ b_{\rm Maj} &= \frac{\lambda^4 M_\chi^2 (M_\phi^4 + M_\chi^4)}{12\pi (M_\phi^2 + M_\chi^2)^4} \ . \end{aligned} \tag{B.2}$$

The Dirac limit can be obtained in the limit $-\mu_1 = \mu_2 = M_\chi$. We obtain

$$\begin{aligned} a_{\rm Dirac} &= \frac{\lambda^4 M_\chi^2}{8\pi (M_\phi^2 + M_\chi^2)^2} \ , \\ b_{\rm Dirac} &= -\frac{\lambda^4 M_\chi^2 (-M_\phi^4 + 3 M_\phi^2 M_\chi^2 + M_\chi^4)}{24\pi (M_\phi^2 + M_\chi^2)^4} \ , \end{aligned} \tag{B.3}$$

in agreement with [50] up to a factor of 4 coming from an extra $\sqrt{2}$ in the definition of our coupling in the Lagrangian.

Let us now compute $a_{\rm eff}$ and $b_{\rm eff}$ by including the effect of coannihilations between the two eigenstates of pseudo-Dirac dark matter. We do this by making an appropriate replacement of the coupling in $a[\mu_1, \mu_2]$ and $b[\mu_1, \mu_2]$ to account for the mixing, multiplying each term by the appropriate Boltzmann factor and finding the weighted average. Therefore, from Eq. (II.25), we have

$$\begin{aligned} a_{\rm eff}(x) &= \lambda^4 [c_\theta^4 a[M_1, M_1] + 2 c_\theta^2 s_\theta^2 a[M_1, M_2] w(x) \\ &\quad + s_\theta^4 a[M_2, M_2] w^2(x)] / [(1 + w(x))^2] \ , \\ b_{\rm eff}(x) &= \lambda^4 [c_\theta^4 b[M_1, M_1] + 2 c_\theta^2 s_\theta^2 b[M_1, M_2] w(x) \\ &\quad + s_\theta^4 b[M_2, M_2] w^2(x)] / [(1 + w(x))^2] \ , \end{aligned} \tag{B.4}$$

where $w(x) = (1+\delta)^{3/2} e^{-x\delta}, \delta = (M_2 - M_1)/M_1$.

APPENDIX C

DIRECT DETECTION FORMULAE

We follow the approach of [226] (see also [227]) to compute the spin-independent scattering cross-section of χ_1 with nucleons, obtained as

$$\sigma_{\rm SI} = \frac{4}{\pi}\mu_N |f_N|^2 \tag{C.1}$$

where μ_N is the $\chi - N$ reduced mass (N=p,n) and f_N is given by

$$\frac{f_N}{m_N} = \sum_{q=u,d} \left(f_q f_{T_q} + \frac{3}{4}(q(2) + \bar{q}(2)) g_q \right) ,$$

with $f_q = \lambda^2 M_\chi / [16(M_{\tilde{q}}^2 - M_\chi^2)^2]$, $g_q = 4 f_q$. Only the quarks that couple to our dark sector are included in the summations given here. The nucleon matrix elements of the quark operators are taken from [50] (see also [228]). The large values of $q(2) + \bar{q}(2)$ make the quark twist-2 contribution the dominant one.

The spin-dependent cross-section for scattering between nucleons and χ is given by [51]

$$\sigma_{\rm SD}^{\rm Maj} = \frac{3}{64\pi} \frac{\lambda^4 \mu_N^2 (\sum_q \Delta_q^N)^2}{(M_{\tilde{q}}^2 - M_\chi^2)^2} , \tag{C.2}$$

where the summation is again over the quarks that couple to the hidden sector and Δ_q^N is defined by $2 s_\mu \Delta_q^N \equiv \langle N | \bar{q} \gamma_\mu \gamma_5 q | N \rangle$ with s_μ the nucleon spin operator. We take bounds from the neutron-dark matter scattering since they are stronger, thus the appropriate matrix elements we use are $\Delta_u^n = -0.427, \Delta_d^n = 0.842$. [229].

APPENDIX D

DECOUPLING BEHAVIOR AT ONE-LOOP LEVEL

We need to use the tadpoles at the one-loop level to solved for the one-loop corrected soft squared mass parameters. Extending Eq. (III.12) to one-loop order leads to the system of three equations,

$$T_i = \frac{\partial V_{\text{Higgs}}}{\partial \phi_i} = \left.\frac{\partial V_{\text{Higgs}}^{\text{tree}}}{\partial \phi_i}\right|_{\{v_k\}} + \left.\frac{\partial \Delta V}{\partial \phi_i}\right|_{\{v_k\}} = T_i^{\text{tree}} + \Delta T_i = 0, \qquad i = 1, 2, 3 \tag{D.1}$$

We again can try to solve for the soft masses $m_{H_u}^2, m_{H_d}^2$ and m_S^2 in terms of the Higgs VEVs. Note that while each T_i^{tree}, as given in Eq. (III.12), contains only its corresponding soft mass $m_{H_i}^2$, ΔT_i in general contain all three soft mass terms. Although obtaining the solutions to such a system of equations maybe straightforward, the computation could become complicated when we expand the full potential around the true electroweak symmetry breaking minimum. We can avoid this difficulty by solving Eq. (D.1) iteratively. We first solve for the tree level soft mass squared parameters $\left(m_{H_u^0}^2\right)^0, \left(m_{H_d^0}^2\right)^0, \left(m_S^2\right)^0$ using Eq. (III.12) and then substitute them into ΔT_i. This approximation linearizes Eq. (D.1) which leads to the one-loop corrected soft mass squared parameters solution

$$m_i^2 = \left(m_i^2\right)^0 - \frac{1}{16\pi^2} \sum_{j=D,S} \frac{M_{A,j}^2}{v_i} \left.\frac{\partial b_j^0}{\partial \phi_i}\right|_{v_i} + ... \tag{D.2}$$

where $\left(m_i^2\right)^0$ is the tree-level solutions of Eq. (III.12), $b_j^0 = b_j\left((m_i^2)^0\right)$, $v_i = (v_u, v_d, s)$, $i = (H_u^0, H_d^0, S)$ and $\phi_i = (H_u^0, H_d^0, S)$. Substituting these solutions

into the total potential and expanding it about the electroweak symmetry breaking minimum we observe that corrections to the CP-even Higgs mass matrix takes the form

$$\left(\Delta M^2_{H^0}\right)^{ab} = \frac{1}{16\pi^2}\sum_{i=D,S}\left(\left.\frac{\partial b_i^{0\,2}}{\partial\phi_a\partial\phi_b}\right|_{\{v_a\}} - \frac{1}{2v_a}\left.\frac{\partial b_i^0}{\partial\phi_a}\right|_{\{v_a\}}\delta_{ab}\right) M^2_{A,i} + ..., \quad \text{(D.3)}$$

By the symmetries of the model, the only field dependences at quadratic order in b_i^0 are $h_u^2, h_d^2, h_u h_d$ and h_s^2. Thus Eq. (D.3) suggests that the coefficient of $M^2_{A_S}$ in the self-energy corrections vanishes and that of $M^2_{A_D}$ will be proportional to

$$-\frac{v^2}{s_\beta c_\beta}\begin{pmatrix} c_\beta^2 & -s_\beta c_\beta & 0 \\ -s_\beta c_\beta & s_\beta^2 & 0 \\ 0 & 0 & 0 \end{pmatrix}. \quad \text{(D.4)}$$

When these correction are rotated into the basis defined in Eq. (III.16) we see that the $(2,2)$ element is the only non-zero element. Therefore the decoupling is manifest even at the one-loop level.

APPENDIX E

EFFECTIVE POTENTIAL DERIVATION

In this section we apply the procedure outlined in Sec. III.2.2 to the computation of one-loop radiative corrections from the Higgs sector. First, we deal with degenerate pseudoscalars, so that all the one-loop corrections come from a single heavy scale. We will call this Case (A). Next, in Case (B), we inspect the effect of splitting the pseudoscalar masses on the one-loop corrections, where they now come from two heavy scales. For simplicity, the soft terms $A_\lambda, A_\kappa, \mu', m_3, m'_S$ are taken to vanish in this case.

(A) **Degenerate pseudoscalars**

From the CP-odd mass matrix in Eq. (III.14), we impose the necessary and sufficient condition for mass degeneracy in the pseudoscalars given by $\left(M_A^2\right)_{12} = 0, \left(M_A^2\right)_{11} = \left(M_A^2\right)_{22} = M_A^2$, to obtain

$$\begin{aligned} \mu' &= A_\lambda, \\ \xi_F &= (M_A^2 s_\beta c_\beta - m_3^2)/\lambda - 2A_\lambda s, \\ \xi_S &= -M_A^2 s - A_\lambda (M_A^2 s_\beta c_\beta - m_3^2 - \lambda v^2 s_{2\beta})/\lambda \end{aligned} \tag{E.1}$$

Respecting this condition, the field-dependent mass matrix for the charged sector

is

$$
\begin{aligned}
M_{11}^{\pm\,2} &= m_{H_u}^2 + \lambda^2 h_s^2 + \frac{g^2}{4}(h_u^2 - h_d^2) + \frac{g_2^2}{2} h_d^2, \\
M_{12}^{\pm\,2} &= (\frac{g_2^2}{2} - \lambda^2) h_u h_d + 2\lambda A_\lambda (h_s - s) + M_A^2 s_\beta c_\beta, \\
M_{22}^{\pm\,2} &= m_{H_d}^2 + \lambda^2 h_s^2 - \frac{g^2}{4}(h_u^2 - h_d^2) + \frac{g_2^2}{2} h_u^2,
\end{aligned}
\tag{E.2}
$$

for the CP-odd sector it is

$$
\begin{aligned}
M_{11}^{P\,2} &= m_{H_u}^2 + \lambda^2 (h_d^2 + h_s^2) + \frac{g^2}{4}(h_u^2 - h_d^2), \\
M_{12}^{P\,2} &= 2\lambda A_\lambda (h_s - s) + M_A^2 s_\beta c_\beta, \\
M_{22}^{P\,2} &= m_{H_d}^2 + \lambda^2 (h_u^2 + h_s^2) - \frac{g^2}{4}(h_u^2 - h_d^2), \\
M_{13}^{P\,2} &= 0, \\
M_{23}^{P\,2} &= 0, \\
M_{33}^{P\,2} &= m_S^2 + \lambda^2 (h_u^2 + h_d^2) + A_\lambda^2 - m_s'^{\,2},
\end{aligned}
\tag{E.3}
$$

and for the CP-even sector it is

$$\begin{aligned}
M_{11}^{S\,2} &= m_{H_u}^2 + \lambda^2(h_d^2 + h_s^2) + \frac{g^2}{4}(3h_u^2 - h_d^2), \\
M_{12}^{S\,2} &= (2\lambda^2 - \frac{g^2}{2})h_u h_d - 2\lambda A_\lambda(h_s - s) + M_A^2 s_\beta c_\beta, \\
M_{22}^{S\,2} &= m_{H_d}^2 + \lambda^2(h_u^2 + h_s^2) - \frac{g^2}{4}(h_u^2 - 3h_d^2), \\
M_{13}^{S\,2} &= 2\lambda^2(h_u h_s - A_\lambda h_d), \\
M_{23}^{S\,2} &= 2\lambda^2(h_d h_s - A_\lambda h_u), \\
M_{33}^{S\,2} &= m_S^2 + \lambda^2(h_u^2 + h_d^2) + A_\lambda^2 + m_s'^{\,2}
\end{aligned} \tag{E.4}$$

The eigenvalues of the charged matrix are given by $M_{1,2}^{\pm\,2} = \frac{1}{2}(\mathrm{Tr}_c \mp \sqrt{\mathrm{Tr}_c^2 - 4\mathrm{Det}_c})$, where $\mathrm{Tr}_c = M_{11}^{\pm\,2} + M_{22}^{\pm\,2}$ and $\mathrm{Det}_c = M_{11}^{\pm\,2} M_{22}^{\pm\,2} - M_{12}^{\pm\,2} M_{21}^{\pm\,2}$. We only include the contribution from the heavier eigenstate corresponding to $M_2^{\pm\,2}$. Note that when we take the supertrace in the charged higgs sector, we obtain a multiplicative factor of 2 since each charged higgs state comprises of two real physical states. In other words, the supertrace is here taken over the full 4×4 squared-mass matrix and not the 2×2 version that is usually written down for brevity.

The eigenvalues of the CP-odd matrix are obtained in a straightforward manner, since the upper left 2×2 block is decoupled from $M_{33}^{P\,2}$. The squared eigenmasses are obtained as $M_{1,p}^2 = \frac{1}{2}(\mathrm{Tr}_p - \sqrt{\mathrm{Tr}_p^2 - 4\mathrm{Det}_p})$, $M_{2,p}^2 = \frac{1}{2}(\mathrm{Tr}_p + \sqrt{\mathrm{Tr}_p^2 - 4\mathrm{Det}_p})$ and $M_{3,p}^2 = M_{33}^2$, where $\mathrm{Tr}_p = M_{11}^{P\,2} + M_{22}^{P\,2}$ and $\mathrm{Det}_p = M_{11}^{P\,2} M_{22}^{P\,2} - M_{12}^{P\,2} M_{21}^{P\,2}$.

Obtaining the CP-even eigenvalues is non-trivial since we need to deal with a rank 3 matrix. However, we can take advantage of the degeneracy of the CP-odd scalars by employing the following simplifying trick.

First, consider the characteristic equation of the CP-even matrix, written as

$$\alpha_3 x^3 + \alpha_2 x^2 + \alpha_1 x + \alpha_0 = 0,$$

whose solutions are the field-dependent eigenmasses $M^2_{i,s}$. The coefficients α_i, in terms of the matrix elements in Eq. (E.4), are

$$\begin{aligned}
\alpha_3 &= 1, \\
\alpha_2 &= -(M_{11}^{S\,2} + M_{22}^{S\,2} + M_{33}^{S\,2}), \\
\alpha_1 &= M_{11}^{S\,2} M_{22}^{S\,2} + M_{22}^{S\,2} M_{33}^{S\,2} + M_{33}^{S\,2} M_{11}^{S\,2} - M_{12}^{S\,2} M_{21}^{S\,2} - M_{23}^{S\,2} M_{32}^{S\,2} - M_{31}^{S\,2} M_{13}^{S\,2}, \\
\alpha_0 &= -[M_{11}^{S\,2}(M_{22}^{S\,2} M_{33}^{S\,2} - M_{23}^{S\,2} M_{32}^{S\,2}) - M_{12}^{S\,2}(M_{21}^{S\,2} M_{33}^{S\,2} - M_{23}^{S\,2} M_{31}^{S\,2}) \\
&\quad + M_{13}^{S\,2}(M_{21}^{S\,2} M_{32}^{S\,2} - M_{22}^{S\,2} M_{31}^{S\,2})]
\end{aligned} \tag{E.5}$$

We also know, in terms of the eigenmasses, that

$$\begin{aligned}
\alpha_2 &= -(M^2_{1,s} + M^2_{2,s} + M^2_{3,s}), \\
\alpha_1 &= M^2_{1,s} M^2_{2,s} + M^2_{2,s} M^2_{3,s} + M^2_{3,s} M^2_{1,s}
\end{aligned} \tag{E.6}$$

Now the CP-even sector contribution to the effective potential, from Eq. (III.18), is

$$\Delta V \supset \frac{1}{64\pi^2}[(M^2_{2,s})^2 + (M^2_{3,s})^2] \log\left(\frac{M_A^2}{M_Z^2}\right). \tag{E.7}$$

The quantity in brackets can be re-written using Eq. (E.6) as simply

$$(M^2_{2,s})^2 + (M^2_{3,s})^2 = \alpha_2^2 - 2\alpha_1 - (M^2_{1,s})^2 \tag{E.8}$$

The coefficients α_1 and α_2 may be read off Eq. (E.5), while we may still have to determine $M^2_{1,s}$ analytically. This is, however, a simple task if we write $M^2_{1,s}$ as a power series in M^2_A :

$$\begin{aligned} M^2_{1,s} &= b_1 + \mathcal{O}\left(\frac{1}{M^2_A}\right) \\ \Longrightarrow\ (M^2_{1,s})^2 &= b_1^2 + \mathcal{O}\left(\frac{1}{M^2_A}\right), \end{aligned} \tag{E.9}$$

where b_1 is at most quadratic in the background fields. Putting Eqs. E.8 and E.9 into Eq. (E.7), we obtain the one-loop effective potential contribution simply as

$$\Delta V \supset \frac{1}{64\pi^2}[\alpha_2^2 - 2\alpha_1 - b_1^2] \log\left(\frac{M^2_A}{M^2_Z}\right), \tag{E.10}$$

where we have discarded $\mathcal{O}(1/M^2_A)$ terms that are irrelevant in obtaining the required self-energy corrections.

After including all the one-loop corrections, the final expressions we obtain for the CP-even mass matrix are now as follows.

$$\left(\overline{M}^2_H\right)_{11} = M^2_Z s^2_\beta + \overline{M}^2_A c^2_\beta + \Pi_{11}; \qquad \left(\overline{M}^2_H\right)_{12} = (2\lambda^2 v^2 - M^2_Z - \overline{M}^2_A) s_\beta c_\beta + \Pi_{12};$$
$$\left(\overline{M}^2_H\right)_{22} = M^2_Z c^2_\beta + \overline{M}^2_A + \Pi_{22}; \qquad \left(\overline{M}^2_H\right)_{13} = 2\lambda v \mu_{\rm eff} s_\beta + \Pi_{13};$$
$$\left(\overline{M}^2_H\right)_{23} = 2\lambda v \mu_{\rm eff} c_\beta + \Pi_{23}; \qquad \left(\overline{M}^2_H\right)_{33} = \overline{M}^2_A + \Pi_{33},$$

where

$$\overline{M}_A^2 \;=\; M_A^2\left(1+\frac{\lambda^2}{8\pi^2}\log\left(\frac{M_A^2}{M_Z^2}\right)\right), \tag{E.11}$$

and

$$\begin{aligned}
\Pi_{11} &= \frac{v^2}{256\pi^2}[-32\lambda^4 s_\beta^2(2c_{2\beta}-s_{2\beta}^2)+2\lambda^2 g^2(3c_{2\beta}-1)(3s_{2\beta}^2+2)\\
&\quad +g^4(4c_W^4+4c_W^2-7s_{2\beta}^2-1-c_{2\beta}(4c_W^4-4c_W^2+5s_{2\beta}^2+3))\\
&\quad +64\lambda^2\frac{A_\lambda\mu_{\rm eff}}{v^2}\cot\beta]\log\left(\frac{M_A^2}{M_Z^2}\right),\\
\Pi_{12} &= \frac{v^2}{256\pi^2}[-32\lambda^4(s_{2\beta}^2-2)-2\lambda^2 g^2 s_{2\beta}(8c_W^2-15s_{2\beta}^2+14)\\
&\quad +g^4 s_{2\beta}(4c_W^4+4c_W^2-7s_{2\beta}^2+3)\\
&\quad -64\lambda^2\frac{A_\lambda\mu_{\rm eff}}{v^2}]\log\left(\frac{M_A^2}{M_Z^2}\right),\\
\Pi_{22} &= \frac{v^2}{256\pi^2}[32\lambda^4 c_\beta^2(2c_{2\beta}+s_{2\beta}^2)-2\lambda^2 g^2(3c_{2\beta}+1)(3s_{2\beta}^2+2)\\
&\quad +g^4(4c_W^4-4c_W^2+7s_{2\beta}^2+1+c_{2\beta}(4c_W^4-4c_W^2+5s_{2\beta}^2+3))\\
&\quad +64\lambda^2\frac{A_\lambda\mu_{\rm eff}}{v^2}\tan\beta]\log\left(\frac{M_A^2}{M_Z^2}\right),\\
\Pi_{13} &= \frac{v\mu_{\rm eff}}{\mu_{\rm eff}}[12\lambda^3 s_\beta^3+\lambda g^2 s_\beta(3c_{2\beta}+2c_W^2+1)\\
&\quad +\frac{\lambda v A_\lambda\cos\beta}{32\pi^2}\left(-\lambda^2(13+3c_{4\beta})+\frac{g^2}{2}(5+4c_W^2-6c_{2\beta}+3c_{4\beta})\right)]\log\left(\frac{M_A^2}{M_Z^2}\right),\\
\Pi_{23} &= \frac{v\mu_{\rm eff}}{\mu_{\rm eff}}[12\lambda^3 c_\beta^3+\lambda g^2 c_\beta(-3c_{2\beta}+2c_W^2+1))\\
&\quad +\frac{\lambda v A_\lambda\sin\beta}{32\pi^2}\left(-\lambda^2(13+3c_{4\beta})+\frac{g^2}{2}(5+4c_W^2+6c_{2\beta}+3c_{4\beta})\right)]\log\left(\frac{M_A^2}{M_Z^2}\right),\\
\Pi_{33} &= \{\frac{4\lambda^2\mu_{\rm eff}^2}{16\pi^2}+\frac{\lambda A_\lambda}{128\pi^2}[\lambda(16A_\lambda(4+c_{4\beta})\\
&\quad +\lambda(64s^2+29v^2)s_{2\beta}+\lambda v^2 s_{6\beta})+g^2v^2s_{2\beta}(3+4c_W^2+c_{4\beta})]\}\log\left(\frac{M_A^2}{M_Z^2}\right)
\end{aligned} \tag{E.12}$$

If we set all NMSSM-specific parameters to zero in the above, we recover the

MSSM limit presented in [153, 154, 155, 156]. The soft term A_λ decouples at one-loop order and does not contribute to the SM Higgs quartic coupling, a property best seen in the basis of Eq. (III.16). The SM Higgs boson mass is then identified as

$$\begin{aligned}
\overline{M}_{hh}^2 &= \lambda^2 v^2 s_{2\beta}^2 + M_Z^2 c_{2\beta}^2 + \Pi_{hh}, \\
\Pi_{hh} &= \frac{v^2}{512\pi^2}[4\lambda^4(31 + 4c_{4\beta} - 3c_{8\beta}) + 4\lambda^2 g^2(-9 - 4c_W^2 + (4c_W^2 - 2)c_{4\beta} + 3c_{8\beta}) \\
&\quad -g^4(-11 + 8c_W^2 - 16c_W^4 + 8c_W^2 c_{4\beta} + 3c_{8\beta})] \log\left(\frac{M_A^2}{M_Z^2}\right)
\end{aligned} \tag{E.13}$$

A_λ is absent in the expression above, confirming its decoupling behavior at the one-loop level. Moreover, if we neglect the electroweak strength corrections, in the limit of large $\tan\beta$ we get

$$\lim_{\tan\beta \gg 1} \Pi_{hh} = \frac{\lambda^4 v^2}{4\pi^2} \log\left(\frac{M_A^2}{M_Z^2}\right), \tag{E.14}$$

in agreement with our heuristic estimate in Eq. (III.25).

(B) **Non-degenerate pseudoscalars: a simple case.**

We now show the effect of a split pseudoscalar spectrum on the radiative corrections. For simplicity, we assume the parameters $A_\lambda, \mu', m_3, m_S'$ vanish. We also neglect g-dependent terms in the one-loop piece, since the largest contributions to the SM Higgs quartic in our model arise from the λ-dependent terms. With these simplifications, the field-dependent squared mass matrices for the charged, CP-odd

and CP-even sectors are respectively given by

$$M_{11}^{\pm\,2} = m_{H_u}^2 + \lambda^2 h_s^2, \quad M_{12}^{\pm\,2} = \lambda^2 h_u h_d + M_{A_D}^2 s_\beta c_\beta, \quad M_{22}^{\pm\,2} = m_{H_d}^2 + \lambda^2 h_s^2; \tag{E.15}$$

$$\begin{aligned} M_{11}^{P\,2} &= m_{H_u}^2 + \lambda^2(h_d^2 + h_s^2), & M_{12}^{P\,2} &= M_{A_D}^2 s_\beta c_\beta, \\ M_{22}^{P\,2} &= m_{H_d}^2 + \lambda^2(h_u^2 + h_s^2), & M_{13}^{P\,2} &= 0, \\ M_{23}^{P\,2} &= 0, & M_{33}^{P\,2} &= m_S^2 + \lambda^2(h_u^2 + h_d^2); \end{aligned} \tag{E.16}$$

$$\begin{aligned} M_{11}^{S\,2} &= m_{H_u}^2 + \lambda^2(h_d^2 + h_s^2), & M_{12}^{S\,2} &= 2\lambda^2 h_u h_d - M_{A_D}^2 s_\beta c_\beta, \\ M_{22}^{S\,2} &= m_{H_d}^2 + \lambda^2(h_u^2 + h_s^2), & M_{13}^{S\,2} &= 2\lambda^2 h_u h_s, \\ M_{23}^{S\,2} &= 2\lambda^2 h_d h_s, & M_{33}^{S\,2} &= m_S^2 + \lambda^2(h_u^2 + h_d^2); \end{aligned} \tag{E.17}$$

Obtaining the eigenvalues of the charged and CP-odd systems is straightforward again, as we found in Case (A). To obtain the eigenvalues of the CP-even matrix, we solve for the roots of its characteristic equation (a cubic polynomial) as a power series in $M_{A_D}^2$ and $M_{A_S}^2$.

After collecting the one-loop contributions from all three sectors and summing over them, we obtain the CP-even mass matrix as

$$\begin{aligned} \left(\overline{M}_H^2\right)_{11} &= M_Z^2 s_\beta^2 + \overline{M}_{A_D}^2 c_\beta^2 + \Pi_{11}; & \left(\overline{M}_H^2\right)_{12} &= (2\lambda^2 v^2 - M_Z^2 - \overline{M}_{A_D}^2) s_\beta c_\beta + \Pi_{12}; \\ \left(\overline{M}_H^2\right)_{22} &= M_Z^2 c_\beta^2 + \overline{M}_{A_D}^2 + \Pi_{22}; & \left(\overline{M}_H^2\right)_{13} &= 2\lambda v \mu_{\text{eff}} s_\beta + \Pi_{13}; \\ \left(\overline{M}_H^2\right)_{23} &= 2\lambda v \mu_{\text{eff}} c_\beta + \Pi_{23}; & \left(\overline{M}_H^2\right)_{33} &= \overline{M}_{A_S}^2 + \Pi_{33} \end{aligned}$$

where

$$\begin{aligned}
\overline{M}^2_{A_D} &= M^2_{A_D}\left(1+\frac{\lambda^2}{8\pi^2}\log\left(\frac{M^2_{A_D}}{M^2_Z}\right)+\frac{\lambda^2}{8\pi^2}\frac{\mu^2_{\rm eff}}{M^2_{A_2}-M^2_{A_1}}\log\left(\frac{M^2_{A_S}}{M^2_{A_D}}\right)\right),\\
\overline{M}^2_{A_S} &= M^2_{A_S}
\end{aligned} \tag{E.18}$$

and

$$\begin{aligned}
\Pi_{11} &= \frac{\lambda^4 v^2}{16\pi^2}s^2_\beta\left[-(4c_{2\beta}+c_{4\beta}+1)\log\left(\frac{M^2_{A_D}}{M^2_Z}\right)+2\log\left(\frac{M^2_{A_S}}{M^2_Z}\right)\right],\\
\Pi_{12} &= \frac{2\lambda^4 v^2}{16\pi^2}s_\beta c_\beta(2+c_{4\beta})\log\left(\frac{M^2_{A_D}}{M^2_Z}\right),\\
\Pi_{22} &= \frac{\lambda^4 v^2}{16\pi^2}c^2_\beta\left[-(-4c_{2\beta}+c_{4\beta}+1)\log\left(\frac{M^2_{A_D}}{M^2_Z}\right)+2\log\left(\frac{M^2_{A_S}}{M^2_Z}\right)\right],\\
\Pi_{13} &= \frac{\lambda^3 v\mu_{\rm eff}}{16\pi^2}s_\beta\left[-(1+3c_{2\beta})\log\left(\frac{M^2_{A_D}}{M^2_Z}\right)+4\log\left(\frac{M^2_{A_S}}{M^2_Z}\right)\right],\\
\Pi_{23} &= \frac{\lambda^3 v\mu_{\rm eff}}{16\pi^2}c_\beta\left[-(1-3c_{2\beta})\log\left(\frac{M^2_{A_D}}{M^2_Z}\right)+4\log\left(\frac{M^2_{A_S}}{M^2_Z}\right)\right],\\
\Pi_{33} &= \frac{4\lambda^2\mu^2_{\rm eff}}{16\pi^2}\log\left(\frac{M^2_{A_D}}{M^2_Z}\right).
\end{aligned} \tag{E.19}$$

We make the following observations concerning the above expressions. First, notice that in the limit $M_{A_D}=M_{A_S}$, they are consistent with the results in Case (A) with $g, A_\lambda \to 0$. Second, we observe that corrections from the heavy doublet Higgses are β-dependent and those from the heavy singlet Higgses are not, as reflected in the co-efficients of $\log(M^2_{A_D}/M^2_Z)$ and $\log(M^2_{A_S}/M^2_Z)$ respectively. Third, there is a marked difference in contributions from the scales M_{A_D} and M_{A_S} to the SM Higgs quartic, which can be understood in the basis of Eq. (III.16). Rotating Π_{ij} into

this basis, the correction to the SM Higgs boson mass is identified as

$$\Pi_{hh} = \frac{\lambda^4 v^2 s_\beta}{16\pi^2}\left[\left(c_\beta^2(2+c_{4\beta}) - s_\beta^2(1+c_{4\beta}+4c_{2\beta})\right)\log\left(\frac{M_{A_D}^2}{M_Z^2}\right) + 2s_\beta^2\log\left(\frac{M_{A_S}^2}{M_Z^2}\right)\right].$$

The difference in the co-efficients of the logarithms are greatest at $\tan\beta \sim 1$, and smallest at $\tan\beta \gg 1$. In the latter limit, we obtain

$$\lim_{\tan\beta\gg 1}\Pi_{hh} = \frac{\lambda^4 v^2}{16\pi^2}\left[2\log\left(\frac{M_{A_D}^2}{M_Z^2}\right) + 2\log\left(\frac{M_{A_S}^2}{M_Z^2}\right)\right],$$

which is consistent with our qualitative estimate in Eq. (III.24).

APPENDIX F

INDIVIDUAL MODES OF SQUARK PRODUCTION

Here we describe the analytic behavior of the individual subprocesses $\tilde{u}_L\tilde{u}_L$ and $\tilde{u}_L\tilde{u}_R$ that are critical in understanding the results of Sec. IV.3.

(a) $\tilde{u}_L\tilde{u}_L$

This amplitude takes the form

$$\frac{-i\mathcal{T}}{g^2 C_F} = \left(c^2_{\theta_{\tilde{g}}} \frac{M_{\tilde{g}2}}{p^2 + M^2_{\tilde{g}2}} + s^2_{\theta_{\tilde{g}}} \frac{-M_{\tilde{g}1}}{p^2 + M^2_{\tilde{g}1}} \right) u_L u_L$$

where $C_F(= 4/3)$ is the appropriate Casimir invariant, u_L is a 2-component spinor denoting an incoming left-handed up quark with spinor indices suppressed, and the second term on the RHS has a minus sign since the mass of $\tilde{g}_1$ is the negative of $M_{\tilde{g}1}$.

In Case I ($M'_m = 0$), using the expressions for the mixing angle in Eq. (IV.9), expanding the amplitude to leading order in $p^2/M^2_{\tilde{g}}$, and then writing it in terms of $M_{\tilde{g}1}$ and $x = M_m/M_d$, we obtain

$$\begin{aligned} \frac{c^2_{\theta_{\tilde{g}}} M_{\tilde{g}2}}{p^2 + M^2_{\tilde{g}2}} - \frac{s^2_{\theta_{\tilde{g}}} M_{\tilde{g}1}}{p^2 + M^2_{\tilde{g}1}} \;&=\; \frac{p^2}{M^3_{\tilde{g}1}} x \left(\sqrt{x^2 + 4} - x \right)^3 \\ &\quad + \mathcal{O}(p^4/M^4_{\tilde{g}1}) \end{aligned} \tag{F.1}$$

In Case II ($M_m = M'_m$), the mixing angle is fixed $c^2_{\theta_{\tilde{g}}} = 1/2$. Expanding the amplitude to leading order in $p^2/M^2_{\tilde{g}}$, and then writing it in terms of $M_{\tilde{g}1}$ and $x = 2M_m/M_d = 2M'_m/M_d$, we obtain

$$\begin{aligned} &= -\frac{x}{M_{\tilde{g}1}(x+2)} + \frac{p^2x^3 + 12x}{M^3_{\tilde{g}1}(x+2)^3} \\ &\quad + \mathcal{O}(p^4/M^4_{\tilde{g}1}) \end{aligned} \tag{F.2}$$

In Case III ($M_m = 0$), again using Eq. (IV.9), expanding the amplitude to leading order in $p^2/M^2_{\tilde{g}}$, and then writing it in terms of $M_{\tilde{g}1}$ and $x' = M'_m/M_d$, we obtain

$$\begin{aligned} &= -\frac{x'(x' + \sqrt{x'^2+4})}{2M_{\tilde{g}1}} + \frac{p^2x(x'^2+2)(\sqrt{x'^2+4} - x')^3}{8M^3_{\tilde{g}1}} \\ &\quad + \mathcal{O}(p^4/M^4_{\tilde{g}1}) \end{aligned} \tag{F.3}$$

Clearly, all of these expressions vanish in the Dirac limit, $x \to 0$. The key difference is how quickly each expression turns on, and its asymptotic form as x gets large (by which we mean near 1). For example, at small x, Case I scales as $p^2x/M^3_{\tilde{g}1}$ whereas Case II and III scale as $x/M_{\tilde{g}1}$. This illustrates that Case I is further suppressed as the Majorana mass M_m is turned on. As a second example, when $x = 1$, Case I becomes $-p^2/M^3_{\tilde{g}1}$, Case II becomes $-1/(2M_{\tilde{g}1})$, and Case III becomes $(1 - \sqrt{5})/(2M_{\tilde{g}1})$. We have checked the the functional form of the squared amplitudes agrees well with our results shown in Figs. 4.5.a, 4.7.a and 4.9.a. Finally, we can recover the heavy pure Majorana case (the MSSM) where $c^2_\theta = 1$ and $M_{\tilde{g}1} = 0, M_{\tilde{g}2} = 5000$ GeV. In this case, the amplitude becomes $M_{\tilde{g}2}/(p^2 + M^2_{\tilde{g}2})$ where $\tilde{g}_2$ is interpreted as the Majorana gluino. This is obviously

suppressed by just one power of the gluino mass, giving a large cross section as indicated by the dashed red line in Figs. 4.5.a, 4.7.a and 4.9.a.

(b) $\tilde{u}_L \tilde{u}_R$

The amplitude for this subprocess is

$$\frac{-i\mathcal{T}}{g^2 C_F} = u_L^\alpha \left(c_{\theta_{\tilde{g}}}^2 \frac{p \cdot \sigma_{\alpha\dot{\beta}}}{p^2 + M_{\tilde{g}2}^2} + s_{\theta_{\tilde{g}}}^2 \frac{p \cdot \sigma_{\alpha\dot{\beta}}}{p^2 + M_{\tilde{g}1}^2} \right) (u_R^\dagger)^{\dot{\beta}} \tag{F.4}$$

where $u_R^\dagger$ denotes an incoming right-handed up quark. For $|p| \ll M_{\tilde{g}}$, this amplitude is suppressed by $1/M^2$. In Case I ($M_m' = 0$), using Eq. (IV.9), expanding the amplitude to leading order in $p^2/M_{\tilde{g}}^2$, and then writing in terms of $M_{\tilde{g}1}$ and $x = M_m/M_d$, we obtain

$$\begin{aligned} \frac{c_{\theta_{\tilde{g}}}^2}{p^2 + M_{\tilde{g}2}^2} &+ \frac{s_{\theta_{\tilde{g}}}^2}{p^2 + M_{\tilde{g}1}^2} \\ &= \frac{(x - \sqrt{x^2+4})^2}{4M_{\tilde{g}1}^2} + \mathcal{O}(p^2/M_{\tilde{g}1}^2) \end{aligned} \tag{F.5}$$

and in Case II ($M_m = M_m'$), writing in terms of $x = 2M_m/M_d = 2M_m'/M_d$ we obtain

$$\begin{aligned} \frac{c_{\theta_{\tilde{g}}}^2}{p^2 + M_{\tilde{g}2}^2} &+ \frac{s_{\theta_{\tilde{g}}}^2}{p^2 + M_{\tilde{g}1}^2} \\ &= \frac{x^2+4}{M_{\tilde{g}1}^2 (x+2)^2} + \mathcal{O}(p^2/M_{\tilde{g}1}^2) \end{aligned} \tag{F.6}$$

and in Case III ($M_m = 0$), writing in terms of $x' = M'_m/M_d$ we obtain

$$\begin{aligned} & \frac{c^2_{\theta_{\tilde{g}}}}{p^2 + M^2_{\tilde{g}2}} + \frac{s^2_{\theta_{\tilde{g}}}}{p^2 + M^2_{\tilde{g}1}} \\ = \; & \frac{(x'^2+1)(x' - \sqrt{x'^2+4})^2}{4M^2_{\tilde{g}1}} + \mathcal{O}(p^2/M^2_{\tilde{g}1})\,. \end{aligned} \tag{F.7}$$

These analytic expressions agree well with our results shown in Figs. 4.5.d, 4.7.d, and 4.9.d.

We observe in Fig. 4.5.d that the cross sections for $x = 0$ and for the pure Majorana gluino are identical in this mode. This is because in the pure Dirac case, $s^2_\theta = c^2_\theta = 0.5$ and $M_{\tilde{g}2} = M_{\tilde{g}1} = M$ (say), rendering the co-efficient of the spinors in the amplitude $p \cdot \sigma_{\alpha\dot{\beta}}/(p^2 + M^2)$, and in the pure Majorana limit, $c^2_\theta = 1$ and we once again have $p \cdot \sigma_{\alpha\dot{\beta}}/(p^2 + M^2)$ in the amplitude.

By inspecting the expressions in Eqs. (F.1), (F.2), (F.3) and comparing with their $\tilde{u}_L\tilde{u}_R$ counterparts, one can also see that (i) in Case I, $\tilde{u}_L\tilde{u}_L$ never catches up with $\tilde{u}_L\tilde{u}_R$ as x goes from 0 to 1, (ii) in Case II, it catches up at about $x = 0.2$, and (iii) in Case III, it catches up at a very small value of x. This is reflected in Figs. 4.5., 4.7. and 4.9. and hence in the respective contour plots.

APPENDIX G

"DIRAC" CHARGINOS

In this section we discuss the differences in the process $pp \to \tilde{u}_L \tilde{d}_L$ (and its equivalents for other generations) for winos that acquire a Majorana mass versus

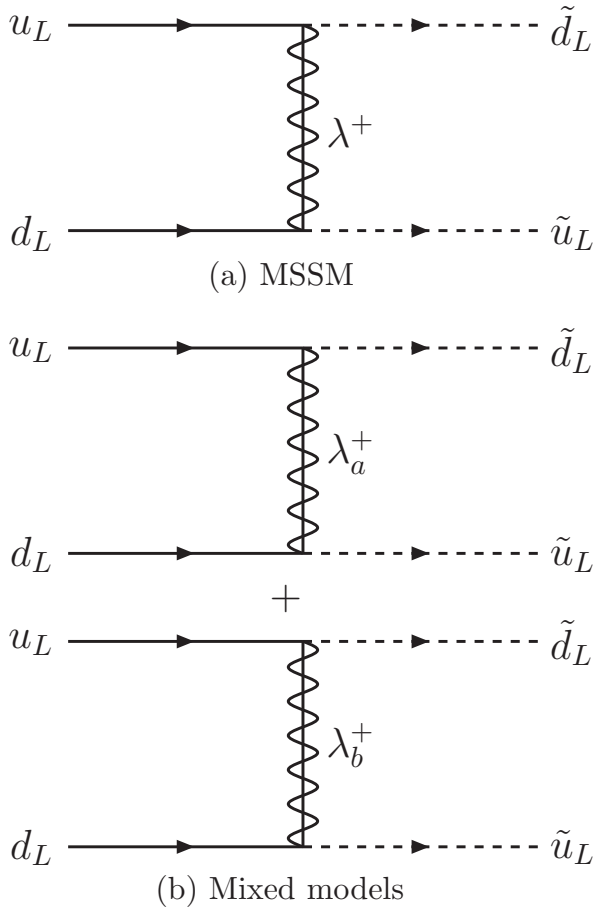

(a) MSSM

(b) Mixed models

Figure G.1: Feynman diagrams for the process $pp \to \tilde{u}_L \tilde{d}_L$ in MSSM and models with both Dirac and Majorana gaugino masses.

winos that acquire a Dirac mass. We note that some aspects of "Dirac" charginos have been discussed previously in [197]. We are specifically interested in the mediation of this process by t-channel charginos. In MSSM, this process is shown in the Feynman diagram in Fig. G.1(a). For mixed models with both Dirac and Majorana wino masses, the Feynman diagrams are given in Fig. G.1(b).

The presence of the extra chargino can be understood by studying the relevant mass terms in the Lagrangian, given in Weyl notation by

$$\mathcal{L}_{\tilde{w}\,\text{mass}} = \frac{1}{2} \begin{pmatrix} w & \psi \end{pmatrix} \begin{pmatrix} \hat{M}_m & \hat{M}_d \\ \hat{M}_d & \hat{M}'_m \end{pmatrix} \begin{pmatrix} w \\ \psi \end{pmatrix} + \text{h.c.} \tag{G.1}$$

where w is the wino, ψ is the triplet fermion partner, and the hatted quantities are to distinguish from the analogous parameters for the gluino. The notation is somewhat an abuse of notation, since the eigenvectors on the left- and right-hand sides of the mass matrix are identical for neutral components of the wino and triplet, whereas the eigenvectors for the charged fields must involve opposite electric charge components that pair w^+, ψ^+ with w^-, ψ^-. Also we have neglected the wino-Higgsino mixings that arise after electroweak symmetry breaking in order to simply understand the differences between a pure Dirac wino and a mixed wino with regard to squark production.

A mixed (Majorana and Dirac mass) neutral wino interacts in a way completely analogous with the gluino. The charged wino is distinct, since of course a chargino

is always a Dirac fermion. In the MSSM, the chargino acquires a Dirac mass by pairing the two charged winos $w^{\pm}$ with the "Majorana" mass term $M_2(w^+w^- + c.c.)$. In models with a Dirac mass for the chargino, the charged wino $w^{\pm}$ acquires mass with a charged fermion partner $\psi^{\mp}$. The mixing is analogous to the mixed gluino, where now

$$\begin{pmatrix} \lambda_a^{\pm} \\ \\ \lambda_b^{\pm} \end{pmatrix} = \begin{pmatrix} \cos\theta_{\tilde{w}} & \sin\theta_{\tilde{w}} \\ \\ -\sin\theta_{\tilde{w}} & \cos\theta_{\tilde{w}} \end{pmatrix} \begin{pmatrix} w^{\pm} \\ \\ \psi^{\pm} \end{pmatrix} \tag{G.2}$$

with the same form of the mass eigenvalues and mixing angles as Eqs. (IV.10) and (IV.9). Since the wino couples to quarks and squarks, while the triplet partner does not, the usual wino interaction terms

$$\mathcal{L} = -g_2 \ (\tilde{u}^*_{L,i}\lambda^+ d_{L,i} + \tilde{d}^*_{L,i}\lambda^- u_{R,i}) + \text{h.c.} \tag{G.3}$$

become

$$\begin{aligned} \mathcal{L} = -g_2 \ (&\tilde{u}^*_{L,i}\lambda^+_a \cos\theta_{\tilde{w}} \ d_{L,i} + \tilde{u}^*_{L,i}\lambda^+_b \sin\theta_{\tilde{w}} \ d_{L,i} \\ &+\tilde{d}^*_{L,i}\lambda^-_a \cos\theta_{\tilde{w}} \ u_{R,i} + \tilde{d}^*_{L,i}\lambda^-_b \sin\theta_{\tilde{w}} \ u_{R,i}) + \text{h.c.} \end{aligned} \tag{G.4}$$

Interestingly, in the pure Dirac mass limit where $\hat{M}_m, \hat{M}'_m = 0$, the mixing angles become maximal, and then for the same reasons that $qq \to \tilde{q}_L\tilde{q}_L$ vanishes for a Dirac gluino, one can show that $qq' \to \tilde{q}_L\tilde{q'}_L$ vanishes for a Dirac wino. We did not utilize this observation in our studies, since our main focus was the interference between Majorana wino and bino with a Dirac gluino.

APPENDIX H

14 TeV EXTRAPOLATION

In this appendix we extend our results to $\sqrt{s} = 14$ TeV at the LHC. Given that the current LHC bound on the squark mass is roughly 800 GeV (with a massless LSP), we illustrate the $\sqrt{s} = 14$ TeV results for $M_{\tilde{q}} = 1200$ GeV. The contour plots in Fig. H.1, parameterized analogously to those of Sec. IV.3.1, show the changes one would observe for this squark mass. Specifically, when compared to Figs. 4.3., 4.6. and 4.8., we find that the cross sections and ratios increase for all three scenarios. Moreover, at 14 TeV the s-channel gluon-mediated diagrams producing squark–anti-squark dominate over squark-squark production at all gluino masses shown in the plots, which was not the case at $\sqrt{s} = 8$ TeV.

Figure H.1: (next page) LEFT: Contours of the ratio of the production cross section of the first two squark generations at LHC with $\sqrt{s} = 14$ TeV (extrapolated) in our model to the cross sections in MSSM. RIGHT: Contours of the cross sections themselves (at leading order), in pb, at LHC with $\sqrt{s} = 14$ TeV. The squark mass here is 1200 GeV and the parameterization of the axes is similar to Figs. 4.3., 4.6. and 4.8.. The critical features are explained in the text.

(a) $M'_m = 0$: ratios

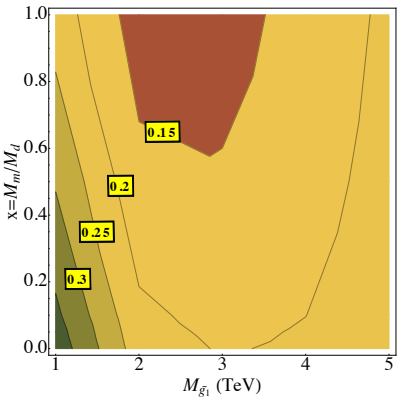

(b) $M'_m = 0$: $d\sigma$

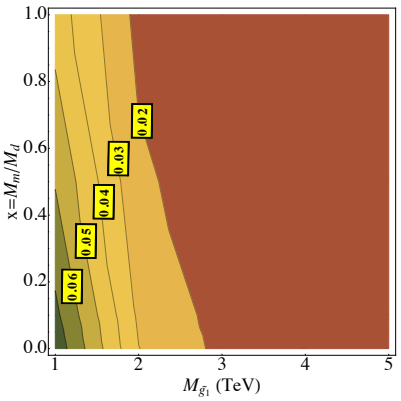

(c) $M_m = M'_m$: ratios

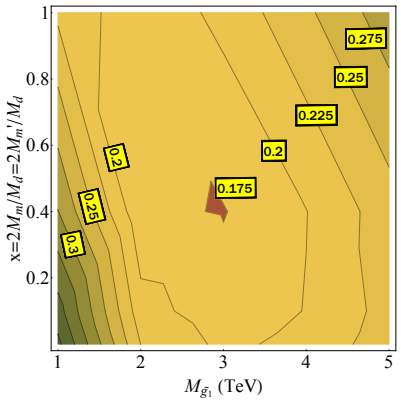

(d) $M_m = M'_m$: $d\sigma$

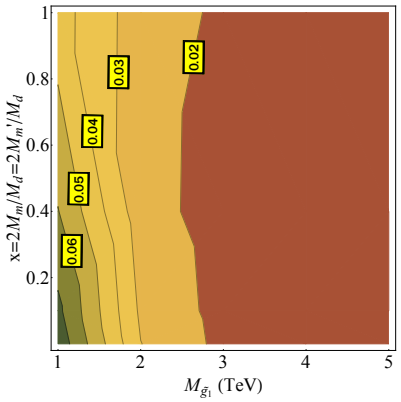

(e) $M_m = 0$: ratios

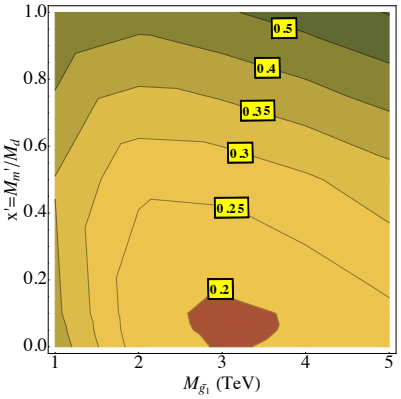

(f) $M_m = 0$: $d\sigma$

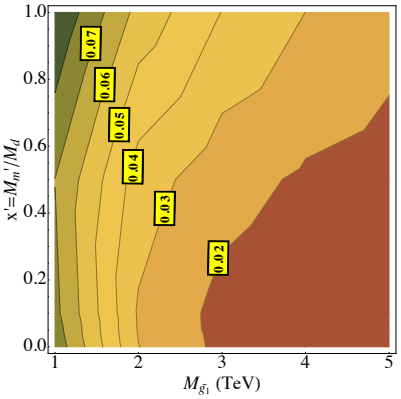

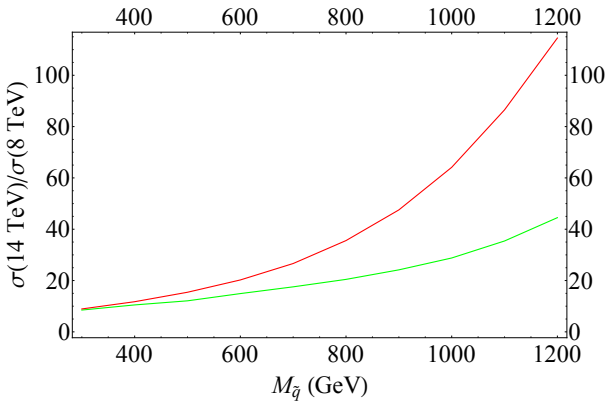

Figure H.2: Ratios of squark production cross sections at $\sqrt{s} = 14$ TeV to those at $\sqrt{s} = 8$ TeV. Here, red: QCD-only Dirac gluino case, green: electroweakinos at their MEI values, which provides an upper bound on the impact of electroweakinos in the presence of a Dirac gluino.

This implies that the features of the ratio and cross section contours for $M_{\tilde{q}} =$ 1200 GeV at $\sqrt{s} = 14$ TeV resemble their equivalents for, say, $M_{\tilde{q}} = 800$ GeV at $\sqrt{s} = 8$ TeV, and this is the trend observed in all of the plots in Fig. H.1.

As for the impact of the mixed electroweak gauginos, a comparison with the $\sqrt{s} = 8$ TeV LHC results is presented in Fig. H.2, where the ratios of squark production cross section at $\sqrt{s} = 14$ TeV to those at $\sqrt{s} = 8$ TeV have been plotted. The green curve indicates electroweakinos at their MEI values while the red curve shows the QCD-only Dirac gluino case. The gluino mass is again taken to be 5 TeV. Here again, we emphasize that the MEI value is not a special point. It merely sets an upper bound on the impact of electroweakinos on a pure Dirac gluino scenario. We note two features: (a) The ratios increase as the squark mass increases. This

happens because at $\sqrt{s} = 14$ TeV, the cross section is dominated by squark–anti-squark production, unlike the case at $\sqrt{s} = 8$ TeV, where at high squark masses there is competition between squark–anti-squark and squark-squark modes; (b) The green curve increases at a slower rate with respect to squark mass than the red curve. The impact of the electroweakinos on the total cross section is by affecting t-channel (mainly left-handed) squark-pair production, and such an impact would weaken as $\sqrt{s}$ is increased. This causes squark–anti-squark production through gluon fusion diagrams and s-channel gluon-mediated subprocesses to dominate. These features show that the impact of the electroweakinos at their MEI values are expected to be much less for LHC operating at 14 TeV.

REFERENCES CITED

[1] S. Weinberg, Phys. Rev. Lett. **19**, 1264 (1967).

[2] G. 't Hooft, NATO Sci. Ser. B **59**, 135 (1980).

[3] S. Weinberg, Phys. Rev. D **13**, 974 (1976).

[4] E. Gildener, Phys. Rev. D **14**, 1667 (1976).

[5] S. Weinberg, Phys. Rev. D **19**, 1277 (1979).

[6] L. Susskind, Phys. Rev. D **20**, 2619 (1979).

[7] P. A. R. Ade *et al.* [Planck Collaboration], arXiv:1502.01589 [astro-ph.CO].

[8] P. Tisserand *et al.* [EROS-2 Collaboration], Astron. Astrophys. **469**, 387 (2007) [astro-ph/0607207].

[9] D. S. Graff and K. Freese, Astrophys. J. **456**, L49 (1996) [astro-ph/9507097].

[10] J. Najita, G. Tiede and J. Carr, Astrophys. J. **541**, 977 (2000) [astro-ph/0005290].

[11] M. Davis, G. Efstathiou, C. S. Frenk and S. D. M. White, Astrophys. J. **292**, 371 (1985).

[12] C. J. Copi, D. N. Schramm and M. S. Turner, Science **267**, 192 (1995) [astro-ph/9407006].

[13] V. Springel, S. D. M. White, A. Jenkins, C. S. Frenk, N. Yoshida, L. Gao, J. Navarro and R. Thacker *et al.*, Nature **435**, 629 (2005) [astro-ph/0504097].

[14] http://chandra.harvard.edu/photo/2015/dark/ [astro-ph/1409.1598]

[15] https://twiki.cern.ch/twiki/bin/view/AtlasPublic/ExoticsPublicResults

[16] https://twiki.cern.ch/twiki/bin/view/CMSPublic/PhysicsResultsEXO

[17] G. D'Amico, M. Kamionkowski and K. Sigurdson, arXiv:0907.1912 [astro-ph.CO].

[18] D. S. Akerib *et al.* [LUX Collaboration], Phys. Rev. Lett. **112**, 091303 (2014) [arXiv:1310.8214 [astro-ph.CO]].

[19] J. Billard, L. Strigari and E. Figueroa-Feliciano, Phys. Rev. D **89**, no. 2, 023524 (2014) [arXiv:1307.5458 [hep-ph]].

[20] S. R. Coleman and J. Mandula, "All Possible Symmetries of the S Matrix" Phys. Rev. **159**, 1251 (1967).

[21] J. Wess and B. Zumino, Nucl. Phys. B **70**, 39 (1974).

[22] R. Haag, J. T. Lopuszanski and M. Sohnius, "All Possible Generators of Supersymmetries of the S Matrix," Nucl. Phys. B **88**, 257 (1975).

[23] S. Dimopoulos and S. Raby, Nucl. Phys. B **192**, 353 (1981).

[24] E. Witten, Nucl. Phys. B **188**, 513 (1981).

[25] M. Dine, W. Fischler and M. Srednicki, Nucl. Phys. B **189**, 575 (1981).

[26] N. Sakai, Z. Phys. C **11**, 153 (1981).

[27] R. K. Kaul and P. Majumdar, Nucl. Phys. B **199**, 36 (1982).

[28] S. Dimopoulos, S. Raby and F. Wilczek, Phys. Rev. D **24**, 1681 (1981).

[29] L. E. Ibanez and G. G. Ross, Phys. Lett. B **105**, 439 (1981).

[30] M. B. Einhorn and D. R. T. Jones, Nucl. Phys. B **196**, 475 (1982).

[31] W. J. Marciano and G. Senjanovic, Phys. Rev. D **25**, 3092 (1982).

[32] H. Goldberg, Phys. Rev. Lett. **50**, 1419 (1983) [Phys. Rev. Lett. **103**, 099905 (2009)].

[33] J. R. Ellis, J. S. Hagelin, D. V. Nanopoulos, K. A. Olive and M. Srednicki, Nucl. Phys. B **238**, 453 (1984).

[34] S. P. Martin, Adv. Ser. Direct. High Energy Phys. **21**, 1 (2010) [hep-ph/9709356].

[35] http : //physicslearning2.colorado.edu/tasi/tasi$_2$011/tasi$_2$011.htm

[36] L. Girardello and M. T. Grisaru, Nucl. Phys. B **194**, 65 (1982).

[37] S. Dimopoulos and H. Georgi, Nucl. Phys. B **193**, 150 (1981).

[38] https://twiki.cern.ch/twiki/bin/view/CMSPublic/SUSYSMSSummaryPlots8TeV

[39] Q. H. Cao, C. R. Chen, C. S. Li and H. Zhang, JHEP **1108**, 018 (2011) [arXiv:0912.4511 [hep-ph]].

[40] M. Beltran, D. Hooper, E. W. Kolb, Z. A. C. Krusberg and T. M. P. Tait, JHEP **1009**, 037 (2010) [arXiv:1002.4137 [hep-ph]].

[41] J. Goodman, M. Ibe, A. Rajaraman, W. Shepherd, T. M. P. Tait and H. B. Yu, Phys. Lett. B **695**, 185 (2011) [arXiv:1005.1286 [hep-ph]].

[42] Y. Bai, P. J. Fox and R. Harnik, JHEP **1012**, 048 (2010) [arXiv:1005.3797 [hep-ph]].

[43] J. Goodman, M. Ibe, A. Rajaraman, W. Shepherd, T. M. P. Tait and H. B. Yu, Phys. Rev. D **82**, 116010 (2010) [arXiv:1008.1783 [hep-ph]].

[44] P. J. Fox, R. Harnik, J. Kopp and Y. Tsai, Phys. Rev. D **84**, 014028 (2011) [arXiv:1103.0240 [hep-ph]].

[45] A. Rajaraman, W. Shepherd, T. M. P. Tait and A. M. Wijangco, Phys. Rev. D **84**, 095013 (2011) [arXiv:1108.1196 [hep-ph]].

[46] P. J. Fox, R. Harnik, J. Kopp and Y. Tsai, Phys. Rev. D **85**, 056011 (2012) [arXiv:1109.4398 [hep-ph]].

[47] K. Cheung, P. Y. Tseng, Y. L. S. Tsai and T. C. Yuan, JCAP **1205**, 001 (2012) [arXiv:1201.3402 [hep-ph]].

[48] J. Goodman and W. Shepherd, arXiv:1111.2359 [hep-ph].

[49] I. M. Shoemaker and L. Vecchi, Phys. Rev. D **86**, 015023 (2012) [arXiv:1112.5457 [hep-ph]].

[50] S. Chang, R. Edezhath, J. Hutchinson and M. Luty, Phys. Rev. D **89**, 015011 (2014) [arXiv:1307.8120 [hep-ph]].

[51] H. An, L. T. Wang and H. Zhang, Phys. Rev. D **89**, 115014 (2014) [arXiv:1308.0592 [hep-ph]].

[52] Y. Bai and J. Berger, JHEP **1311**, 171 (2013) [arXiv:1308.0612 [hep-ph]].

[53] A. DiFranzo, K. I. Nagao, A. Rajaraman and T. M. P. Tait, JHEP **1311**, 014 (2013) [arXiv:1308.2679 [hep-ph]].

[54] M. Papucci, A. Vichi and K. M. Zurek, arXiv:1402.2285 [hep-ph].

[55] Y. Bai and J. Berger, JHEP **1408**, 153 (2014) [arXiv:1402.6696 [hep-ph]].

[56] S. Chang, R. Edezhath, J. Hutchinson and M. Luty, Phys. Rev. D **90**, 015011 (2014) [arXiv:1402.7358 [hep-ph]].

[57] M. Garny, A. Ibarra, S. Rydbeck and S. Vogl, JHEP **1406**, 169 (2014) [arXiv:1403.4634 [hep-ph]].

[58] O. Buchmueller, M. J. Dolan, S. A. Malik and C. McCabe, arXiv:1407.8257 [hep-ph].

[59] J. Abdallah, A. Ashkenazi, A. Boveia, G. Busoni, A. De Simone, C. Doglioni, A. Efrati and E. Etzion *et al.*, arXiv:1409.2893 [hep-ph].

[60] S. Dittmaier and M. Huber, JHEP **1001**, 060 (2010) [arXiv:0911.2329 [hep-ph]].

[61] A. Freitas and S. Westhoff, arXiv:1408.1959 [hep-ph].

[62] P. Harris, V. V. Khoze, M. Spannowsky and C. Williams, arXiv:1411.0535 [hep-ph].

[63] G. Aad *et al.* [ATLAS Collaboration], arXiv:1407.2410 [hep-ex].

[64] G. Aad *et al.* [ATLAS Collaboration], arXiv:1405.4123 [hep-ex].

[65] S. Chatrchyan *et al.* [CMS Collaboration],Phys. Lett. B **720**, 63 (2013) H. An, L. -T. Wang and H. Zhang, [arXiv:1212.6175 [hep-ex]].

[66] CMS Collaboration, CMS-PAS-EXO-12-020.

[67] For example, see
`http://www.nps.gov/care/naturescience/index.htm`

[68] G. Aad *et al.* [ATLAS Collaboration], JHEP **1301**, 029 (2013) [arXiv:1210.1718 [hep-ex]].

[69] G. D. Kribs and N. Raj, Phys. Rev. D **89**, 055011 (2014) [arXiv:1307.7197 [hep-ph]].

[70] K. Hsieh, Phys. Rev. D **77**, 015004 (2008) [arXiv:0708.3970 [hep-ph]].

[71] A. De Simone, V. Sanz and H. P. Sato, Phys. Rev. Lett. **105**, 121802 (2010) [arXiv:1004.1567 [hep-ph]].

[72] S. P. Martin, Phys. Rev. D **61**, 035004 (2000) [hep-ph/9907550].

[73] J. Kile and A. Soni, Phys. Rev. D **84**, 035016 (2011) [arXiv:1104.5239 [hep-ph]].

[74] B. Batell, J. Pradler and M. Spannowsky, JHEP **1108**, 038 (2011) [arXiv:1105.1781 [hep-ph]].

[75] P. Agrawal, S. Blanchet, Z. Chacko and C. Kilic, Phys. Rev. D **86**, 055002 (2012) [arXiv:1109.3516 [hep-ph]].

[76] P. Agrawal, M. Blanke and K. Gemmler, JHEP **1410**, 72 (2014) [arXiv:1405.6709 [hep-ph]].

[77] J. Kile, A. Kobach and A. Soni, arXiv:1411.1407 [hep-ph].

[78] D. S. M. Alves, J. Galloway, J. T. Ruderman and J. R. Walsh, arXiv:1410.6810 [hep-ph].

[79] E. Remiddi, Helv. Phys. Acta **54**, 364 (1982).

[80] A. D. Martin, W. J. Stirling, R. S. Thorne and G. Watt, Eur. Phys. J. C **63**, 189 (2009) [arXiv:0901.0002 [hep-ph]].

[81] S. Chatrchyan *et al.* [CMS Collaboration], Phys. Lett. B **718**, 752 (2013) [arXiv:1207.3973 [hep-ex]].

[82] J. C. Collins and D. E. Soper, Phys. Rev. D **16**, 2219 (1977).

[83] Y. Bai and W. Y. Keung, arXiv:1407.6355 [hep-ph].

[84] S. Chatrchyan *et al.* [CMS Collaboration], JHEP **1406**, 055 (2014) [arXiv:1402.4770 [hep-ex]].

[85] G. Aad *et al.* [ATLAS Collaboration], JHEP **1409**, 176 (2014) [arXiv:1405.7875 [hep-ex]].

[86] E. Aprile *et al.* [XENON100 Collaboration], Phys. Rev. Lett. **109**, 181301 (2012) [arXiv:1207.5988 [astro-ph.CO]].

[87] E. Aprile *et al.* [XENON100 Collaboration], Phys. Rev. Lett. **111**, no. 2, 021301 (2013) [arXiv:1301.6620 [astro-ph.CO]].

[88] P. A. R. Ade *et al.* [Planck Collaboration], Astron. Astrophys. (2014) [arXiv:1303.5076 [astro-ph.CO]].

[89] F. Jegerlehner and A. Nyffeler, Phys. Rept. **477**, 1 (2009) [arXiv:0902.3360 [hep-ph]].

[90] S. Schael *et al.* [ALEPH and DELPHI and L3 and OPAL and LEP Electroweak Collaborations], Phys. Rept. **532**, 119 (2013) [arXiv:1302.3415 [hep-ex]].

[91] J. Alwall, M. Herquet, F. Maltoni, O. Mattelaer and T. Stelzer, JHEP **1106**, 128 (2011) [arXiv:1106.0522 [hep-ph]].

[92] J. Pumplin, D. R. Stump, J. Huston, H. L. Lai, P. M. Nadolsky and W. K. Tung, JHEP **0207**, 012 (2002) [hep-ph/0201195].

[93] K. Griest and D. Seckel, Phys. Rev. D **43**, 3191 (1991).

[94] P. Agrawal, Z. Chacko and C. B. Verhaaren, JHEP **1408**, 147 (2014) [arXiv:1402.7369 [hep-ph]].

[95] A. Hook and A. Katz, JHEP **1409**, 175 (2014) [arXiv:1407.2607 [hep-ph]].

[96] T. Cohen, T. Golling, M. Hance, A. Henrichs, K. Howe, J. Loyal, S. Padhi and J. G. Wacker, JHEP **1404**, 117 (2014) [arXiv:1311.6480 [hep-ph]].

[97] M. Low and L. T. Wang, JHEP **1408**, 161 (2014) [arXiv:1404.0682 [hep-ph]].

[98] S. Gori, S. Jung, L. T. Wang and J. D. Wells, arXiv:1410.6287 [hep-ph].

[99] G. Salam and A. Weiler http://collider-reach.web.cern.ch/collider-reach/

[100] H. P. Nilles, Phys. Rept. **110**, 1 (1984).

[101] G. Aad *et al.* [ATLAS Collaboration], Phys. Lett. B **716**, 1 (2012) [arXiv:1207.7214 [hep-ex]].

[102] S. Chatrchyan *et al.* [CMS Collaboration], Phys. Lett. B **716**, 30 (2012) [arXiv:1207.7235 [hep-ex]].

[103] Y. Okada, M. Yamaguchi and T. Yanagida, Prog. Theor. Phys. **85**, 1 (1991).

[104] H. E. Haber and R. Hempfling, Phys. Rev. Lett. **66**, 1815 (1991).

[105] J. R. Ellis, G. Ridolfi and F. Zwirner, Phys. Lett. B **257**, 83 (1991).

[106] R. Barbieri, M. Frigeni and F. Caravaglios, Phys. Lett. B **258**, 167 (1991).

[107] J. A. Casas, J. R. Espinosa, M. Quiros and A. Riotto, Nucl. Phys. B **436**, 3 (1995) [Erratum-ibid. B **439**, 466 (1995)] [hep-ph/9407389].

[108] M. S. Carena, J. R. Espinosa, M. Quiros and C. E. M. Wagner, Phys. Lett. B **355**, 209 (1995) [hep-ph/9504316].

[109] M. S. Carena, M. Quiros and C. E. M. Wagner, Nucl. Phys. B **461**, 407 (1996) [hep-ph/9508343].

[110] H. E. Haber, R. Hempfling and A. H. Hoang, Z. Phys. C **75**, 539 (1997) [hep-ph/9609331].

[111] S. Heinemeyer, W. Hollik and G. Weiglein, Eur. Phys. J. C **9**, 343 (1999) [hep-ph/9812472].

[112] M. S. Carena, H. E. Haber, S. Heinemeyer, W. Hollik, C. E. M. Wagner and G. Weiglein, Nucl. Phys. B **580**, 29 (2000) [hep-ph/0001002].

[113] S. P. Martin, Phys. Rev. D **67**, 095012 (2003) [hep-ph/0211366].

[114] G. G. Ross and K. Schmidt-Hoberg, Nucl. Phys. B **862**, 710 (2012) [arXiv:1108.1284 [hep-ph]].

[115] R. Harnik, G. D. Kribs, D. T. Larson and H. Murayama, Phys. Rev. D **70**, 015002 (2004) [hep-ph/0311349].

[116] S. Chang, C. Kilic and R. Mahbubani, Phys. Rev. D **71**, 015003 (2005) [hep-ph/0405267].

[117] A. Delgado and T. M. P. Tait, JHEP **0507**, 023 (2005) [hep-ph/0504224].

[118] N. Craig, D. Stolarski and J. Thaler, JHEP **1111**, 145 (2011) [arXiv:1106.2164 [hep-ph]].

[119] E. Hardy, J. March-Russell and J. Unwin, JHEP **1210**, 072 (2012) [arXiv:1207.1435 [hep-ph]].

[120] L. Randall and M. Reece, JHEP **1308**, 088 (2013) [arXiv:1206.6540 [hep-ph]].

[121] R. Barbieri, L. J. Hall, Y. Nomura and V. S. Rychkov, Phys. Rev. D **75**, 035007 (2007) [hep-ph/0607332].

[122] J. Cao and J. M. Yang, Phys. Rev. D **78**, 115001

[123] R. Franceschini and S. Gori, JHEP **1105**, 084 (2011)

[124] L. J. Hall, D. Pinner and J. T. Ruderman, JHEP **1204**, 131 (2012) [arXiv:1112.2703 [hep-ph]].

[125] S. Kanemura, T. Shindou and T. Yamada, Phys. Rev. D **86**, 055023 (2012) [arXiv:1206.1002 [hep-ph]].

[126] M. Perelstein and B. Shakya, Phys. Rev. D **88**, no. 7, 075003 (2013) [arXiv:1208.0833 [hep-ph]].

[127] B. Kyae and C. S. Shin, Phys. Rev. D **88**, no. 1, 015011 (2013) [arXiv:1212.5067 [hep-ph]].

[128] T. Gherghetta, B. von Harling, A. D. Medina and M. A. Schmidt, JHEP **1302**, 032 (2013) [arXiv:1212.5243 [hep-ph]].

[129] R. Barbieri, D. Buttazzo, K. Kannike, F. Sala and A. Tesi, Phys. Rev. D **87**, no. 11, 115018 (2013) [arXiv:1304.3670 [hep-ph]].

[130] M. Farina, M. Perelstein and B. Shakya, JHEP **1404**, 108 (2014) [arXiv:1310.0459 [hep-ph]].

[131] T. Gherghetta, B. von Harling, A. D. Medina and M. A. Schmidt, JHEP **1404**, 180 (2014) [arXiv:1401.8291 [hep-ph]].

[132] S. Zheng, arXiv:1405.6907 [hep-ph].

[133] J. Cao, D. Li, L. Shang, P. Wu and Y. Zhang, JHEP **1412**, 026 (2014) [arXiv:1409.8431 [hep-ph]].

[134] U. Ellwanger and C. Hugonie, Phys. Lett. B **623**, 93 (2005) [hep-ph/0504269].

[135] XENON1T collaboration Collaboration, E. Aprile, The XENON1T Dark Matter Search Experiment, arXiv:1206.6288

[136] C. Csaki, Y. Shirman and J. Terning, Phys. Rev. D **84**, 095011 (2011) [arXiv:1106.3074 [hep-ph]].

[137] C. Csaki, L. Randall and J. Terning, Phys. Rev. D **86**, 075009 (2012) [arXiv:1201.1293 [hep-ph]].

[138] C. Cheung, L. J. Hall, D. Pinner and J. T. Ruderman, JHEP **1305**, 100 (2013) [arXiv:1211.4873 [hep-ph]].

[139] U. Ellwanger, C. Hugonie and A. M. Teixeira, Phys. Rept. **496**, 1 (2010) [arXiv:0910.1785 [hep-ph]].

[140] S. P. Martin, Adv. Ser. Direct. High Energy Phys. **21**, 1 (2010) [hep-ph/9709356].

[141] S. Dimopoulos and G. F. Giudice, Phys. Lett. B **357**, 573 (1995) [hep-ph/9507282].

[142] G. D. Kribs, A. Martin and A. Menon, Phys. Rev. D **88**, 035025 (2013) [arXiv:1305.1313 [hep-ph]].

[143] ATLAS Collaboration, ATLAS-CONF-2013-037

[144] ATLAS Collaboration, ATLAS-CONF-2013-024

[145] CMS Collaboration, CMS-PAS-SUS-12-023

[146] S. P. Martin, K. Tobe and J. D. Wells, Phys. Rev. D **71**, 073014 (2005) [hep-ph/0412424].

[147] K. A. Olive *et al.* [Particle Data Group Collaboration], Chin. Phys. C **38**, 090001 (2014).

[148] http://lepsusy.web.cern.ch/lepsusy/ www/inoslowdmsummer02/charginolowdm_pub.html

[149] http://lepsusy.web.cern.ch/lepsusy/ www/sleptons_summer04/slep_final.html

[150] N. Arkani-Hamed, A. Delgado and G. F. Giudice, Nucl. Phys. B **741**, 108 (2006) [hep-ph/0601041].

[151] N. Zhou, Z. Khechadoorian, D. Whiteson and T. M. P. Tait, Phys. Rev. Lett. **113**, 151801 (2014) [arXiv:1408.0011 [hep-ph]].

[152] K. Griest and D. Seckel, Phys. Rev. D **43**, 3191 (1991).

[153] H. E. Haber and R. Hempfling, Phys. Rev. D **48**, 4280 (1993) [hep-ph/9307201].

[154] A. V. Gladyshev and D. I. Kazakov, Mod. Phys. Lett. A **10**, 3129 (1995) [hep-ph/9411209].

[155] D. M. Pierce, J. A. Bagger, K. T. Matchev and R. j. Zhang, Nucl. Phys. B **491**, 3 (1997) [hep-ph/9606211].

[156] A. Dobado, M. J. Herrero, W. Hollik and S. Penaranda, Phys. Rev. D **66**, 095016 (2002) [hep-ph/0208014].

[157] ATLAS Collaboration, ATLAS-CONF-2013-047.

[158] CMS Collaboration, CMS-SUS-13-012.

[159] G. D. Kribs and A. Martin, Phys. Rev. D **85**, 115014 (2012) [arXiv:1203.4821 [hep-ph]].

[160] P. J. Fox, A. E. Nelson and N. Weiner, JHEP **0208**, 035 (2002) [hep-ph/0206096].

[161] P. Fayet, Phys. Lett. B **78**, 417 (1978).

[162] J. Polchinski and L. Susskind, Phys. Rev. D **26**, 3661 (1982).

[163] L. J. Hall and L. Randall, Nucl. Phys. B **352**, 289 (1991).

[164] A. E. Nelson, N. Rius, V. Sanz and M. Unsal, JHEP **0208**, 039 (2002) [hep-ph/0206102].

[165] Z. Chacko, P. J. Fox, H. Murayama, Nucl. Phys. **B706**, 53-70 (2005). [hep-ph/0406142].

[166] L. M. Carpenter, P. J. Fox and D. E. Kaplan, hep-ph/0503093.

[167] I. Antoniadis, A. Delgado, K. Benakli, M. Quiros and M. Tuckmantel, Phys. Lett. B **634**, 302 (2006) [hep-ph/0507192].

[168] Y. Nomura, D. Poland and B. Tweedie, Nucl. Phys. B **745**, 29 (2006) [hep-ph/0509243].

[169] I. Antoniadis, K. Benakli, A. Delgado and M. Quiros, Adv. Stud. Theor. Phys. **2**, 645 (2008) [hep-ph/0610265].

[170] G. D. Kribs, E. Poppitz and N. Weiner, Phys. Rev. D **78**, 055010 (2008) [arXiv:0712.2039 [hep-ph]].

[171] S. D. L. Amigo, A. E. Blechman, P. J. Fox and E. Poppitz, JHEP **0901**, 018 (2009) [arXiv:0809.1112 [hep-ph]].

[172] K. Benakli and M. D. Goodsell, Nucl. Phys. B **816**, 185 (2009) [arXiv:0811.4409 [hep-ph]].

[173] A. E. Blechman, Mod. Phys. Lett. A **24**, 633 (2009) [arXiv:0903.2822 [hep-ph]].

[174] L. M. Carpenter, JHEP **1209**, 102 (2012) [arXiv:1007.0017 [hep-th]].

[175] G. D. Kribs, T. Okui and T. S. Roy, Phys. Rev. D **82**, 115010 (2010) [arXiv:1008.1798 [hep-ph]].

[176] S. Abel and M. Goodsell, JHEP **1106**, 064 (2011) [arXiv:1102.0014 [hep-th]].

[177] C. Frugiuele and T. Gregoire, Phys. Rev. D **85**, 015016 (2012) [arXiv:1107.4634 [hep-ph]].

[178] H. Itoyama and N. Maru, Int. J. Mod. Phys. A **27**, 1250159 (2012) [arXiv:1109.2276 [hep-ph]].

[179] J. Unwin, Phys. Rev. D **86**, 095002 (2012) [arXiv:1210.4936 [hep-ph]].

[180] S. Abel and D. Busbridge, arXiv:1306.6323 [hep-th].

[181] J. Hisano, M. Nagai, T. Naganawa and M. Senami, Phys. Lett. B **644**, 256 (2007) [hep-ph/0610383].

[182] K. Hsieh, Phys. Rev. D **77**, 015004 (2008) [arXiv:0708.3970 [hep-ph]].

[183] A. E. Blechman and S. -P. Ng, JHEP **0806**, 043 (2008) [arXiv:0803.3811 [hep-ph]].

[184] G. D. Kribs, A. Martin and T. S. Roy, JHEP **0901**, 023 (2009) [arXiv:0807.4936 [hep-ph]].

[185] S. Y. Choi, M. Drees, A. Freitas and P. M. Zerwas, Phys. Rev. D **78**, 095007 (2008) [arXiv:0808.2410 [hep-ph]].

[186] T. Plehn and T. M. P. Tait, J. Phys. G G **36**, 075001 (2009) [arXiv:0810.3919 [hep-ph]].

[187] R. Harnik and G. D. Kribs, Phys. Rev. D **79**, 095007 (2009) [arXiv:0810.5557 [hep-ph]].

[188] S. Y. Choi, M. Drees, J. Kalinowski, J. M. Kim, E. Popenda and P. M. Zerwas, Phys. Lett. B **672**, 246 (2009) [arXiv:0812.3586 [hep-ph]].

[189] G. D. Kribs, A. Martin and T. S. Roy, JHEP **0906**, 042 (2009) [arXiv:0901.4105 [hep-ph]].

[190] G. Belanger, K. Benakli, M. Goodsell, C. Moura and A. Pukhov, JCAP **0908**, 027 (2009) [arXiv:0905.1043 [hep-ph]].

[191] K. Benakli and M. D. Goodsell, Nucl. Phys. B **830**, 315 (2010) [arXiv:0909.0017 [hep-ph]].

[192] A. Kumar, D. Tucker-Smith and N. Weiner, in the MRSSM," JHEP **1009**, 111 (2010) [arXiv:0910.2475 [hep-ph]].

[193] E. J. Chun, J. -C. Park and S. Scopel, JCAP **1002**, 015 (2010) [arXiv:0911.5273 [hep-ph]].

[194] K. Benakli and M. D. Goodsell, Nucl. Phys. B **840**, 1 (2010) [arXiv:1003.4957 [hep-ph]].

[195] R. Fok and G. D. Kribs, Phys. Rev. D **82**, 035010 (2010) [arXiv:1004.0556 [hep-ph]].

[196] A. De Simone, V. Sanz and H. P. Sato, Phys. Rev. Lett. **105**, 121802 (2010) [arXiv:1004.1567 [hep-ph]].

[197] S. Y. Choi, D. Choudhury, A. Freitas, J. Kalinowski, J. M. Kim and P. M. Zerwas, JHEP **1008**, 025 (2010) [arXiv:1005.0818 [hep-ph]].

[198] E. J. Chun, Phys. Rev. D **83**, 053004 (2011) [arXiv:1009.0983 [hep-ph]].

[199] S. Y. Choi, D. Choudhury, A. Freitas, J. Kalinowski and P. M. Zerwas, Phys. Lett. B **697**, 215 (2011) [Erratum-ibid. B **698**, 457 (2011)] [arXiv:1012.2688 [hep-ph]].

[200] R. Davies, J. March-Russell and M. McCullough, JHEP **1104**, 108 (2011) [arXiv:1103.1647 [hep-ph]].

[201] K. Benakli, M. D. Goodsell and A. -K. Maier, Nucl. Phys. B **851**, 445 (2011) [arXiv:1104.2695 [hep-ph]].

[202] P. Kumar and E. Ponton, JHEP **1111**, 037 (2011) [arXiv:1107.1719 [hep-ph]].

[203] R. Davies and M. McCullough, Phys. Rev. D **86**, 025014 (2012) [arXiv:1111.2361 [hep-ph]].

[204] M. Heikinheimo, M. Kellerstein and V. Sanz, JHEP **1204**, 043 (2012) [arXiv:1111.4322 [hep-ph]].

[205] B. Fuks, Int. J. Mod. Phys. A **27**, 1230007 (2012) [arXiv:1202.4769 [hep-ph]].

[206] D. Goncalves-Netto, D. Lopez-Val, K. Mawatari, T. Plehn and I. Wigmore, Phys. Rev. D **85**, 114024 (2012) [arXiv:1203.6358 [hep-ph]].

[207] R. Fok, G. D. Kribs, A. Martin and Y. Tsai, arXiv:1208.2784 [hep-ph].

[208] R. Fok, arXiv:1208.6558 [hep-ph].

[209] C. Frugiuele, T. Gregoire, P. Kumar and E. Ponton, arXiv:1210.0541 [hep-ph].

[210] C. Frugiuele, T. Gregoire, P. Kumar and E. Ponton, arXiv:1210.5257 [hep-ph].

[211] K. Benakli, M. D. Goodsell and F. Staub, arXiv:1211.0552 [hep-ph].

[212] P. Agrawal and C. Frugiuele, arXiv:1304.3068 [hep-ph].

[213] E. Hardy, arXiv:1306.1534 [hep-ph].

[214] M. R. Buckley, D. Hooper and J. Kumar, arXiv:1307.3561 [hep-ph].

[215] L. Randall and R. Sundrum, Nucl. Phys. B **557**, 79 (1999) [hep-th/9810155].

[216] G. F. Giudice, M. A. Luty, H. Murayama and R. Rattazzi, JHEP **9812**, 027 (1998) [hep-ph/9810442].

[217] J. Alwall, M. Herquet, F. Maltoni, O. Mattelaer and T. Stelzer, JHEP **1106**, 128 (2011) [arXiv:1106.0522 [hep-ph]].

[218] W. Beenakker, R. Hopker, M. Spira and P. M. Zerwas, Nucl. Phys. B **492**, 51 (1997) [hep-ph/9610490].

[219] C. Borschensky, M. Krämer and A. Kulesza, http://web.physik.rwth-aachen.de/service/wiki/bin/view/Kraemer/SquarksandGluinos

[220] A. G. Cohen, T. S. Roy and M. Schmaltz, JHEP **0702**, 027 (2007) [hep-ph/0612100].

[221] I. Jack and D. R. T. Jones, Phys. Lett. B **457**, 101 (1999) [hep-ph/9903365].

[222] J. Germer, W. Hollik, E. Mirabella and M. K. Trenkel, JHEP **1008**, 023 (2010) [arXiv:1004.2621 [hep-ph]].

[223] G. Bozzi, B. Fuks, B. Herrmann and M. Klasen, Nucl. Phys. B **787**, 1 (2007) [arXiv:0704.1826 [hep-ph]].

[224] S. Weinberg, Phys. Rev. Lett. **29**, 1698 (1972).

[225] T. Hahn and M. Perez-Victoria, Comput. Phys. Commun. **118**, 153 (1999) [hep-ph/9807565].

[226] J. Hisano, K. Ishiwata, N. Nagata and M. Yamanaka, Prog. Theor. Phys. **126**, 435 (2011) [arXiv:1012.5455 [hep-ph]].

[227] M. Drees and M. Nojiri, Phys. Rev. D **48**, 3483 (1993) [hep-ph/9307208].

[228] A. Crivellin, M. Hoferichter and M. Procura, Phys. Rev. D **89**, 054021 (2014) [arXiv:1312.4951 [hep-ph]].

[229] A. Airapetian *et al.* [HERMES Collaboration], Phys. Rev. D **75**, 012007 (2007) [hep-ex/0609039].